Optimization of CLIC Final Focus System at 380 GeV and implementation studies for Ultra-low β^* at ATF2

Andrii Pastushenko

université PARIS-SACLAY

Optimization of CLIC Final Focus System at 380 GeV and implementation studies for Ultra-low β^* at ATF2

Optimisation du FFS pour le CLIC à 380 GeV et applications pour l'ultra-low β^* à l'ATF2

Thèse de doctorat de l'université Paris-Saclay

École doctorale n° 576, Particules, hadrons, énergie et noyau: instrumentation, imagerie, cosmos et simulation (PHENIICS)
Spécialité de doctorat: Physique des accélérateurs
Graduate School: Physique. Référent: Faculté des sciences d'Orsay

Thèse préparée dans l'unité de recherche **IJCLab** (Université Paris-Saclay, CNRS), sous la direction d'**Angeles FAUS-GOLFE**, Ingénieure de recherche, et le co-encadrement de **Rogelio TOMÁS GARCIA**, Ingénieur de recherche

Thèse soutenue à Paris-Saclay, le 25 Février 2022, par

Andrii PASTUSHENKO

Composition du jury

Achille STOCCHI Professeur, ICJLAB et Université Paris-Saclay	Président
Andrea LATINA Ingénieur de recherche, HDR, Centre Européen pour la Recherche Nucléaire	Rapporteur & Examinateur
Philip BURROWS Professeur, Oxford University	Rapporteur & Examinateur
Barbara DALENA Ingénieur de recherche, HDR, CEA-Saclay	Examinatrice
Toshiyuki OKUGI Professeur, Sokendai University et KEK	Examinateur
Benito GIMENO Professeur, University of Valencia	Examinateur
Angeles FAUS-GOLFE Ingénieure de recherche, ICJLAB et Université Paris-Saclay	Directrice de thèse

THESE DE DOCTORAT
NNT : 2022UPASP021

université PARIS-SACLAY

ÉCOLE DOCTORALE
Particules, hadrons, énergie et noyau : instrumentation, imagerie, cosmos et simulation (PHENIICS)

Titre: Optimisation du FFS pour le CLIC à 380 GeV et applications pour l'ultra-low β^* à l'ATF2
Mots clés: Collisionneurs linéaires, dynamique des faisceaux, luminosité, Collisionneur Linéaire Compact (CLIC)

Résumé: Le collisionneur e^+e^- est considéré comme l'un des accélérateurs les plus appropriés pour mesurer avec précision les paramètres du modèle standard aux énergies de Higgs. Actuellement, existent deux types de collisionneurs e+e- proposés : les collisionneurs circulaires et les collisionneurs linéaires. Les projets de collisionneurs circulaires e^+e^- à l'étude sont : le futur collisionneur circulaire (FCCee) et le collisionneur circulaire électron-positon (CEPC). Alternativement, les deux projets de collisionneurs linéaires e^+e^- sont : le collisionneur linéaire international (ILC) et le collisionneur linéaire compact (CLIC). Cette thèse porte sur les collisionneurs linéaires e^+e^-. Les deux projets de collisionneurs linéaires e^+e^- sont conceptuellement similaires et composés de sous-systèmes similaires. En partant de la source de particules jusqu'au point d'interaction (IP), les principaux sous-systèmes sont : les sources de positons et d'électrons, l'anneau d'amortissement (DR), le transport de l'anneau vers le linac principal (RTML), le linac principal (ML), et le Beam Delivery System (BDS). En particulier, le BDS est composé: d'une section de diagnostic, d'une section de collimation de l'énergie et du bêtatron, et d'un Final Focus System (FFS) où le faisceau est fortement focalisé jusqu'à plusieurs nanomètres au moyen d'un Final Doublet (FD) de quadrupôles. La conception du FFS de l'ILC et du CLIC est basée sur le schéma de correction de chromaticité locale. Il utilise des paires d'aimants sextupôlaires entrelacés pour corriger simultanément les chromaticités horizontales et verticales. L'Accelerator Test Facility 2 (ATF2) à KEK (Japon) est une mise en œuvre à une énergie plus bas d'un BDS comme ceux de l'ILC ou du CLIC, comprenant un système FFS. Au cours des dernières années, les réalisations uniques et exceptionnelles de l'ATF2 ont déjà vérifié la faisabilité technique minimale du FFS des collisionneurs linéaires tels que ILC ou CLIC. Cette thèse porte sur l'optimisation du système CLIC FFS pour le premier étage énergétique avec une énergie du centre de masse de 380 GeV. Dans la première partie, l'étude du raccourcissement de la FD pour réduire la chromaticité et une conception optique alternative avec un nouveau profil de dispersion dans la FFS est présentée. Dans la deuxième partie, les études analytique et expérimentale d'une optique FFS de type CLIC pour ATF2, appelée "optique ultra-low β^*" sont rapportées. Ces études comprennent : une nouvelle technique d'alignement des octupôles, un nouvel ensemble de "knobs" de réglage à "ultra-low β^*" pour mieux contrôler les aberrations et une nouvelle stratégie de réglage alternative comprenant les erreurs statiques effectuées lors des campagnes expérimentales ATF2 en juin 2019, décembre 2019 et mars 2020.

université PARIS-SACLAY

ÉCOLE DOCTORALE
Particules, hadrons, énergie et noyau : instrumentation, imagerie, cosmos et simulation (PHENIICS)

Title: Optimization of CLIC Final Focus System at 380 GeV and implementation studies for Ultra-low β^* at ATF2

Keywords: Linear collider, beam dynamics, luminosity, the Compact Linear Collider (CLIC)

Abstract: The e^+e^- collider is considered as one of the most suitable accelerator to precisely measure the Standard Model parameters at Higgs **energies**. Currently, there are two kinds of e^+e^- colliders proposed: the circular and the linear colliders. The e^+e^- circular colliders projects under study are: the Future Circular Collider (FCCee) and the Circular electron-positron Collider (CEPC). Alternatively, the two e^+e^- linear colliders projects are: the International Linear Collider (ILC) and the Compact Linear Collider (CLIC). This PhD is focused in the e^+e^- linear colliders. Both e^+e^- linear colliders projects are conceptually similar and composed of similar sub-systems. Starting from the particles source to the Interaction Point (IP) the main sub-systems are: the positron and the electron sources, the Damping Ring (DR), the Ring to Main Linac transport (RTML), the Main Linac (ML), and the Beam Delivery System (BDS). In particular the BDS is composed of: a diagnostic section, an energy and a betatron collimation sections, and a Final Focus System (FFS) where the beam is strongly focused down to several nanometers by means of a Final Doublet (FD) of quadrupoles. The design of the FFS of both ILC and CLIC is based on the local chromaticity correction scheme. It uses an interleaved pairs of sextupole magnets to simultaneously correct the horizontal and vertical chromaticities. The Accelerator Test Facility 2 (ATF2) at KEK (Japan) is an energy-scaled down implementation of a linear collider BDS like the ILC or CLIC ones, including a FFS system. During the last years the unique and outstanding ATF2 achievements have already verified the minimum technical feasibility of the FFS of linear colliders such as ILC or CLIC. This thesis focuses on the optimization of the CLIC FFS system for the first energy stage with a center-of-mass energy of 380 GeV. In the first part the study of shortening the FD to reduce chromaticity and an alternative optics design with a novel dispersion profile in the FFS is presented. In the second part the analytical and experimental tunability studies of a CLIC-like FFS optics for ATF2, called "ultra-low β^* optics" is reported. These studies include: new alignment technique for the octupoles, new set of ultra-low β^* tuning knobs to better control the aberrations and new alternative tuning strategy including the static errors performed during the ATF2 experimental campaigns in June 2019, December 2019, and March 2020.

Synthèse en français

Le collisionneur e^+e^- est considéré comme l'un des accélérateurs les plus appropriés pour mesurer avec précision les paramètres du modèle standard aux énergies du Higgs. Actuellement, existent deux types de collisionneurs e^+e^- proposés: les collisionneurs circulaires et les collisionneurs linéaires. Les projets de collisionneurs circulaires e^+e^- à l'étude sont: le futur collisionneur circulaire (FCCee) et le collisionneur circulaire électron-positon (CEPC). Dans un premier temps, le FCCee vise à fournir des collisions e^+e^- pour des énergies comprises entre 90 et 400 GeV et, à terme, offre la possibilité d'héberger un collisionneur de hadrons appelé FCC-hh avec c.o.m. de 100 TeV. Le CEPC est un projet de collisionneur e^+e^- en Chine qui cible les énergies du centre de masse compris entre 90 et 240 GeV. Alternativement, les deux projets de collisionneurs linéaires e^+e^- sont le Collisionneur linéaire compact (CLIC) et l'International Linear Collider (ILC). CLIC offre une grande extensibilité énergétique du centre de masse, de 380 GeV à 3 TeV, et ILC vise à fournir les collisions avec des énergies comprises entre 250 GeV et 500 GeV avec une éventuelle mise à niveau jusqu'à 1 TeV. La principale différence entre le collisionneur linéaire et circulaire réside dans l'approche utilisée pour accélérer les particules. Dans un collisionneur circulaire, le faisceau est accéléré dans l'anneau et traverse plusieurs fois la structure de l'accélérateur jusqu'à ce que l'énergie souhaitée soit atteinte. Dans le collisionneur linéaire, le faisceau ne se propage qu'une seule fois à travers la structure accélératrice. Les collisionneurs circulaires peuvent accueillir plus d'une expérience, mais l'énergie maximale est limitée par les pertes dues au rayonnement synchrotron (SR). Afin de pouvoir fournir l'énergie aux particules légères, telles que les électrons (avec l'énergie de repos de 511 keV), il faut avoir un rayon d'anneau suffisamment grand. Dans le cas du FCCee, la circonférence de l'anneau devrait être de 100 km. Les collisionneurs circulaires surpassent les collisionneurs linéaires à basse énergie, mais ils ne peuvent pas fournir la même extensibilité énergétique que les collisionneurs linéaires en raison de SR. Cela s'applique également au coût total de la machine. Le coût estimé du collisionneur linéaire évolue linéairement avec l'énergie, et dans le cas du collisionneur circulaire, il est quadratique sur l'énergie. De plus, les faisceaux pourraient être polarisés dans des collisionneurs linéaires, ce qui améliore considérablement la précision des mesures. Cette thèse se concentre uniquement sur les collisionneurs linéaires e^+e^-. Les deux projets de collisionneurs linéaires e^+e^- de l'ILC et du CLIC sont conceptuellement similaires et composés de sous-systèmes similaires. Partant de la source des particules jusqu'au point d'interaction (IP), les principaux sous-systèmes sont les sources de positrons et d'électrons, l'anneau d'amortissement (DR), le transport

de l'anneau vers le linac principal (RTML), le linac principal (ML), et le Beam Delivery System (BDS). En particulier, le BDS est composé: d'une section de diagnostic, de sections d'énergie et de collimation des bêtatrons, et d'un Final Focus System (FFS) où le faisceau est fortement focalisé jusqu'à plusieurs nanomètres au moyen d'un Final Doublet (FD) de quadrupôles. La conception du FFS de l'ILC et du CLIC est basée sur le schéma de correction de chromaticité locale. Il utilise des paires entrelacées d'aimants sextupôles pour corriger simultanément les chromaticités horizontales et verticales. Le sextupôle "apparié" assure l'annulation des aberrations géométriques, et la dispersion est produite par les dipôles situés entre les deux. L'Accelerator Test Facility 2 (ATF2) à KEK (Japon) est une mise en œuvre à énergie réduite d'un collisionneur linéaire BDS, comme ceux de l'ILC ou du CLIC, y compris un système FFS. Au cours des dernières années, les réalisations uniques et exceptionnelles d'ATF2 ont déjà vérifié la faisabilité technique minimale du FFS de collisionneurs linéaires tels que ILC ou CLIC. Cette thèse couvre sur l'optimisation du FFS de CLIC à 380 GeV et les études d'implémentation de l'optique "ultra-low β_y^*" à ATF2. Dans la première partie, l'étude du raccourcissement du FD pour réduire la chromaticité et une conception d'optique alternative avec un nouveau profil de dispersion dans le FFS est expliquée. Dans la deuxième partie, les études analytiques et expérimentales d'accordabilité d'une optique FFS de type CLIC pour ATF2, appelée optique "ultra-low" β^* sont rapportées. Ces études incluent une nouvelle technique d'alignement pour les octupôles, un nouvel ensemble de "knobs" de réglage "ultra-low β^*" pour un meilleur contrôle des aberrations, et une nouvelle stratégie de réglage alternative, y compris les erreurs statiques effectuées lors des campagnes expérimentales ATF2 en juin 2019, décembre 2019 et mars 2020.

La première partie du travail consiste à optimiser l'optique FFS de CLIC à l'étage d'énergie initiale de 380 GeV. La partie cruciale du FFS est le FD. Il est composé de 2 quadrupôles, à savoir QF1 et QD0. QD0 est le dernier quadrupôle avant IP. La distance entre QD0 et IP est de L^*, et dans le cas de CLIC, elle est de 6 m pour les deux options 380 GeV et 3 TeV. Pour cette valeur de L^*, QD0 est situé complètement à l'extérieur du détecteur, et une telle conception est généralement appelée optique "Longer L^*". Il est maintenant considéré comme une référence pour CLIC, et les études antérieures ont été consacrées à la mise à l'échelle de l'ancien FFS avec L^* de 4.3 m vers la nouvelle version avec 6 m. Cependant, il a également été indiqué que QF1 et QD0, dans une telle conception, ont une force magnétique inférieure à celle du reste des aimants BDS. Il est également bien en dessous de la limite que QD1 et QD0 peuvent supporter. Le champ de "pole tip" de QF1 et QD0 est estimé à 0.23 T et 0.68 T. Dans le cas particulier de l'aimant QD0 de conception "hybride", le champ pourrait atteindre 2.2 T. Nous avons décidé de réduire la longueur de QF1 et QD0 pour équilibrer leurs forces et réduire la chromaticité qu'ils génèrent. Ces manipulations affectent l'optique du faisceau et par conséquent la taille et la luminosité du faisceau à l'IP. Donc, tout d'abord, nous avons réapparié les forces des quadrupôles dans le FFS pour fournir les paramètres Twiss conçus à l'IP. Pour cela, nous avons utilisé MAD-X. Le schéma de correction de chromaticité locale nécessite que la même quantité de chromaticité horizontale soit générée en amont que celle générée par le FD. Il

est nécessaire d'annuler simultanément la chromaticité horizontale et la dispersion d'ordre 2^{em}. Les modifications des forces des quadrupôles dans le FFS ont changé l'équilibre des chromaticités, il faut donc le restaurer. Dans le même temps, tout changement dans les forces FD affecterait directement les paramètres Twiss à l'IP, donc la seule option est de modifier le réseau en amont du FD. Nous avons étudié comment la petite taille du faisceau à l'IP change lorsque la chromaticité horizontale en amont n'est pas optimale. Le modèle analytique évalué dans cette thèse montre que la plus petite taille de faisceau de second ordre pouvant être obtenue avec les sextupôles est une fonction quadratique de la chromaticité horizontale en amont. Cela signifie qu'en évaluant la taille du faisceau pour l'ensemble des chromaticités en amont, nous pouvons estimer l'optimum en appliquant l'ajustement parabolique. La valeur obtenue doit être proche de la chromaticité horizontale FD. Pour régler la chromaticité différente en amont, on modifie la distance entre le FD et les dipôles situés en amont. Il permet de changer le niveau des fonctions bêta dans le FFS, ce qui a un impact direct sur la chromaticité. Pour chaque valeur de chromaticité, nous adaptons les paramètres de Twiss à l'IP et réduisons autant que possible la taille du faisceau de second ordre vers la cible. Pour estimer la taille du faisceau, nous utilisons Mapclass. Il prend la carte de transfert entre l'entrée BDS et l'IP et renvoie la taille du faisceau. La carte de transfert est évaluée avec MAD-X et PTC. La plus petite taille de faisceau est ensuite trouvée en itérant les forces des sextupôles dans MAD-X. Pour trouver la chromaticité optimale en amont, nous avons dû déplacer le FD de 4.75 m plus loin des dipôles. De plus, nous optimisons la taille du faisceau à l'IP en utilisant la carte de transfert de cinquième ordre. Ceci est fait pour s'assurer que les aberrations d'ordre élevé sont également supprimées. Habituellement, il sature à partir du cinquième ordre. Les tailles de faisceau obtenues sont $\sigma_x^* = 143.02$ nm et $\sigma_y^* = 2.59$ nm. La taille du faisceau cible ou dite linéaire (évaluée à partir des paramètres de Twiss) est $\sigma_x^* = 143$ nm et $\sigma_y^* = 2.38$ nm. En comparaison avec l'optique du FD d'origine, on n'a plus besoin d'octupôles. La luminosité évaluée pour cette optique à l'aide de Placet et Guinea-Pig est de 1.66×10^{34} $\text{cm}^{-2}\text{s}^{-1}$. La luminosité peak ou la luminosité qui inclut uniquement les collisions avec une énergie de collision qui ne diffère pas de l'énergie cible de plus de 1 % est de 0.96 $\times10^{34}$ $\text{cm}^{-2}\text{s}^{-1}$. Plus la dispersion aux emplacements des sextupôles est grande, plus les sextupôles sont faibles pour annuler la chromaticité, et plus les aberrations sont faibles à l'IP. D'autre part, un niveau de dispersion élevé nécessite des dipôles plus puissants et conduit finalement à une perte d'énergie et à une croissance de l'émittance du faisceau en raison de la SR. Ces deux effets doivent être équilibrés afin d'atteindre la luminosité la plus élevée. Pour trouver l'optimum, nous modifions le niveau de dispersion par étapes en mettant à l'échelle les angles de courbure des dipôles dans le FFS et en évaluant la luminosité. Dans les calculs, les champs dipolaires ont été balayées dans la plage relative de 0.37 à 1.31 de leur intensité d'origine avec un pas de 6.25 %. Pour chaque force de dipôle, nous réapparions les forces des sextupôles en minimisant la taille du faisceau de cinquième ordre, puis évaluons la luminosité. Au scan, on a obtenu que le gain de luminosité était négligeable, on a donc gardé la même dispersion. Bien que la luminosité obtenue soit la même que dans la conception avec le FD d'origine, la nouvelle optique a une plus grande bande passante

d'énergie et ne nécessite plus d'octupôles. De plus, il a été trouvé qu'en inverse la force de l'un des quadrupôles du FFS, à savoir QD6B, un nouveau profil de dispersion peut être établie pour le FFS. Il fournit une dispersion supérieure de 20 % dans la région FD pour les mêmes angles de flexion et pourrait éventuellement permettre d'assouplir les paramètres du sextupôle. Pour explorer les avantages possibles, nous devons réadapter l'optique à nouveau. Comme pour l'optique précédente, nous adaptons les paramètres de Twiss à l'IP et effectuons le balayage de la chromaticité horizontale en amont. Mais dans ce cas, nous effectuons les deux simultanément en définissant la contrainte sur la chromaticité en amont à l'intérieur de la correspondance de Twiss. La chromaticité est estimée à partir de l'approximation de la lentille mince. En appliquant l'ajustement parabolique au scan, nous avons réussi à réduire la taille du faisceau à l'IP à $\sigma_x^* = 144.31$ nm et $\sigma_y^* = 3.92$ nm. On peut remarquer qu'ils sont loin de la cible. En étudiant comment la taille du faisceau à l'IP dépend de l'ordre de la carte de transfert, nous avons conclu qu'il fallait en outre ajuster l'emplacement du sextupôle SD5 et introduire la paire de décapoles. Le premier est fait pour traiter les termes de couplage du troisième ordre dans la taille du faisceau vertical. Dans les calculs, SD5 est décalé d'un pas de 1 m suivit de l'adaptation de la taille du faisceau du cinquième ordre. L'optimum a été trouvé à environ 6 m loin de l'emplacement d'origine, vers l'IP. Et les décapoles sont nécessaires pour corriger les aberrations résiduelles du quatrième ordre dans les plans horizontaux et verticaux. Après ces optimisations, les tailles de faisceau sont de 143.82 nm × 2.67 nm. Enfin, le balayage de dispersion a montré que nous pouvons détendre les angles de courbure des dipôles de 12.5 % pour maximiser les luminosités: $\mathcal{L}_{total} = 1.74\times10^{34}$ cm $^{-2}$s^{-1} et $\mathcal{L}_{peak} = 1.01\times10^{34}$ cm^{-2}s^{-1}. C'est 5% plus grand que la luminosité maximale que nous avions dans les conceptions précédentes. Le principal inconvénient de cette optique est la plus petite bande passante d'énergie de 0.3% par rapport à 0.35% et 0.42% pour l'optique avec FD d'origine et FD court, respectivement. Enfin, nous avons vérifié que deux nouvelles optiques sont compatibles avec la conception actuelle de la section de collimation du bêtatron. Dans le BDS, il a l'intention de nettoyer le halo du faisceau de sorte que ni les particules ni les photons émis n'atteignent QF1, QD0 ou l'intérieur parti du détecteur. Dans la conception actuelle, il supprime les particules avec des décalages transversaux supérieurs à $15\sigma_x$ dans le plan horizontal et $55\sigma_y$ dans le plan vertical. En simulant le halo du faisceau et en le suivant à travers la région FD et IP, nous avons vérifié que la collimation fonctionne avec la nouvelle optique. Nous avons également évalué l'ouverture pour l'ensemble du BDS et pour les quadrupôles FD en particulier. Nous avons fixé les gradients de QF1 et QD0 à 13.3 T/m et 73.7 T/m, respectivement. Leurs champs de pointe polaire sont évalués à 0.51 T pour QF1 et 1.99 T pour QD0.

La deuxième partie du travail se concentre sur les études de réglage de l'ATF2 au KEK. ATF2 a été construit en 2009 en prolongeant la ligne d'extraction ATF avec une ligne de lumière de test FFS. L'optique de l'ATF2 est une version à l'échelle de l'optique FFS à utiliser en ILC. Cette optique est appelée optique nominale. À la fin du FFS, une "IP virtuelle" est située au point de focalisation du FD. L'un des principaux objectifs d'ATF2 est de réduire le faisceau d'électrons au niveau du nanomètre dans le plan vertical

à l'adresse IP virtuelle. Le but de mon étude est de prouver l'accordabilité du FFS avec un niveau de chromaticité similaire à celui du CLIC. Pour cette raison, une optique spécifique est utilisée, appelée optique "ultra-low β_y", qui fonctionne à une fonction bêta IP verticale quatre fois plus petite par rapport à l'optique ATF2 nominale. La taille du faisceau vertical cible pour l'optique nominale est de 37 nm, tandis que pour l'optique "ultra-low β_y", elle est d'environ 20 nm. Pour ce faire, il faut l'instrumentation appropriée pour mesurer une taille de faisceau aussi minuscule. Pour cela, ATF2 a adopté une version améliorée d'un moniteur Shintake, précédemment utilisé à la FFTB. Il permet de mesurer les tailles de faisceau dans la plage de 6 μm à 25 nm, et il est crucial pour les opérations de réglage de la taille du faisceau. Pour régler la taille du faisceau, nous utilisons un ensemble de soi-disant "knobs" de réglage pour corriger les aberrations au niveau de l'IP virtuelle. Chaque "knob" corrige indépendamment les aberrations associées et utilise soit les décalages transversaux des sextupôles, soit leurs variations de force. Dans les opérations de réglage passées avec une optique "ultra-low β_y", nous avons utilisé les "knobs" de réglage conçus pour l'optique nominale. Afin d'améliorer l'efficacité du réglage, nous construisons les "knobs" de réglage spécifiquement pour l'optique "ultra-low". Dans les simulations, nous avons décalé chaque sextupôle dans la ligne de lumière ATF2 et observé le changement de la corrélation des coordonnées à l'IP. De plus, nous construisons les matrices de réponse pour chaque décalage. Les "knobs" sont évalués en appliquant la décomposition en valeurs singulières (SVD) sur les matrices de réponse. De plus, nous les normalisons de manière à ce que l'amplitude 1.0 du "knob" corresponde à la contribution de la taille du faisceau de 100 nm. Nous appelons ces "knobs" des "knobs" linéaires car ils corrigent les décalages de taille, la dispersion et le couplage. Les non linéaires sont construits de manière similaire sur les variations de forces des sextupôles. Ils sont destinés à corriger la chromaticité verticale, les aberrations géométriques, etc. Pour s'assurer que les "knobs" ont été correctement construits, nous avons vérifié qu'ils sont orthogonaux. Ensuite, nous les avons testés dans les simulations de réglage pour explorer les avantages possibles de l'utilisation d'un nouvel ensemble de "knobs" de réglage à ATF2. Nous avons réalisé cela avec le logiciel écrit en langage de script Python, qui utilise Mapclass et est interfacé à MAD-X et PTC. Nous avons pris en compte les désalignements des aimants et des BPM, les rouleaux, les erreurs de force, la précision BBA et les erreurs de lecture pour les erreurs statiques. Par souci de comparaison, nous effectuons également les simulations de réglage avec les "knobs" nominales. Dans les deux cas, la valeur médiane est d'environ 26 nm. Néanmoins, une amélioration apparaît pour les tailles de faisceau supérieurs à 70 nm. Le réglage avec les "knobs" "ultra-low" est plus résistant au blocage d'une grande taille de faisceau ($>$ 70-100 nm). Le pourcentage de machines qui n'ont pas atteint 100 nm lorsqu'elles sont réglées avec les nouveaux "knobs" est de 4 %, contre 12 % lorsque des "knobs" nominaux sont utilisés. Suite à l'installation de la paire d'octupôles en 2017, l'étude de la technique d'alignement efficace était en cours. Les octupôles sont d'une extrême importance pour l'optique "ultra-low" car ils peuvent annuler les aberrations chromatiques du troisième ordre. Les sources dominantes de ces aberrations sont les composantes multipolaires du QD0FF (le dernier quadrupôle avant l'IP virtuelle) et les champs marginaux dans le FD.

Dans cette thèse, nous avons étudié les différentes possibilités d'alignement des octupôles. Il comprend le Beam-Based Alignment (BBA) traditionnel et la nouvelle technique basée sur le mouvement de point focalize à l'IP virtuelle. Un octupôle mal aligné génère un coup de pied quadrupolaire normal, qui se propage à l'IP virtuel et provoque un décalage longitudinal de la point focalize. Le changement de point focalise est ensuite mesuré en effectuant le scan du "knob" dédié avec le moniteur Shintake. Alors que l'application du BBA traditionnel pourrait être problématique en raison de la précision limitée des BPM et également en raison de la gigue, le nouvel alignement avec le décalage de la taille offre une précision d'environ 100 μm. Trois campagnes dédiées de réglage optique "ultra-low β_y" ont été réalisées au cours de cette thèse en juin 2019, décembre 2019 et mars 2020. En juin 2019, la taille du faisceau a été réduite à 51$\pm$6 nm et s'est stabilisée au niveau de 60 nm pendant une longue période. Malheureusement, le dernier mode de l'IPBSM, qui permet de mesurer la taille du faisceau dans la gamme 25-100 nm, n'était pas accessible en décembre 2019 et mars 2020. Ainsi, dans ces deux opérations, le faisceau a été réglé jusqu'à environ $<$100 nm. De plus, lors de ces sessions de réglage, un alignement OCT2FF utilisant le mouvement de point focalise a été effectué et le centre magnétique a été évalué à (87$\pm$135, 78$\pm$49) μm en décembre 2019 et (-161$\pm$57, 128$\pm$108) μm en mars 2020. Pour explorer le potentiel de réglage des octupôles, des performances stables du moniteur Shintake sont nécessaires. En décembre 2019, les performances de la machine ont été gâchées par la présence de dérives d'orbite rapides qui n'ont pas pu être compensées par la rétroaction. Le premier test des nouveaux "knobs" de réglage a été effectué en décembre 2019, et toute la session de réglage de mars 2020 a été effectuée avec des "knobs" "ultra-low". Ces nouveaux "knobs" de réglage se sont avérés plus robustes pour le réglage du faisceau et semblent prometteurs pour les futures opérations de réglage du faisceau.

Abstract

The e^+e^- collider is considered as one of the most suitable accelerator to precisely measure the Standard Model parameters at Higgs energies. Currently, there are two kinds of e^+e^- colliders proposed: the circular and the linear colliders. The e^+e^- circular colliders projects under study are: the Future Circular Collider (FCCee) and the Circular electron-positron Collider (CEPC). Alternatively, the two e^+e^- linear colliders projects are: the International Linear Collider (ILC) and the Compact Linear Collider (CLIC). This PhD is focused in the e^+e^- linear colliders. Both e^+e^- linear colliders projects are conceptually similar and composed of similar sub-systems. Starting from the particles source to the Interaction Point (IP) the main sub-systems are: the positron and the electron sources, the Damping Ring (DR), the Ring to Main Linac transport (RTML), the Main Linac (ML), and the Beam Delivery System (BDS). In particular the BDS is composed of: a diagnostic section, an energy and a betatron collimation sections, and a Final Focus System (FFS) where the beam is strongly focused down to several nanometers by means of a Final Doublet (FD) of quadrupoles. The design of the FFS of both ILC and CLIC is based on the local chromaticity correction scheme. It uses an interleaved pairs of sextupole magnets to simultaneously correct the horizontal and vertical chromaticities. The Accelerator Test Facility 2 (ATF2) at KEK (Japan) is an energy-scaled down implementation of a linear collider BDS like the ILC or CLIC ones, including a FFS system. During the last years the unique and outstanding ATF2 achievements have already verified the minimum technical feasibility of the FFS of linear colliders such as ILC or CLIC. This thesis focuses on the optimization of the CLIC FFS system for the first energy stage with a center-of-mass energy of 380 GeV. In the first part the study of shortening the FD to reduce chromaticity and an alternative optics design with a novel dispersion profile in the FFS is presented. In the second part the analytical and experimental tunability studies of a CLIC-like FFS optics for ATF2, called "ultra-low β^* optics" is reported. These studies include: new alignment technique for the octupoles, new set of ultra-low β^* tuning knobs to better control the aberrations and new alternative tuning strategy including the static errors performed during the ATF2 experimental campaigns in June 2019, December 2019, and March 2020.

Acknowledgements

I wish to thank everyone who helped and supported me throughout the last three years of preparation of this PhD work.

First, I wish to express my foremost thanks go to my supervisors, Dr. Rogelio Tomás from CERN and Dr. Angeles Faus-Golfe from IJCLab. Their guidance and motivation were essential for the successful completion of the PhD project. The experience I received under their supervision is invaluable.

My sincere gratitude to Renjun Yang and Fabien Plassard for sharing their knowledge on CLIC and ATF2, that I extensively benefited from. Also, I wish to thank Vera Cilento for assisting with the ATF2 beam tunning and for the fruitful discussions on the CLIC optics design.

I would like to express my strong gratitude to ATF and KEK staff for their help and hospitality. In particular, I want to thank Toshiyuki Okugi, Kiyoshi Kubo, Nobuhiro Terunuma, Takashi Naito, and Shigeru Kuroda for teaching me how to operate the ATF2 and for their invaluable help during ATF2 tuning runs with Ultra-low β^* optics.

Finally, I would like to deeply thank my parents, sister, and friends for their endless encouragement and support.

Contents

Chapter 1

Introduction to FFS systems of FLCs

1.1 Introduction

Particle colliders are of paramount importance for High Energy Physics (HEP) advances. All the heavier particles of the Standard Model (SM) have been produced in the colliders. In particular, the tau lepton and the charm quark at SPEAR [1] in the 70s, the $W^{\pm}$ and Z^0 bosons at the SppS [2] in the 80s, the top quark at the Tevatron in the 90s [3], and recently in 2012 the Higgs boson at the LHC [4, 5]. Currently, LHC is being prepared for its Run 3 (2022), where the integrated luminosity is expected to be approximately 350 fb^{-1} for the collisions with a center-of-mass energy of 13-14 TeV. After Run 3, a major LHC upgrade is foreseen to occur in 2025, referred to as High Luminosity LHC (HL-LHC) [6]. After the upgrade, the luminosity is expected to increase by more than a factor of 5 with respect to the nominal luminosity.

As discussed in the key points of the 2020 Update of the European Strategy for Particle Physics, the next e^+e^- collider or a so-called Higgs factory is a priority for the HEP community in the "post-LHC" period [7]:

"An electron-positron Higgs factory is the highest-priority next collider. For the longer term, the European particle physics community has the ambition to operate a proton-proton collider at the highest achievable energy. Accomplishing these compelling goals will require innovation and cutting-edge technology:

- *the particle physics community should ramp up its R&D effort focused on advanced accelerator technologies, in particular, that for high-field superconducting magnets, including high-temperature superconductors;*

- *Europe, together with its international partners, should investigate the technical and financial feasibility of a future hadron collider at CERN with a centre-of-mass energy of at least 100 TeV and with an electron-positron Higgs and electroweak factory as a possible first stage. Such a feasibility study of the colliders and related infrastructure should be established as a global endeavour and be completed on the timescale of the next Strategy update.*

The timely realisation of the electron-positron International Linear Collider (ILC) in Japan would be compatible with this strategy and, in that case, the European particle physics community would wish to collaborate."

Such a collider is more suitable for the precise measurements of the SM parameters due to the lower experimental background among others. Currently, two kinds of e^+e^- colliders at Higgs energies are being proposed: the circular and the linear ones. In the case of the circular collider, two projects are under study: the Future Circular Collider (FCC) [8] and the Circular Electron Positron Collider (CEPC) [9]. In a first step the FCCee aims to provide e^+e^- collisions for energies between 90 and 400 GeV and, in the long-term, offers the possibility to host a hadron collider called FCC-hh with c.o.m. of 100 TeV [10]. The CEPC is a project of e^+e^- collider in China that targets center-of-mass energies in the range between 90 and 240 GeV. Alternatively, the two projects of linear e^+e^- colliders : the Compact Linear Collider (CLIC) [11] and the International Linear Collider (ILC) [12]. CLIC offers a great center-of-mass energy extendability, from 380 GeV up to 3 TeV and ILC aims to provide the collisions with the energies between 250 GeV and 500 GeV with the possible upgrade up to 1 TeV.

The main difference between the linear and circular collider is in the approach used to accelerate the particles. In a circular collider, the beam is accelerated in the ring and passes through the accelerator structure multiple times until the desired energy is reached. In the linear collider, the beam propagates through the accelerating structure only once. Circular colliders can host more than one experiment, but the maximum energy is limited by the losses due to the Synchrotron Radiation (SR). As discussed in Sec. 1.4.5, the instantaneous radiated power by a bent particle is given by: $P_\gamma \propto E^4/(\rho^2 m^3)$. In order to be able to deliver the energy to light particles, such as the electrons (rest energy $m_e c^2 = 511$ keV), one needs to have a large enough ring radius. In the case of the FCCee, the ring circumference is expected to be 100 km.

The luminosity over the center-of-mass energy for the proposals of the future Higgs factories are shown in Fig. 1.1. While circular colliders surpass the linear colliders at low energies, they cannot provide the same energy extendibility as the linear colliders due to SR. It also applied to the total cost of the machine. The estimated cost of the linear collider scales linearly with the energy, and in the case of the circular collider, it is quadratic on the energy. Furthermore, beams could be polarized in linear colliders, which significantly improves the measurement precision.

1.1.1 Linear Collider main sub-systems

Both proposals of e^+e^- linear colliders, CLIC, and ILC are conceptually similar and composed of similar sub-systems. The typical structure of a half-linear collider, starting from the particles source to the Interaction Point (IP) is shown in Fig. 1.2.

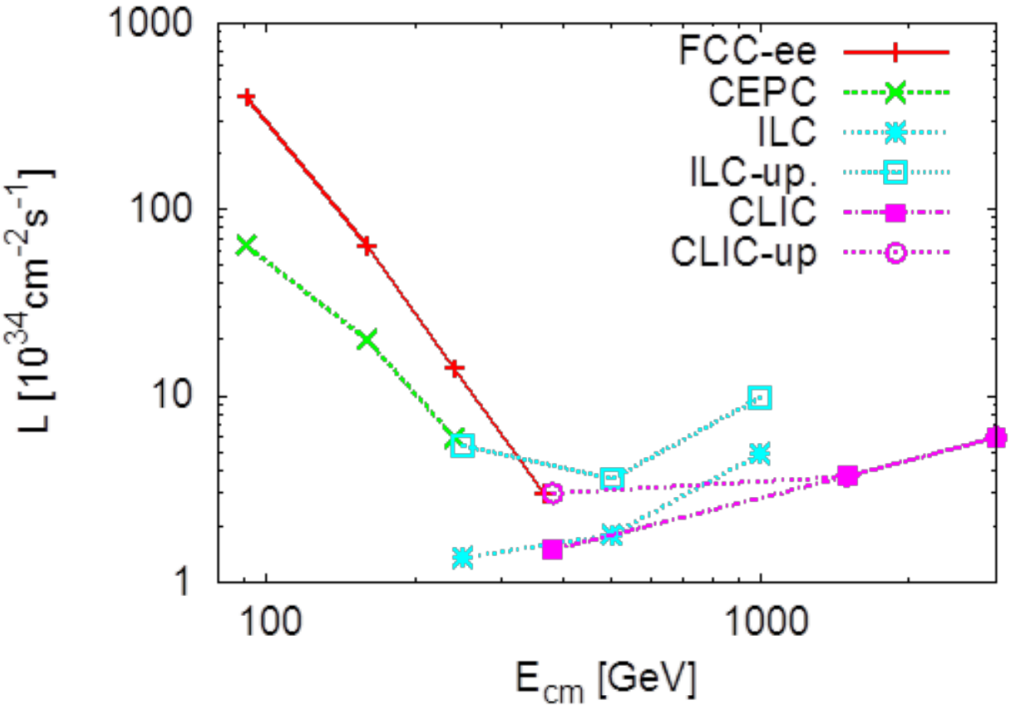

Figure 1.1: Design luminosities for the future e^+e^- colliders as function of the center-of-mass energy [13].

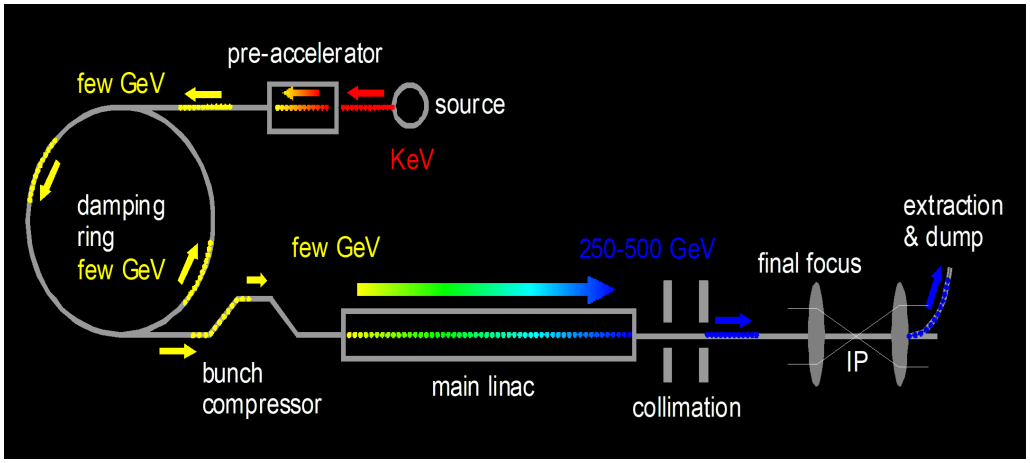

Figure 1.2: Schematic layout of a half-linear collider [14].

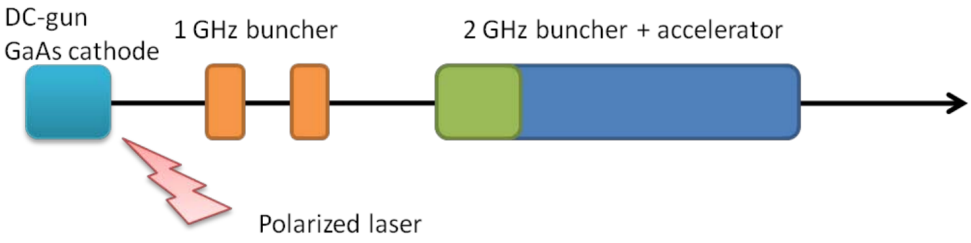

Figure 1.3: Schematic representation of the electron beams production at CLIC [11].

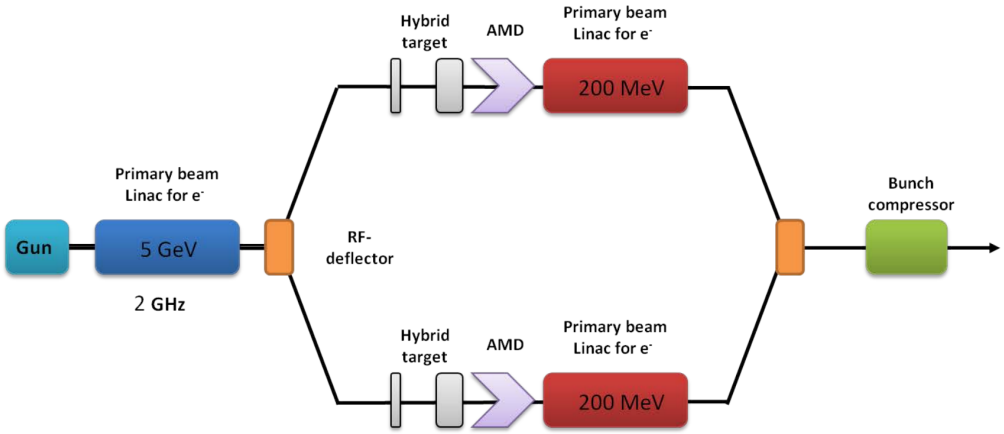

Figure 1.4: Schematic representation of the positron beams production for CLIC 500 GeV [11].

e^- and e^+ sources

The e^- are extracted from a cathode through the interaction with an intense laser in a DC gun as shown in Fig. 1.3 taking CLIC as an example. After, the beam is pre-bunched and pre-accelerated to meet the requirements of the Damping Ring (DR).

The production of e^+ is based on the process of e^+e^- pair production and has a different implementation in CLIC and ILC. At CLIC, the photon beam is generated in the crystal by axial channeling radiation. After, the photons hit an amorphous tungsten target, where positrons are extracted (see Fig. 1.4). In the case of ILC, the photon beam is produced when the electron beam passes through the superconducting helical undulator. The e^+e^- pairs are generated after the photons interact with the Ti-alloy target. In both projects, the electron beam can be polarized if needed.

Damping Rings (DR)

In the DRs, the transverse emittance of the e^- and e^+ beams is reduced by several orders of magnitude by means of damping. The energy that the beam losses in the bending sections and in the dedicated wigglers is compensated only in the longitudinal plane. Small

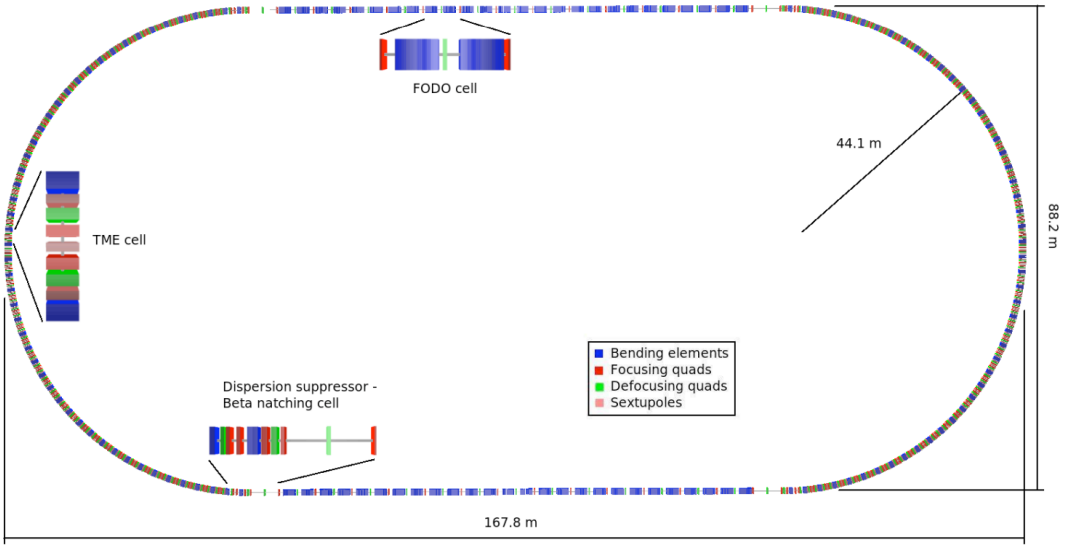

Figure 1.5: Schematic layout of the CLIC 500 GeV main Damping Ring [11].

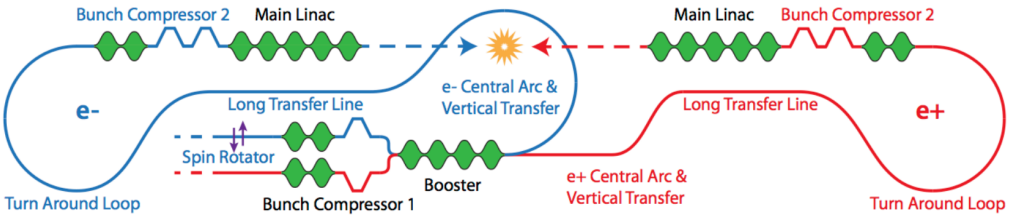

Figure 1.6: Sketch of the RTML system for CLIC 380 GeV [15].

emittances are needed to achieve the nanometer-level beam size at the Interaction Point (IP). The schematic layout of the DR for CLIC 500 GeV is shown in Fig. 1.5.

Ring to Main Linac Transport (RTML)

The RTML system transports the beams from the DR to the entrance of the Main Linac. It serves several goals: preserve the small emittance from the DR, increase the beam energy, and reduce the bunch length by means of bunch compressors. The schematic layout of RTML of CLIC 380 GeV is shown in Fig. 1.6 as example.

Main Linac (ML)

In the ML, the beams are accelerated to the design energy while keeping the small emittance. It is composed of multiple sections of the coupled Radio-Frequency (RF) cavities. In the case of ILC, 1.3 GHz superconducting RF (SCRF) cavities with an average gradient of 31.5 MV/m are planned to be used (see Fig. 1.7). Alternatively, CLIC utilizes normal conducting RF (NCRF) cavities with an average gradient of 72 MV/m achieved by means

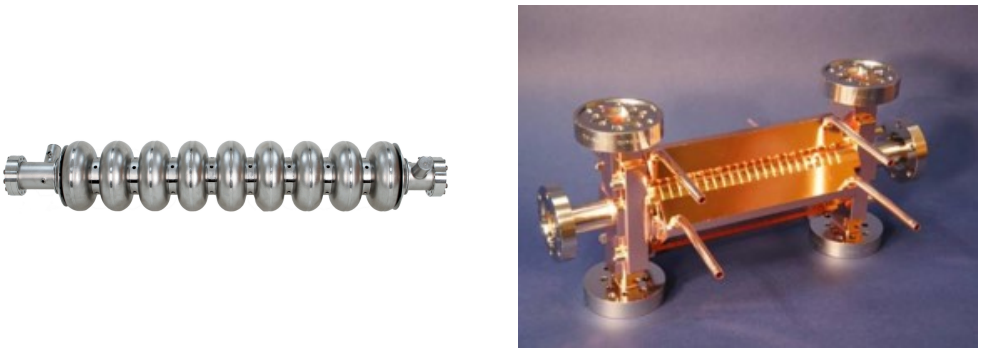

Figure 1.7: ILC SC RF cavity [12] (left) and CLIC NC RF cavity [11] (right).

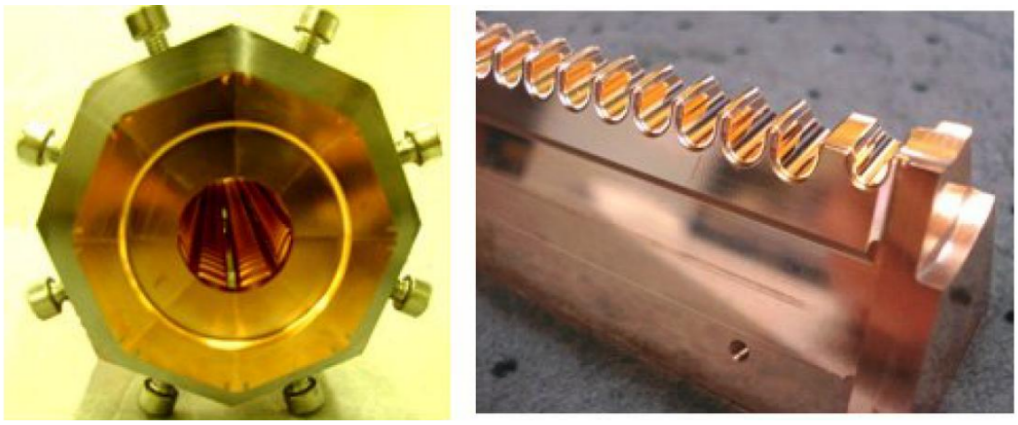

Figure 1.8: Front view of the pre-assembled PETS (left) composed of 8 octants (right) [11].

of a two-beam acceleration scheme. In this case, the power extracted in the Power Extraction and Transfer structure (PETS) (see Fig. 1.8) from the decelerated Drive Beam is delivered to the Main Beam.

Beam Delivery System (BDS)

The BDS transports the beam towards the IP. It comprises several sub-systems: the diagnostic section, the energy collimation, the betatron collimation, and the Final Focus System (FFS). As an example, the schematic layout of the BDS for CLIC 380 GeV is shown in Fig. 1.9. In the energy collimation, the particles with an energy offset larger than the designed value are removed from the beam. Similarly, the betatron collimation is designed to remove the halo particles with too large transverse offsets. In the FFS, the beam is strongly focused down to several nanometers with a pair of quadrupoles QF1 and QD0, referred to as a Final Doublet (FD). Since the beam coming from the ML is not fully monochromatic, the particles with different energies are focused differently, producing a wide spot at the IP. In this sense, the FFS is one of the most challenging systems of a LC

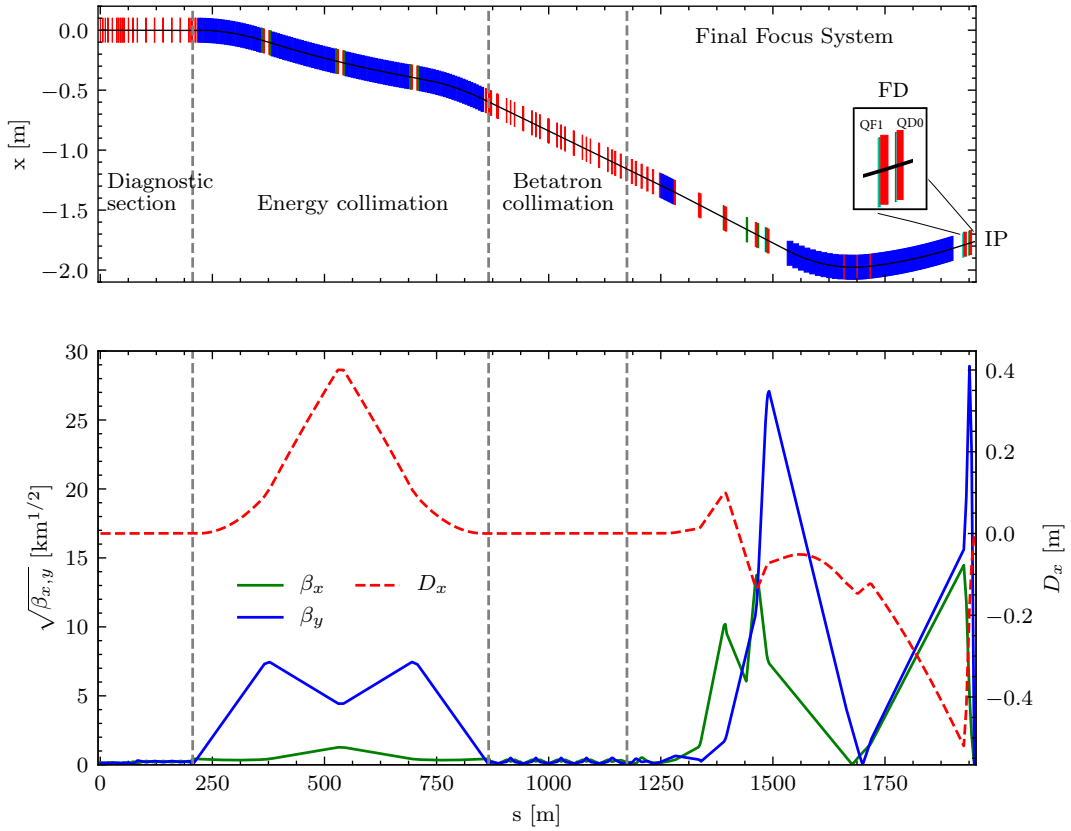

Figure 1.9: Layout (top) and optics (bottom) of the Beam Delivery system for CLIC 380 GeV. In the top figure, dipoles are shown in blue, quadrupoles in red, and sextupoles in green.

due to its extremely large beta functions (see Fig. 1.9 (bottom)). Hence, the design of the FFS is driven by the need to correct the chromatic effects, mainly produced in the FD. Both CLIC and ILC adopted a FFS design with a local chromaticity correction scheme [16], see Fig. 1.10. The full details of such an optics are described in Sec. 1.4.4.

1.2 Overview of current FLCs Projects

1.2.1 The International Linear Collider

The International Linear Collider [12] is a future e^-e^+ linear collider to be located in Japan. It relies on an ML composed of 1.3 GHz SCRF accelerating cavities with an average gradient of 31.5 MV/m. The same technology is implemented in the accelerating cavities of XFEL at DESY [17]. ILC aims to provide e^-e^+ collisions at the IP with a baseline configuration at 250 GeV and with potential upgrades up to 500 GeV and 1 TeV. The main parameters of the ILC are summarized in Tab. 1.1 and the schematic layout of

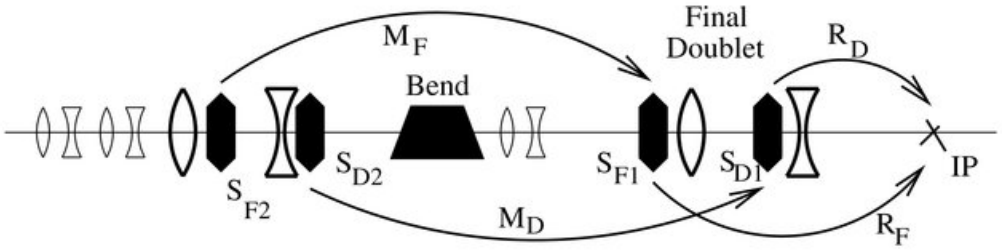

Figure 1.10: Schematic layout of the FFS with local chromaticity correction scheme [16].

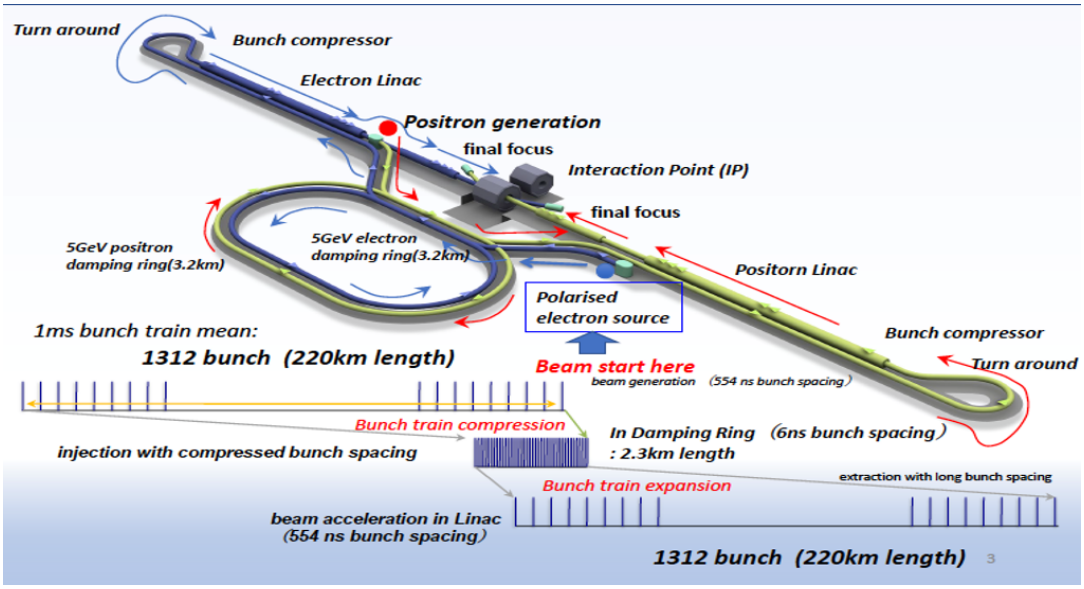

Figure 1.11: Schematic layout of the ILC with the center-of-mass energy of 250 GeV.

the baseline configuration at 250 GeV is shown in Fig. 1.11. The ILC is configured to host two detectors in a "push-pull" configuration sharing the same IP. Both detectors will be mounted on movable platforms, which would allow switching between the detectors within 24 hours.

1.2.2 The Compact Linear Collider

The Compact Linear Collider (CLIC) [11] is a future linear e^-e^+ collider to be located at CERN, aiming to provide e^-e^+ collisions up to 3 TeV center-of-mass energy [18]. In the recent update of the CLIC staging strategy [19], the initial stage of the project is foreseen to be at 380 GeV, with further upgrades to 1.5 TeV and 3 TeV as shown in Fig. 1.12. The BDS at 380 GeV was obtained by scaling down the 500 GeV lattice [20] introduced in the CDR. The physics potential of operating at 380 GeV is discussed in detail in [21]. The

Table 1.1: Summary table of the key parameters of ILC.

Center-of-mass energy [GeV]	250	500	1000
Normalized emittance (IP) $\epsilon_{n,x}/\epsilon_{n,y}$ [nm]	5000/35	10000/20	10000/30
IP beam size σ_x^*/σ_y^* [nm]	551/7.7	474/5.9	335/2.7
Bunch length σ_z [μm]	300	300	225
Number of particles in one bunch N [$\times 10^{10}$]	2.0	2.0	1.737
Number of bunches in one train N_b	1312	1312	2450
Repetition rate f [Hz]	5	5	4
Bunch separation Δt_b [ns]	554	554	366
Pulse length τ_{RF} [ms]	200	200	200
Total luminosity $\mathcal{L}$ [10^{34}cm^{-2}s^{-1}]	1.35	1.79	5.11
Peak luminosity $\mathcal{L}_{peak}$ [10^{34}cm^{-2}s^{-1}]	1.0	1.04	2.30
Main tunnel length [km]	20.5	31	40
Estimated power consumption P_{site} [MW]	111	173	300

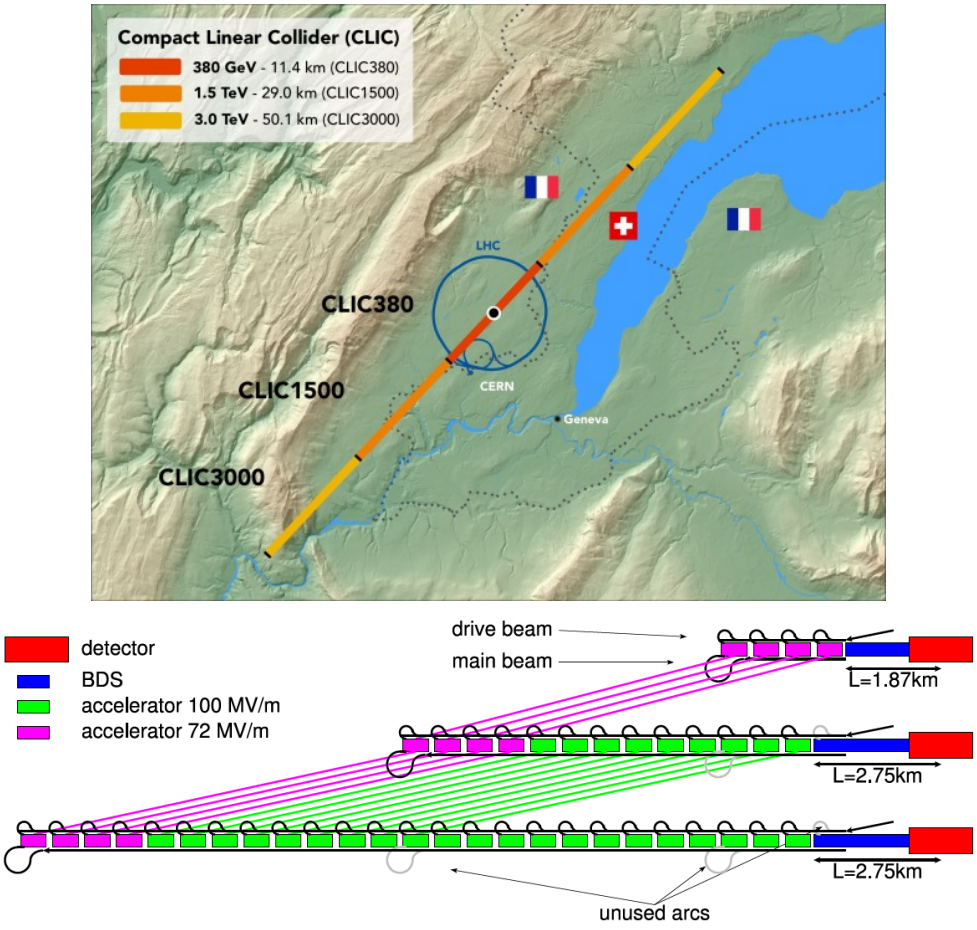

Figure 1.12: Layout of the CLIC project with the 380, 1500 and 3000 GeV energy stages [15] (top) and linacs stages (bottom).

Table 1.2: Summary table of the key parameters of CLIC.

Center-of-mass energy [GeV]	380	1500	3000
Normalized emittance (IP) $\epsilon_{n,x}/\epsilon_{n,y}$ [nm]	950/30	660/20	660/20
IP beam size σ_x^*/σ_y^* [nm]	144/2.6	60/1.5	40/0.9
Bunch length σ_z [μm]	70	44	44
Number of particles in one bunch N [$\times 10^9$]	5.2	3.72	3.72
Number of bunches in one train N_b	352	312	312
Repetition rate f [Hz]	50	50	50
Bunch separation Δt [ns]	0.5	0.5	0.5
Pulse length τ_{RF} [ns]	244	244	244
Total luminosity $\mathcal{L}$ [10^{34}cm^{-2}s^{-1}]	1.6	3.7	5.9
Peak luminosity $\mathcal{L}_{peak}$ [10^{34}cm^{-2}s^{-1}]	0.9	1.4	2
Main tunnel length [km]	11.4	29.0	50.1
Estimated power consumption P_{site} [MW]	252	364	589

main conceptual difference of this energy stage with respect to 3 TeV design is that only one drive beam complex is planned to be used for accelerating both e^-e^+. The schematic layouts of CLIC 380 GeV and 3 TeV are shown in Fig. 1.13.

In Tab. 1.2 the key parameters for each stage of CLIC are shown. All energy stages will share the same detector, called CLICdet [22]. It has a total length of 11.4 m, and including the end coil dimension, the half-length of the detector is 5.918 m. Originally, in the CDR [11] design, the last quadrupole QD0 was located inside the detector acceptance. To simplify the machine detector interface (MDI) and to exclude the need for shielding QD0 with the anti-solenoid, in the PIP [15], a so-called longer L^* optics with L^* of 6 m, (4.3 m in the CDR) has been proposed, where QD0 is entirely outside of the detector. All the details of this optics design can be founded in [23]. In this thesis, we will focus only on the baseline or first energy stage of CLIC at 380 GeV.

1.3 Test Facilities for FLCs Projects

Several test facilities have been built and are being operated in order to investigate the main techniques for FLCs. The most relevant are: the CLIC Test Facility (CTF3) at CERN and the Accelerator Test Facility 2 (ATF2) at KEK.

1.3.1 The CLIC Test Facility

The CLIC Test Facility [25] (see Fig. 1.14) was built in 2002 at CERN to demonstrate the feasibility of the two-beam acceleration scheme, which is to be used in CLIC. CTF3 consisted of: a 150 MeV e^- linac, a Delay Loop (DL) of 42 m in circumference, and a Combiner Ring (CR) of 84 m in circumference. After producing the beam of the design energy and current, it was sent into the CLIC Experimental Area (CLEX), where it was

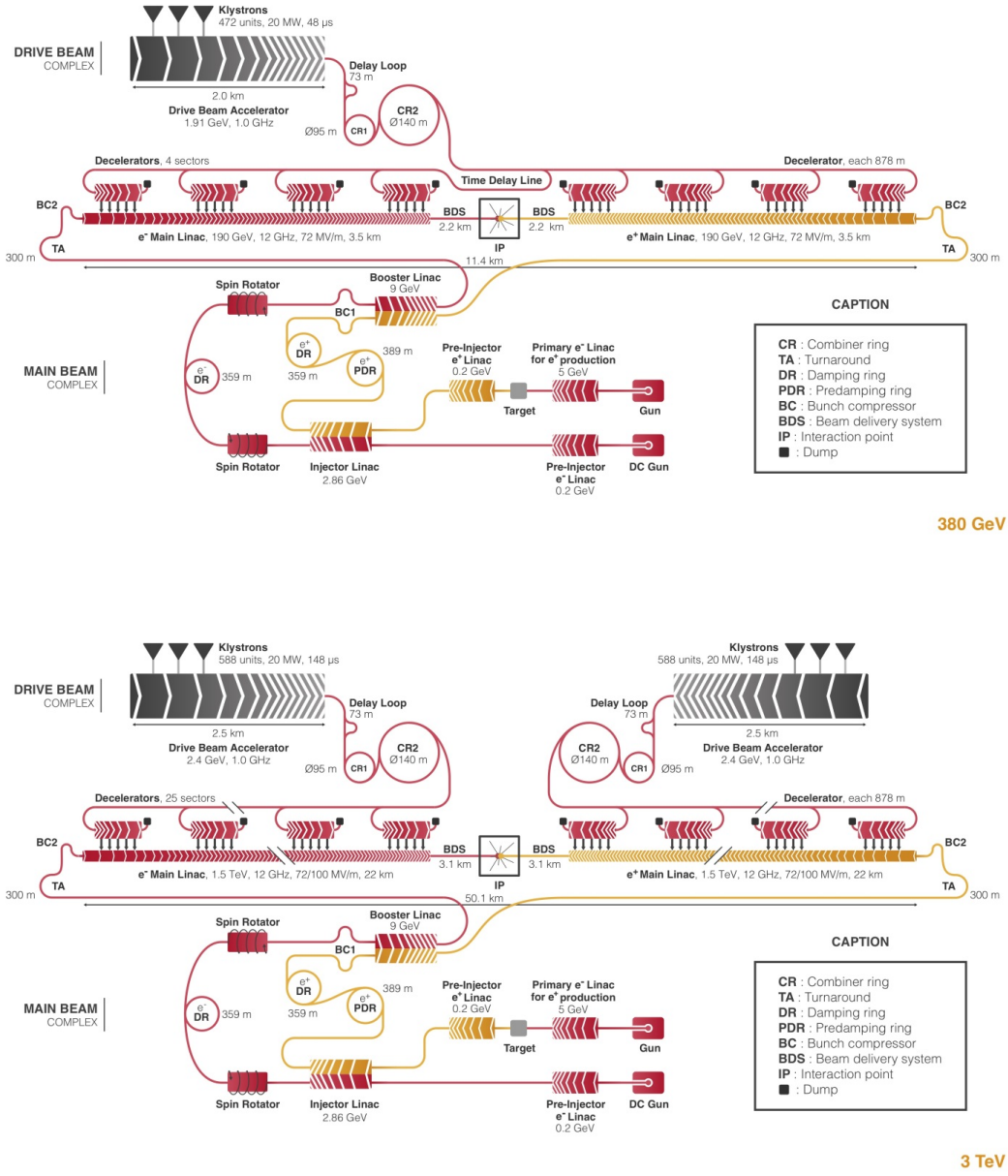

Figure 1.13: Schematic layout of CLIC 380 GeV with one drive beam complex (top) and CLIC 3 TeV with two drive beam complexes (bottom) [24].

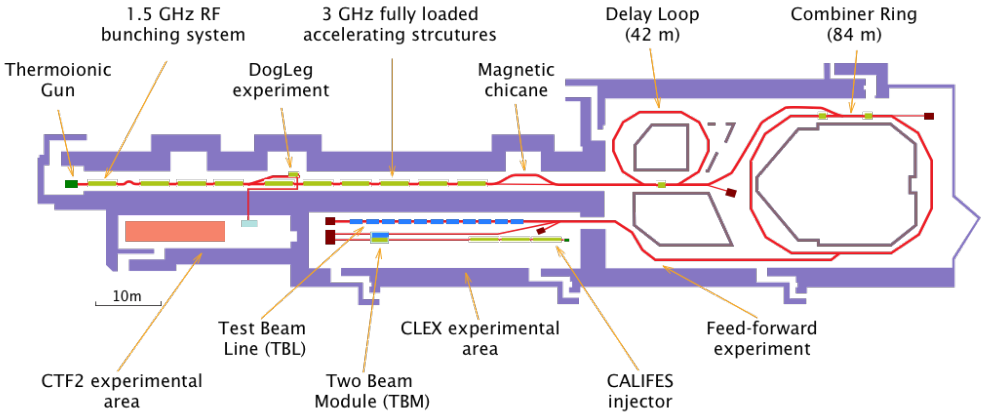

Figure 1.14: Schematic layout of the CTF3.

decelerated in order to extract the RF power at 12 GHz by means of the PETS. This power was then delivered to a probe beam into the CALIFES injector. The two main concepts explored in this test facility were the efficient generation of the high-current drive beam on one hand and the RF power production in the PETS on the other hand. A gradient up to 150 MV/m was achieved through two-beam acceleration in 2012 [26]. The beam parameters used at the CTF3 were scaled with respect to the CLIC design.

1.3.2 The Accelerator Test Facility 2

The FLCs, both CLIC and ILC, rely on the collisions at the IP with extremely small vertical beam sizes at the level of several nanometers. The two essential ingredients needed to achieve nanobeamsizes are the low emittances and the nanobeam sizes at the IP. The first was the subject of the investigation in the Accelerator Test Facility (ATF) in KEK. ATF was designed and constructed in the early 1990s and consisted of: an RF Gun, a 1.3 GeV S-band linac, a Damping Ring (DR), and an Extraction line (EXT) as shown in Fig. 1.15. In 2003, a vertical emittance of 4 pm was achieved [27]. The second, is being investigated in the Accelerator Test Facility 2 (ATF2) [29]. ATF2 was constructed in 2009 by extending the ATF extraction line with an FFS test beamline. At the end of the FFS, a "Virtual IP" is located in the focalization point of the Final Doublet (FD). In a real collider, this location will correspond to IP. The ATF2 beamline design is based on a scaled version of the FFS of ILC. It is supposed to target similar tuning difficulties that will affect the ILC operation. The two main objectives of ATF2 are:

- Achievement of 37 nm beam size: demonstration of a compact FFS based on local chromaticity correction and maintenance of the small beam size.
- Control of beam position: demonstration of beam orbit stabilization with nanometer precision at the IP and establishment of beam jitter controlling techniques at the nano-meter level with an ILC-like beam.

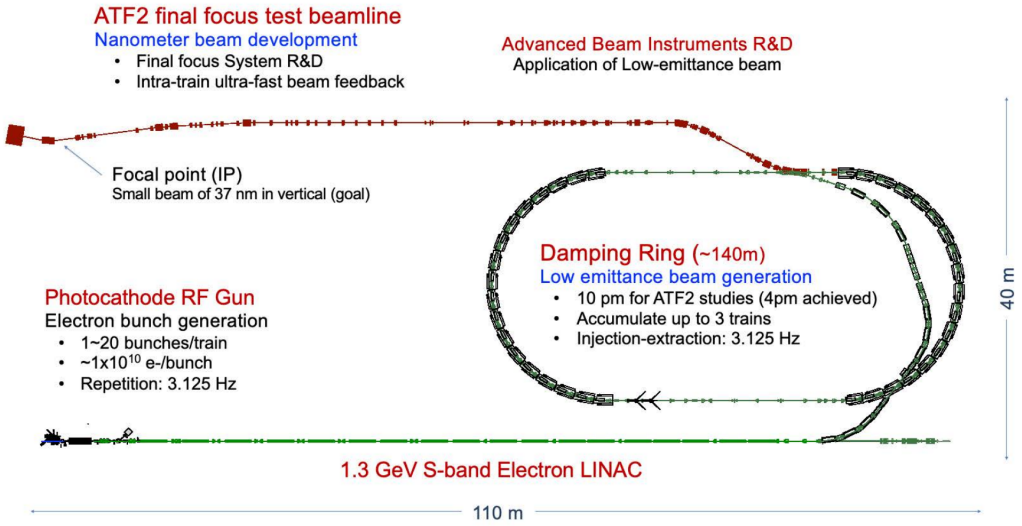

Figure 1.15: Schematic representation of the ATF-ATF2 [28].

The small beam size of 41 nm at the ATF2 IP was successfully achieved with an intra-train orbit feedback (FONT) in 2016 [30] as shown in Fig. 1.16 (top). This demonstrates the functionality of a compact FFS based on local chromaticity correction and the practical effectiveness of intra-train orbit feedback. This small beam was realized under a low aberration optics with ten times higher horizontal beta function at the IP, this optics is labeled as "nominal" $10\beta_x^* \times \beta_y^*$, and under lower beam intensity because of the significant impact of wakefields on the IP beam size (Fig. 1.16 (bottom)). Since the wakefields depend on the internal geometric structure of the beamline, it was suggested to distinguish the wakefield issues of the ATF2 beamline from the proof of the FFS [31]. The wakefield effect on small beam becomes the important study target as "the third goal" of ATF2 [32].

ATF2 also plays a crucial role for CLIC, as it allows studying the beam tuning under conditions similar to what is expected on CLIC, where the FD chromaticity is approximately four times larger than the nominal ATF2 design optics. For testing the CLIC-like optics at ATF2, a so-called "ultra-low" β_y^* optics was designed [34]. The ultra-low β_y^* optics has four times smaller vertical beta-function at the IP and consequently four times higher chromaticity. In this thesis, we refer to the original "design" optics at ATF2 as $\beta_x^* \times \beta_y^*$, and the ultra-low β_y^* optics as $\beta_x^* \times 0.25\beta_y^*$. In 2017, a pair of octupoles [35] was installed in the lattice to support the ultra-low β_y^* optics tuning. They are intended to help in the beam tuning by means of canceling the 3$^{\text{rd}}$ order chromatic aberrations in the lattice. The key parameters of the nominal and ultra-low optics at ATF2 in comparison with the ILC and CLIC are given in Tab. 1.3. The cumulative results of the beam size tuning at ATF2, for the ultra-low β_y^* and half-β_y^* [36] are also shown in Fig. 1.16. Chapter 3 of this thesis is dedicated to the simulation studies of ultra-low β_y^* optics and also reports on the beam tuning results, including the new octupole alignment technique.

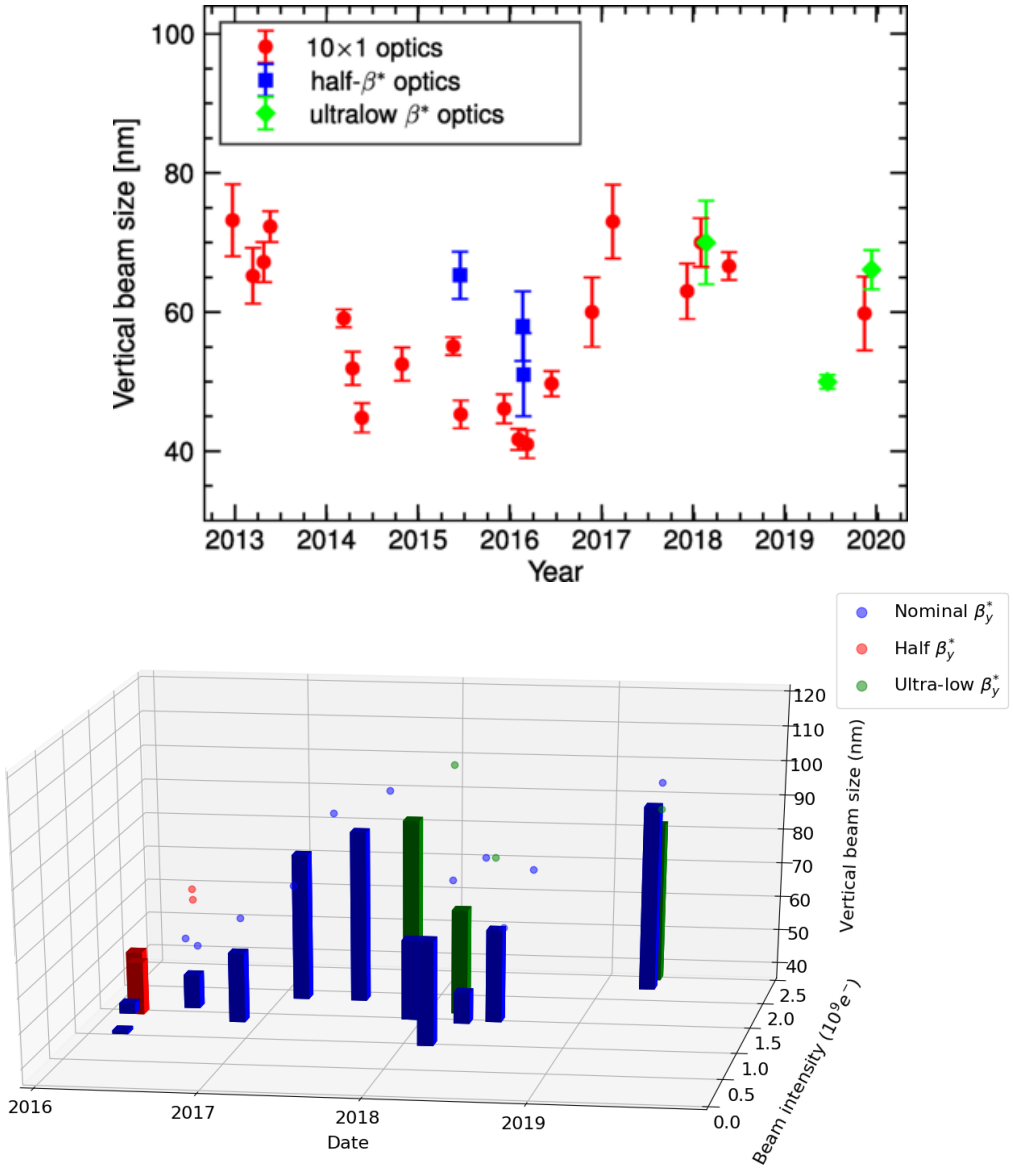

Figure 1.16: Top: Smallest vertical beam sizes achieved in each beam tuning operation in the period 2012 - 2020 [33]. Here, measurements in 174° mode of the IPBSM, with a modulation depth of at least 0.2, are taken. Bottom: Smallest beam sizes achieved at ATF2 in the period from June 2016 to April 2019 as a function of the beam intensity.

Table 1.3: Comparison of the key parameters of ATF2 and FLCs.

	ATF2 optics		ILC	CLIC	CLIC
	Nominal $10\beta_x^* \times \beta_y^*$	Ultra-low $\beta_x^* \times 0.25\beta_y^*$			
Beam energy [GeV]	1.3		250	380	3000
Vertical emittance [pm]	12		0.035	0.008	0.003
Horizontal emittance [nm]	1.2		5.0	2.55	0.2
Energy spread [%]	0.008		0.2	0.3	0.3
Beta-function β_x^*/β_y^* [mm]	4/0.1	4/0.025	13/0.4	8/0.07	4/0.007
Vertical chromaticity $\frac{L^*}{\beta_y^*}$	10000	40000	10000	86000	50000
Vertical beam size [nm]	37	27 (20[a])	7.7	2.4	1.0

[a]with octupoles.

1.4 Beam dynamics challenges in the FFS of FLCs

This section focuses on the key concepts of the nonlinear transverse beam dynamics relevant for the FFS of Linear Colliders. In particular, the magnetic field of the multipoles, such as sextupoles, octupoles, etc., the equations of motion from the Hamiltonian formalism and the transport notation and the map formalism, which efficiently describe the particle transport along a beamline, such as the FFS, is reviewed. The chromaticity and its correction as well as the luminosity are also reported. Finally, an overview of the main static and dynamic imperfections that can be found in the FFS is presented.

The basic of the linear transverse beam dynamics is comprehensively described in [37–41].

1.4.1 Multipole field expansion

The transverse magnetic field inside a vacuum beam pipe can be described with a multipolar expansion. In Cartesian coordinates, it is given by [42]:

$$B_y + iB_x = \sum_{n=1}^{+\infty} (b_n + ia_n)(x + iy)^{n-1} \ , \tag{1.1}$$

where, a_n is the skew component, b_n is the normal component of the n-th order multipole, $i^2 = -1$, and x and y are the transverse coordinates. In the general form, the magnetic flux density $\vec{B}$ relates to the vector potential $\vec{A}$ as following:

$$\vec{B} = \vec{\nabla} \times \vec{A} \ . \tag{1.2}$$

It is assumed that no longitudinal magnetic field is present in the accelerator, so the vector-potential has only longitudinal component $A_z(x, y)$, and the magnetic field could

be written as:

$$B_x = \frac{\partial A_z}{\partial y} , \tag{1.3}$$

$$B_y = -\frac{\partial A_z}{\partial x} . \tag{1.4}$$

Hence one can derive the vector-potential:

$$A_z(x,y) = -\Re\left(\sum_{n=1}^{+\infty}(b_n + ia_n)\frac{(x+iy)^n}{n}\right) . \tag{1.5}$$

Considering a single n-th order multipole, the magnetic field writes as:

$$B_{ny} + iB_{nx} = (b_n + ia_n)(x+iy)^{n-1} . \tag{1.6}$$

Following the convention used in MADX [43], we could define the normal k_{n-1}^N and skew k_{n-1}^S strengths of such a multipole as:

$$k_{n-1}^N \equiv \frac{1}{B_0\rho}\frac{\partial^{n-1}B_{ny}}{\partial x^{n-1}} , \tag{1.7}$$

$$k_{n-1}^S \equiv \frac{1}{B_0\rho}\frac{\partial^{n-1}B_{nx}}{\partial x^{n-1}} , \tag{1.8}$$

where $B_0\rho$ is the magnetic rigidity, k_1^N is the magnetic strength of a normal quadrupole, k_2^N is the magnetic strength of a normal sextupole, etc. Using Eq. (1.6), one can easily connect the normal b_n and the skew a_n components with the corresponding strength as:

$$b_n = \frac{1}{(n-1)!}\frac{\partial^{n-1}B_{ny}}{\partial x^{n-1}} = \frac{B_0\rho}{(n-1)!}k_{n-1}^N , \tag{1.9}$$

$$a_n = \frac{1}{(n-1)!}\frac{\partial^{n-1}B_{nx}}{\partial x^{n-1}} = \frac{B_0\rho}{(n-1)!}k_{n-1}^S . \tag{1.10}$$

The vector-potential for such an n-th order multipole then writes as:

$$A_{z,n} = -B_0\rho\frac{k_{n-1}^N}{n!}\Re\{(x+iy)^n\} - B_0\rho\frac{k_{n-1}^S}{n!}\Im\{(x+iy)^n\}. \tag{1.11}$$

Usually, we use only one type of the multipole, either normal or skew.

1.4.2 Hamiltonian formalism

The Hamiltonian of a relativistic particle in the Frenet-Serret coordinate system, where s is an independent variable, writes as [41]:

$$H = -\frac{e}{p_0(1+\delta)}A_s - \left(1+\frac{x}{\rho}\right)\sqrt{1-p_x^2-p_y^2} , \tag{1.12}$$

where $\delta = \frac{\Delta p}{p_0}$ is the relative energy offset of the particle, and ρ is the curvature of the trajectory. The vector potential is given by $A_s = (1 + \frac{x}{\rho})\vec{A} \cdot \vec{s}$. The canonical momentum $p_{x,y}$, assuming $A_x = A_y = 0$ relates to the kinetic momentum as:

$$p_x = \frac{\gamma m \dot{x}}{p_0} \ , \ p_y = \frac{\gamma m \dot{y}}{p_0} \ , \tag{1.13}$$

with m being the mass of the particle. For small angles Hamiltonian simplifies as:

$$H = -\frac{e}{p_0(1+\delta)} A_z \left(1 + \frac{x}{\rho}\right) - \frac{x}{\rho} + \frac{p_x^2 + p_y^2}{2} \ , \tag{1.14}$$

The equations of motion in the horizontal and vertical plane could be derived from the corresponding Hamiltonian as:

$$x' = \frac{\partial H}{\partial p_x} = p_x \ , \tag{1.15}$$

$$\frac{dp_x}{ds} = x'' = -\frac{\partial H}{\partial x} \ . \tag{1.16}$$

$$y' = \frac{\partial H}{\partial p_y} = p_y \ , \tag{1.17}$$

$$\frac{dp_y}{ds} = y'' = -\frac{\partial H}{\partial y} \ . \tag{1.18}$$

In the particular case of the FFS magnets, the Hamiltonians are:

- Dipoles with nominal magnetic field B_0, excluding the weak focusing ($A_{z,1} \approx -B_0 x$):

$$H = -\frac{x}{\rho(1+\delta)} - \frac{x}{\rho} + \frac{x'^2 + y'^2}{2} \approx -\frac{\delta}{\rho} x + \frac{x'^2 + y'^2}{2} \tag{1.19}$$

- Normal quadrupole ($n = 2$) with strength k_1^N:

$$H = k_1^N \frac{x^2 - y^2}{2} \frac{1}{(1+\delta)} + \frac{x'^2 + y'^2}{2} \tag{1.20}$$

- Skew quadrupole ($n = 2$) with strength k_1^S:

$$H = k_1^S xy \frac{1}{(1+\delta)} + \frac{x'^2 + y'^2}{2} \tag{1.21}$$

- Normal sextupole ($n = 3$) with strength k_2^N:

$$H = \frac{k_2^N}{6}(x^3 - 3xy^2) \frac{1}{(1+\delta)} + \frac{x'^2 + y'^2}{2} \tag{1.22}$$

- Skew sextupole ($n = 3$) with strength k_2^S:

$$H = \frac{k_2^S}{6}(3x^2y - y^3)\frac{1}{(1+\delta)} + \frac{x'^2 + y'^2}{2} \tag{1.23}$$

- Normal octupole ($n = 4$) with strength k_3^N:

$$H = \frac{k_3^N}{24}(x^4 - 6x^2y^2 + y^4)\frac{1}{(1+\delta)} + \frac{x'^2 + y'^2}{2} \tag{1.24}$$

- Skew octupole ($n = 4$) with strength k_3^S:

$$H = \frac{k_3^S}{6}xy(x^2 - y^2)\frac{1}{(1+\delta)} + \frac{x'^2 + y'^2}{2} \tag{1.25}$$

- Normal decapole ($n = 5$) with strength k_4^N:

$$H = \frac{k_4^N}{120}x(x^4 - 10x^2y^2 + 5y^4)\frac{1}{(1+\delta)} + \frac{x'^2 + y'^2}{2} \tag{1.26}$$

- Skew decapole ($n = 5$) with strength k_4^S:

$$H = \frac{k_4^S}{120}y(5x^4 - 10x^2y^2 + y^4)\frac{1}{(1+\delta)} + \frac{x'^2 + y'^2}{2} \tag{1.27}$$

The corresponding equations of motion are given by introducing the Hamiltonians in Eqs. (1.16), (1.18).

1.4.3 Map formalism

The transformation of the particles' coordinates through the lattice in the linear approximation is performed by means of transfer matrices. In this case, each drift, dipole magnet, and quadrupole is associated with the corresponding transfer matrix R_{ij}. In the presence of the high-order elements as sextupoles, octupoles, etc., the matrix formalism is extended. In Transport notation, described in [44], the final coordinates of the particle $\vec{u} \equiv (x\ x'\ y\ y'\ \delta)^T$ connect with the initial coordinates $\vec{u_0} \equiv (x_0\ x'_0\ y_0\ y'_0\ \delta_0)^T$ as follows:

$$u_i = \sum_{j=1}^{5} R_{ij}u_{0j} + \sum_{j=1}^{5}\sum_{k=j}^{5} T_{ijk}u_{0j}u_{0k} \tag{1.28}$$

where T_{ijk} represent the 2^{nd}-order matrix elements. Similarly, the 3^{rd}-order terms can be introduced with U_{ijkl}. This formalism could be extended for any order by using the map X_{jklmm}, as in [45] (Fig. 1.17). In this format, the index j indicates the power of coordinate x_0, the index k indicates the power of coordinate x'_0, etc.:

$$\vec{u} = \sum_{jklmn} \vec{X}_{jklmn}{x_0}^j{x'_0}^k{y_0}^l{y'_0}^m{\delta_0}^n \tag{1.29}$$

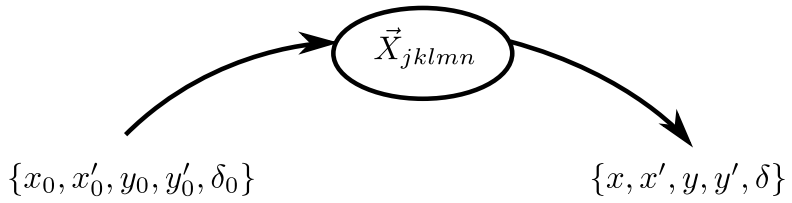

Figure 1.17: Schematic representation of the Map formalism.

where $\vec{X}_{jklmn}$ represents the transformation for each of 5 coordinates in $\vec{u}$. Usually, in the analysis, the transfer map $\vec{X}$ is truncated at the given order q, with $j+k+l+m+n \leq q$. Unsing this formalism we can evaluate the horizontal and vertical beam size at the final point as:

$$\sigma_{x,y}{}^2 = \sum_{\substack{jklmn \\ j'k'l'm'n'}} X(Y)_{jklmn} X(Y)_{j'k'l'm'n'} \int x_0{}^{j+j'} x'_0{}^{k+k'} y_0{}^{l+l'} y'_0{}^{m+m'} \delta_0{}^{n+n'} \rho_0 \, dv_0 \tag{1.30}$$

where ρ_0 is the phase-space density at the starting point. Having, the X and Y maps truncated to a given order and the initial particles distribution we could evaluate the beam size at the IP, without performing a particle tracking. This is the basis of the computational code MAPCLASS [46–48]. This code uses the map coefficients X_{ijklmn} estimated with the Polymorphic Tracking Code (PTC) [49] embedded in MADX to calculate the beam size as well as various coupling between the coordinates at the IP.

1.4.4 Chromaticity in the LCs and its correction

The main source of the beam size growth at the IP is the chromaticity $\xi_{x,y}$ [37]:

$$\sigma^*_{x,y}{}^2 = \epsilon_{x,y} \beta^*_{x,y} (1 + \xi^2_{x,y} \delta^2_p) \ , \tag{1.31}$$

where $\epsilon_{x,y}$ is the beam emittance, $\beta^*_{x,y}$ is the beta-function at the IP, δ_p is the relative momentum spread of the beam. The primary source of the chromaticity at the IP are the FD quadrupoles. Due to this effect particles with different energy offsets experiment different focusing properties.

Chromaticity generated by quadrupoles

The equations of motion inside a quadrupole magnet, based on Eqs. (1.16), (1.18), (1.20) writes as:

$$\begin{cases} x'' & = -k_1^N x \frac{1}{(1+\delta)} \approx -k_1^N x (1-\delta) \\ y'' & = k_1^N y \frac{1}{(1+\delta)} \approx k_1^N y (1-\delta) \end{cases} , \tag{1.32}$$

which, in general, are the 2^{nd}-order equations on x, y, and δ. The transformation of the coordinates through a quadrupole in a dispersion free region in Transport notation writes

as:

$$\begin{cases} x &= R_{11}x_0 + R_{12}x'_0 + T_{116}x_0\delta_0 + T_{126}x'_0\delta_0 \\ x' &= R_{21}x_0 + R_{22}x'_0 + T_{216}x_0\delta_0 + T_{226}x'_0\delta_0 \end{cases} , \tag{1.33}$$

$$\begin{cases} y &= R_{33}y_0 + R_{34}y'_0 + T_{336}y_0\delta_0 + T_{346}y'_0\delta_0 \\ y' &= R_{43}y_0 + R_{44}y'_0 + T_{436}y_0\delta_0 + T_{446}y'_0\delta_0 \end{cases} , \tag{1.34}$$

where R_{ij} is the transfer matrix of the quadrupoles, $\{x_0, x'_0, y_0, y'_0, \delta_0\}$ is the set of the coordinates at the quadrupole entrance, and $\{x, x', y, y', \delta\}$ is the set of the coordinates at the quadrupole exit. Neglecting the impact of the synchrotron radiation and assuming that the energy of the particle remains constant, thus $\delta = \delta_0$. The terms not included here are identically zero. Taking from [44], the nonzero terms of T_{ijk} for a focusing quadrupole:

$$\begin{cases} T_{116} &= \frac{\sqrt{k}L}{2}\sin\sqrt{k}L \\ T_{126} &= \frac{1}{2\sqrt{k}}\sin\sqrt{k}L - \frac{L}{2}\cos\sqrt{k}L \\ T_{216} &= \frac{\sqrt{k}}{2}\{\sqrt{k}L\cos\sqrt{k}L + \sin\sqrt{k}L\} \\ T_{226} &= \frac{\sqrt{k}L}{2}\sin\sqrt{k}L \\ T_{336} &= -\frac{\sqrt{k}L}{2}\sinh\sqrt{k}L \\ T_{346} &= \frac{1}{2}(\frac{1}{\sqrt{k}}\sinh\sqrt{k}L - L\cosh\sqrt{k}L) \\ T_{436} &= -\frac{\sqrt{k}}{2}(\sqrt{k}L\cosh\sqrt{k}L + \sinh\sqrt{k}L) \\ T_{446} &= -\frac{\sqrt{k}L}{2}\sinh\sqrt{k}L \end{cases} , \tag{1.35}$$

where k is the magnetic strength of the quadrupole, and L is the length of the quadrupole, the equations (1.33) and (1.34) could be rewritten as:

$$(x\ x'\ y\ y')^T = \left(\begin{pmatrix} R_x & 0 \\ 0 & R_y \end{pmatrix} + \begin{pmatrix} T_x & 0 \\ 0 & T_y \end{pmatrix}\delta\right)(x_0\ x'_0\ y_0\ y'_0)^T , \tag{1.36}$$

where

$$T_x = \begin{pmatrix} T_{116} & T_{126} \\ T_{216} & T_{226} \end{pmatrix} , \ T_y = \begin{pmatrix} T_{336} & T_{346} \\ T_{436} & T_{446} \end{pmatrix} . \tag{1.37}$$

Defining $\widetilde{T}_x$ and $\widetilde{T}_y$ as the matrices of the 2$^{\text{nd}}$-order terms between the starting point and the IP:

$$\widetilde{T}_{x,y} = R^{Q\to IP}_{x,y} T_{x,y} R^{s_0\to Q}_{x,y} , \tag{1.38}$$

where $R^{Q\to IP}_x$ and $R^{Q\to IP}_y$ are the horizontal and vertical parts of the transfer matrix $R^{Q\to IP}$, the particles' coordinates at the IP could be written as:

$$\begin{cases} x^* &= x^*_\beta + \widetilde{T}_{116}x_{s0}\delta + \widetilde{T}_{126}x'_{s0}\delta \\ y^* &= y^*_\beta + \widetilde{T}_{336}y_{s0}\delta + \widetilde{T}_{346}y'_{s0}\delta \end{cases} , \tag{1.39}$$

thus the beam size writes as:

$$\begin{cases} \sigma^{*2}_x &= \epsilon_x\beta^*_x + \widetilde{T}^2_{116}\sigma^2_{x_{s_0}}\delta^2_p + \widetilde{T}^2_{126}\sigma^2_{x'_{s_0}}\delta^2_p + 2\widetilde{T}_{116}\widetilde{T}_{126}\sigma_{x_{s_0},x'_{s_0}}\delta^2_p \\ \sigma^{*2}_y &= \epsilon_y\beta^*_y + \widetilde{T}^2_{336}\sigma^2_{y_{s_0}}\delta^2_p + \widetilde{T}^2_{346}\sigma^2_{y'_{s_0}}\delta^2_p + 2\widetilde{T}_{336}\widetilde{T}_{346}\sigma_{y_{s_0},y'_{s_0}}\delta^2_p \end{cases} , \tag{1.40}$$

with

$$\sigma^2_{x_{s_0}} = \epsilon_x \beta_{x,s_0} \ , \ \sigma^2_{x'_{s_0}} = \epsilon_x \gamma_{x,s_0} \ , \sigma_{x_{s_0},x'_{s_0}} = -\epsilon_x \alpha_{x,s_0} \ ,$$
$$\sigma^2_{y_{s_0}} = \epsilon_y \beta_{y,s_0} \ , \ \sigma^2_{y'_{s_0}} = \epsilon_y \gamma_{y,s_0} \ , \sigma_{y_{s_0},y'_{s_0}} = -\epsilon_y \alpha_{y,s_0} \ .$$

Comparing Eq. (1.40) and Eq. (1.31) the chromaticity is given by:

$$\begin{cases} \xi_x^2 & = \widetilde{T}^2_{116} \frac{\beta_{x,s_0}}{\beta^*_x} + \widetilde{T}^2_{126} \frac{\gamma_{x,s_0}}{\beta^*_x} - 2\widetilde{T}_{116}\widetilde{T}_{126} \frac{\alpha_{x,s_0}}{\beta^*_x} \\ \xi_y^2 & = \widetilde{T}^2_{336} \frac{\beta_{y,s_0}}{\beta^*_y} + \widetilde{T}^2_{346} \frac{\gamma_{y,s_0}}{\beta^*_y} - 2\widetilde{T}_{336}\widetilde{T}_{346} \frac{\alpha_{y,s_0}}{\beta^*_y} \end{cases} \tag{1.41}$$

This expression is compatible with the chromaticity definition in [50], when $\alpha_{x,s_0} = 0$ and $\alpha_{y,s_0} = 0$ we have:

$$\xi^2_{x,y} = \widetilde{T}^2_{116(336)} \frac{\beta_{x,y,s_0}}{\beta^*_{x,y}} + \widetilde{T}^2_{126(346)} \frac{1}{\beta^*_{x,y}\beta_{x,y,s_0}} \ . \tag{1.42}$$

In the thin-lens approximation, the length of the magnet is assumed to be zero, but with a finite integrated strength $k_L = kL$. For a quadrupole, the 2$^{\text{nd}}$ order terms in Eq. (1.35) are negligible, except for $T_{216} \approx k_L$, and $T_{436} \approx -k_L$. Considering a single quadrupole, located at the FD phase ($\pi/2$ phase advance from the IP), with transfer matrix:

$$\hat{R}^{Q\to IP}_{x,y} = \begin{pmatrix} \sqrt{\frac{\beta^*_{x,y}}{\beta_{x,y}}}\alpha_{x,y} & \sqrt{\beta_{x,y}\beta^*_{x,y}} \\ -\frac{1}{\sqrt{\beta_{x,y}\beta^*_{x,y}}} & 0 \end{pmatrix} \ , \tag{1.43}$$

where β_x, and α_x are the Twiss functions at the quadrupole location and taking the quadrupole entrance as a starting point, the chromaticity generated by a single thin quadrupole is given by:

$$\xi^q_{x,y} \approx \widetilde{T}_{116(336)} \sqrt{\frac{\beta_{x,y}}{\beta^*_{x,y}}} = T_{216(436)} R^{Q\to IP}_{12(34)} \sqrt{\frac{\beta_{x,y}}{\beta^*_{x,y}}} = \pm k_L \beta_{x,y} \ . \tag{1.44}$$

We could see from Eq.1.44 that a strong quadrupole located in the high $\beta_{x,y}$ region generates high chromaticity. The sub-nanometer beam sizes the IP, required for the linear colliders, needs extremely small values of the beta-functions at the IP hence strong quadrupoles in the Final Doublet. Such configuration becomes the dominant source of chromaticity at the IP.

In the case of the last quadrupole usptream of the IP, namely QD0, see Fig. 1.18, the expression of the vertical chromaticity can be further simplified. The beta-function in the region between the IP an QD0, at a distance $s \leq L^*$ from the IP is given by:

$$\beta_{x,y}(s) = \beta^*_{x,y} + \frac{s^2}{\beta^*_{x,y}} \ . \tag{1.45}$$

Considering that $\beta^*_{x,y} \ll L^*$, the beta-functions at QD0 location approximates as: $\beta_{x,y} \approx \frac{L^{*2}}{\beta^*_{x,y}}$. In the vertical plane, the distance L^* is a good approximation of the focal length for

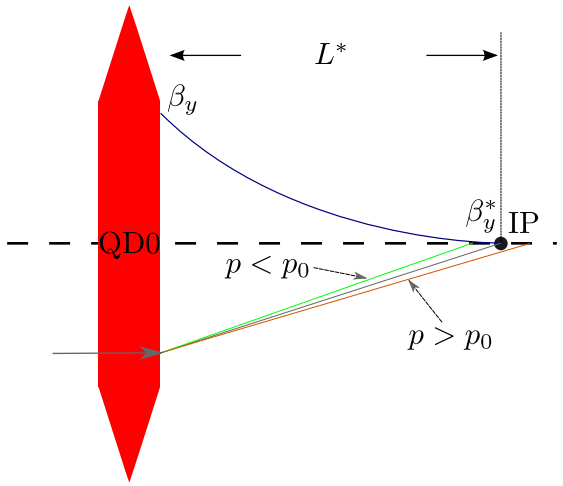

Figure 1.18: Schematic representation of the energy dependent focusing in the vertical plane by QD0 quadrupole. The particles with and energy different from the reference one p_0, are focused with a different focal length, hence wider beam spot at the IP.

QD0, so we could take: $k_L \approx 1/L^*$. Taking these approximations, Eq. (1.44) is simplified as:

$$\xi_y^{QD0} = -k_L \beta_y \approx -\frac{L^*}{\beta_y^*} \ . \tag{1.46}$$

This expression gives a good approximation of the chromaticity level in the FFS of LCs. In the case of CLIC 380 GeV, QD0 generates a vertical chromaticity at the level of $\xi_y^{QD0} \approx 0.9 \times 10^5$ for $L^* = 6$ m and $\beta_y^* = 70$ μm.

Thin quadrupole in a dispersive region

When the quadrupole is located in a region with horizontal dispersion D_x, we could set $x_0 \to x_0 + D_x\delta$, hence in the thin-lens approximation, Eq. (1.33) becomes:

$$\begin{cases} x &= R_{11}(x_0 + D_x\delta) + R_{12}x_0' \\ x' &= R_{21}(x_0 + D_x\delta) + R_{22}x_0' + T_{216}(x_0 + D_x\delta)\delta \end{cases} , \tag{1.47}$$

where D_x is the horizontal dispersion at the quadrupole location. Neglecting the vertical dispersion, the coordinate transformation in the vertical plane remains the same. In this case we have an additional pure chromatic term given by:

$$T_{266} \equiv T_{216} D_x \ , \tag{1.48}$$

which is the source of the 2$^{\text{nd}}$-order dispersion at the IP, and it is given by:

$$\widetilde{T}_{166} = T_{266} R_{12}^{Q \to IP} = k_L D_x \sqrt{\beta_x \beta_x^*} = \xi_x^q D_x \sqrt{\frac{\beta_x^*}{\beta_x}} \ . \tag{1.49}$$

Chromaticity generated by a sextupole

The transfer map of a thin sextupole is given by:

$$\begin{cases} x &= x_0 \\ x' &= x'_0 + T^s_{211}x_0^2 + T^s_{233}y_0^2 \\ y &= y_0 \\ y' &= y'_0 + T^s_{413}x_0y_0 \end{cases} , \tag{1.50}$$

with $T^s_{211} \approx -k^s_L/2$, $T^s_{233} \approx k^s_L/2$, and $T_{413} \approx k^s_L$, where k^s_L is the integrated strength of the sextupole. The 2$^{\text{nd}}$-order terms are taken from [44]. To generate chromaticity, the sextupole needs to be located in a dispersive region. Setting $x_0 \to x_0 + D_x\delta$, the 2$^{\text{nd}}$-order chromatic terms are given by:

$$\begin{cases} T^s_{216} &\equiv 2T^s_{211}D_x = -k^s_L D_x \\ T^s_{266} &\equiv T^s_{211}D_x^2 = \frac{1}{2}k^s_L D_x^2 \\ T^s_{436} &\equiv T^s_{413}D_x = k^s_L D_x \end{cases} . \tag{1.51}$$

Similarly to the quadrupole, we could evaluate the chromaticity of the sextupole, supposing that is located at the same location of the quadrupole, applying the transformation from Eq. (1.38) with Eq. (1.43), and taking the same definitions of Eq. (1.41), the chromaticity writes as:

$$\xi^s_{x,y} \approx \widetilde{T}^s_{116(336)}\sqrt{\frac{\beta_{x,y}}{\beta^*_{x,y}}} = \mp k^s_L D_x \beta_{x,y} . \tag{1.52}$$

Apart from the terms $\widetilde{T}^s_{116}$ and $\widetilde{T}^s_{336}$ that contribute to the horizontal and vertical chromaticities, respectively, there are residual terms that impact to the particle's coordinate at the IP. These terms are given by:

$$\begin{cases} \widetilde{T}^s_{111} \equiv T^s_{211}R^{Q\to IP}_{12} &= -\frac{1}{2}k^s_L\sqrt{\beta_x\beta^*_x} \\ \widetilde{T}^s_{133} \equiv T^s_{233}R^{Q\to IP}_{12} &= \frac{1}{2}k^s_L\sqrt{\beta_x\beta^*_x} \\ \widetilde{T}^s_{166} \equiv T^s_{266}R^{Q\to IP}_{12} &= \frac{1}{2}k^s_L D_x^2\sqrt{\beta_x\beta^*_x} = -\frac{1}{2}\xi^s_x D_x\sqrt{\frac{\beta^*_x}{\beta_x}} \\ \widetilde{T}^s_{313} \equiv T^s_{413}R^{Q\to IP}_{34} &= k^s_L\sqrt{\beta_y\beta^*_y} \end{cases} . \tag{1.53}$$

The terms $\widetilde{T}^s_{111}$, $\widetilde{T}^s_{133}$, and $\widetilde{T}^s_{313}$ are pure geometrical terms, if not corrected, they are the source of the geometrical aberrations at the IP. The last term $\widetilde{T}^s_{166}$, is the source of the pure chromatic aberrations, and is called 2$^{\text{nd}}$-order dispersion.

Chromaticity correction

In the FFS of CLIC 380 GeV, the chromaticity generated by QD0 is about $\xi^{QD0}_x \approx 0.9\times10^5$, according to the Eq. (1.46). If not corrected, the vertical beam size would be five orders of magnitude larger than the target one. To correct the chromaticity in both horizontal and vertical planes produced by a quadrupole, sextupoles located in a dispersive region

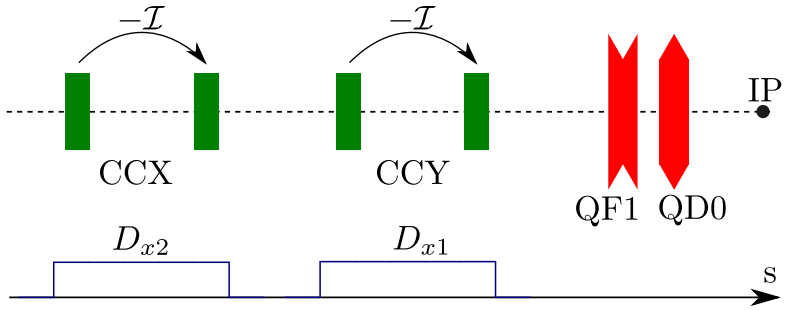

Figure 1.19: Schematic representation of the global chromaticity correction with "even" dispersion. Horizontal and vertical chromaticities upstream of the FD in the designated sections, referred as CCX and CCY. Quadrupoles are shown in red and sextupoles in green.

are used. If the horizontal and vertical chromaticities generated by the FD are ξ_x^{FD} and ξ_y^{FD} respectively, the strengths of the sextupoles intended to cancel them, have to be set to the following values:

$$\begin{cases} k_L^{SX} = \xi_x^{FD}/(D_{x2}\beta_x) \\ k_L^{SY} = \xi_y^{FD}/(D_{x1}\beta_y) \ , \end{cases} \tag{1.54}$$

where D_{x1} is the dispersion at the sextupole location cancelling the vertical chromaticity, D_{x2} is the dispersion at the sextupole location cancellling the horizontal chromaticity, and $\beta_{x,y}$ are the horizontal beta-function at the sextupole locations. We assume, they are located at FD phase. The main source of horizontal chromaticity in the FD is QF1, similarly the main source of vertical chromaticity is QD0.

The sextupoles are also source of the geometrical aberrations in both planes, such as $\widetilde{T}^s_{111}$, $\widetilde{T}^s_{133}$, and $\widetilde{T}^s_{313}$. To cancel them, additional "paired" sextupoles of equal strength and with $-\mathcal{I}$ transformation between the magnets within a "pair", located upstream are required, . The cancellation of the remaining term, the 2$^{\text{nd}}$-order dispersion, could be made in different ways. Two approaches are being used for the chromaticity cancellation in the FFS, known in the literature as: the global [51], and the local [16] chromaticity correction schemes.

Global chromaticity correction scheme

In the global chromaticitycorrection scheme, the horizontal and the vertical chromaticities are compensated upstream of the FD in dedicated sections, CCX and CCY in Fig. 1.19 . To cancel the 2$^{\text{nd}}$-order dispersion that is generated mainly in CCX, the "paired" sextupole are located at the same dispersion. In this case, both sextupoles in the "pair" produce chromaticity, so their strengths are reduced by half. An alternative design [52], suggests to use different dispersion within the sextupoles in each "pair". In this case, the 2$^{\text{nd}}$-order dispersion is canceled by adjusting the amounts produced by CCX and CCY.

The main drawback of the global chromaticity correction scheme is the need to have

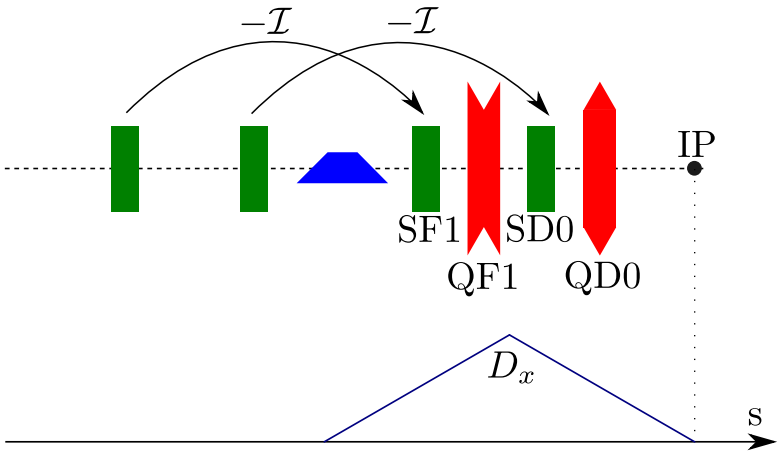

Figure 1.20: Schematic representation of the FFS design with the local chromaticity correction using interleaved sextupole "pairs". Quadrupoles are shown in red, sextupoles in green, and dipoles in blue

long dipole sections to produce dispersion locally in CCX and CCY. The dipole magnets in the FFS have to be sufficiently long and weak to minimize the energy spread created by the synchrotron radiation. The length of the FFS scales linearly with the energy [53]:

$$L_{FFS}[\text{km}] \propto E(\text{TeV}) \ . \tag{1.55}$$

Local chromaticity correction scheme

In this design, the chromaticity correction is made in the location where is produced, i.e. in the FD. On the contrary to the global chromaticity correction, the sextupoles intended for the chromaticity correction are placed next to the FD quadrupoles, as shown in Fig. 1.20. The sextupole located next to the QD0 quadrupole is traditionally named SD0 and the next one to the QF1 is named SF1. The dispersion needed for the chromaticity correction in SF1 and SD0 is generated upstream of the FD with dipole magnets and is zeroed at the IP with a nonzero slope. The "paired" sextupoles to SD0 and SF1 are placed upstream of the dipole region in a dispersion-free region to provide $-\mathcal{I}$ transformation within each pair. In this design, both QF1 and QD0 are located in the dispersion region and become the source of the 2$^{\text{nd}}$-order dispersion. Due to significantly larger horizontal beta-function, QF1 is the primary source. To cancel the vertical chromaticity, the strength of SD0 have to be set to $k_L^{SD0} = k_L^{QD0}/D_x$. To cancel the horizontal aberrations, SF1 have to be set to twice the strength, required to cancel the horizontal chromaticity generated by QF1, $k_L^{SF1} = 2k_L^{QF1}/D_x$. From Eqs. (1.49) and (1.53) we could see that the 2$^{\text{nd}}$-order dispersion from QF1 and SF1 is cancelled. Since the horizontal chromaticity got overcompensated, we need to generate an additional amount, equal to what QF1 creates, in the upstream dispersion free region.

Compared to the global chromaticity correction scheme, this scheme is more adequate

for energy scaling. As evaluated in [16], in the best case, the length of the FFS scales as $L_{FFS} \propto E^{2/5}$. In the current design of CLIC 3 TeV, the FFS optics is based on a local chromaticity correction scheme and has a length of 450 m [20] with $L^* = 3.5$ m. In comparison, the design with a global chromaticity correction scheme [54] for the same configuration requires a FFS with a total length of about 1.5 km.

1.4.5 Synchrotron Radiation

A charged particle under acceleration emits electromagnetic radiation known as Synchrotron Radiation (SR). The instantaneous radiated power by a particle in a dipole magnet with bending radius ρ is given by [38]:

$$P_\gamma = \frac{2}{3} r_e mc^3 \frac{\beta\gamma}{\rho^2} \propto \frac{E^4}{\rho^2 m^3} \ , \tag{1.56}$$

where r_e is the classical electron radius, m is the particle mass, c is the speed of light, $\beta = V/c$ is the reduced velocity, and γ is the Lorentz factor. One can see that light particles, such as e^- and e^+, will loose much more energy than p of the same energy. Such relation limits the energies accessible for the lepton circular colliders. In LCs the beam is accelerated in a single pass structure with no bending magnets, so from the point of view of SR the LCs could reach higher energies than the circular colliders.

Although the LCs do not need the bending magnets for the beam steering, some dipole magnets are still utilized. In the BDS, it is particularly driven by the need to generate the dispersion for collimation and for chromaticity correction. So, particles will lose some portion of their energy by SR, leading to transverse emittance growth and beam size dilution at the IP. For the FFS with local correction of the chromaticity, the vertical beam size dilution scales as [37]:

$$\frac{\Delta\sigma_y^*}{\sigma_y^*} \propto \frac{\gamma^5}{L_{FFS}^2} D_b'^3 \ , \tag{1.57}$$

where D_b' is the angular horizontal dispersion produced by the bend magnets and γ is the Lorentz factor.

The Oide effect

The emission of SR becomes significant for the strong focusing quadrupoles of the FD and for QD0 in particular. SR impacts the focusing properties in the vertical plane, as flat beams ($\sigma_x^* \gg \sigma_y^*$) are used. The smaller β_y^* requires stronger QD0, which increases the radiation in QD0, and effectively is a source of emittance growth leading to a vertical IP beam size growth, known as "Oide effect" [55] and given by:

$$\sigma_y^{*2} = \epsilon_y \beta_y^* + \frac{110}{3\sqrt{6\pi}} r_e \lambda_e \gamma^5 F\left(\sqrt{k}L, \sqrt{k}L^*\right) \left(\frac{\epsilon_y}{\beta_y^*}\right)^{5/2} \ , \tag{1.58}$$

where r_e is the classical electron radius, λ_e is the Compton wavelength, k is the magnetic strength of the quadrupole, and L is the length of the quadrupole. The dimensionless

function F is given by:

$$F\left(\sqrt{k}L, \sqrt{k}L^*\right) \equiv \int_0^{\sqrt{K}L} |\sin\phi + \sqrt{K}L^*\cos\phi|^3 \times \left\{\int_0^{\phi} (\sin\phi' + \sqrt{K}l^*\cos\phi')^2 d\phi'\right\}^2 d\phi \ . \tag{1.59}$$

The residual contribution to the to the beam size due to the Oide effect limits the minimum vertical beam size achievable, being in some cases the dominant term. The smallest beam size one can get taking into account the Oide effect is given by:

$$\sigma^*_{y,min} = \left(\frac{7}{5}\right)^{1/2} \left(\frac{275}{3\sqrt{6\pi}} r_e \lambda_e F\left(\sqrt{k}L, \sqrt{(}k)L^*\right)\right)^{1/7} (\gamma\epsilon_y)^{5/7} \ . \tag{1.60}$$

corresponding to a minimum vertical beta-function of:

$$\beta^*_{y,min} = \left(\frac{275}{3\sqrt{6\pi}} r_e \lambda_e F\left(\sqrt{k}L, \sqrt{(}k)L^*\right)\right)^{2/7} \gamma(\gamma\epsilon_y)^{3/7} \ . \tag{1.61}$$

In practice the vertical beta-function in the IP has to be larger than the minimum value estimated taking into account the Oide effect. The minimum is defined by the beam emittance and the configuration of the FD. A detailed study of the impact of the SR in the quadrupoles on the horizontal beam size, or the so-called 2D-Oide effect, was investigated in [56].

1.4.6 Luminosity and luminosity limiting factors

Apart of the energy, the luminosity is the most important parameter in colliders. To characterize the colliding beams independently of the studied process, the luminosity parameter $\mathcal{L}$, is introduced [57], as

$$\dot{R} = \mathcal{L}\sigma_p \ , \tag{1.62}$$

where $\dot{R}$ is the event rate and σ_p is the cross-section for a certain particle interaction. Traditionally, the luminosity is measured in units of $\mathrm{cm^{-2}s^{-1}}$. In order to be able to study the rare processes with extremely small σ_p, the luminosity has to be sufficiently large. For two equal Gaussian beams colliding head-on with no offset or crossing angle, the luminosity is given by:

$$\mathcal{L} = \frac{N^2 f N_b}{4\pi\sigma^*_x\sigma^*_y} \equiv \mathcal{L}_0 \ . \tag{1.63}$$

where N is the number of particles in one bunch, f is the repetition rate, N_b is the number of bunches in a train and σ^*_x, and σ^*_y are the horizontal and the vertical beam sizes at the IP. In this form, the luminosity does not consider interactions between the particles. To include the various factors that could impact the luminosity, such as the crossing angle, the Hourglass effect, the beam-beam forces, etc., the luminosity scaling parameter R_L is introduced:

$$\mathcal{L} = \frac{N^2 f N_b}{4\pi\sigma^*_x\sigma^*_y} R_L \ . \tag{1.64}$$

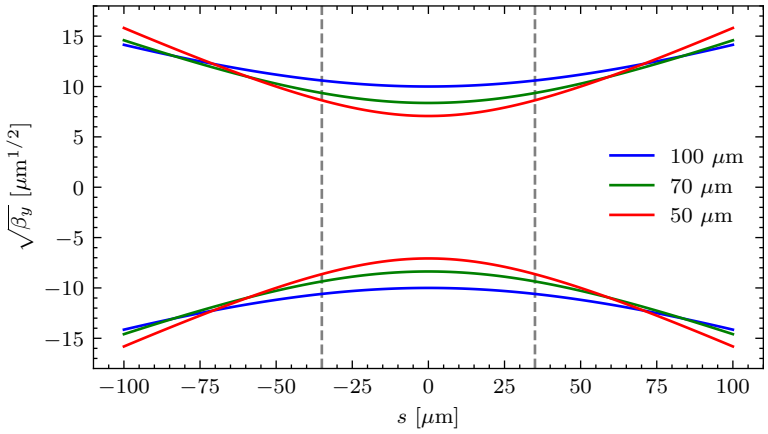

Figure 1.21: Vertical beta-function around the IP for different vertical beta-functions at the IP, for CLIC 380 GeV with a bunch length of $\sigma_z = 70$ μm. The space between vertical dashed lines corresponds to a single bunch (one sigma).

One can notice that the luminosity as defined in Eq. (1.62) does not take into account the collision energy of the particles. In this context, an important figure of merit is the peak luminosity $\mathcal{L}_{peak}$, that could be introduced as the luminosity of the collisions with a collision energy E that does not differ from the target energy E_0 more than 1%:

$$\mathcal{L}_{peak} = \mathcal{L}\left\{\frac{|E - E_0|}{E_0} \leq 1\%\right\} \ . \tag{1.65}$$

The most important effects that could impact the total luminosity are:

Hourglass effect

The beta-function $\beta_{x,y}$ in the close vicinity of the IP changes according to Eq. (1.45). The geometrical luminosity given in Eq. (1.63) considers that the beam size is constant within a single bunch, but when the bunch length is comparable with the beta-function at the IP, the particles collide with different beam sizes, depending on how far they are from the IP. This effec is known as the Hourglass effect. Fig. 1.21 iilustrates this effect. In the figure the vertical beta-function dependence on the distance from the waist is shown, for the case of CLIC 380 GeV with a bunch lenght of $\sigma_z = 70$ μm. The luminosity reduction factor due to the Hourglass effect could be written as [37]:

$$R_L = \frac{1}{\sqrt{\pi}} \int_{-\infty}^{+\infty} \frac{e^{-t^2} dt}{\sqrt{\left(1 + \frac{t^2}{t_x^2}\right)\left(1 + \frac{t^2}{t_y^2}\right)}} \ . \tag{1.66}$$

For symmetric beams, the coefficients t_x and t_y are:

$$t_x = \frac{\beta_x^*}{\sigma_z} \ , \ t_y = \frac{\beta_y^*}{\sigma_z} \ . \tag{1.67}$$

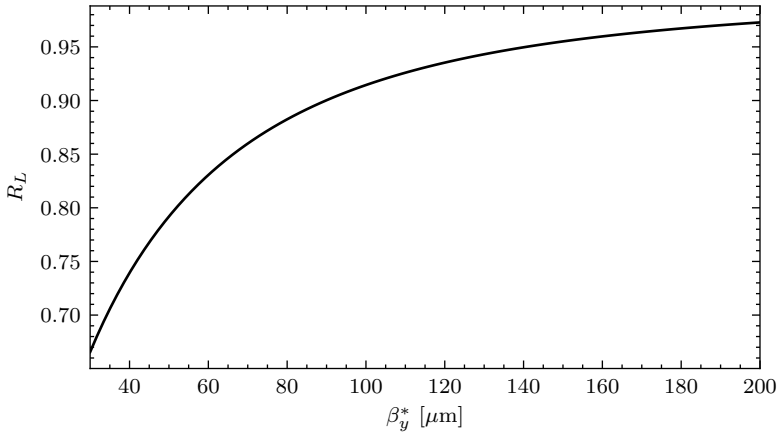

Figure 1.22: Luminosity scaling factor R_L due to the Hourglass effect evaluated for different values of the vertical beta-function at the IP for CLIC 380 GeV. The beam is assumed to be flat, and the bunch length is $\sigma_z = 70$ μm.

For the latest CLIC 380 GeV design [58] with $\beta_x^* = 8$ mm, and $\beta_y^* = 70$ μm, the reduction factor simplifies and is given by:

$$R_L \approx \frac{1}{\sqrt{\pi}} \int_{-\infty}^{+\infty} \frac{e^{-t^2} dt}{\sqrt{\left(1 + \frac{t^2}{t_y^2}\right)}} = \frac{t_y}{\sqrt{\pi}} e^{t_y^2/2} K_0(t_y^2/2) \ , \tag{1.68}$$

where $K_0(x)$ is the modified Bessel function of the second kind. Fig. 1.22 shows the dependence of the factor R_L as a function of β_y^*.

Crossing angle

In LCs after the collision the beams are extracted and dumped, so the design of both CLIC and ILC foresees that the beams do not collide head-on but with a given angle ϕ in the horizontal plane in order to accommodate the extractlin line. The typical angles for CLIC 3 TeV and 380 GeV are 20 mrad and 16.5 mrad respectively [20]. Since the effective beam size at the crossing increases, the luminosity produced is smaller. In the general case, the impact from Hourglass effect and crossing angle is not separated, and the total reduction factor for flat beams writes as [37]:

$$\begin{aligned} R_L &= \sqrt{\frac{2}{\pi}} a e^b K_0(b) \ , a = \frac{\beta_y}{\sqrt{2}\sigma_z} \ , \\ b &= a^2 \left(1 + \left(\frac{\sigma_z}{\sigma_x^*} \tan\phi\right)^2\right) \ . \end{aligned} \tag{1.69}$$

One can notice, that for head-on collisions ($\phi = 0$), it is equal to Eq. (1.68). If the Houglass effect is negligible, we have:

$$R_L \approx \left(1 + \left(\frac{\sigma_z}{\sigma_x^*} \tan\phi\right)^2\right)^{-1/2} . \tag{1.70}$$

For CLIC 380 GeV with an horizontal IP beam size of about 143 nm, the reduction factor is $R_L \approx 0.12$, which means that the luminosity is reduced by one order of magnitude. This shows the importance of having crab cavities to adjust the head and tail of the bunch for head-on like collisions at the IP [59].

Beam-beam effects and disruption parameter

The electron and positron beams generate strong electromagnetic fields in the vicinity of the IP. The interactions between the particles within a single bunch are ignored as the forces vanish as $1/\gamma^2$, where γ is the Lorentz-factor. The impact of these forces includes bending or disruption of the particles' trajectories around the IP and the beamstrahlung effect [60, 61], which is the radiation, and consequently energy loss, due to the disruption. In the linear approximation, for beams with no transverse offsets, the disruption can be seen as focusing of the beam and is called the pinch effect. The amount of focusing is described with the so-called disruption parameter $D_{x,y}$:

$$D_{x,y} \equiv \frac{2Nr_e}{\gamma} \frac{\sigma_z}{\sigma_{x,y}^*(\sigma_x^* + \sigma_y^*)} , \tag{1.71}$$

where $r_e \approx 2.8$ fm is the classical electron radius and Gaussian beams are assumed. When $D_{x,y} \ll 1$, the final deflecting angles of the particle depend on the initial coordinate linearly as:

$$\begin{cases} \Delta x' &= -\frac{D_x}{\sigma_z} x_0 \\ \Delta y' &= -\frac{D_y}{\sigma_z} y_0 \end{cases} \tag{1.72}$$

In this case, the disruption acts as a thin lens focusing reducing the effective beam size in both horizontal and vertical planes and consequently increasing the luminosity. When, $D_{x,y} \gg 1$, the particles will move transversely during the passage through the incoming bunch, and the motion will be nonlinear. By analogy, this is seen as a thick-lens focusing. For CLIC 380 GeV the disruption factors are: $D_x \approx 0.3$ and $D_y \approx 15.8$. The smaller beam size due to the disruption leads to the larger luminosity, which is effectively increased by the factor $\mathcal{H}_D$, which is called the enhancement factor due to the disruption:

$$\mathcal{H}_D \equiv \frac{\mathcal{L}}{\mathcal{L}_0} . \tag{1.73}$$

According to [62], for round beams ($\sigma_x^* = \sigma_y^*$), we have:

$$\mathcal{H}_D \approx 1 + D^{1/4} \left(\frac{D^3}{1 + D^3}\right) \left[\ln\left(\sqrt{D} + 1\right) + 2\ln 0.8t\right] , \tag{1.74}$$

where $D \equiv D_x = D_y$ and $t \equiv t_x = t_y = \frac{\beta^*}{\sigma_z}$. Usually the exact values of $\mathcal{H}_D$ are evaluated from the simulations. For the flat beams ($\sigma_y^* \ll \sigma_x^*$) it scales as:

$$\mathcal{H}_D \approx \left(1 + D_y^{1/4}\left(\frac{D_y^3}{1+D_y^3}\right)\left[\ln\left(\sqrt{D}+1\right) + 2\ln 0.8 t_y\right]\right)^{1/3} . \tag{1.75}$$

For CLIC 380 GeV with $t_y = 1$ and $D_y \approx 15.8$, the enhancement factor is $\mathcal{H}_D \approx 1.5$.

Due to the orbit deviation because of the disruption, the particles will radiate photons and loose energy. The emitted radiation is characterized by the critical energy $\hbar\omega_c$ [63]:

$$\hbar\omega_c = \frac{3}{2}\frac{\hbar\gamma^3 c}{\rho} , \tag{1.76}$$

where ρ is the curvature radius of the trajectory, and c is the speed of light. To characterize this effect known as beamstrahlung, a dimensionless parameter Υ is introduced:

$$\Upsilon \equiv \frac{2}{3}\frac{\hbar\omega_c}{E} = \frac{\lambda_e \gamma^2}{\rho} , \tag{1.77}$$

where E is the particle's energy before the radiation and λ_e is the Compton wavelength. This parameter changes throughout the collision. The maximum and the average values are given by:

$$\Upsilon_{max} \approx \frac{2Nr_e^2\gamma}{\alpha\sigma_z(\sigma_x^* + 1.85\sigma_y^*)} , \ \langle\Upsilon\rangle \approx \frac{5}{6}\frac{Nr_e^2\gamma}{\alpha\sigma_z(\sigma_x^* + \sigma_y^*)} , \tag{1.78}$$

where $\alpha = \frac{1}{137}$ is the fine structure constant. For $\langle\Upsilon\rangle \ll 1$, the beamstrahlung spectrum corresponds to the SR spectrum, and is called a classical regime. In the case when $\langle\Upsilon\rangle \gg 1$, the critical energy is larger then the beam energy and the radiation is partially suppressed. Such regime is called quantum regime. For CLIC 380 GeV with $\langle\Upsilon\rangle \approx 0.17$ we are in the the classical regime, while for CLIC 3 TeV with $\langle\Upsilon\rangle \approx 11.02$ we are in the quantum regime.

The energy emitted by each particle due to the disruption can be characterized by the number of photons n_γ emitted as:

$$n_\gamma \propto \langle\Upsilon\rangle\frac{\sigma_z}{\gamma} \propto \frac{N}{\sigma_x^* + \sigma_y^*} , \tag{1.79}$$

with the average energy given by:

$$E_\gamma \propto \langle\Upsilon\rangle\frac{1}{\gamma} \propto \frac{N}{(\sigma_x^* + \sigma_y^*)\sigma_z} . \tag{1.80}$$

To limit the beamstrahlung and consequently decrease the energy losses - one needs to keep the sum $(\sigma_x^* + \sigma_y^*)$ large, keeping in mind that luminosity scales as $1/(\sigma_x^*\ \sigma_y^*)$. The balance is found by utilizing the flat beams, where normally $\sigma_x^* \gg \sigma_y^*$. This is valid for both CLIC 380 GeV and CLIC 3 TeV as well as for ILC.

1.4.7 Static and dynamic imperfections impact in FFS

In order to provide the design luminosity, the beam size in the linear colliders has to be squeezed to the nanometer level. This implies tight tolerances to magnetic field quality and alignment precision for magnets. Unfortunately, it is not possible to achieve that level of precision without the live tuning techniques that are based on the actual beam data. The traditional FFS relies on quadrupoles to provide the optical focusing of the beam, dipoles to generate the dispersion, and sextupole for chromaticity correction. Any magnetic field or alignment imperfection of these magnets will propagate to the IP and could be a source of various aberrations. Ultimately it leads to beam size dilution, and to luminosity drop.

The most relevant static imperfections in the FFS are:

Magnetic field errors

It covers all the cases, when the nominal strength of the magnet differs from the design.

- The dipole with incorrect magnetic field distorts the beam orbit and is a source of residual dispersion. Defining the magnetic field of the dipole as: $B = B_0(1 + \frac{\Delta B}{B_0})$, where ΔB is the field offset so the Hamiltonian of the particle writes as:

$$H = \frac{x}{\rho}\frac{\Delta B}{B_0} - \frac{x}{\rho}\left(1 + \frac{\Delta B}{B_0}\right)\delta + \frac{x'^2 + y'^2}{2} \ . \tag{1.81}$$

  then equation of motion is given by:

$$x'' = \frac{\delta}{\rho} - \frac{1}{\rho}\frac{\Delta B}{B_0}(1 - \delta) \ . \tag{1.82}$$

  The additional angular kick that the particle receives approximates as

$$\theta_x \approx -\frac{1}{\rho}\frac{\Delta B}{B_0}(1 - \delta)L_d \ , \tag{1.83}$$

  where L_d is the length of the dipole. The change of the particle's horizontal coordinate at location s downstream of the dipole is:

$$\delta\vec{x} = \begin{pmatrix} R_{12}^{D\to s} \\ R_{22}^{D\to s} \end{pmatrix}\theta_x = \begin{pmatrix} \sqrt{\beta_{x,D}\beta_{x,s}}\sin\Delta\phi_x \\ \sqrt{\frac{\beta_{x,D}}{\beta_{x,s}}}(\cos\Delta\phi_x - \alpha_{x,s}\sin\Delta\phi_x) \end{pmatrix}\theta_x \ , \tag{1.84}$$

  where $\beta_{x,D}$ and $\beta_{x,s}$ are the horizontal beta-function at the dipole location and at the arbitrary point s, and $\Delta\phi_x$ is the horizontal phase advance between them. The constant part of θ_x adds the orbit distortion, while the energy dependent part is a source of additional dispersion. Such dispersion is the source of various chromatic aberrations in the downstream elements. Similarly, if the particle receives a kick θ_y in the vertical plane, the vertical coordinate change is given by:

$$\delta\vec{y} = \begin{pmatrix} R_{34}^{D\to s} \\ R_{44}^{D\to s} \end{pmatrix}\theta_y = \begin{pmatrix} \sqrt{\beta_{y,D}\beta_{y,s}}\sin\Delta\phi_y \\ \sqrt{\frac{\beta_{y,D}}{\beta_{y,s}}}(\cos\Delta\phi_y - \alpha_{y,s}\sin\Delta\phi) \end{pmatrix}\theta_y \ . \tag{1.85}$$

  Such field errors may lead to a non zero beam transverse position and dispersion at the IP, such that the opposing beams can miss each other.

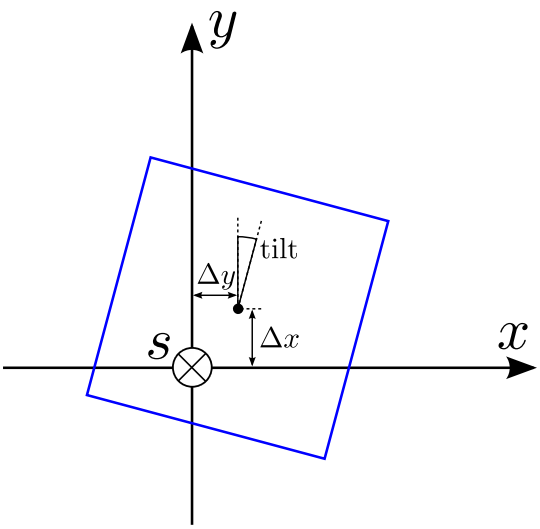

Figure 1.23: Schematic representation of the alignment errors for a magnet.

- The field error of a normal quadrupole is the source of the distortion of the optical parameters in the FFS. The error will propagate to the IP and could be a source of waist shift and residual dispersion. It becomes significant when the quadrupole is at the FD phase. If the quadrupole is a skew quadrupole, then it becomes the source of skew coupling at the IP.

- If the magnetic strength of the sextupole is not correct, it impacts the chromaticity correction in the FFS. The sextupole will over-compensate or under-compensate the chromaticity, and break $-\mathcal{I}$ inside the sextupole "pair".

Alignment errors

It includes the transverse offsets of the magnet in horizontal and vertical planes, and the tilt along the longitudinal axis, see Fig. 1.23. The magnet with a certain transverse offset is a source of feed down to lower order multipoles magnetic field: quadrupole becomes the source of the dipolar field, sextupole becomes the source of the quadrupolar and dipolar fields, etc. In general these fields are a mix of normal and skew components. When the magnet, which is the source of the normal multipole, is tilted, could also generates skew multipole component and vice versa.

The impact of the misalignments in the main magnets is described in the following.

- Ideally, the dipolar field does not depend on the transverse coordinate. A tilted dipole magnet adds a steering in the vertical plane and is the source of undesirable vertical dispersion.

- The normal quadrupole with a transverse offset is a source of the dipolar field.

Setting $x \to x + \Delta x$ and $y \to y + \Delta y$ in Eq. (1.20) gives us:

$$\begin{aligned} H &= k_1^N \frac{x^2 - y^2}{2} \frac{1}{(1+\delta)} + \overbrace{\frac{k_1^N \Delta x}{1+\delta} x}^{\text{Dipole}} - \overbrace{\frac{k_1^N \Delta y}{1+\delta} y}^{\text{Skew dipole}} + \frac{x'^2 + y'^2}{2} \\ &\approx k_1^N \frac{x^2 - y^2}{2}(1-\delta) + k_1^N \Delta x (1-\delta) x - k_1^N \Delta y (1-\delta) y + \frac{x'^2 + y'^2}{2} \ . \end{aligned} \tag{1.86}$$

The equation of motion is similar to the case of the dipole magnet with field errors. If $k_{1,L}^N$ is the integrated strength of the quadrupole, the kicks received by a particle are: $\theta_x \approx -k_{1,L}^N \Delta x (1-\delta)$ and $\theta_y \approx k_{1,L}^N \Delta y (1-\delta)$. In such a way, the steering in the horizontal plane depends linearly on the horizontal offset Δx, and the vertical steering depends on the vertical offset Δy. For a misaligned skew quadrupole the Hamiltonian will be given by:

$$H = k_1^S xy \frac{1}{(1+\delta)} + \overbrace{\frac{k_1^N \Delta y}{1+\delta} x}^{\text{Dipole}} - \overbrace{\frac{k_1^N \Delta x}{1+\delta} y}^{\text{Skew dipole}} + \frac{x'^2 + y'^2}{2} \ . \tag{1.87}$$

In this case, the vertical offset creates a horizontal steering, and horizontal offset creates a vertical steering.

- The transversely misaligned sextupole becomes the source of various low-order fields. Similarly, setting $x \to x + \Delta x$ and $y \to y + \Delta y$ and based on Eq. (1.22) the Hamiltonian writes as:

$$\begin{aligned} H = \frac{k_2^N}{6}(x^3 - 3xy^2) \frac{1}{(1+\delta)} + \overbrace{\frac{k_2^N \Delta x}{(1+\delta)} \frac{x^2 - y^2}{2}}^{\text{Norm. quad.}} - \overbrace{\frac{k_2^N \Delta y}{(1+\delta)} xy}^{\text{Skew quad.}} \\ + \overbrace{\frac{k_2^N}{(1+\delta)} \frac{\Delta x^2 - \Delta y^2}{2} x}^{\text{Dipole}} - \overbrace{\frac{k_2^N \Delta x \Delta y}{(1+\delta)} y}^{\text{Skew dipole}} + \frac{x'^2 + y'^2}{2} \ . \end{aligned} \tag{1.88}$$

We could notice, that being $k_{2,L}^N$ the integrated strength of the sextupole, such a sextupole also acts like a normal quadrupole with strength $k_2^N \Delta x$, a skew quadrupole with strength $-k_2^N \Delta y$, a dipole magnet with $\theta_x \approx k_{2,L}^N \frac{\Delta x^2 - \Delta y^2}{2}(1-\delta)$ and a skew dipole with $\theta_y \approx -k_{2,L}^N \Delta x \Delta y (1-\delta)$.

Similarly in the case of a skew sextupole:

$$\begin{aligned} H = \frac{k_2^S}{6}(3x^2 y - y^3) \frac{1}{(1+\delta)} + \overbrace{\frac{k_2^S \Delta y}{(1+\delta)} \frac{x^2 - y^2}{2}}^{\text{Norm. quad.}} + \overbrace{\frac{k_2^N \Delta x}{(1+\delta)} xy}^{\text{Skew quad.}} \\ + \overbrace{\frac{k_2^N}{(1+\delta)} \frac{\Delta x^2 - \Delta y^2}{2} y}^{\text{Skew dipole}} + \overbrace{\frac{k_2^N \Delta x \Delta y}{(1+\delta)} x}^{\text{Dipole}} + \frac{x'^2 + y'^2}{2} \ . \end{aligned} \tag{1.89}$$

As in case of the normal sextipole, such a magnet generates normal a quadrupolar field of strength $k_2^S \Delta y$, a skew quadrupolar field of strength $k_2^S \Delta x$, a dipolar field of $\theta_x \approx k_{2,L}^S \Delta x \Delta y (1-\delta)$, and a skew dipolar field of $\theta_y \approx k_{2,L}^N \frac{\Delta x^2 - \Delta y^2}{2}(1-\delta)$.

Dynamic errors

The dynamic errors in the FFS are due to the fluctuation of the magnets' strength or the time-varying misalignment of the magnets. In this case, the errors vary between different bunches or between the trains. They could be given by:

- Power supply fluctuation or ripple, being this effect the source of the strength variation of the magnets.
- Beam jitter that makes the bunches or the trains have different transverse offsets.
- Ground motion and vibration, that could lead to time-dependent feed down, so lowering the multipole order of the magnetic fields.

These effects lead to a reduction of the average luminosity and are difficult to mitigate. The correction approaches comprise active feedback systems, a system of this type has been developed and it is being tested at ATF2 [64].

Chapter 2

CLIC 380 GeV FFS optimization with Short FD and new dispersion layout

In this chapter we report the optimizations of the FFS optics of CLIC 380 GeV based on the reduction of the length of the FD. We have shortened FD quadrupoles by approximately 50 % to reduce the chromaticity. As a result, two optics have been designed, one with a traditional dispersion profile and another with a novel dispersion profile.

A current state of the CLIC FFS and motivation of the shortening of the FD is given in Sec. 2.1. In Sec. 2.2 we introduce an analytical approximation for evaluating the horizontal beam size, that we will be used to numerically optimize the optics. The optics with the current dispersion profile but with shorther dipoles is discussed in Sec. 2.3 and the optics with a novel dispersion profile is described in Sec. 2.4. In Sec. 2.5 we make a complete evaluation of the different options including beam sizes, luminosities, energy bandwidth, and we reevaluate the apertures based on the collimation depth.

2.1 Current FFS optics and motivation for the Short FD

The current CLIC 380 GeV FFS optics has a longer L^*, as described in the CLIC Project implementation Plan (PIP) [15]. It was designed by scaling up the original optics with $L^* = 4.3$ m, all drifts and magnet lengths were increased correspondingly to reach $L^* = 6$ m. As a result, the length of the FFS increased from 550 m to 770 m [20]. To tackle the 3^{rd} order chromatic aberrations, a pair of octupoles was added to the lattice. A schematic layout of the FFS is shown in Fig. 2.1, highlighting the key elements of the lattice. Further, a new optics with a reduced β_y^*, 100 μm to 70 μm [58], to increase luminosity and approach the Hourglass effect [57] limitation was designed. Henceforward, this optics is refereed as the "current" one. The optical functions for the original optics from PIP with $\beta_y^* = 100$ μm and the current optics $\beta_y^* = 70$ μ m are shown in Fig. 2.2 and all the relevant parameters

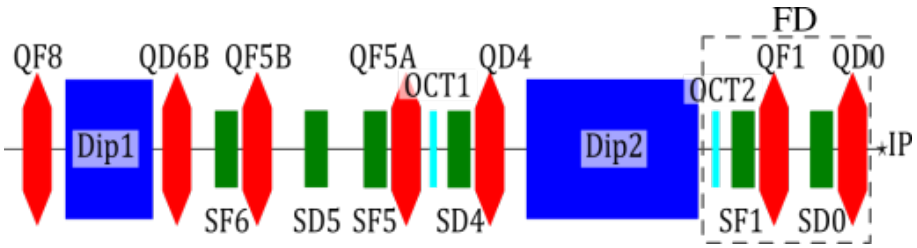

Figure 2.1: Schematic layout of the CLIC FFS. Quadrupoles are shown in red, sextupoles in green, dipoles in blue and octupoles in cyan.

Table 2.1: Summary table of the key parameters of the recent designs of the FFS of CLIC 380 GeV.

CLIC 380 GeV FFS	PIP $\beta_y^* = 100$ μm	Current $\beta_y^* = 70$ μm
Final Drift L^* [m]	6	6
FFS length [m]	770	770
Normalized emittance (IP) $\epsilon_{n,x}/\epsilon_{n,y}$ [nm]	950/30	950/30
Beta function (IP) β_x^*/β_y^* [mm]/[μm]	8/100	8/70
IP beam size σ_x^*/σ_y^* [nm]	145/3.0	145/3.0
Bunch length σ_z [μm]	70	70
RMS energy spread δ_p [%]	0.3	0.3
Number of particles in one bunch N [$\times 10^9$]	5.2	5.2
Number of bunches in one train N_b	352	352
Repetition rate f [Hz]	50	50
Total luminosity $\mathcal{L}$ [10^{34}cm^{-2}s^{-1}]	1.63	1.66
Peak luminosity $\mathcal{L}_{peak}$ [10^{34}cm^{-2}s^{-1}]	0.94	0.96
Vertical chromaticity $\xi_y^* \approx L^*/\beta_y^*$	60000	86000

are given in Tab.2.1.

The apertures for the BDS magnets have also been evaluated and they are shown in Fig. 2.3. The calculations are based on the collimation depth of $15\sigma_x \times 55\sigma_y$ introduced in the betatron collimation section of the BDS. We also apply the minimum aperture of approximately 15 mm to limit the wakefields effect in the beampipe. We see that almost all the magnets, except for few quadrupoles at the BDS entrance, feature less than 1.5 T pole tip field imposed by the iron saturation limitation [65]. For the dipoles, the magnetic field is homogeneous, while for the other magnets it is a function of the aperture:

$$\begin{cases} B_{dipole}[\mathrm{T}] & = 3.333\ p[\mathrm{GeV/c}]\ \frac{1}{\rho[\mathrm{m}]} \\ B_{quadrupole}[\mathrm{T}] & = 3.333\ p[\mathrm{GeV/c}]\ k_1[\mathrm{m}^{-2}]\ A[\mathrm{m}] \\ B_{sextupole}[\mathrm{T}] & = 3.333\ p[\mathrm{GeV/c}]\ k_2[\mathrm{m}^{-3}]\ \frac{A^2[\mathrm{m}]}{2} \\ B_{octupole}[\mathrm{T}] & = 3.333\ p[\mathrm{GeV/c}]\ k_3[\mathrm{m}^{-4}]\ \frac{A^3[\mathrm{m}]}{6} \end{cases} \tag{2.1}$$

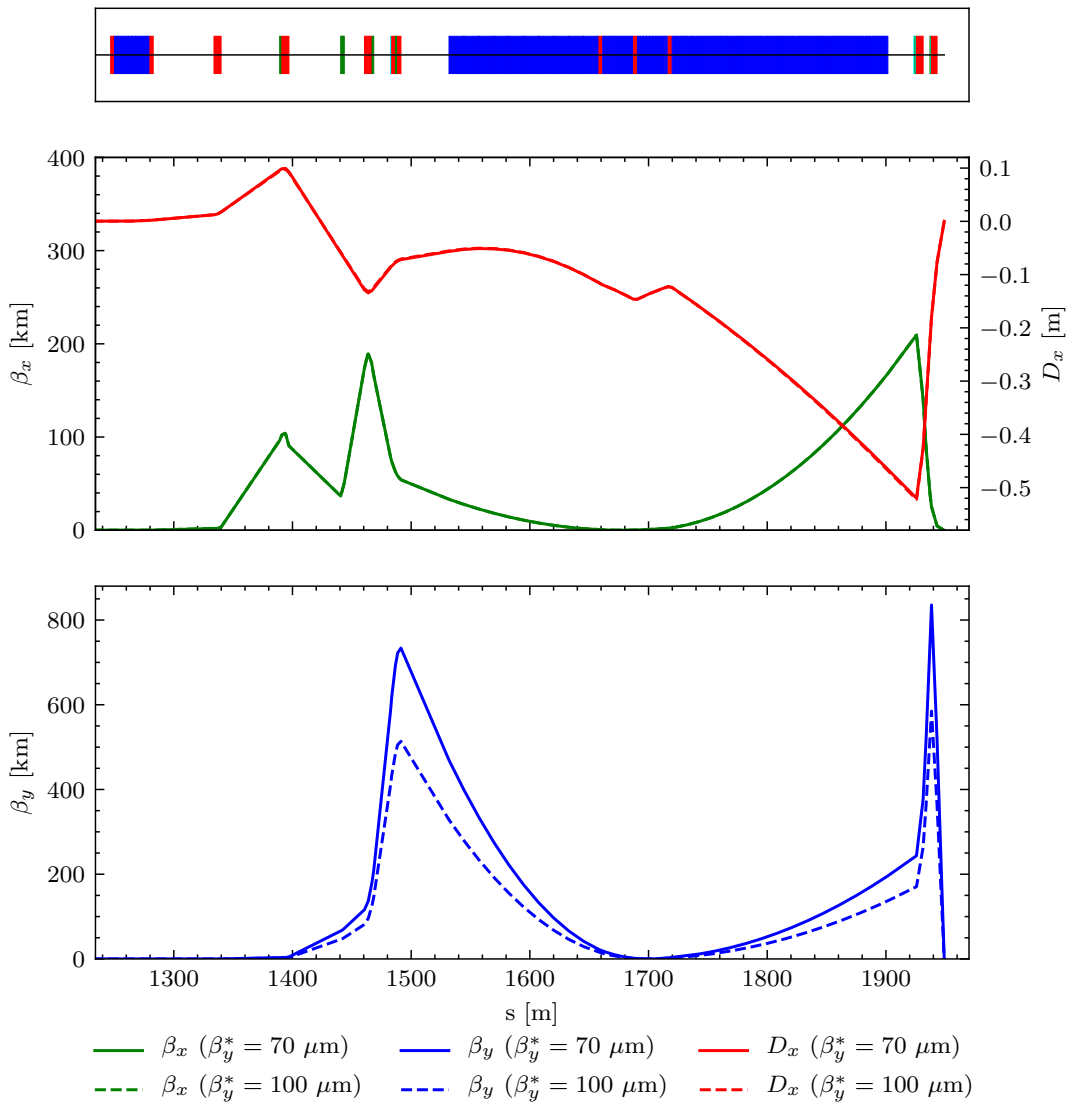

Figure 2.2: Twiss functions for the latest designs of the FFS of CLIC 380 GeV.

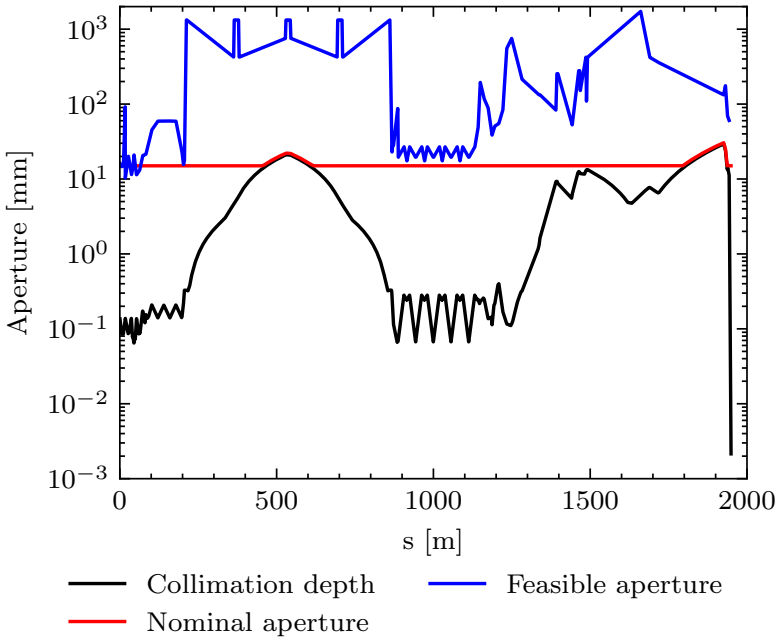

Figure 2.3: Apertures of the magnets along the BDS. The feasible aperture (blue) corresponds to the maximum aperture, which allows the pole tip field to be less than 1.5 T.

Table 2.2: Key parameters of the FD quadrupoles for the current optics.

	QF1	QD0
Magnetic length [m]	5.59	4.69
Integrated strength k_{1L} [m^{-1}]	0.076	-0.184
Aperture [mm]	27.4	27.4
Pole tip field [T]	0.23	0.68

where k_1, k_2, and k_3 are the magnetic strengths of the quadrupoles, sextupoles, and octupoles respectively, A is the aperture of the magnet, ρ is the bending radius, and p is the beam momentum. In the particular case of the QD0 magnet with an "hybrid" design [66], the field could be up to 2.2 T. Table 2.2 shows the FD quadrupoles settings for the current design.

2.2 Analytical approximations for the optimization of the upstream horizontal chromaticity.

The approaches used to simultaneously correct the horizontal and vertical chromaticity, as well as 2nd order dispersion have been discussed in Sec. 1.4.4. When chromaticity is

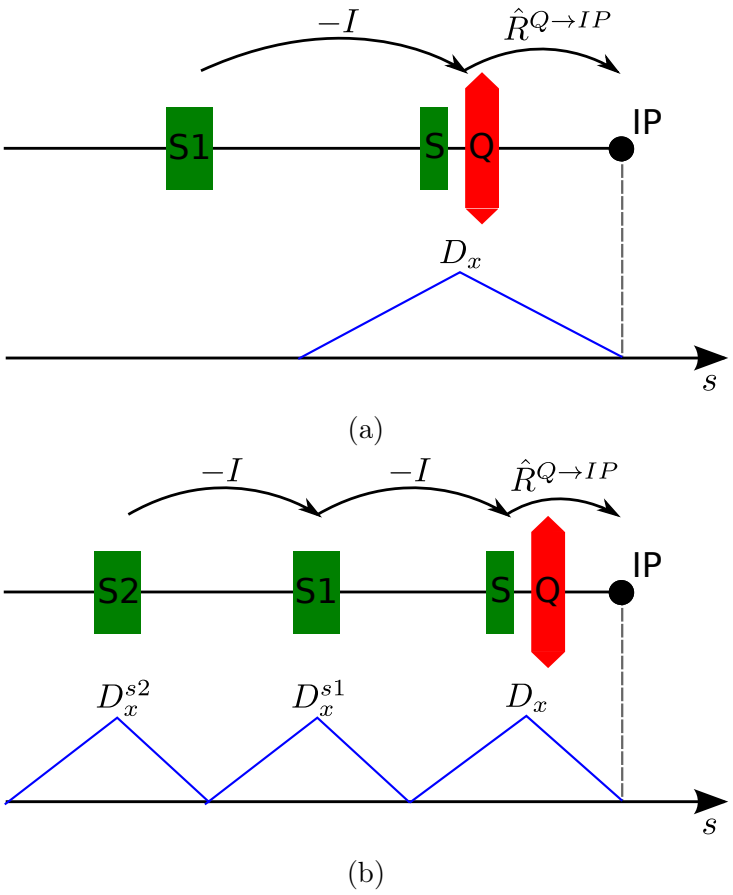

Figure 2.4: Minimum scheme required for the correction of the horizontal chromaticity and 2[nd] order dispersion in the FFS (a) and scheme of the correction of the horizontal aberrations used in CLIC FFS (b).

corrected locally, the vertical sextupole (SD0) is set to correct the vertical chromaticity and the horizontal sextupole (SF1) is set to twice overcompensate the horizontal chromaticity. The additional horizontal chromaticity is generated upstream of the FD. In this section, we investigate how the small beam size at the IP changes when the upstream horizontal chromaticity is not optimal. We will focus on the horizontal beam size, because the vertical one should not be affected.

In the first case, we have two sextupoles, one sextupole is placed next to a quadrupole and the second is located in the upstream dispersion-free region to provide $-I$ transformation between them, see Fig. 2.4a. We use the thin-lens approximation for the magnets and we assume that geometrical aberrations of the sextupoles are mutually canceled. The horizontal coordinate of the particle at the IP for such a system writes as:

$$x^* = x^*_\beta + (\widetilde{T}^q_{116} + \widetilde{T}^s_{116})x_0\delta + (\widetilde{T}^q_{166} + \widetilde{T}^s_{166})\delta^2 \ . \tag{2.2}$$

where x_0 is the particle's coordinate at the entrance of the FD, δ is the energy offset,

$\widetilde{T}^q_{116}$ and $\widetilde{T}^q_{166}$ are the 2nd order terms generated by a quadrupole, and $\widetilde{T}^s_{116}$ and $\widetilde{T}^s_{166}$ are the 2nd order terms generated by a sextupole. Introducing the additional chromaticity ξ^{up}_x, generated by the quadrupoles upstream in the dispersion-free region and combining Eqs. (1.44), (1.49), (1.52), and (1.53), the horizontal beam size at the IP is:

$$\sigma^{*2}_x = \epsilon_x\beta^*_x + \epsilon_x\beta^*_x(\xi^{up}_x + \xi^q_x + \xi^s_x)^2\delta^2_p + 3\frac{\beta^*_x}{\beta_x}D^2_x(\xi^q_x + \xi^s_x/2)^2\delta^4_p \ . \tag{2.3}$$

One can see that to cancel the aberrations we need:

$$\begin{cases} \xi^{up}_x + \xi^q_x + \xi^s_x & = 0 \\ \xi^q_x + \xi^s_x/2 & = 0 \end{cases} \tag{2.4}$$

For this we set first the chromaticity of the sextupole to $\xi^s_x = -2\xi^q_x$. Therefore to cancel the chromaticity we need an additional contribution with value $\xi^{up}_x = \xi^q_x$. When the optics is not tuned well, the natural chromaticity generated upstream is not optimal $\xi^{up}_x = \xi^q_x + \Delta\xi_x$. Then we have to search for a new amount of the chromaticity generated by the sextupole $\xi^s_x = -2\xi^q_x + \Delta\xi^s_x$, to minimize the horizontal beam size by solving $\frac{d}{d\Delta\xi^s_x}\sigma^{*2}_x = 0$. Introducing Eq. 2.3 and solving it, we could find the optimal chromaticity for the sextupole:

$$\Delta\xi^s_x = -\frac{\Delta\xi_x}{1 + \frac{3}{4}\frac{D^2_x}{\beta_x\epsilon_x}\delta^2_p} \tag{2.5}$$

Putting back Eq. 2.5 in Eq. 2.3, we could evaluate the horizontal beam size:

$$\frac{\sigma^2_x}{\epsilon_x\beta^*_x} = 1 + (\Delta\xi_x + \Delta\xi^s_x)^2\delta^2_p + \frac{3}{4}\frac{D^2_x}{\beta_x\epsilon_x}(\Delta\xi^s_x)^2\delta^4_p = 1 + \frac{\Delta\xi^2_x\delta^2_p}{1 + \frac{4}{3}\frac{\epsilon_x\beta_x}{D^2_x\delta^2_p}} \tag{2.6}$$

In the second case, the dispersion at the upstream sextupole S1 (refer to Fig. 2.4a) is nonzero. This means that it is also contributing to the horizontal beam size via the chromaticity and the 2nd order dispersion at the IP as:

$$\begin{aligned} \sigma^{*2}_x = \epsilon_x\beta^*_x + \epsilon_x\beta^*_x(\xi^{up}_x + \xi^q_x + \xi^s_x + \xi^{s1}_x)^2\delta^2_p + \\ +3\frac{\beta^*_x}{\beta_x}D^2_x\left(\xi^q_x + \xi^s_x/2 - \xi^{s1}_x/2\frac{D^{s1}_x}{D_x}\right)^2\delta^4_p \ , \end{aligned} \tag{2.7}$$

where D^{s1}_x is the dispersion at the upstream sextupole and $\xi^{s1}_x = -k_{s,L1}\beta_x D^{s1}_x$ is the chromaticity it generates. The minus sign in the 2nd order dispersion contribution appears due to the $-I$ transformation. The strength of the upstream sextupole is set $k^{s1}_L = k^s_L$ to cancel the geometrical aberrations. The optimal upstream chromaticity is given by:

$$\xi^{up}_x = \xi^q_x\frac{1 + D^{s1}_x/D_x}{1 - D^{s1}_x/D_x} \ . \tag{2.8}$$

It requires the sextupoles haveto be set to produce the following chromaticities:

$$\xi^s_x = -\frac{2\xi^q_x}{1 - \left(\frac{D^{s1}_x}{D_x}\right)^2} \ , \quad \xi^{s1}_x = -\frac{2\xi^q_x}{1 - \left(\frac{D^{s1}_x}{D_x}\right)^2}\frac{D^{s1}_x}{D_x} \ , \tag{2.9}$$

leading to the full cancellation of the above aberrations. In the presence of additional upstream chromaticity $\Delta\xi_x$, the cancellation of the geometrical aberrations does not strictly correspond to the minimum IP horizontal beam size. One has to include the geometrical and chromo-geometrical terms to evaluate the minimum IP horizontal beam size.

Given the fact that in CLIC FFS design, there are six sextupoles, we exlore the third case, that corresponds to Fig. 2.4b. Here, we also need to include the impact from the rest of the sextupoles located at large β_x locations. In the current CLIC design, we have one additional sextupole, namely SF6, referred as S2 in Fig. 2.4b. This additional sextupole is located in a dispersive region with D_x^{s2} dispersion and at 2π phase advance from the FD. Similarly to Eq. (2.2) we could evaluate the horizontal coordinate at the IP, including also the geometrical terms:

$$\begin{aligned} x^* = x^*_{betatron} + (\widetilde{T}^q_{116} + \widetilde{T}^s_{116} + \widetilde{T}^{s1}_{116} + \widetilde{T}^{s2}_{116})x_0\delta \\ +(\widetilde{T}^q_{166} + \widetilde{T}^s_{166} - \widetilde{T}^{s1}_{166} + \widetilde{T}^{s2}_{166})\delta^2 \\ -(\widetilde{T}^s_{111} - \widetilde{T}^{s1}_{111} + \widetilde{T}^{s2}_{111})x_0^2 + (\widetilde{T}^s_{133} - \widetilde{T}^{s1}_{133} + \widetilde{T}^{s2}_{133})y_0^2 \ . \end{aligned} \tag{2.10}$$

We could connect the pure geometrical terms of the sextupoles with the chromaticity of the corresponding magnet, as follows:

$$\widetilde{T}^s_{111} = -\widetilde{T}^s_{133} = \frac{\xi^s_x}{2D_x}\sqrt{\frac{\beta^*_x}{\beta_x}} \ . \tag{2.11}$$

When the horizontal chromaticity generated upstream differs from the value given in Eq. (2.8) by $\Delta\xi_x$, we could adjust the amount of chromaticity generated by the sextupoles S and S1 by $\Delta\xi^s_x$ and $\Delta\xi^{s1}_x$ with respect to Eq. (2.9). At the same time, if we would like to find the optimal settings for S2 sextupole, $\xi^{s2}_x = -k^{s2}_L\beta_x D^{s2}_x$ to minimize the horizontal beam size at the IP. The IP horizontal beam size for such a system, based on Eq. (2.10) with upstream chromaticity $\xi^{up}_x = \xi^q_x\frac{1+D^{s1}_x/D_x}{1-D^{s1}_x/D_x} + \Delta\xi_x$ and including Eq. (2.11) writes as:

$$\begin{aligned} \sigma^{*2}_x = \epsilon_x\beta^*_x + \epsilon_x\beta^*_x(\Delta\xi_x + \Delta\xi^s_x + \Delta\xi^{s1}_x + \xi^{s2}_x)^2\delta^2_p \\ 3\frac{\beta^*_x}{\beta_x}D^2_x\left(\frac{\Delta\xi^s_x}{2} - \frac{\Delta\xi^{s1}_x}{2}\frac{D^{s1}_x}{D_x} + \frac{\xi^{s2}_x}{2}\frac{D^{s2}_x}{D_x}\right)^2\delta^4_p \\ +\frac{3}{4}\frac{\beta^*_x}{\beta_x}\left(\frac{\Delta\xi^s_x}{D_x} - \frac{\Delta\xi^{s1}_x}{D^{s1}_x} + \frac{\xi^{s2}_x}{D^{s2}_x}\right)^2[(\epsilon_x\beta_x)^2 + (\epsilon_y\beta_y)^2] + \\ +\frac{\beta^*_x}{\beta_x}\left(\frac{\Delta\xi^s_x}{D_x} - \frac{\Delta\xi^{s1}_x}{D^{s1}_x} + \frac{\xi^{s2}_x}{D^{s2}_x}\right)\times \\ \times\left(\frac{\Delta\xi^s_x}{2} - \frac{\Delta\xi^{s1}_x}{2}\frac{D^{s1}_x}{D_x} + \frac{\xi^{s2}_x}{2}\frac{D^{s2}_x}{D_x}\right)D_x\delta^2_p(\epsilon_y\beta_y - \epsilon_x\beta_x) \end{aligned} \tag{2.12}$$

The minimum could be found by solving the following system of equations:

$$\begin{cases} \dfrac{\partial}{\partial \Delta\xi_x^s}\sigma_x^{*2} & = 0 \\ \dfrac{\partial}{\partial \Delta\xi_x^{s1}}\sigma_x^{*2} & = 0 \\ \dfrac{\partial}{\partial \xi_x^{s2}}\sigma_x^{*2} & = 0 \end{cases} \tag{2.13}$$

Using $\vec{\xi} = (\Delta\xi_x^s, \Delta\xi_x^{s1}, \xi_x^{s2})^T$ we could simplify Eq. (2.12) as:

$$\sigma_x^{*2} = \epsilon_x\beta_x^* + \epsilon_x\beta_x^* \left(\Delta\xi_x + \sum_{i=1}^{3}\xi_i\right)^2 \delta_p^2 + \sum_{i=1}^{3}\sum_{j=i}^{3} A_{ij}\xi_i\xi_j \ , \tag{2.14}$$

where A_{ij} are the terms one gets after comparing Eq. (2.14) and Eq. (2.12). The derivatives are:

$$\frac{\partial}{\partial\xi_l}\sigma_x^{*2} = 2\epsilon_x\beta_x^* \left(\Delta\xi_x + \sum_{i=1}^{3}\xi_i\right)\delta_p^2 + \sum_{i=1}^{3}\sum_{j=i}^{3} A_{ij}(\delta_{il}\xi_j + \delta_{jl}\xi_i) \ , \tag{2.15}$$

where δ_{ij} is the Kronecker delta. By introducing the Heaviside step function $\mathcal{H}$, with $\mathcal{H}(0) = 1$, we could rewrite the sum as:

$$\frac{\partial}{\partial\xi_l}\sigma_x^{*2} = 2\epsilon_x\beta_x^*\delta_p^2\Delta\xi_x + \sum_{i=1}^{3}\xi_i(2\epsilon_x\beta_x^*\delta_p^2 + A_{il}(\mathcal{H}(i-l) + \mathcal{H}(l-i))) \ . \tag{2.16}$$

In this format, the solution of Eq. (2.13) could be simplified as:

$$\hat{M}\vec{\xi} = \Delta\xi_x\vec{b}, \quad \vec{\xi} = (\Delta\xi_x^s, \Delta\xi_x^{s1}, \xi_x^{s2})^T \ , \tag{2.17}$$

where $\hat{M}$ and $\vec{b}$ are the matrix and the vector estimated depending on the configuration of the sextupoles respectively. The solution is proportional to $\Delta\xi_x$, which leads to a quadratic dependence of σ_x^{*2} on $\Delta\xi_x$, similarly to Eq. (2.6). This property will be used to find the optimal upstream chromaticity in the following.

2.3 Matching of the FFS optics with Short FD

The pole tip field for both QF1 and QD0 is lower than 2.2 T, which allows to decrease their length. Based on this, we decrease the length of QF1 and QD0 to approximately 2.79 m and 1.69 m respectively. The advantage of a FD with shorter magnets is that it generates less chromaticity and potentially reduces the beta-function level in the whole FFS.

To design the optics with short QF1 and QD0 magnets, we reduce their length, but we increase their magnetic fields to keep the same integrated strength. We keep the centers of both magnets unchanged and we adjust the length of the final drift L^* to be exactly 6 m (see the schematic in Fig. 2.5). Further, the optics is matched with MADX [43], for the same Twiss parameters at the IP as in Tab. 2.1, see Fig. 2.6.

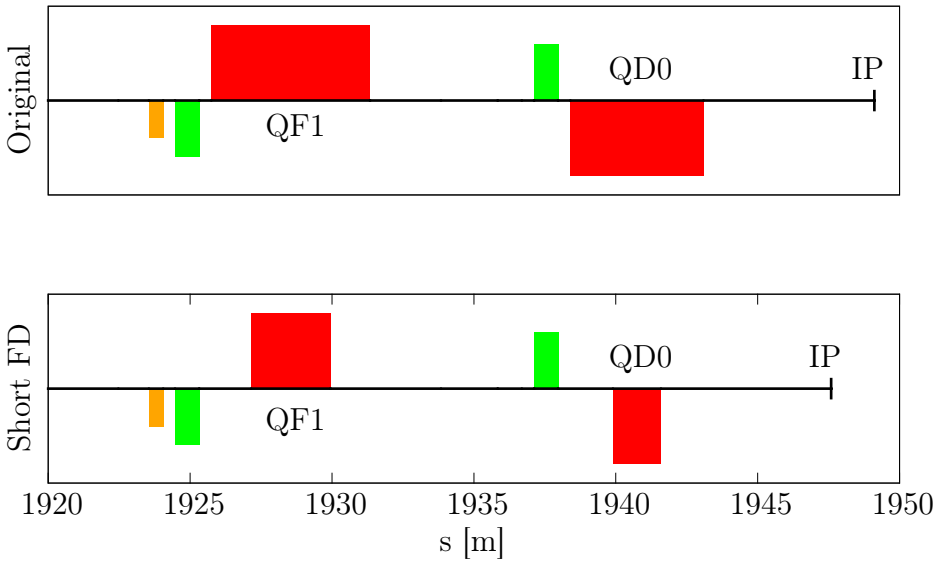

Figure 2.5: Schematic view of the length reduction for QF1 and QD0. The quadrupoles are shown in red, sextupoles in green, and octupoles in orange.

To match the beam sizes at the IP we use the six available sextupoles, namely SD0, SF1, SD4, SF5, SD5, SF6 and the two octupoles, namely OCT1 and OCT2 (refer to Fig. 2.1). For the calculations, we use MADX with PTC [49] to generate the transfer map and Mapclass [45] to evaluate the beam sizes at the IP.

In order to minimize the horizontal beam size at the IP, we need to find the optimal upstream chromaticity. In general it should be close to the chromaticity generated by the FD. As evaluated in Sec. 2.2, the square of the minimum horizontal beam size at the IP is a quadratic function of the upstream chromaticity. We denote ξ_x^{FD} as the horizontal chromaticity generated at the IP by the FD and ξ_x^{up} - the horizontal chromaticity generated at the IP by the upstream elements to the FD. The chromaticity difference impacting the horizontal beam size at the IP is:

$$\Delta\xi_x = \xi_x^{FD} - \xi_x^{up} \ . \tag{2.18}$$

To modify ξ_x^{up}, the distance between the section of the dipole magnets Dip2 and the FD is changed (refer to Fig. 2.1). In this case, the FD chromaticity remains the same, while the beta-function level along the FFS is affected, which directly impacts the upstream chromaticity, since the chromaticity of a single quadrupoles is proportional to the beta-function at its location, according to Eq. 1.44. For each distance change, the Twiss paramaters are matched with the quadrupoles first , after the 2^{nd} order beam size is matched using the sextupoles. Figure 2.7 shows the plot of the 2^{nd} order horizontal beam size as a function of chromaticity difference $\Delta\xi_x$ evaluated for each distance change between Dip2 and FD. Also, Fig. 2.8 connects $\Delta\xi_x$ with the change of the distance between Dip2 and FD. The parabolic fit of the square of the horizontal beam size gives the optimal difference of $\Delta\xi_x \approx 47$. This

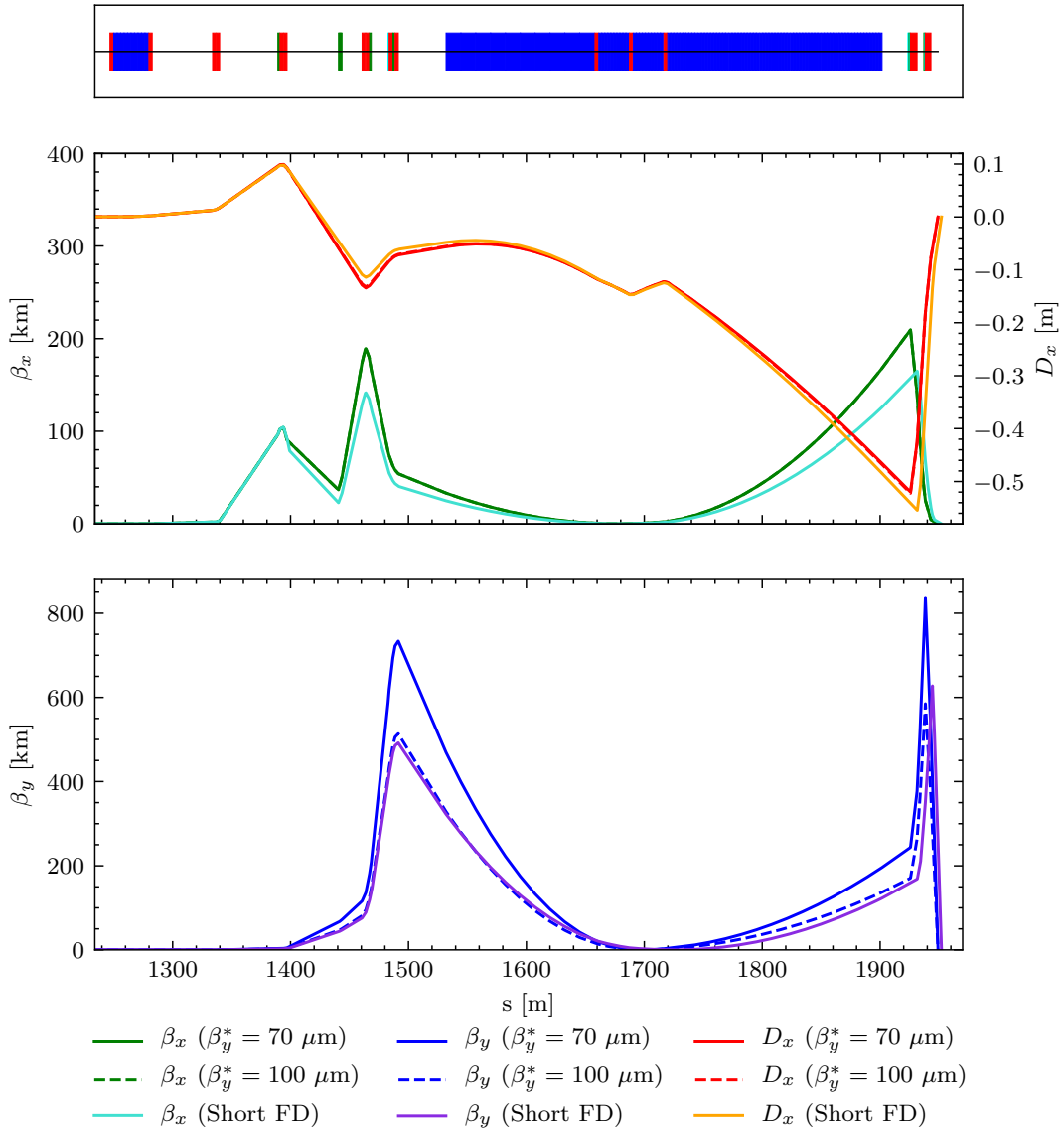

Figure 2.6: Beta-functions and dispersion for the new optics with short FD.

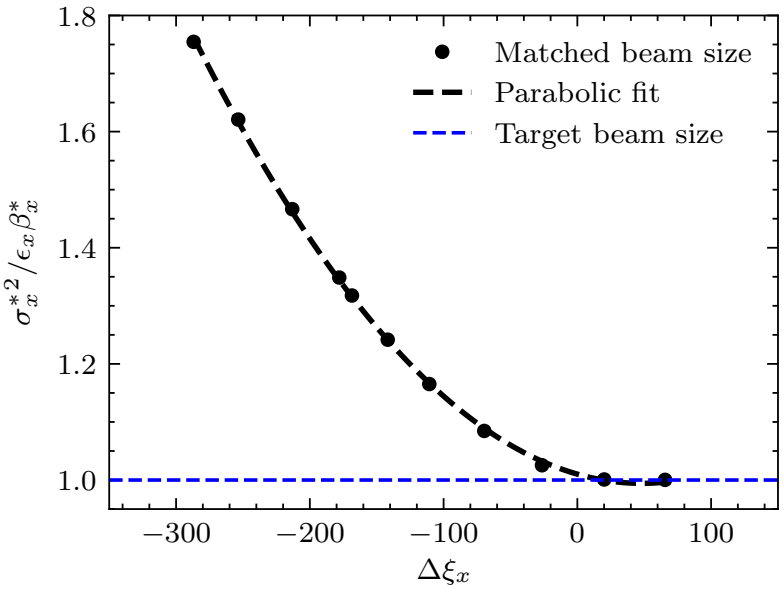

Figure 2.7: 2nd order horizontal beam size normalized to the linear beam size at the IP as the function of the difference between the FD and upstream chromaticity.

Table 2.3: Optimized integrated strength of the sextupoles.

Magnet	SD0	SF1	SD4	SF5	SD5	SF6
Strength k_{2L} [m^{-2}]	1.18	-0.21	0.71	-0.38	2.02	0.41

is achieved by inserting an additional drift of length $\Delta L \approx 4.75$ m between Dip2 and the FD. Finally, to optimize the upstream horizontal chromaticity, we perform the matching of the 5th order horizontal and vertical beam sizes. Table 2.3 gives the optimal magnetic strengths of each sextupole to get the smallest IP beam sizes of $\sigma_x^* = 143.02$ nm and $\sigma_y^* = 2.59$ nm, see Fig. 2.9. To reach this, we did not use octupoles anymore.

Calculation of the total luminosity ($\mathcal{L}_{total}$) and peak luminosity ($\mathcal{L}_{peak}$) is done with the particle tracking codes Placet [67,68] and Guinea-Pig [69,70]. At first, we generate the beam distribution at the BDS entrance. In the transverse plane, the Gausian distribution based on the optical parameters is used. In the longitudinal plane, a flat top profile is used with a 1 % energy spread width. Then, we do the tracking with Placet and we calculate the particle distribution at the IP and the corresponding beam sizes. For comparison, we perform the tracking with and without SR. Finally, the distribution at the IP is used to calculate the luminosity with Guinea-Pig. For this optics, we get a total luminosity of 1.66×10^{34} $cm^{-2}s^{-1}$ and a peak luminosity of 0.96×10^{34} $cm^{-2}s^{-1}$. In the calculations, we assumed head-on collisions, and do not take into account the impact of the detector solenoid field.

The larger the dispersion at the sextupole locations are, the weaker sextupoles are needed to compensate the chromaticity and the lower the aberrations are at the IP. On the

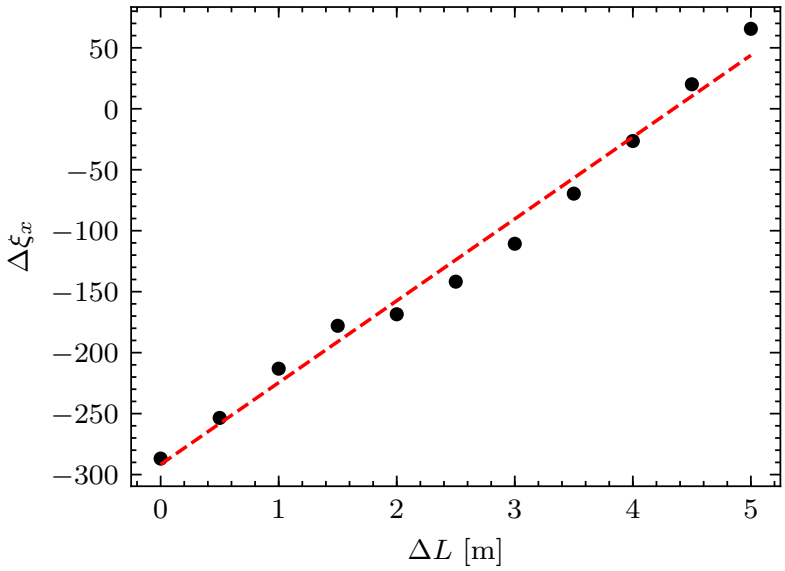

Figure 2.8: Difference between the FD and upstream chromaticity as a function of the distance change (ΔL) between Dip2 and FD.

other hand, a large dispersion level requires stronger dipoles and ultimately leads to energy loss and beam emittance growth due to SR. These two effects have to be balanced in order to reach the highest luminosity. To find the optimum, we could modify the dispersion level in steps by means of scaling the bending angles of the dipoles in the FFS and evaluate the luminosity. In the calculations, the dipole strengths were scanned in the relative range of 0.37 - 1.31 of their original strength with a step of 6.25 %. The dispersion profile for the different scaling factors is shown in Fig. 2.10. For each scale factor, the sextupole settings were adjusted to optimize the beam sizes at the IP with MADX and Mapclass. The impact of the dispersion change on the horizontal and vertical beam sizes evaluated with Placet, with and without SR included, are shown in Fig. 2.11. One can notice, that small dispersion is not enough to provide a proper aberrations correction, while large dispersion results in σ_x^* growth due to the synchrotron aberration. Finally, we calculate the luminosity for each dispersion level. Such a scan is shown in Fig. 2.12. One can see that the dispersion level established in the nominal design is still the optimal choice for the current optics and does not require any changes.

2.4 Nonlinear optimization of FFS with short FD and alternative dispersion profile

It has been found that by inverting the strength of one of the quadrupoles of the FFS, namely QD6B (refer to Fig. 2.1), a new dispersion profile can be established for the FFS, see Fig. 2.13. In this case, the quadrupole inverts the dispersion slope, allowing larger

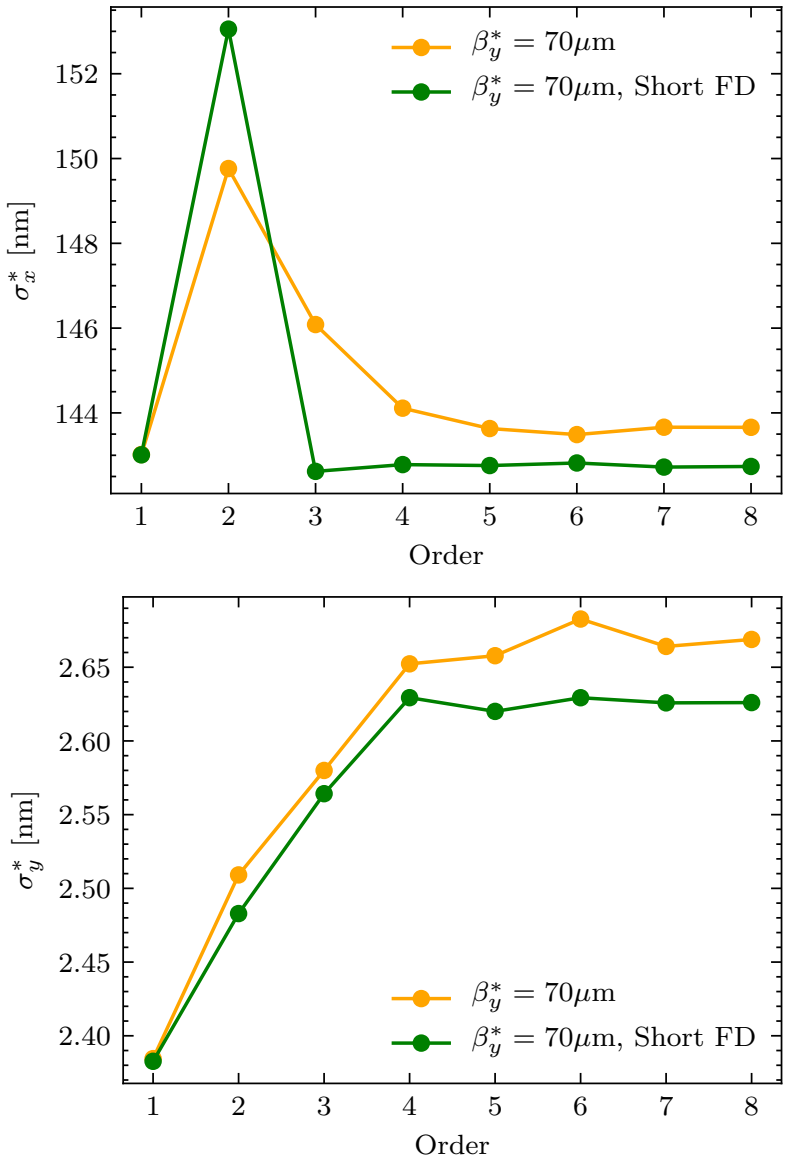

Figure 2.9: Horizontal (top) and vertical (bottom) beam sizes at the IP as a function of the map order.

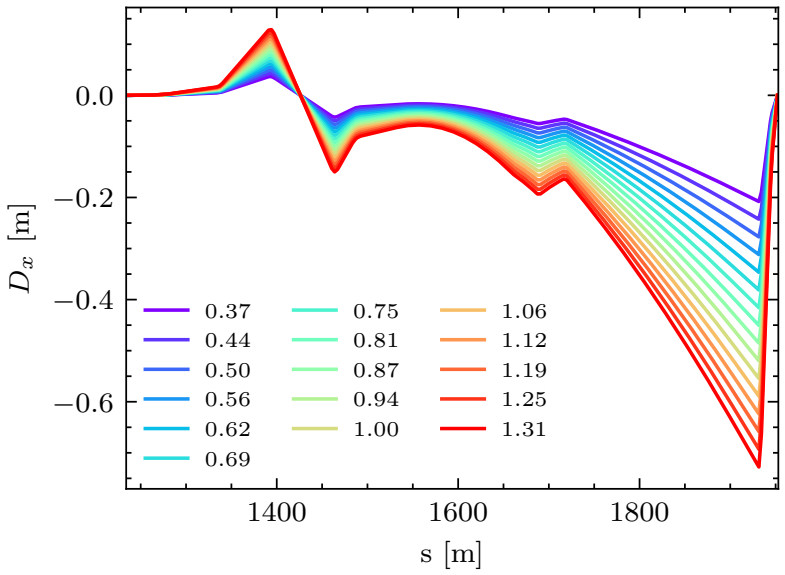

Figure 2.10: Dispersion in the FFS for different scales of the bending angle of the dipoles for the optics with $\beta_y^* = 70$ μm and short FD quadrupoles.

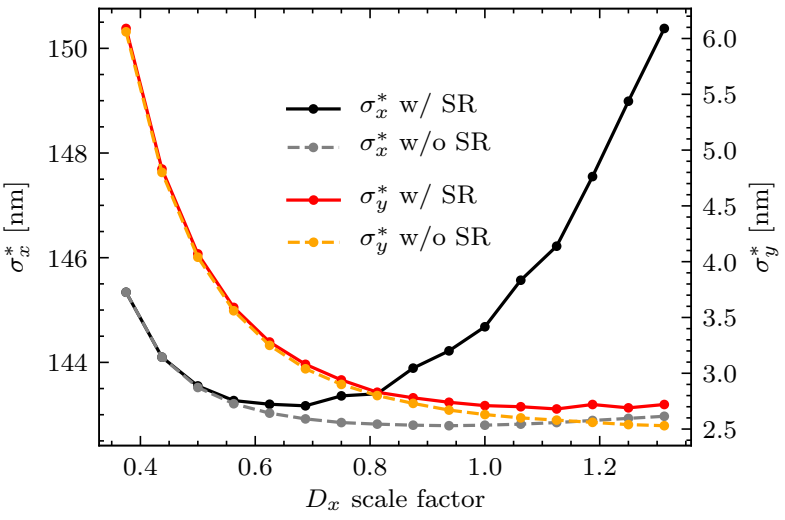

Figure 2.11: Horizontal and vertical beam sizes at the IP, as function of the D_x scale for the optics with $\beta_y^* = 70$ μm and Short FD.

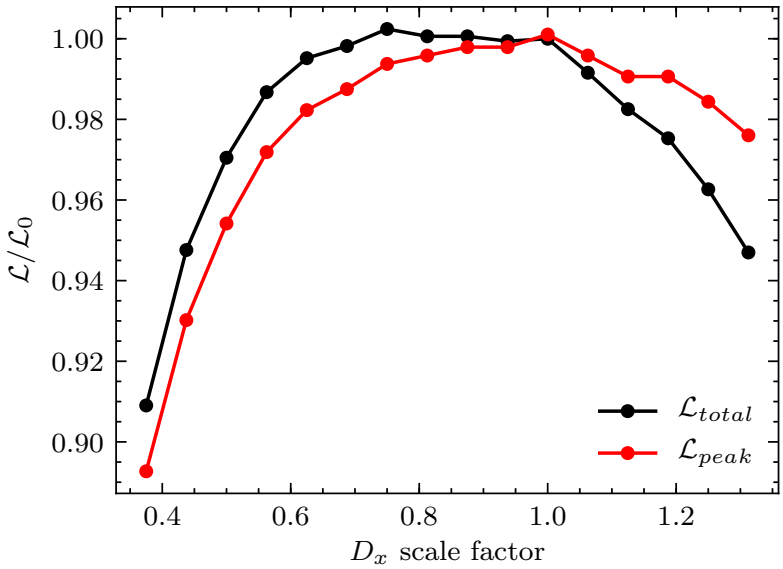

Figure 2.12: Luminosity dependence of the dispersion level along the FFS for the optics with $\beta_y^* = 70$ μm and short FD quadrupoles.

dispersion at the FD for the same dipoles bending angles.

The optics requires the similar upstream chromaticity adjustment as in Sec. 2.3, due to the new dispersion profile. An approach that was used is based on the simultaneous matching of the IP Twiss parameters and the upstream chromaticity to the given value, using the quadrupoles upstream of the FD. After, for each chromaticity value we minimize the 2$^{\text{nd}}$ order beam size with the sextupoles, see Fig. 2.14. By applying the parabolic fit, one can find the minimum, which corresponds to the chromaticity difference of $\Delta\xi_x^* \approx 171$. The sextupole settings are obtained from the numerical optimization with MADX and Mapclass, strengths are varied to minimize the 5$^{\text{th}}$ order beam sizes. Beam sizes obtained after the optimization are $\sigma_x^* = 144.31$ nm and $\sigma_y^* = 3.92$ nm and they are far from the target. The beam sizes as a function of the order of transfer map are given in Fig. 2.17 and is labeled as "Before optimization". The vertical beam size σ_y^* is large, mainly due to the 3$^{\text{rd}}$ order contributions, similarly to the designs with long FD when the octupoles are switched off. The horizontal beam size is dominated by the contributions from high-order terms.

To analyze the obtained IP beam sizes, the transfer map is truncated at 5$^{\text{th}}$ order. The terms inside the sum in Eq. (1.30) are evaluated with Mapclass and sorted in descending order. Figure 2.15 shows the largest contributions to the horizontal and vertical beam sizes. For simplicity the 1$^{\text{st}}$ and 2$^{\text{nd}}$ order map terms are represented in Transport notation [44]:

$$u_{f,i} = \sum_{j=1}^{5} R_{ij} u_{0,j} + \sum_{j=1}^{5} \sum_{k=j}^{5} T_{ijk} u_{0,j} u_{0,k} \ . \tag{2.19}$$

Looking at these results, several outlines can be made for this design:

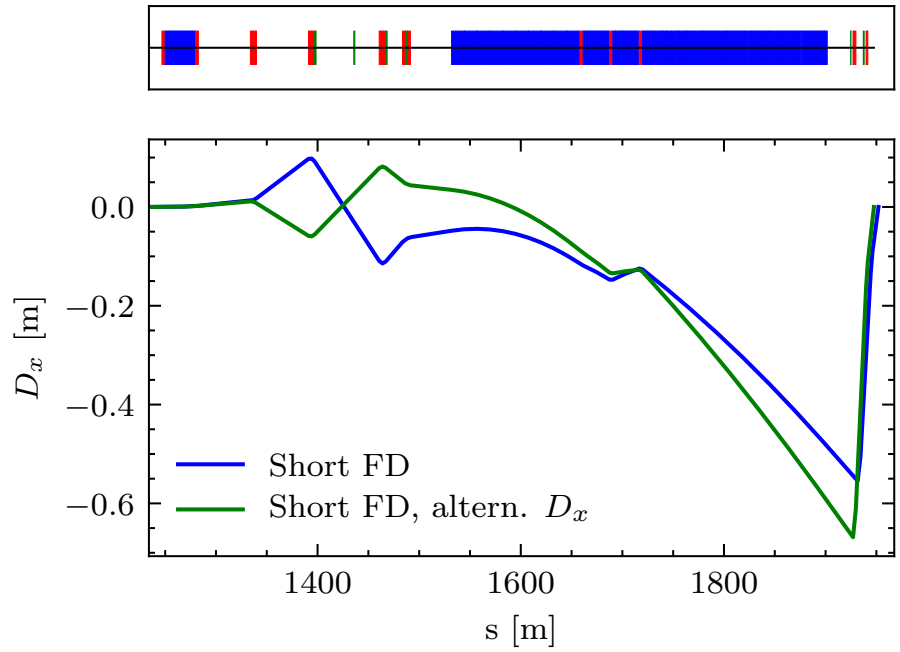

Figure 2.13: Comparison between the original and the alternative dispersion profile in the FFS.

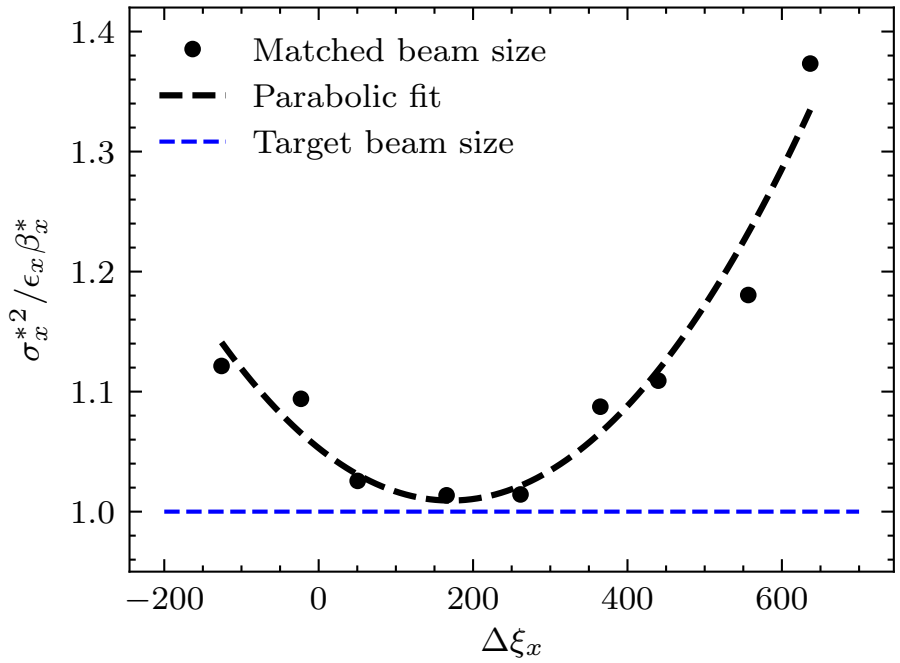

Figure 2.14: The 2nd order horizontal beam size normalized to the linear beam size at the IP as function of the difference between the FD and upstream chromaticities.

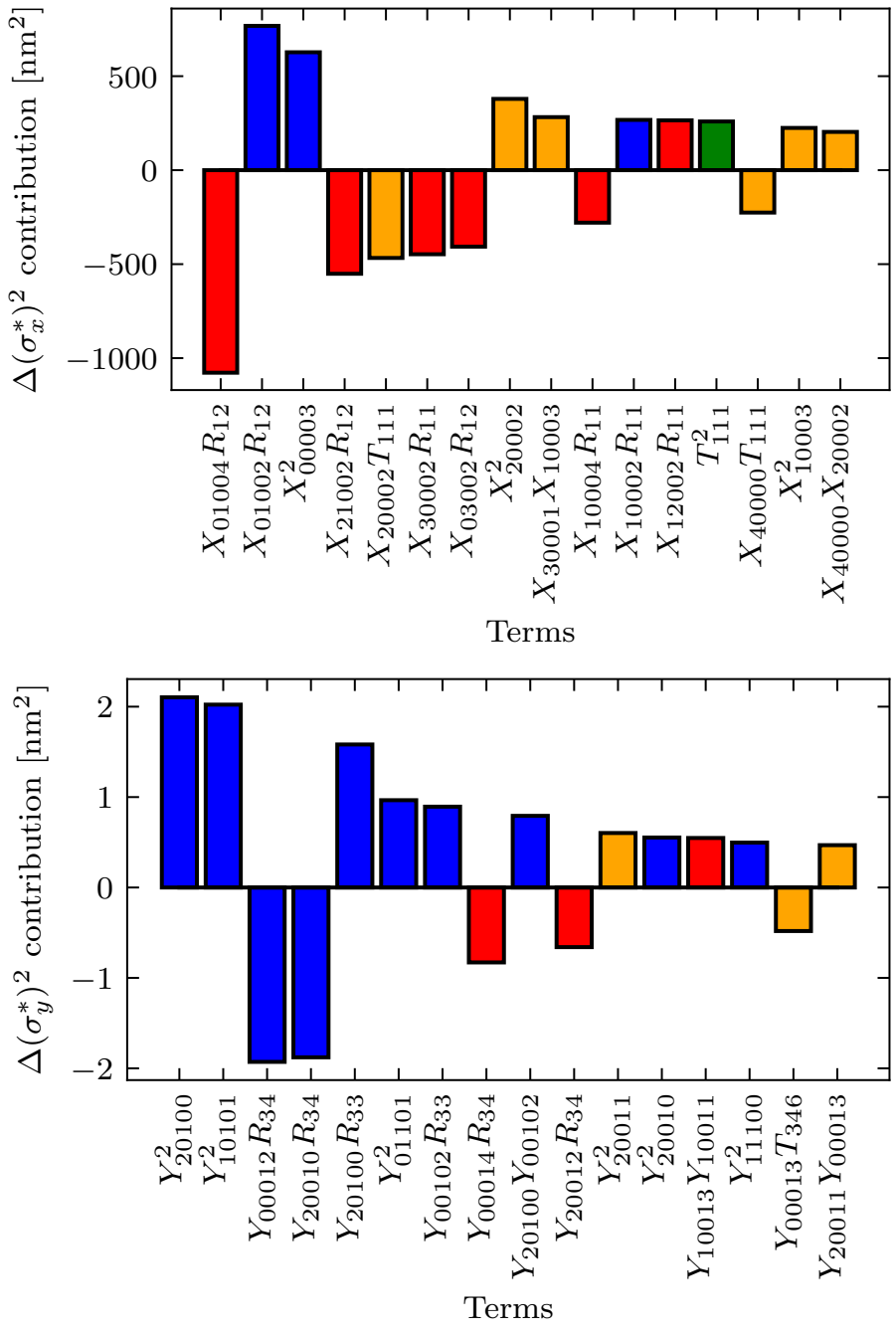

Figure 2.15: The largest contributions to the square of the horizontal (top) and vertical (bottom) beam size, excluding the linear parts. The contributions of 2$^{\text{nd}}$ order are shown in green, 3$^{\text{rd}}$ order in blue, 4$^{\text{th}}$ order in orange, and 5$^{\text{th}}$ order in red.

- The horizontal beam size at 2nd order is well corrected, but with noticeable pure geometrical contribution from T^2_{111}. The 3rd order chromatic terms such $X_{01002}R_{12}$ and X^2_{00003} are dominant and are responsible for the large σ^*_x growth at 3rd order.
- The horizontal beam size is reduced close to the linear value, mainly at 5th order, with the largest reduction coming from $X_{01004}R_{12}$.
- The vertical beam size is almost twice the target value at 5th order. It is dominated by the 3rd order contributions, like the coupling terms Y^2_{20100} and Y^2_{20001}.

One of the main issues limiting the IP beam size is the distribution of sextupoles in the FFS and the transfer matrices between them. In this context, few improvements could be done:

- Scan the location of SD5 to find the best position which gives the smallest beam size at the IP. For each SD5 location, the beam size at the IP is matched with the sextupoles. The results of such a scan are shown in Fig. 2.16, from the figure we could notice that it is possible to reduce the IP vertical beam size down to 2.49 nm when SD5 is shifted by 6 m further from the IP, without the need of the octupoles.
- Add a pair of decapoles to correct the 4th order horizontal and vertical beam sizes growth. Although the 5th order beam size is numerically optimized, the presence of 4th order aberrations would strongly impact the beam size dependence on the energy offset and, consequently - energy bandwidth. It is suggested to put the pair of decapoles in the FD region to correct it, named DEC1 and DEC2, which are located next to the SF1 and SD0 sextupoles respectively.

The comparison of the beam sizes before and after the above optimizations, evaluated with MADX and Mapclass is shown in Fig. 2.17. The beam sizes obtained after these optimisations are 143.82 nm × 2.67 nm, see Tab. 2.4. To optimize the lattice in terms of luminosity at the IP and find the balance between emittance growth due to SR and aberrations control, one needs to find the optimum dispersion scale factor. As it is shown in Tab. 2.4, the IP vertical beam size is around 13 % larger when SR is considered. This fact could limit the total luminosity and reduce the peak luminosity at the IP. Dispersion scale factors within ±50 % from the initial value are also explored, see Fig. 2.18. The highest values of $\mathcal{L}_{total}$ = 1.74×10^{34} cm^{-2}s^{-1} and $\mathcal{L}_{peak}$ = 1.01×10^{34} cm^{-2}s^{-1} are obtained by reducing dispersion by 12.5 %. The final sextupole and decapole settings are given in Tab. 2.5.

2.5 Performance evaluation of the CLIC FFS optics with the new designs

In this section we compare the performance of the PIP optics with β^*_y = 100 μm, the current design with β^*_y = 100 μm and the 2 proposed optics with Short FD, and with

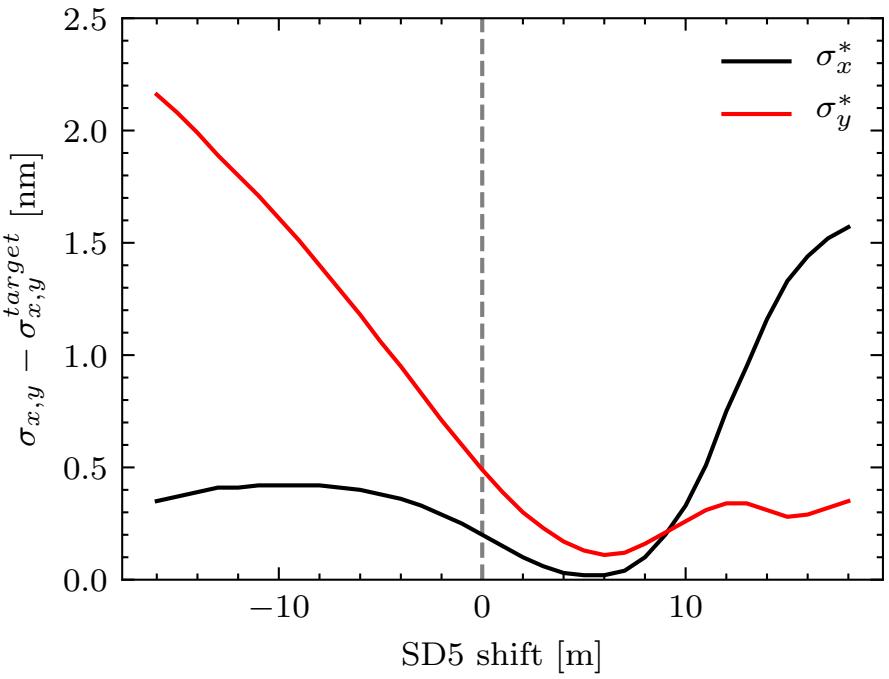

Figure 2.16: 5th order horizontal and vertical beam sizes at the IP as a function of SD5 sextupole location. The target values are $\sigma_x^{target} = 143.00$ nm and $\sigma_y^{target} = 2.38$ nm.

Table 2.4: Beam size and luminosity comparisons before and after dispersion optimization for the optics with the alternative dispersion profile. Calculations with PLACET are performed including SR.

	Mapclass		PLACET + Guinea-Pig			
	σ_x^* [nm]	σ_y^* [nm]	σ_x^* [nm]	σ_y^* [nm]	$\mathcal{L}_{total}$ [10^{34}cm^{-2}s^{-1}]	$\mathcal{L}_{peak}$ [10^{34}cm^{-2}s^{-1}]
Before	142.97	2.52	145.62	2.87	1.73	1.00
After	142.43	2.45	143.82	2.67	1.74	1.01

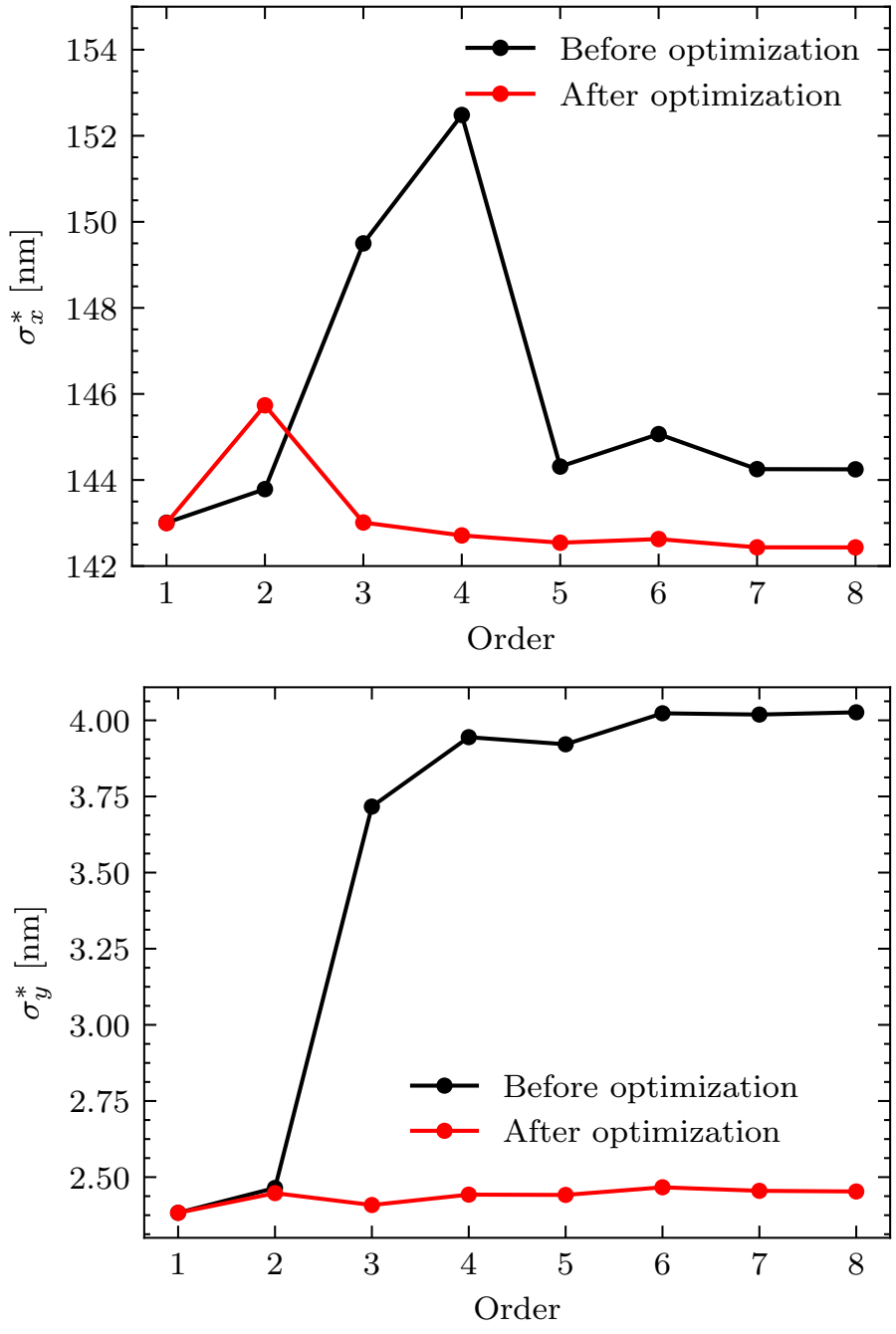

Figure 2.17: Horizontal (top) and vertical (bottom) beam sizes square at the IP before and after the SD5 location scan and with a pair of decapoles.

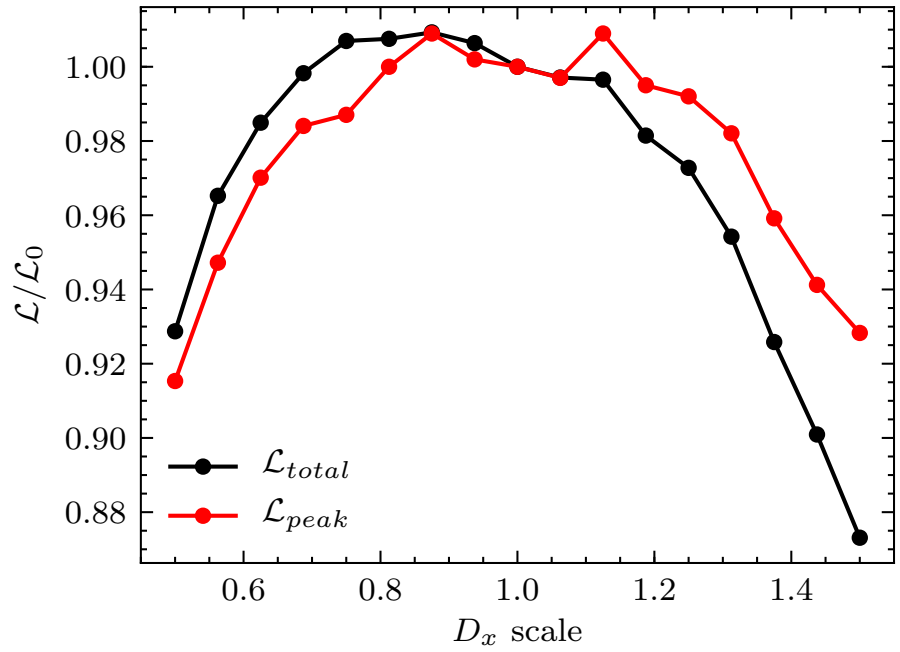

Figure 2.18: Luminosity dependence of the dispersion level along the FFS for the optics with $\beta_y^* = 70$ μm, short FD and the alternative dispersion profile.

Table 2.5: Optimized integrated strength of the sextupoles and decapoles for the optics with the alternative dispersion profile.

Magnet	Strength	
	k_{2L} [m^{-2}]	k_{4L} [m^{-4}]
SD0	1.21	-
SF1	-0.29	-
SD4	0.77	-
SF5	-0.47	-
SD5	4.67	-
SF6	0.50	-
DEC1	-	-370
DEC2	-	9120

Table 2.6: Beam sizes calculated with PLACET including SR and with Mapclass including transfer map terms up to the 8$^{\text{th}}$ order and Luminosities calculated with Guinea-Pig.

	MAPCLASS		PLACET + Guinea-Pig				
	σ_x^*	σ_y^*	σ_x^*	σ_y^*	bandwidth	$\mathcal{L}_{total}$	$\mathcal{L}_{peak}$
Optics	[nm]		[nm]		[%]	[10^{34}cm^{-2}s^{-1}]	
$\beta_y^* = 100$ μm	141.90	3.14	144.22	3.14	0.52	1.63	0.93
$\beta_y^* = 70$ μm	143.48	2.72	145.78	2.74	0.35	1.66	0.96
$\beta_y^* = 70$ μm, Short FD	142.74	2.63	144.72	2.71	0.42	1.66	0.96
$\beta_y^* = 70$ μm, Short FD + altern. D_x	142.43	2.45	143.82	2.67	0.30	1.74	1.01

Short FD and alternative dispersion profile. We evaluate them in terms of beam sizes, luminosity, and energy bandwidth. Lastly, we confirm the compliance of the collimation depth with the new optics designs.

2.5.1 Beam sizes and luminosity

The beam sizes are calculated with MadX-PTC and Mapclass, including the map terms up to the 8$^{\text{th}}$ order and with PLACET tracking. Luminosity is calculated with Guinea-Pig. The results are given in Tab. 2.6.

The horizontal beam size is well matched to the linear value of 143 nm for each optics. The vertical beam size of the optics with $\beta_y^* = 100$ μm is at 15 % larger than the largest beam size of the optics with $\beta_y^* = 70$ μm. Among the different designs, the optics with short FD and with new dispersion profile provides the best aberration control, providing almost linear value of σ_y^*, see Fig. 2.19. As a result, the optics with short FD and with new dispersion profile provides also the largest luminosity giving the boost of 7% compared to the previous optics with $\beta_y^* = 100$ μm and 5% if compared with the $\beta_y^* = 70$ μm optics.

2.5.2 Energy bandwidth

The term energy bandwidth is used to describe the beam size or the luminosity dependence with the energy offset. Here the definition from [71] is used.

It is defined as the width of the region where the beam size does not grow more than 10 %, compared to the on-momentum beam size. For the simulation, a particle tracking with PLACET is used for the beam with an energy offset in the range of ±1%. It is worth mentioning that no energy collimation is applied so that the particle can have an energy offset larger than 1.3 %. Overall it increases the beam size and total luminosity but does not affect the peak luminosity. Fig. 2.20 shows the calculation results for the different optics. The estimated bandwidth it is given in Tab. 2.6.

One can see that the vertical beam size rapid growth for the off-momentum beam is responsible for the small energy bandwidth. Although it is possible to control the linear

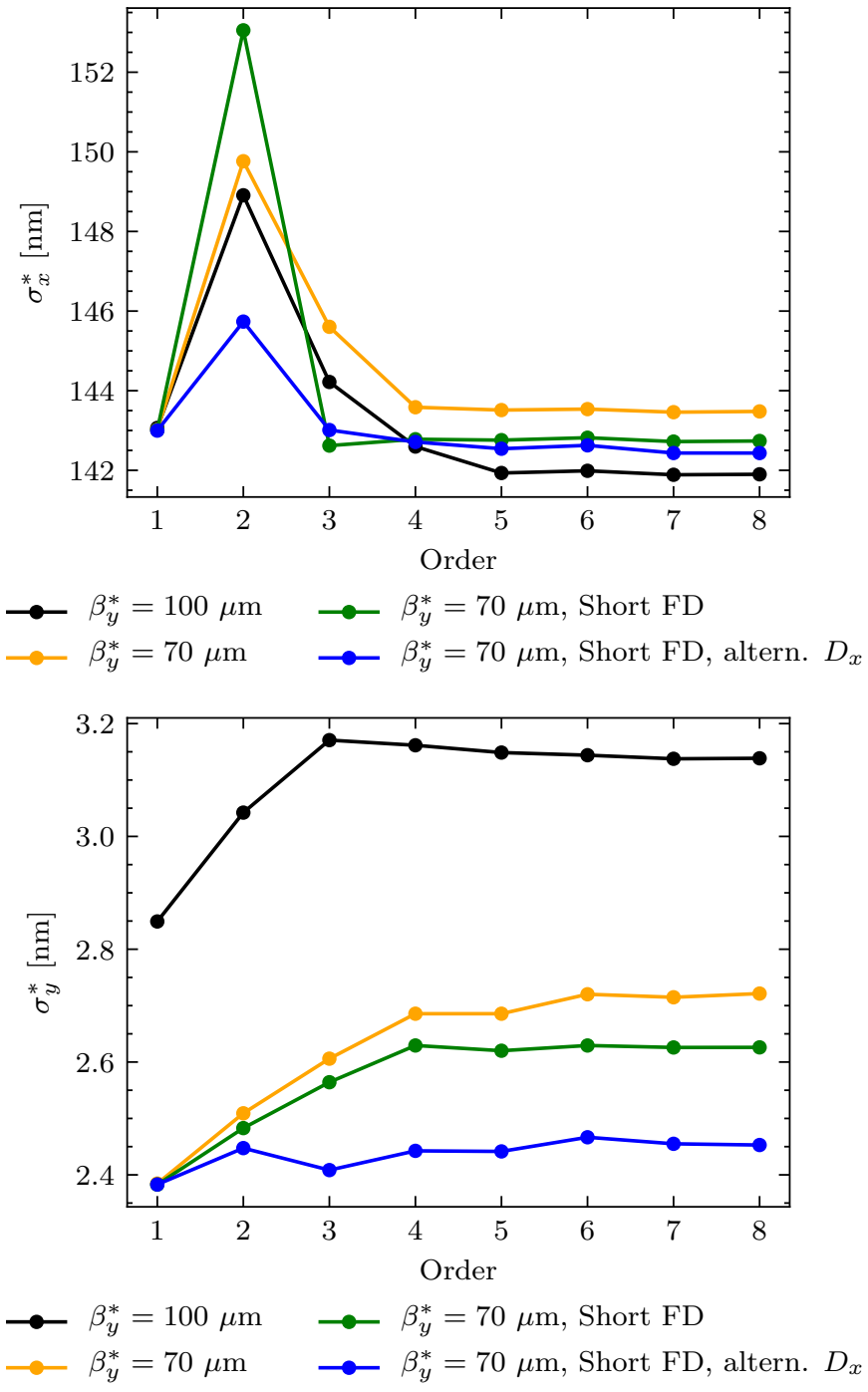

Figure 2.19: Horizontal (top) and vertical (bottom) beam size as the function of the order of the map considered.

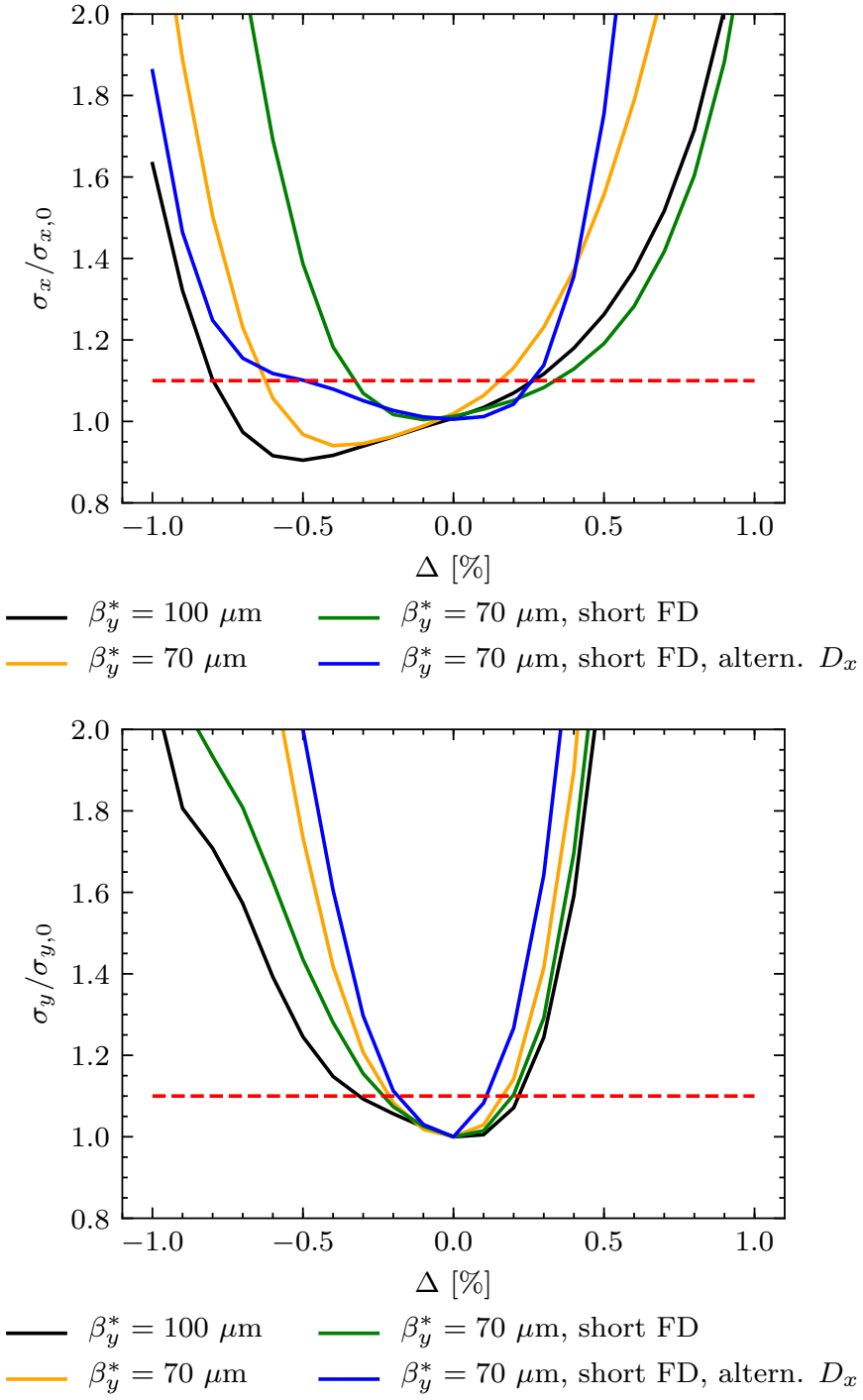

Figure 2.20: Normalized horizontal (top) and vertical (bottom) beam size evaluated with PLACET including SR as the function of the energy offset. The red dashed line correspond to 10 % beam size increase.

optics very well by adding higher-order magnets, such as octupoles and decapoles, 2nd order beam size remains large. This is mainly due to the large vertical chromaticity, which blow up the vertical beam size once the chromaticity correction fails to work.

To analyze how the luminosity changes with the energy offset, the beam distributions obtained earlier are given to Guinea-Pig. The results are shown in Fig. 2.21. One can see that the original optics with $\beta_y^* = 100$ μm has the largest bandwidth for $\mathcal{L}_{total}$ mainly because of the horizontal beam size reduction for negative δp. Peak luminosity bandwidth is similar, except for the optics with different D_x profile, which is about 25 % smaller.

2.5.3 Collimation depth

The CLIC collimation section at 380 GeV was scaled down from 3 TeV and preserves the same collimation depth. The collimation section consists of an energy and a betatron collimation section respectively. The energy collimation removes the particles from the beam with an energy offset larger than 1.3 % [72]. The betatron section aims to clean the beam halo, such that neither particles nor emitted photons hit QF1, QD0, or the inner part of the detector. Simulation studies in [73], established the optimal collimation depth of $15\sigma_x$ and $55\sigma_y$ for 3 TeV stage. In the 380 GeV lattice, the nominal aperture is larger than the 3 TeV one and it is comparable with the CLICdet [22] inner dimension.

The vertex detector is located in close proximity to the interaction region and has an inner radius of 31 mm, with the beam pipe of 29.4 mm inner radius. To simulate the beam halo, a monochromatic beam with large emittance is generated at the FFS entrance and tracked with PLACET thorough the FFS. Collimation cuts are applied at the FD entrance, limiting the occupied phase space to:

$$|x| < 15\sigma_x, \ |x'| < 15\sigma_{x'} \ , \tag{2.20}$$

$$|y| < 55\sigma_y, \ |y'| < 55\sigma_{y'} \ . \tag{2.21}$$

The beam distribution at the FD entrance is given in Fig. 2.22. Particles passing through QF1 and QD0 emit photons due to the SR. The photon emission cone's opening angle is $1/\gamma \approx 2.6$ μrad and it is small compared to the particle angles x' and y'. In this case, the photons are assumed to travel along the emission direction, calculated for each particle at the entrance, center, and exit of QF1 and QD0 using the PLACET tracking. In Fig. 2.23, the photons flux is shown, including the reference apertures of the detector. One can see that photons do not hit it. QD0's aperture is adjusted based on the cone radii at their location to avoid the photons hitting the FD. For QF1, it is the nominal aperture, based on the collimation depth and for QD0, it is around 27.0 mm from simulations (see Tab. 2.7).

The photon flux emitted in QF1 and QD0 has an elliptic shape in the transverse plane with radii of around 27 mm $\times$ 18 mm at the IP location. It satisfies the requirements, as the photons do not hit the detector nor the FD.

Based on the estimated aperture for the FD and including the studies of the resistive wall effects in [74], the apertures for BDS of CLIC 380 GeV are shown in Fig. 2.24. The nominal apertures, which are calculated based on the collimation depth, are increased

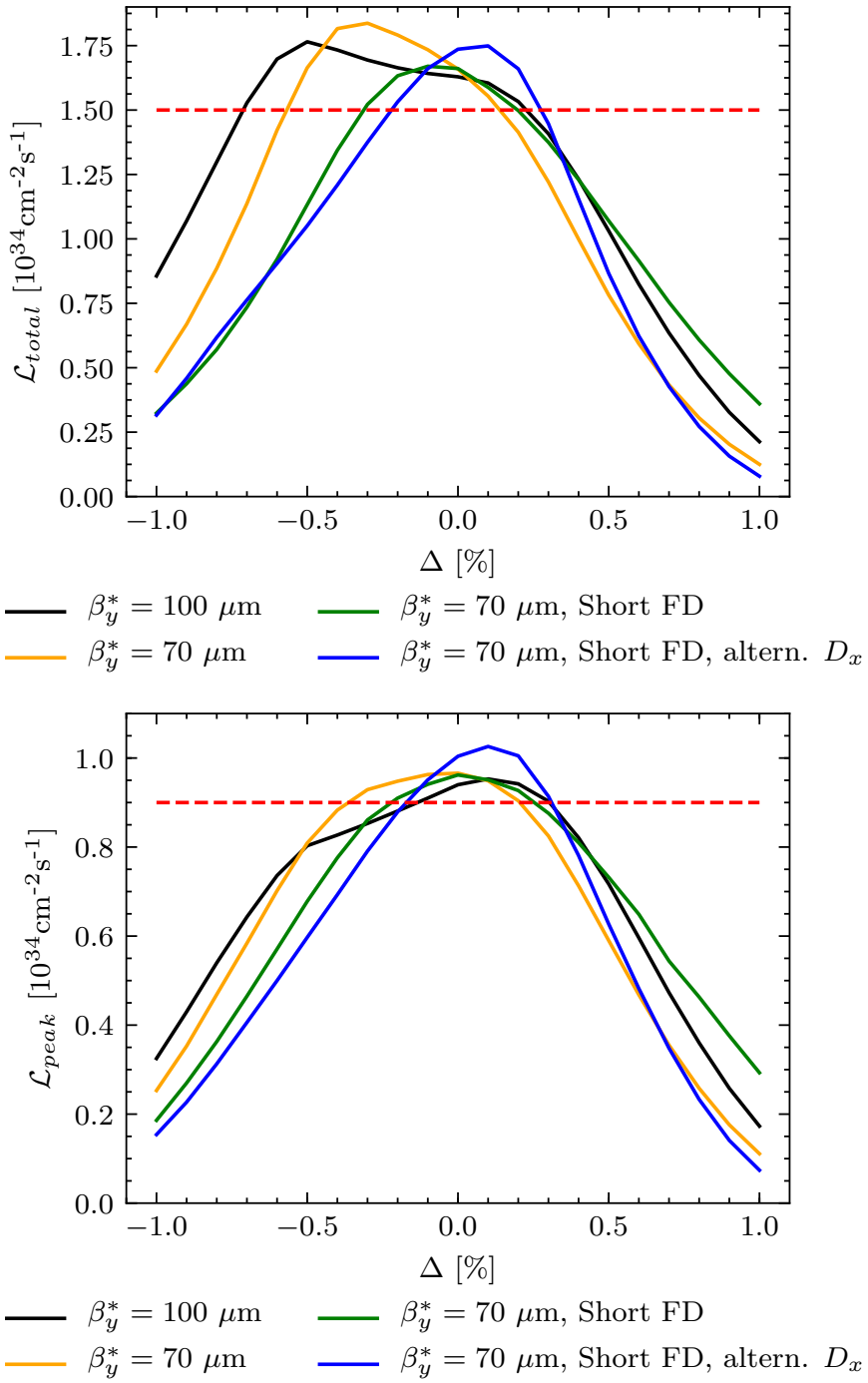

Figure 2.21: Total (top) and peak (bottom) luminosity change with the energy offset normalized to the corresponding values of on-momentum beam. Red dashed line corresponds to the nominal values from Tab. 2.1

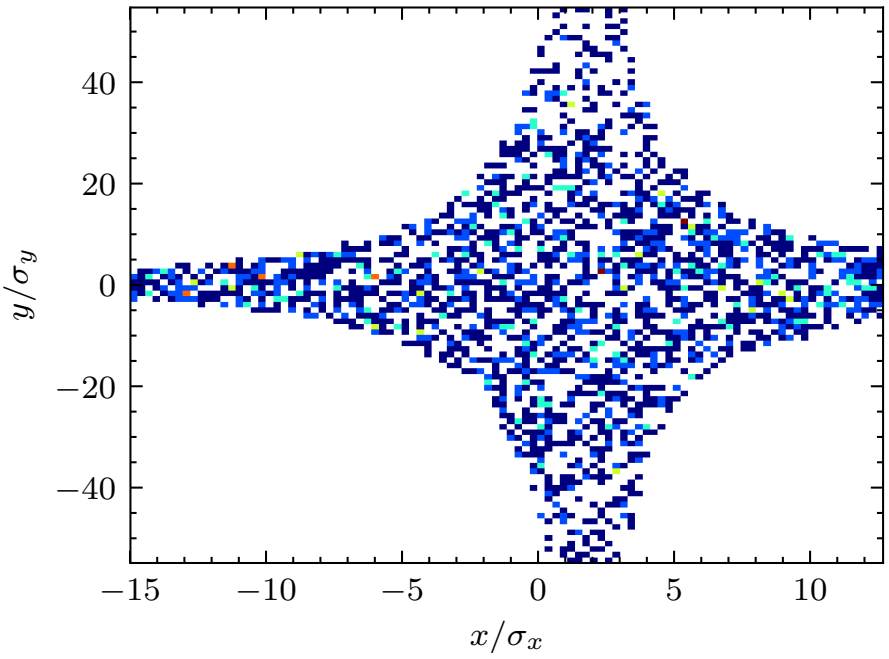

Figure 2.22: Cross section of the collimated beam halo at the FD entrance.

Table 2.7: Gradients and apertures of the FD.

	QF1	QD0
Gradient [T/m]	16.3	73.7
Aperture [mm]	31.2	27.0
Pole tip field [T]	0.51	1.99

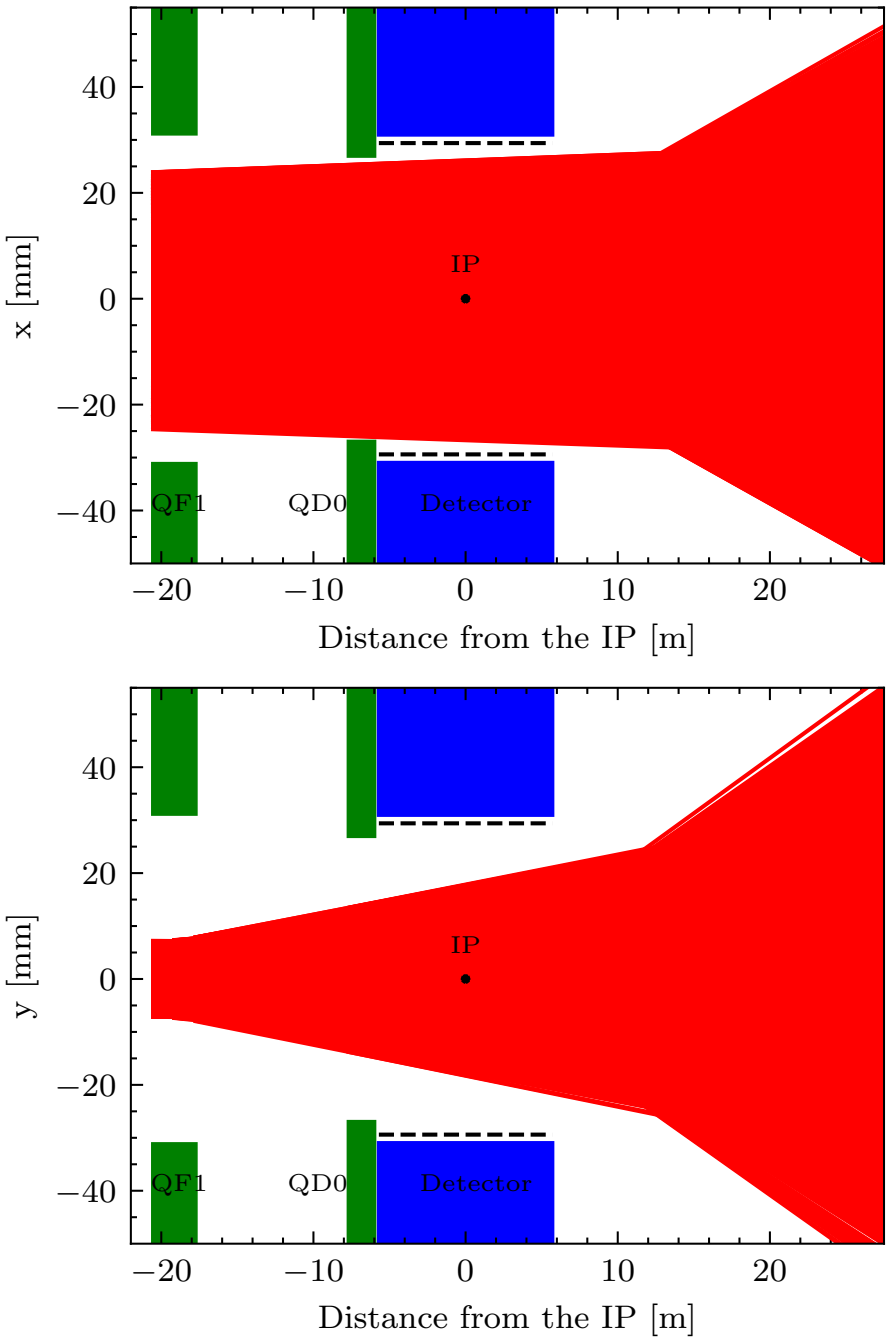

Figure 2.23: Horizontal (top) and vertical (bottom) position of the emitted photons extrapolated to the entrance of the first dipole magnet in the post-collision line. In dashed is the beam pipe smallest radius around the IP.

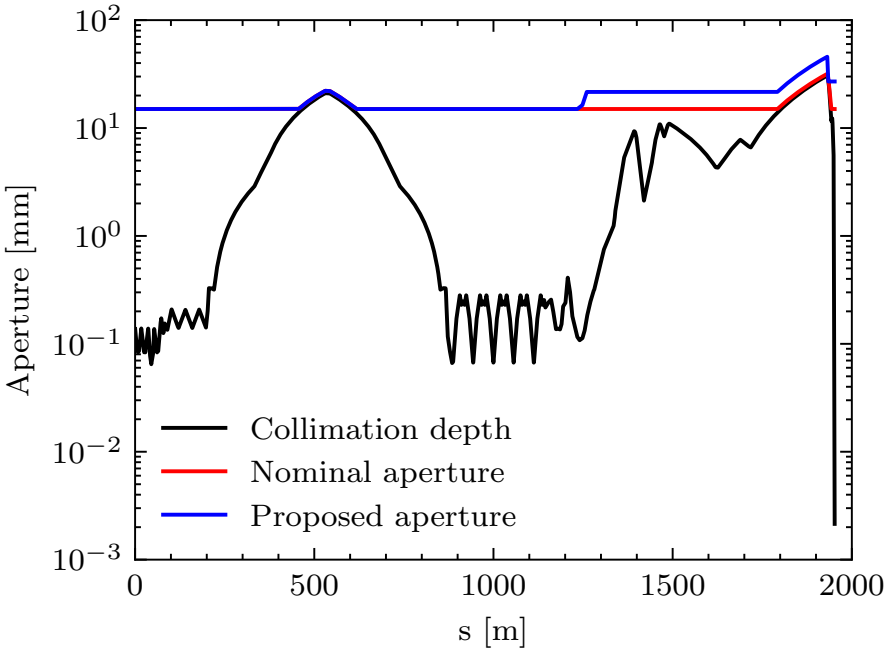

Figure 2.24: Beam pipe apertures (radius) distribution along the BDS.

everywhere outside the FD by 44 %, and the FD aperture is set to 27 mm from the photon flux radii.

2.6 Summary

Two new optics for the FFS of CLIC 380 GeV have been designed and fully optimized. Both of them have a vertical IP beta function of 70 μm and shorter FD quadrupoles by about a factor 2. The first optics is conceptually similar to the previous design. It provides the same luminosity as the optics with longer FD but has 30 % larger energy bandwidth and does not require octupoles. The second optics proposes the use of a different dispersion profile within the FFS. This optics features higher total and peak luminosities, which are around 5% larger than the other optics with $\beta_y^* = 70$ μm, but has a smaller energy bandwidth and also requires a pair of decapoles. Considering the large luminosity gain for the same vertical beta-functions, the optics with an alternative dispersion profile is preferred option for the Final Focus of CLIC at 380 GeV.

The collimation depth has been verified to protect the FD and the detector from the photon flux.

Chapter 3

FFS tunability studies and implementation at ATF2

As described in Section 1.4.4, the local chromaticity correction scheme has been demonstrated in ATF2 accelerator complex. The optical design of the ATF2 beamline is a scaled-down version of the FFS of ILC [12]. To study the potential beam tuning related issues on ILC, the optics used at ATF2 targets the same chromaticity level as ILC. One of the crucial aspects to successfully reach the target beam size of 37 nm is to have an effective tuning strategy to deal with the different types of imperfections in the ATF2 beamline. In the particular case of CLIC, the chromaticity is 5 times larger than in the "nominal" design of ATF2, hence to study the CLIC's tunability, an optics with 4 times smaller β_y^* called "ultra-low" β^* optics with a target vertical beam size of 23 nm [34, 35]. This optics is more sensitive to the beamline imperfections and therefore possesses more tuning difficulties. In this Chapter we describe first in detail the ATF2 accelerator complex optics and hardware relevant for the ultra-low β^* studies in Section 3.1. Section 3.2 is dedicated to the new tuning knobs and strategy for ultra-low β^* optics. Then, in Section 3 we report the simulations studies of the tuning strategy for the ultra-low β^* optics with and without octupoles. Finally, in Section 3.5 the overview of the ATF2 the results of the Ultra-low β^* tuning campaigns between June 2019 and March 2020 is described in detail.

3.1 ATF2 ultra-low β^* optics and related hardware

An ultra-low β_y^* optics had been proposed in 2010 [34]. It features a 4 times smaller vertical beta-function at the IP and consequently 4 times higher chromaticity. The optics is referred as $\beta_x^* \times 0.25\beta_y^*$, and in terms of vertical chromaticity, it approaches the CLIC 3 TeV optics. The Twiss parameters for such an optics with comparison with the nominal optics are shown in Fig. 3.2.

Similarly to the nominal optics $10\beta_x^* \times \beta_y^*$, the impact of the multipolar errors is reduced by running the ultra-low β_y optics with 25 times larger horizontal beta-function, $25\beta_x^* \times 0.25\beta_y^*$ [33]. The reduction of the IP beta-function always leads to a linear beta-

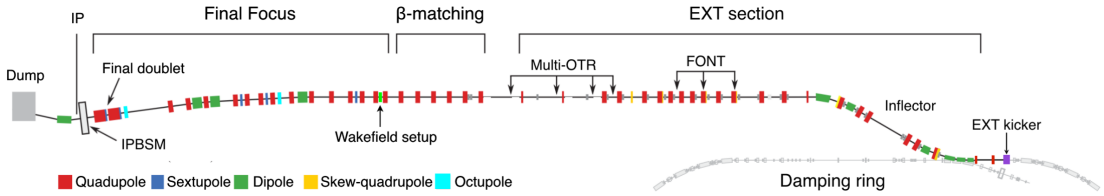

Figure 3.1: Schematic layout of the ATF2 beamline from [33].

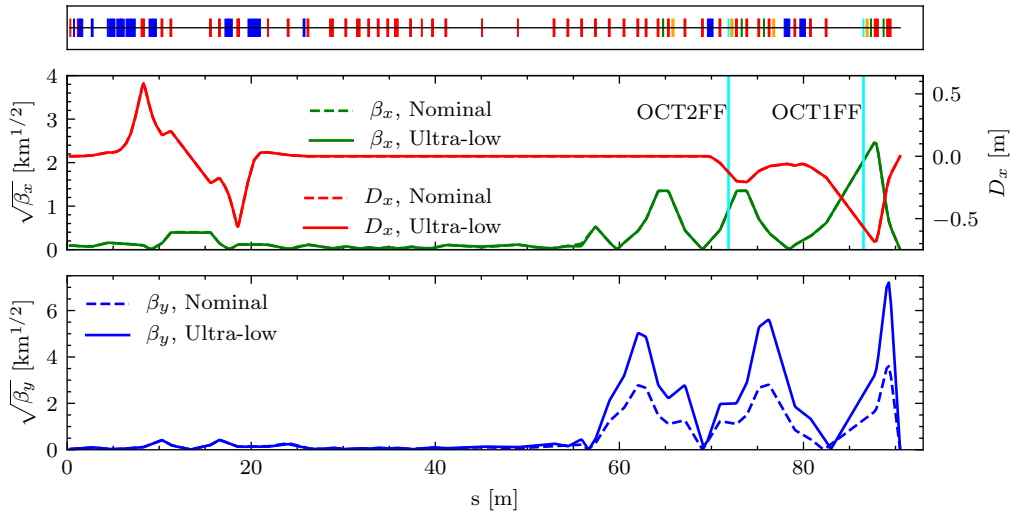

Figure 3.2: Horizontal and vertical beta-functions and horizontal dispersion in the ATF2 beamline for the ultra-low $1\beta_x^*\times0.25\beta_y^*$ optics and nominal $\beta_x^*\times0.25\beta_y^*$ optics. The dipoles are shown in blue, quadrupoles in red, sextupoles in orange, and octupoles in cyan. Vertical cyan lines indicate the octupoles locations.

function growth in the FD. In the case of the ultra-low β_y optics, furthemore it gives a significant increase of the 3$^{\text{rd}}$ order chromatic aberrations [20] The dominant sources of these aberrations are the multipole components of the QD0FF (the last quadrupole before the virtual IP) [75], and the fringe fields in the FD [76]. To cancel them, a pair of octupoles had been installed in 2016, according to the specifications in [77] (see Fig. 3.3). The minimum beam size achievable with the ultra-low β_y including the octupoles is around 20 nm. The key parameters of these octupoles are given in Tab. 3.1. Both magnets are air-cooled and are mounted in micrometric tables with a dynamic range of ± 1 mm. They are located in the beamline with a $-\mathcal{I}$ transformation between them, with OCT1FF located in a high horizontal dispersion region, and OCT2FF located in a low horizontal dispersion region, see Fig. 3.2. One can notice, that OCT1FF is designed stronger than OCT2FF. At the same time, in the optics designs we need OCT2FF to be stronger for the proper aberrations cancellation (see Tab. 3.1). It is valid for both ultra-low β_y^* optics and is very important for $25\beta_x^* \times 0.25\beta_y^*$. In Fig. 3.4 one can observe the σ_y^* reduction due to the octupoles.

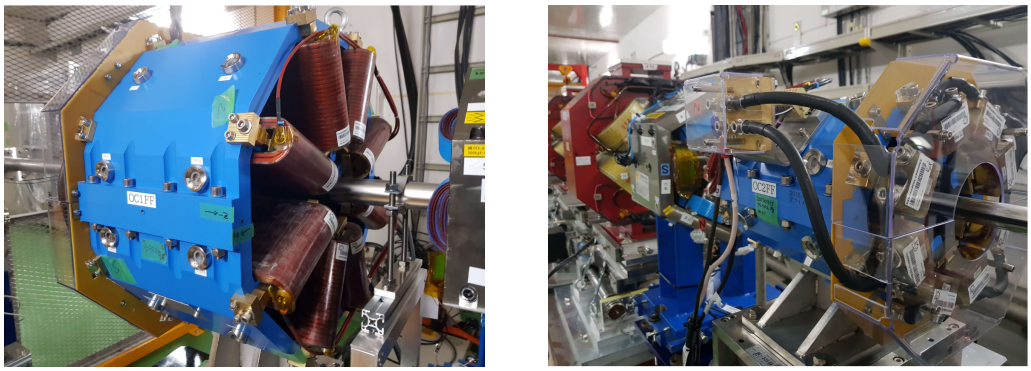

(a) (b)

Figure 3.3: Octupoles installed in the ATF2 beamline: OCT1FF (a) and OCT2FF (b) from [20].

So, in order to be able to see the impact of the octupoles with $25\beta_x^* \times 0.25\beta_y^*$ optics, the octupoles' positions were swapped in 2019.

Table 3.1: Octupole main parameters.

	OCT1FF	OCT2FF
Max. integr. gradient [T/m^2]	7663	390
Max. integr. strength [m^{-3}]	730	90
Max. current [A]	50	50
Magnetic length [mm]	300	300
Designed integrated strength [m^{-3}]		
$\beta_x \times 0.25\beta_y$	-19.24	102.61
$25\beta_x \times 0.25\beta_y$	-35.51	730.0

3.1.1 IP Beam size measurement (IPBSM)

One of the main goals of ATF2 is to shrink the electron beam to the nanometer level in the vertical plane at the Virtual IP. The target beam size for the nominal optics is 37 nm, while for ultra-low β_y^* it is approximately 20 nm. To accomplish that, one needs the proper instrumentation to measure such an extremely tiny beam size. For this, ATF2 adopted an upgraded version of a Shintake monitor [78, 79], previously used at FFTB [80, 81]. It allows measuring the beam sizes in the range from 6 μm down to 25 nm and it is crucial for the beam size tuning operations.

The key property used in the design of the Shintake monitor is the interaction between the electron and the laser beams, called Compton scattering. The laser beam of wavelength $\lambda = 532$ nm is generated and splitted into so-called lower and upper paths, as shown in Fig. 3.5. Both paths are designed in a way that the laser beams are focused at the

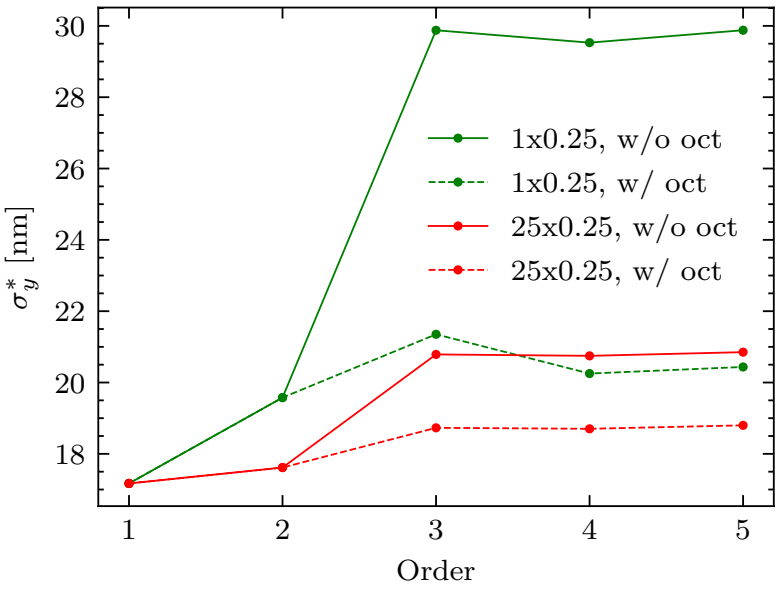

Figure 3.4: Vertical beam size at the virtual IP as the function of the map order for $\beta_x^* \times 0.25\beta_y^*$ (green) and $25\beta_x^* \times 0.25\beta_y^*$ (red) ultra-low optics. The vertical beam size without octupoles is shown in solid.

virtual IP and cross the path of the incoming electron beam perpendicularly. As a result, in the intersection region, two laser beams generate the interference pattern. Also, the upper path has an embedded optical delay line, which allows changing the phase of the incoming laser. By making so, we can adjust whether it is a maximum or a minimum of the interference pattern at the Virtual IP. When the electron beam crosses the interaction region, it Compton scatters the photons towards the Gamma Detector located downstream. The number of scattered photons depends on the distribution of the particles in the electron beam and also on the configuration of the fringe pattern. After the interaction, the electron beam is safely sent into a beam dump with a dipole magnet (BDUMP), such that the electron beam does not interfere with the gamma detector. When we continuously scan the fringe pattern by varying the phase of one of the laser beams, we might observe the signal correlation at the Gamma Detector, see Fig. 3.5. It requires the transverse dimensions of the electron beam to be smaller than the dimension of the fringe pattern. In this case, the maximum signal corresponds to the maximum of the interference pattern, and the minimum corresponds to the minimum of the interference pattern. If the vertical dimension of the electron beam is comparable or larger than the dimension of the fringe pattern, the correlation will be small or even negligible. We define N_{max} and N_{min} as the maximum and minimum signals at the Gamma Detector and introduce the modulation depth M:

$$M = \frac{N_{max} - N_{min}}{N_{max} + N_{min}} \ . \tag{3.1}$$

For Gaussian beams, the modulation depth writes as a function of the vertical beam size

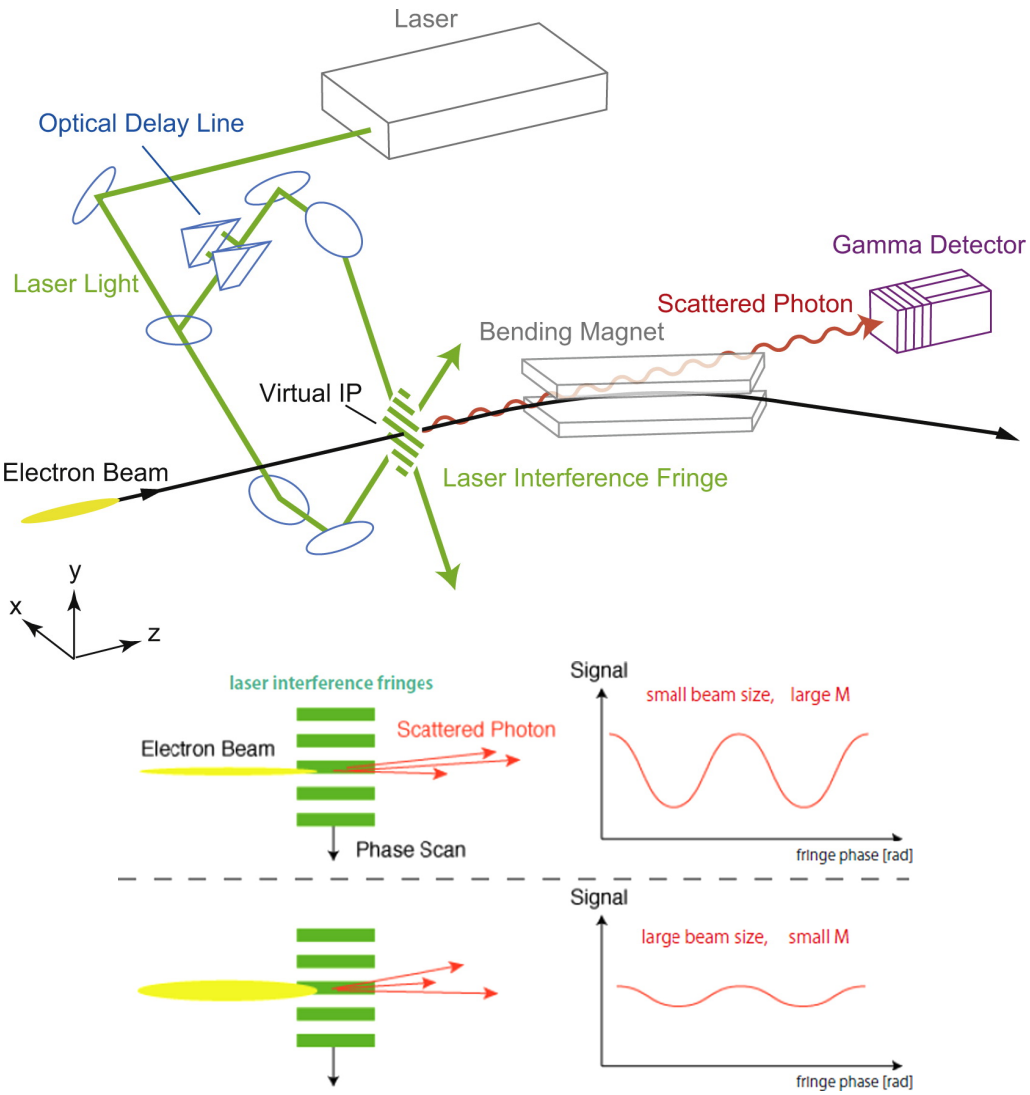

Figure 3.5: Schematic layout of Shintake Monitor (top) and principle of work (bottom). Figure taken from [78].

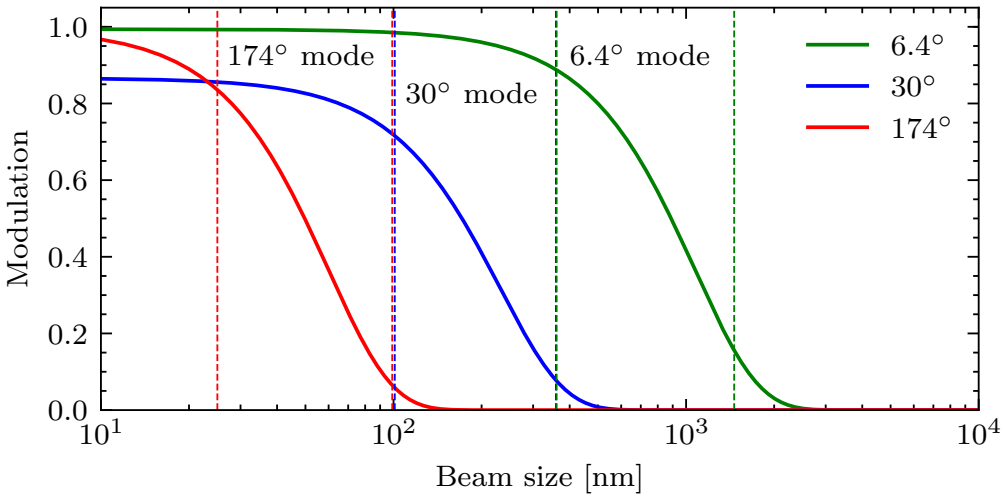

Figure 3.6: Modulation at IPBSM evaluated for different laser crossing angles. In dashed, the beam size range of the corresponding working mode is indicated.

at the IP (σ_y^*) as:

$$M = C|\cos\theta| \exp^{-2k_y^2\sigma_y^{*2}}] \ , \ k_y = \frac{\pi}{d} \ , \tag{3.2}$$

where d is the fringe pitch and it depends on the wavelength (λ) and the angle between the two laser paths (θ): $d = \frac{\lambda}{2\sin\theta/2}$ and C is the modulation reduction factor, which includes various types of the systematic errors taking place throughout the measurements [33, 82]. The beam size at the IP is given by:

$$\sigma_y^* = \frac{d}{2\pi}\sqrt{2\ln\left(\frac{C|\cos\theta|}{M}\right)} \ . \tag{3.3}$$

There are three crossing angles available for the measurements, 2°-8° (usually we utilize 6.4° angle), 30°, and 174°, see Tab. 3.2. Depending on the laser crossing angles, there are 3 working modes of the Shintake monitor, adapted for different beam size ranges, see Fig. 3.6. To detect the Compton scattered photons either CsI scintillating detector or

Table 3.2: Different laser crossing modes of Shintake monitor.

Crossing angle θ	2°	6.4°	8°	30°	174°
Fringe pitch d [μm]	15.2	4.77	3.81	1.03	0.27
σ_y^* [nm], Upper limit	6000	1600	1400	360	100
σ_y^* [nm], Lower limit	1200	360	350	100	20

Cherenkov radiation detector is utilized. In Fig. 3.7, a typical modulation scan is shown, performed in March 2019 ultra-low β_y^* tuning operation.

The larger beam sizes can also be measured with a wire scanner installed at the IP [83]. The wire scanner consists of a carbon wire with 5 μm diameter. The configuration of

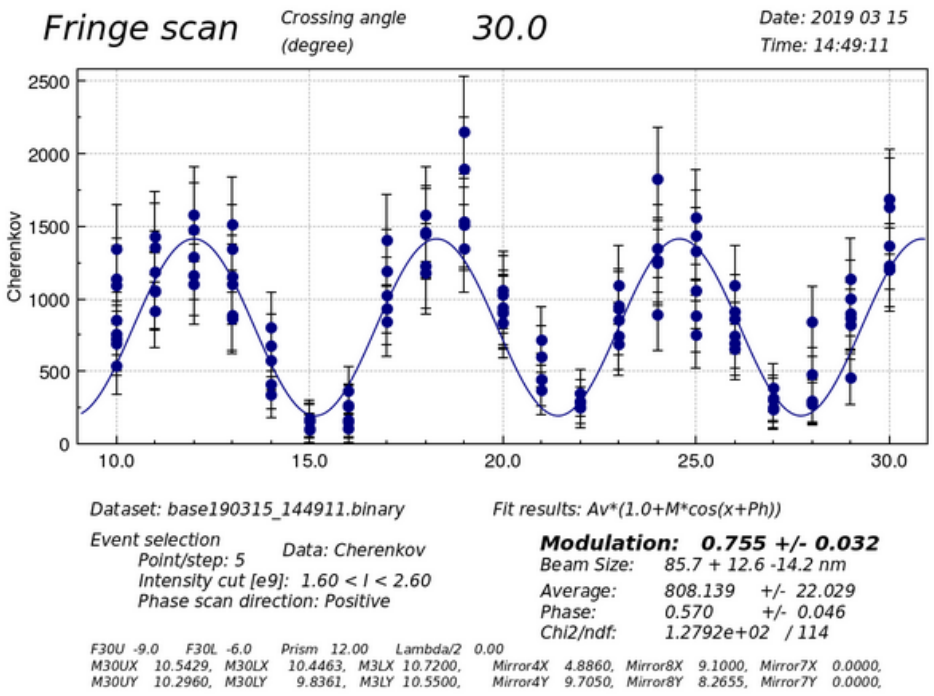

Figure 3.7: Measurement of the vertical IP beam size performed with Shintake monitor in 30° mode in March 2019 ultra-low β_y^* tuning operation. Estimated modulation is 0.76.

the wire scanner allows measuring the beam sizes in both horizontal and vertical planes. When the beam interacts with the wire, it generates bremsstrahlung photons, which are then collected downstream in the plastic scintillating detector (referred to as Background detector). The detector is located at the same location as the Gamma detector of the Shintake monitor.

3.1.2 Measurement of the optics functions at the IP

The measurements of the beta-functions at the IP $\beta^*_{x,y}$ are crucial to verify the proper implementation of the optics. For this, at ATF2, a quadrupole scan method is used. Such a scan also provides the initial beam waist alignment at the IP. It is performed by scanning the strengths of the FD quadrupoles (QF1FF and QD0FF) while measuring the beam size at the IP. Based on Eq. (1.45) the beam size in the close vicinity of the beam waist depends on the distance $s_{x,y}$ from the waist as:

$$\sigma^{*}_{x,y}{}^2 = \epsilon_{x,y}\beta^*_{x,y} + \epsilon_{x,y}\frac{s^2_{x,y}}{\beta^*_{x,y}} \ . \tag{3.4}$$

In most of the cases, the beam waist is not located at the Virtual IP at the beginning of the beam tuning and requires further adjustment. To evaluate the optical beam sizes from the the Wire Scanner, we need to take into account the dispersion at the IP, and also the finite dimension of the wire:

$$\sigma^{*}_{x,y}{}^2 = \sigma^{*}_{x,y;measured}{}^2 - D^2_{x,y}\delta^2_p - \left(\frac{d}{4}\right)^2 \ , \tag{3.5}$$

where δ_p is the momentum spread of the beam, d is the diameter of the wire, and $D_{x,y}$ is the dispersion at the Virtual IP. For small variations of the FD quadrupoles strengths Δk_L of QF1 and QD0, the added waist shift is $\Delta s_{x,y} \sim \Delta k_L$. The absolute amount depends on the optics, and in particular, on the beta-functions at the quadrupoles location. The horizontal waist is more sensitive to variations of the strength of QF1FF, while vertical is more sensitive to the variations of the strength of QD0FF. So, the strength of each quadrupole is varied while measuring the beam size with the Wire Scanner. Then, the data is fitted with a parabola to evaluate both the emittance and the IP beta-function. At ATF2, we use a flat beam, so while the horizontal beam size varies from 2.8 μm for β^*_x optics to 14 μm for $25\beta^*_x$ optics, the vertical beam size, even before beam size tuning, is expected to be less than 1 μm. So, in the vertical plane, the minimum beam size that we measure with Wire Scanner will correspond to the physical dimensions of the wire. Therefore, the beam size at the waist cannot be trusted, and only the beam divergence is evaluated from the fit:

$$\epsilon_y\frac{s^2_y}{\beta^*_y} \approx \sigma^{*}_{x,y;measured}{}^2 - D^2_y\delta^2_p - \left(\frac{d}{4}\right)^2 \ . \tag{3.6}$$

In this case, we could not evaluate the vertical emittance and beta-function at the IP simultaneously, but the beam divergence ϵ_y/β^*_y instead. To calculate the exact value of

the β_y^* we either rely on the vertical emittance measurements in the damping ring or we evaluate it with the Multi-OTR system [84], located in the matching section of the FFS.

3.1.3 Orbit and dispersion correction

The beam position along the ATF2 beamline is evaluated by means of 38 BPMs of 2 types: 13 stripline-BPMs and 25 Cavity-BPMs (C-BPMs). The stripline BPMs are composed of four metal strip-like electrodes to be able to measure the beam orbit in both directions. The resolution of such BPM varies between 5 μm and 20 μm. The C-BPMs [85] used at ATF2 are based on the induced EM files in a specific resonant cavity when the beam passes through. They are designed to operate in the dipole mode (TM110) at a frequency of 6.422 GHz. In this case, the amplitude of the signal depends linearle on the beam offset. The resolution of such BPMs is usually smaller than 1 μm and can reach 200 nm. The beam orbit is flattened with 13 horizontal and 13 vertical correctors distributed along the ATF2 beamline.

After the beam orbit is corrected, we evaluate the dispersion in the beamline. For this, we slightly change the beam energy at the exit of the damping ring. The orbit change at each particular BPM will depend on the dispersion at its location, as follows:

$$\Delta x(\Delta y) = D_{x,y}\frac{\Delta p}{p}\ , \tag{3.7}$$

where $\Delta p/p$ is the relative momentum change. The beam energy is changed by slightly changing the RF frequency cavities in the damping ring with a step of $\Delta f = 2$ kHz. Being he designed frequency of the RF cavity $f_0 = 714$ MHz, the energy change is given approximately by:

$$\frac{\Delta p}{p} = \frac{\Delta f}{f_0 \alpha_c}\ , \tag{3.8}$$

where $\alpha_c = 0.00214$ is the momentum compaction of the ATF damping ring. Changing the frequency by 2 kHz leads to a beam energy change of about 1.3 %. The horizontal and vertical dispersions are corrected with two pairs of normal and skew quadrupoles, being the two quadrupoles within a pair separated by 2π phase advance in the horizontal plane and π in the vertical plane and located at the same horizontal dispersion but of opposite sign. At ATF2, there is a dedicated pair of normal quadrupoles (QF6X, QF1X) for horizontal dispersion correction and a pair of skew quadrupoles (QS1X, QS2X) for the vertical dispersion correction. Both pairs are located almost identically at the dispersion peaks in the extraction line, see Fig. 3.8. To correct the horizontal dispersion, we vary the strengths of QF6X and QF1X simultaneously. Similarly, to correct the vertical dispersion, we vary the strengths of QS1X and QS2X simultaneously, we will refer in the following as $\sum$-knob. The change of the strengths of QS1X and QS2X in opposite directions, will be refered in the following as Δ-knob. In this case, the pair of skew quadrupoles is the source of $\langle x, y\rangle$ coupling. This is especially useful when used in combiation with the meaurement in the multi-OTR system for minimizing the vertical emittance.

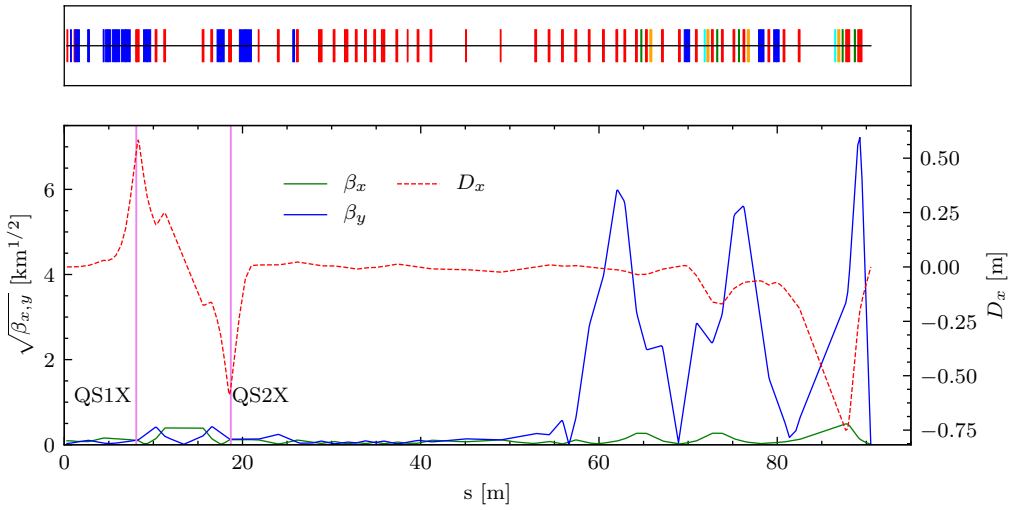

h

Figure 3.8: Horizontal and vertical beta-functions and horizontal dispersion along the ATF2 beamline for Ultra-low β^* optics. In violet, the locations of skew quadrupoles QS1X and QS2X are indicated. Normal quadrupoles QF6X and QF1X are located in close vicinity to QS1X and QS2X respectively, in a range of 20 cm.

3.1.4 Beam tuning knobs

At ATF2, we use a set of so-called tuning "knobs" to correct the aberrations at the virtual IP. Each knob corrects the associated aberrations independently and uses either sextupoles' transverse offsets or their strength variations. The list of the knobs available at ATF2 with a short description is given in Tab. 3.3. The details on how they are constructed are given in Sec. 3.2.1.

Table 3.3: Tuning knobs used at ATF2 and the corresponding aberrations they correct at the virtual IP.

Knob	Aberration at the virtual IP
A_y	Longitudinal location of the vertical waist.
E_y	Vertical dispersion.
$Coup_2$	$\langle y, x' \rangle$ coupling.
Y_{24}	Geometrical aberration $\langle y, x', y' \rangle$.
Y_{46}	Vertical chromaticity $\langle y, y', \delta \rangle$.
Y_{22}	Geometrical aberration $\langle y, x', x' \rangle$.
Y_{26}	Chromo-geometrical aberration $\langle y, x', \delta \rangle$.
Y_{44}	Geometrical aberration $\langle y, y', y' \rangle$.
Y_{66}	2^{nd} order vertical dispersion $\langle y, \delta, \delta \rangle$.

3.2 Tuning knobs construction for $25\beta_x^*\times 0.25\beta_y^*$ optics

Some studies of the ultra-low β_y optics tuning have been performed before in ATF2 [33,35]. In these studies the nominal tuning optics strategy has been used [86], obtaining beam sizes of the order of 50 nm (see Fig. 1.16). In order to improve these achievements a dedicated tuning knob strategy for the $25\beta_x^* \times 0.25\beta_y^*$ optics has been made in this thesis. In the following I will present the new knobs definition and the simulation studies to test the orthogonality and the efficiency of these knobs in comparison with the nominal ones. We construct a new set of the knobs for $25\beta_x^*\times 0.25\beta_y^*$. As discussed in Sec. 1.4.7, static magnets imperfections are the sources of various errors at the IP, such as waist shift, dispersion, coupling, and also the nonlinear terms, such as chromaticity and geometrical aberrations.

3.2.1 Knobs definition

Under the presence of the alignment imperfections and magnetic field errors in the FFS, the beam size at the IP is no longer linear but is dominated by various linear and nonlinear aberrations. Linear aberrations include the longitudinal shift of the horizontal and vertical waists, residual dispersion in both planes, and coupling. These errors are mainly generated by the quadrupoles. They can be corrected with normal sextupoles displacements, using the feed-down to quadrupole field. The sextupole, displaced transversely by Δx and Δy additionally kicks the particle approximately by:

$$\begin{cases} \Delta x' & \approx -k_{2,L}^N x\Delta x + k_{2,L}^N y\Delta y - k_{2,L}^N D_x \Delta x\delta \\ \Delta y' & \approx k_{2,L}^N x\Delta y + k_{2,L}^N y\Delta x + k_{2,L}^N D_x \Delta y\delta \end{cases} . \tag{3.9}$$

where $k_{2,L}^N$ is the integrated strength of the sextupole, x and y are the transverse coordinates at the sextupole entrance, and δ is the energy offset. The dipolar terms that are quadratic on the deviations are not considered here. They are the source of the orbit distortion and the residual dispersion. The dispersion generated by these dipolar components is negligible compared to what is created by the quadrupolar component since usually $\Delta x(y) \ll D_x$. Such kicks produces a displacement at the IP given by:

$$\begin{cases} \Delta x^* = -k_{2,L}^N R_{12}^{S\to IP}\Delta x x + k_{2,L}^N R_{12}^{S\to IP}\Delta y y - k_{2,L}^N R_{12}^{S\to IP} D_x \Delta x\delta \\ \Delta y^* = k_{2,L}^N R_{34}^{S\to IP}\Delta y x + k_{2,L}^N R_{34}^{S\to IP}\Delta x y + k_{2,L}^N D_x R_{34}^{S\to IP}\Delta y\delta \end{cases} , \tag{3.10}$$

where $R^{S\to IP}$ is the transfer matrix between the sextupole and the IP. The sextupoles are located in the FD phase for proper chromaticity correction, such $\Delta\mu_{x,y} = \pi/2 + \pi n_{x,y}$ with $n_{x,y}$ a whole number. In this case the transfer matrix terms are:

$$R_{12}^{S\to IP} = (-1)^{n_x}\sqrt{\beta_x^*\beta_x} \ , \ R_{34}^{S\to IP} = (-1)^{n_y}\sqrt{\beta_y^*\beta_y} \ . \tag{3.11}$$

Furthermore, for the sextupoles at the FD phase the following relations hold (see Eq. 1.43):

$$\begin{cases} x'^* = R_{21}^{S\to IP} x = -1/R_{12}^{S\to IP} x \\ y'^* = R_{43}^{S\to IP} x = -1/R_{34}^{S\to IP} x \end{cases} . \tag{3.12}$$

We could connect the displacements Δx^* and Δy^* at the IP from Eq. (3.12) with the angles x'^*, y'^* using the Eq. 3.12 as:

$$\begin{cases} \Delta x^* = \widetilde{R}^*_{12} x'^* + \widetilde{R}^*_{14} y'^* + \widetilde{R}^*_{16} \delta \\ \Delta y^* = \widetilde{R}^*_{32} x'^* + \widetilde{R}^*_{34} y'^* + \widetilde{R}^*_{36} \delta \end{cases} , \tag{3.13}$$

with the corresponding terms:

$$\begin{cases} \widetilde{R}^*_{12} & \equiv k^N_{2,L} (R^{S\to IP}_{12})^2 \Delta x \\ \widetilde{R}^*_{14} & \equiv -k^N_{2,L} R^{S\to IP}_{12} R^{S\to IP}_{34} \Delta y \\ \widetilde{R}^*_{16} = D^*_x & \equiv -k^N_{2,L} R^{S\to IP}_{12} D_x \Delta x \\ \widetilde{R}^*_{32} & \equiv -k^N_{2,L} R^{S\to IP}_{12} R^{S\to IP}_{34} \Delta y \\ \widetilde{R}^*_{34} & \equiv k^N_{2,L} (R^{S\to IP}_{34})^2 \Delta x \\ \widetilde{R}^*_{36} = D^*_y & \equiv k^N_{2,L} R^{S\to IP}_{34} D_x \Delta y \end{cases} \tag{3.14}$$

One can see that by offsetting a sextupole in the horizontal direction, we introduce a waist shift in both horizontal and vertical planes and also we create a horizontal dispersion D^*_x. An offset in the vertical plane introduces coupling between planes and also vertical dispersion D^*_y. Setting $\Delta x^* = x^* - x^*_\beta$ and $\Delta y^* = y^* - y^*_\beta$, where x^*_β and y^*_β are the non-perturbed or betatron coordinates, we get:

$$\begin{cases} x^* = x^*_\beta + \widetilde{R}^*_{12} x'^* + \widetilde{R}^*_{14} y'^* + D^*_x \delta \\ y^* = y^*_\beta + \widetilde{R}^*_{32} x'^* + \widetilde{R}^*_{34} y'^* + D^*_y \delta \end{cases} \tag{3.15}$$

We could evaluate the coordinates correlations as:

$$\begin{cases} \langle x^*, x'^* \rangle & = \widetilde{R}^*_{12} \langle x'^*, x'^* \rangle \\ \langle x^*, y'^* \rangle & = \widetilde{R}^*_{14} \langle y'^*, y'^* \rangle \\ \langle x^*, \delta \rangle & = \widetilde{R}^*_{16} \delta^2_p \\ \langle y^*, x'^* \rangle & = \widetilde{R}^*_{32} \langle x'^*, x'^* \rangle \\ \langle y^*, y'^* \rangle & = \widetilde{R}^*_{34} \langle y'^*, y'^* \rangle \\ \langle y^*, \delta \rangle & = \widetilde{R}^*_{36} \delta^2_p \end{cases} \tag{3.16}$$

We could introduce the **linear knobs**, as:

$$\mathrm{X}_i \equiv \frac{\langle x^*, u_i \rangle}{\sqrt{\langle u_i, u_i \rangle}} , \ \mathrm{Y}_i \equiv \frac{\langle y^*, u_i \rangle}{\sqrt{\langle u_i, u_i \rangle}} , \tag{3.17}$$

where u^*_i is one of the particle' coordinates $\{x^*, x'^*, y^*, y'^*, t, \delta\}$ at the IP. The beam size at the IP then writes:

$$\begin{cases} \langle x^*, x^* \rangle = \epsilon_x \beta^*_x + \mathrm{X}^2_2 + \mathrm{X}^2_4 + \mathrm{X}^2_6 \\ \langle y^*, y^* \rangle = \epsilon_y \beta^*_y + \mathrm{Y}^2_2 + \mathrm{Y}^2_4 + \mathrm{Y}^2_6 \end{cases} \tag{3.18}$$

One can see that each particular sextupole, displaced by Δx and Δy, is the source of the various effects at the IP, which are linear on the magnitude of the displacements. By

utilizing several sextupoles, we could establish the combination of the shifts, such each particular aberration is changed independently. Such a configuration of the shifts is called a linear tuning knob. Additionally, the terms $\widetilde{R}_{14}^*$ and $\widetilde{R}_{32}^*$ are identical for each sextupole, so the knobs X_4 and Y_2 would be the same. This means that only one can be used at the same time. To construct five linear knobs, we require at least three sextupoles, and in the ATF2 beamline, there are five normal sextupoles available.

Nonlinear aberrations at the IP are associated with the field errors in the sextupoles. When the strength of the normal thin sextupole is changed by $\Delta k_{2,L}^N$, the kick a particle receives is:

$$\begin{cases} \Delta x' &= -\frac{\Delta k_{2,L}^N}{2}((x+D_x\delta)^2 - y^2) \\ \Delta y' &= \Delta k_{2,L}^N (x+D_x\delta) y \end{cases} . \tag{3.19}$$

Such kicks propagate to the IP, causing the following coordinate change:

$$\Delta x^* = -\overbrace{\frac{\Delta k_{2,L}^N}{2} R_{12}^{S\to IP}(x^2-y^2)}^{\text{Geometrical aberrations}} - \overbrace{\frac{\Delta k_{2,L}^N}{2} R_{12}^{S\to IP} D_x^2\delta^2}^{\text{2nd-order dispersion}} - \overbrace{\Delta k_{2,L}^N R_{12}^{S\to IP} D_x x\delta}^{\text{Horizontal chromaticity}} , \tag{3.20}$$

$$\Delta y^* = \overbrace{\Delta k_{2,L}^N R_{34}^{S\to IP} xy}^{\text{Geometrical aberrations}} + \overbrace{\Delta k_{2,L}^N R_{34}^{S\to IP} D_x y\delta}^{\text{Vertical chromaticity}} . \tag{3.21}$$

Based on that, we set:

$$\begin{cases} \widetilde{T}_{324}^* &\equiv \Delta k_{2,L}^N R_{12}^{S\to IP}(R_{34}^{S\to IP})^2 \\ \widetilde{T}_{346}^* &\equiv -\Delta k_{2,L}^N (R_{34}^{S\to IP})^2 D_x \\ \widetilde{T}_{122}^* &\equiv -\frac{\Delta k_{2,L}^N}{2}(R_{12}^{S\to IP})^3 \\ \widetilde{T}_{126}^* &\equiv \Delta k_{2,L}^N D_x (R_{12}^{S\to IP})^2 \\ \widetilde{T}_{144}^* &\equiv \frac{\Delta k_{2,L}^N}{2} R_{12}^{S\to IP} R_{34}^{S\to IP} \\ \widetilde{T}_{166}^* &\equiv -\frac{\Delta k_{2,L}^N}{2} D_x^2 R_{12}^{S\to IP} R_{34}^{S\to IP} \end{cases} \tag{3.22}$$

In this way, the particles' coordinates at the IP are:

$$\begin{cases} x^* = x_0^* + \widetilde{T}_{122}^* x'^{*2} + \widetilde{T}_{144}^* y'^{*2} + \widetilde{T}_{126}^* x'^*\delta + \widetilde{T}_{166}^*\delta^2 \\ y^* = y_0^* + \widetilde{T}_{324}^* x'^* y'^* + \widetilde{T}_{346}^* y'^*\delta \end{cases} , \tag{3.23}$$

here x_0^* and y_0^* are the not perturbed coordinates. We can construct the nonlinear correlations between the coordinates as:

$$\begin{cases} \langle y^*, x'^*, y'^*\rangle &= \widetilde{T}_{324}^* \langle x'^*, x'^*\rangle\langle y'^*, y'^*\rangle \\ \langle y^*, y'^*, \delta\rangle &= \widetilde{T}_{346}^* \langle y'^*, y'^*\rangle\delta_p^2 \\ \langle x^*, x'^*, x'^*\rangle &= 3\widetilde{T}_{122}^* \langle x'^*, x'^*\rangle^2 + \widetilde{T}_{144}^* \langle x'^*, x'^*\rangle\langle y'^*, y'^*\rangle + \widetilde{T}_{166}^* \langle x'^*, x'^*\rangle\delta_p^2 \\ \langle x^*, y'^*, y'^*\rangle &= \widetilde{T}_{122}^* \langle x'^*, x'^*\rangle\langle y'^*, y'^*\rangle + 3\widetilde{T}_{144}^* \langle y'^*, y'^*\rangle^2 + \widetilde{T}_{166}^* \langle y'^*, y'^*\rangle\delta_p^2 \\ \langle x^*, x'^*, \delta\rangle &= \widetilde{T}_{126}^* \langle x'^*, x'^*\rangle\delta_p^2 \\ \langle x^*, \delta, \delta\rangle &= \widetilde{T}_{122}^* \langle x'^*, x'^*\rangle\delta_p^2 + \widetilde{T}_{144}^* \langle y'^*, y'^*\rangle\delta_p^2 + 3\widetilde{T}_{166}^*\delta_p^4 \end{cases} . \tag{3.24}$$

We could introduce the nonlinear knobs as follows:

$$\mathrm{Y}_{ij} \equiv \frac{\langle y^*, u_i^*, u_j^* \rangle}{\sqrt{\langle u_i^*, u_i^* \rangle \langle u_i^*, u_i^* \rangle}} \ , \ \mathrm{X}_{ij} \equiv \frac{\langle x^*, u_i^*, u_j^* \rangle}{\sqrt{\langle u_i^*, u_i^* \rangle \langle u_i^*, u_i^* \rangle}} \ , \tag{3.25}$$

Extracting the terms of $\widetilde{T}^*$ from the system in Eq. (3.24) and evaluating the beam size [86] we have:

$$\begin{cases} \langle x^*, x^* \rangle = \epsilon_x \beta_x^* + \frac{2}{5}(\mathrm{X}_{22}^2 + \mathrm{X}_{44}^2 + \mathrm{X}_{66}^2) - \frac{1}{5}(\mathrm{X}_{22}\mathrm{X}_{44} + \mathrm{X}_{44}\mathrm{X}_{66} + \mathrm{X}_{66}\mathrm{X}_{22}) + \mathrm{X}_{26}^2 \\ \langle y^*, y^* \rangle = \epsilon_y \beta_y^* + \mathrm{Y}_{24}^2 + \mathrm{Y}_{46}^2 \end{cases} \tag{3.26}$$

The knobs X_{ij} and Y_{ij} are linear on the terms of $\widetilde{T}^*$ and consequently they are linear on the strength deviation of the sextupole $\Delta k_{2,L}^N$. For several sextupoles, their contributions to the map $\widetilde{T}^*$ are summed. We can establish the combination of the strengths deviations of the sextupoles in a way to correct a particular aberration associated with the knob. To fully construct all six knobs, we need at least six sextupoles. In the ATF2 beamline, there are only five normal sextupoles available. As discussed in [86] the contribution from X_{44} is expected to be insignificant, so this knob is neglected.

Besides, in the ATF2 beamline, there are four skew sextupoles, namely SK1, SK2, SK3, and SK4. To correct the potential skew sextupole fields errors we construct the tuning knobs on the strengths deviations of these sextupoles. By swapping the horizontal and vertical coordinates in the solution for the normal sextupoles we introduce the knobs Y_{22}, Y_{44}, Y_{26}, Y_{66}, X_{24}, and X_{46}, using the defintion given in Eq. (3.25). The contributions to the beam size is:

$$\begin{cases} \langle x^*, x^* \rangle = \epsilon_x \beta_x^* + \mathrm{X}_{24}^2 + \mathrm{X}_{46}^2 \\ \langle y^*, y^* \rangle = \epsilon_y \beta_y^* + \frac{2}{5}(\mathrm{Y}_{22}^2 + \mathrm{Y}_{44}^2 + \mathrm{Y}_{66}^2) - \frac{1}{5}(\mathrm{Y}_{22}\mathrm{Y}_{44} + \mathrm{Y}_{44}\mathrm{Y}_{66} + \mathrm{Y}_{66}\mathrm{Y}_{22}) + \mathrm{Y}_{26}^2 \end{cases} \tag{3.27}$$

Further, we only focus on the tuning knobs dedicated to the correction of the vertical beam size.

3.2.2 Knobs construction

To construct the tuning knobs, we need to establish the set of the transverse offsets of the normal sextupoles and the set of the strengths deviations of the nominal and skew sextupoles in a way that only one correlation at the IP is changed independently. We start with the linear tuning knobs. Each sextupole in the ATF2 beamline (SD0, SF1, SD4, SF5, and SF6) is misaligned transversely by Δx_i and Δy_i, and we observe the change of the coordinates correlation at the IP, in the form of the knobs in Eq. (3.17). Further, we construct the response matrices R_x and R_y as follows:

$$R_x = \begin{bmatrix} \frac{1}{\Delta x_1}\Delta\left(\frac{\langle x^*, x'^* \rangle}{\sqrt{\langle x'^*, x'^* \rangle}}\right) & \frac{1}{\Delta x_2}\Delta\left(\frac{\langle x^*, x'^* \rangle}{\sqrt{\langle x'^*, x'^* \rangle}}\right) & \cdots & \frac{1}{\Delta x_5}\Delta\left(\frac{\langle x^*, x'^* \rangle}{\sqrt{\langle x'^*, x'^* \rangle}}\right) \\ \frac{1}{\Delta x_1}\Delta\left(\frac{\langle x^*, \delta \rangle}{\delta_p}\right) & \frac{1}{\Delta x_2}\Delta\left(\frac{\langle x^*, \delta \rangle}{\delta_p}\right) & \cdots & \frac{1}{\Delta x_5}\Delta\left(\frac{\langle x^*, \delta \rangle}{\delta_p}\right) \\ \frac{1}{\Delta x_1}\Delta\left(\frac{\langle y^*, y'^* \rangle}{\sqrt{\langle y'^*, y'^* \rangle}}\right) & \frac{1}{\Delta x_2}\Delta\left(\frac{\langle y^*, y'^* \rangle}{\sqrt{\langle y'^*, y'^* \rangle}}\right) & \cdots & \frac{1}{\Delta x_5}\Delta\left(\frac{\langle y^*, y'^* \rangle}{\sqrt{\langle y'^*, y'^* \rangle}}\right) \end{bmatrix} , \tag{3.28}$$

$$R_y = \begin{bmatrix} \frac{1}{\Delta y_1}\Delta\left(\frac{\langle y^*, x'^*\rangle}{\sqrt{\langle x'^*, x'^*\rangle}}\right) & \frac{1}{\Delta y_2}\Delta\left(\frac{\langle y^*, x'^*\rangle}{\sqrt{\langle x'^*, x'^*\rangle}}\right) & \cdots & \frac{1}{\Delta y_5}\Delta\left(\frac{\langle y^*, x'^*\rangle}{\sqrt{\langle x'^*, x'^*\rangle}}\right) \\ \frac{1}{\Delta y_1}\Delta\left(\frac{\langle y^*, \delta\rangle}{\delta_p}\right) & \frac{1}{\Delta y_2}\Delta\left(\frac{\langle y^*, \delta\rangle}{\delta_p}\right) & \cdots & \frac{1}{\Delta y_5}\Delta\left(\frac{\langle y^*, \delta\rangle}{\delta_p}\right) \end{bmatrix} . \quad (3.29)$$

The coordinate correlations for each corresponding sextupole offset are evaluated with a dedicated software in Python [87] that has been written for knobs handling and tuning studies at ATF2. It uses Mapclass to calculate the correlations. The transfer map for Mapclass is generated with PTC in MADX. In the calculations, the ultra-low $25\beta_x^* \times 0.25\beta_y^*$ optics is utilized with no errors. Each sextupole was shifted by a basic step of 1 μm in horizontal and vertical planes. The knobs are evaluated by applying the singular value decomposition (SVD) on the response matrices R_x and R_y. In this case we factorize the response matrix $R_{x,y} = USV^T$. The rows of the matrix V^T are taken as the knobs. The shifts associated with the knobs are also scaled in a way that the amplitude 1.0 of the knob corresponds to the beam size contribution of 100 nm. The knobs construction results are shown in Tab. 3.4. Here, we utilize the same naming as in the ATF2 machine (see Tab. 3.3)

Table 3.4: Linear and nonlinear knobs constructed on the transverse shifts and strength variations of the normal sextupoles respectively. The shifts of the sextupoles are shown in [μm].

	SF6		SF5		SD4		SF1		SD0	
	Δx	Δy	Δx	Δy	Δx	Δy	Δx	Δy	Δx	Δy
A_x	4.0	-	0.3	-	1.1	-	-1.4	-	1.1	-
A_y	1.7	-	-0.1	-	-7.9	-	-1.6	-	-0.4	-
E_x	8.9	-	6.4	-	-0.8	-	16.4	-	-12.7	-
E_y	-	-0.1	-	7.1	-	50.5	-	17.3	-	-36.2
$Coup_2$	-	20.1	-	1.7	-	8.7	-	-4.8	-	10.1
	Δk_2^N [m^{-3}]		Δk_2^N [m^{-3}]		Δk_2^N [m^{-3}]		Δk_2^N [m^{-3}]		Δk_2^N [m^{-3}]	
Y_{24}	-0.1		0.1		0.1		-0.4		-0.9	
Y_{46}	1.6		2.9		5.4		0.1		0.6	

Similarly, we construct the nonlinear knobs on the strength deviations. The strength of each sextupole is changed by Δk_i. In the simulations, a step of 0.1 m^{-3} is used. Then, the coordinates correlations associated with knobs Y_{24}, Y_{46}, X_{22}, X_{26}, and X_{66} are calculated.

The response matrix evaluates as:

$$R_{kn} = \begin{bmatrix} \frac{1}{\Delta k_1}\Delta\left(\frac{\langle y^*,x'^*,y'^*\rangle}{\sqrt{\langle x'^*,x'^*\rangle\langle y'^*,y'^*\rangle}}\right) & \cdots & \frac{1}{\Delta k_5}\Delta\left(\frac{\langle x^*,x'^*,y'^*\rangle}{\sqrt{\langle x'^*,x'^*\rangle\langle y'^*,y'^*\rangle}}\right) & \cdots \\ \frac{1}{\Delta k_1}\Delta\left(\frac{\langle y^*,y'^*,\delta\rangle}{\sqrt{\langle y'^*,y'^*\rangle}\delta_p}\right) & \cdots & \frac{1}{\Delta k_5}\Delta\left(\frac{\langle x^*,y'^*,\delta\rangle}{\sqrt{\langle y'^*,y'^*\rangle}\delta_p}\right) & \cdots \\ \frac{1}{\Delta k_1}\Delta\left(\frac{\langle x^*,x'^*,x'^*\rangle}{\langle x'^*,x'^*\rangle}\right) & \cdots & \frac{1}{\Delta k_5}\Delta\left(\frac{\langle x^*,x'^*,x'^*\rangle}{\langle x'^*,x'^*\rangle}\right) & \cdots \\ \frac{1}{\Delta k_1}\Delta\left(\frac{\langle x^*,x'^*,\delta\rangle}{\sqrt{\langle x'^*,x'^*\rangle}\delta_p}\right) & \cdots & \frac{1}{\Delta k_5}\Delta\left(\frac{\langle x^*,x'^*,\delta\rangle}{\sqrt{\langle x'^*,x'^*\rangle}\delta_p}\right) & \cdots \\ \frac{1}{\Delta k_1}\Delta\left(\frac{\langle y^*,\delta,\delta\rangle}{\delta_p^2}\right) & \cdots & \frac{1}{\Delta k_5}\Delta\left(\frac{\langle x^*,\delta,\delta\rangle}{\delta_p^2}\right) & \cdots \end{bmatrix}. \tag{3.30}$$

By applying the SVD method, we extract the sets of strength deviations of the normal sextupoles for Y_{24} and Y_{46} knobs. They are also adjusted to produce the contributions of 100 nm when applied. The details are given in Tab. 3.4. Finally, we build the nonlinear knobs Y_{22}, Y_{44}, Y_{26}, and Y_{66} on the strength variations of the skew sextupoles. Similarly, we change the strength of one of the sextupoles by 0.1 m^{-3} and we calculate the response matrix R_{ks}:

$$R_{ks} = \begin{bmatrix} \frac{1}{\Delta k_1}\Delta\left(\frac{\langle y^*,x'^*,x'^*\rangle}{\langle x'^*,x'^*\rangle}\right) & \cdots & \frac{1}{\Delta k_4}\Delta\left(\frac{\langle y^*,x'^*,x'^*\rangle}{\langle x'^*,x'^*\rangle}\right) & \cdots \\ \frac{1}{\Delta k_1}\Delta\left(\frac{\langle y^*,y'^*,y'^*\rangle}{\langle x'^*,x'^*\rangle}\right) & \cdots & \frac{1}{\Delta k_4}\Delta\left(\frac{\langle y^*,y'^*,y'^*\rangle}{\langle x'^*,x'^*\rangle}\right) & \cdots \\ \frac{1}{\Delta k_1}\Delta\left(\frac{\langle y^*,x'^*,\delta\rangle}{\sqrt{\langle x'^*,x'^*\rangle}\delta_p}\right) & \cdots & \frac{1}{\Delta k_4}\Delta\left(\frac{\langle y^*,x'^*,\delta\rangle}{\sqrt{\langle x'^*,x'^*\rangle}\delta_p}\right) & \cdots \\ \frac{1}{\Delta k_1}\Delta\left(\frac{\langle y^*,\delta,\delta\rangle}{\delta_p^2}\right) & \cdots & \frac{1}{\Delta k_4}\Delta\left(\frac{\langle y^*,\delta,\delta\rangle}{\delta_p^2}\right) & \cdots \end{bmatrix}. \tag{3.31}$$

The knobs are given in Tab. 3.5

Table 3.5: Nonlinear knobs constructed on the strength variation of the skew sextupoles.

	SK4 Δk_2^S [m^{-3}]	SK3 Δk_2^S [m^{-3}]	SK2 Δk_2^S [m^{-3}]	SK1 Δk_2^S [m^{-3}]
Y_{22} knob	0.0	7.5	-0.1	35.7
Y_{26} knob	0.0	-11.5	-0.1	23.6
Y_{44} knob	0.2	1.4	0.6	0.5
Y_{66} knob	0.6	-0.9	0.0	-1.9

3.2.3 Orthogonality validation of the tuning knobs for ultra-low β_y^* optics

The tuning knobs have been evaluated in a way, that when the knob is applied, only the associated aberration is impacted. In total there are nine tuning knobs for the vertical

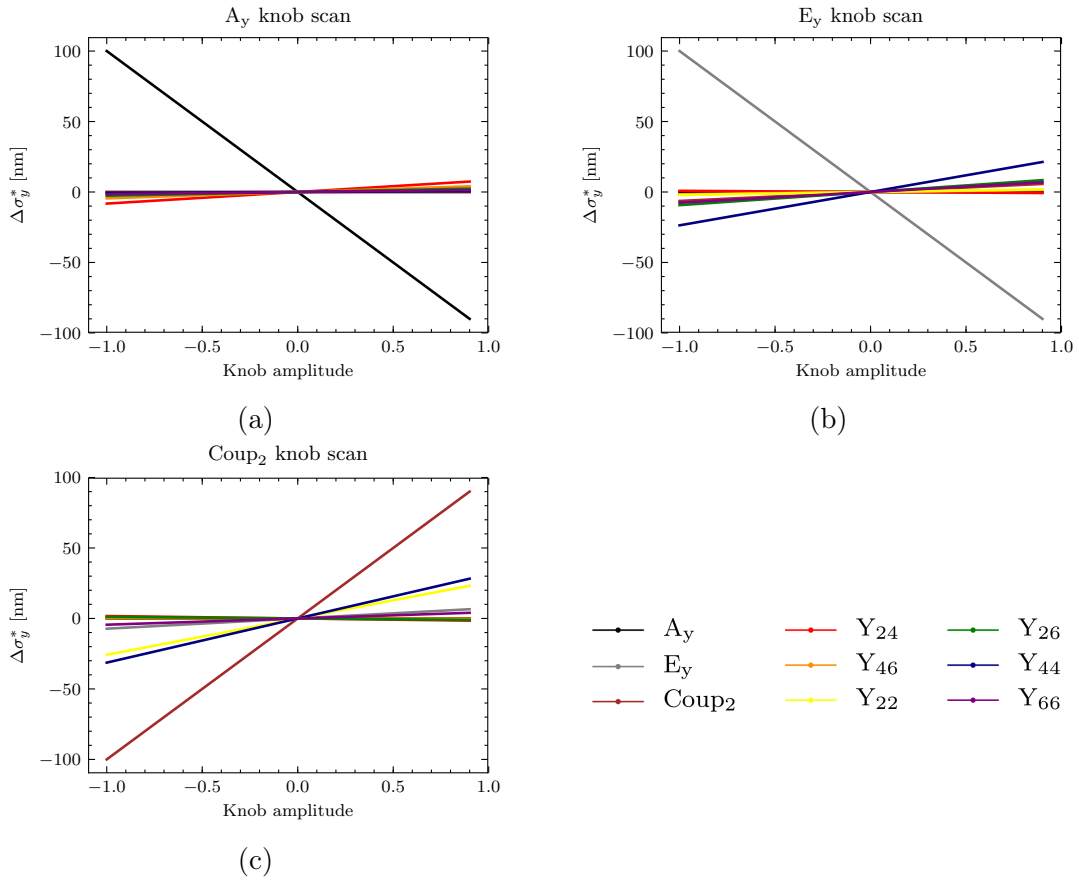

Figure 3.9: Vertical beam size contributions resulting from the scans of the linear tuning knobs A_y (a), E_y (b), and $Coup_2$ (c).

beam size. Combining Eqs. (3.18), (1.40), (3.27) the vertical beam size for an error-free lattice writes as:

$$\sigma_y^{*2} = \epsilon_y\beta_y^* + {A_y}^2 + {Coup_2}^2 + {E_y}^2 + Y_{24}^2 + Y_{46}^2 + \frac{2}{5}\left(Y_{22}^2 + Y_{44}^2 + Y_{66}^2\right) - \frac{1}{5}\left(Y_{22}Y_{44} + Y_{44}Y_{66} + Y_{22}Y_{66}\right) + Y_{26}^2 \,. \tag{3.32}$$

When the knobs are constructed properly, the application of the knob A_y results in a beam size growth with the largest contribution coming from A_y, etc. We call this an orthogonal set of the knobs. To verify such a property, we test each knob and check the beam size contributions from all the knobs. The detailed results of these calculations are shown in Figs. 3.9 and 3.10. Simulations show the satisfactory orthogonality level of the tuning knobs. The best results are achieved for the linear knobs. In the case of the nonlinear knobs, a considerable amount of the beam size contributions comes from the "coupled" knobs. By "coupled" knobs, we refer to the knobs that change the same parameters in the beamline, sextupole horizontal shifts, strength deviation, etc, for example Y_{24} and Y_{46}.

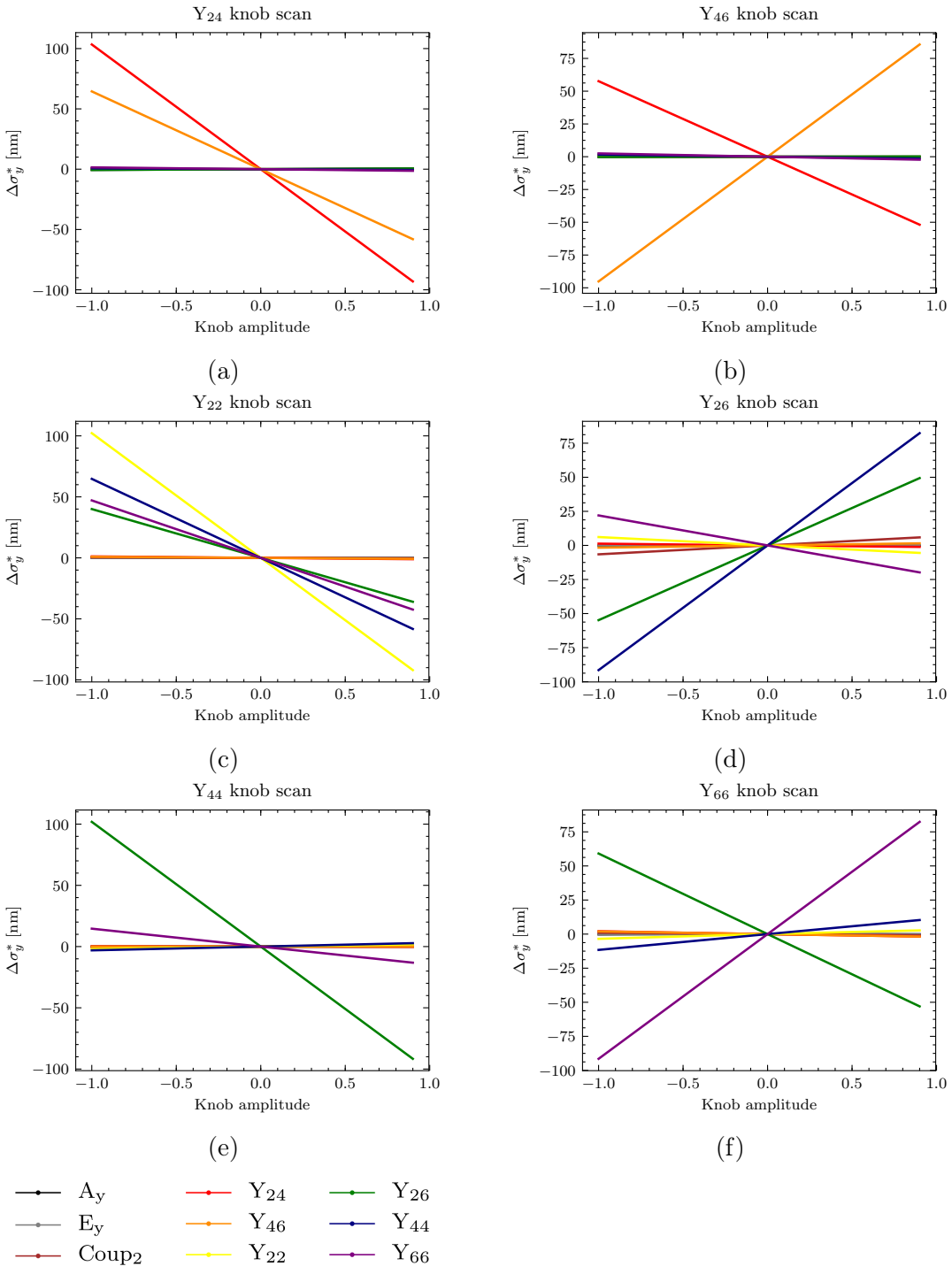

Figure 3.10: Vertical beam size contributions resulting from the scans of the non-linear tuning knobs Y_{24} (a), Y_{46} (b), Y_{22} (c), Y_{26} (d), Y_{44} (e), Y_{66} (f).

This means that these knobs may require several iterations to simultaneously correct the aberrations associated with them.

3.3 Tuning simulations including static imperfections with $25\beta_x^* \times 0.25\beta_y^*$ optics

In this section, the simulations of the tuning process at ATF2, using the ultra-low β_y^* optics, are presented. The presence of various imperfections in the beamline leads to numerous aberrations at the virtual IP, such as waist shift, residual dispersion, coupling, and also high-order aberrations, such as geometrical aberrations and chromaticity. The origins of these aberrations are discussed in Sec. 1.4.7. To deal with them in ATF2, a tuning routine is followed. In this work we simulate this tuning routine to explore the possible benefits of using a new set of tuning knobs at ATF2. The tuning simulations are performed with the software that is used to construct the tuning knobs [87]. It is based on the Python scripting language and uses Mapclass [46] and is interfaced to MADX. The full list of the static errors considered in the simulations is listed in Tab. 3.6. Also, the full details of the experimental setup at ATF2 are given in Sec. 3.1. Initially, we randomly allocate

Table 3.6: Summary table of the errors considered in the tuning studies.

Element	Error	
Quadrupole, Sextupole, Octupole, BPM	Misalignment [μm]	100
	Roll [μrad]	200
	Strength [%]	0.1
	BBA accuracy [μm]	100[a]
Strip line BPM	Accuracy [μm]	5
C-band cavity BPM	Accuracy [μm]	0.2

[a] Uniform distribution.

misalignments, rolls, and strength errors to the magnets following a Gaussian distribution. Then, we follow the tuning routine at ATF2:

1. Beam orbit correction:
   We use all the available BPMs in the ATF2 beamline. We also introduce the precision of the orbit measurements, based on the type of the BPM: Stripline BPM or C-band cavity BPM. In the simulations, the orbit is corrected with the MADX internal routine, which uses SVD to evaluate the optimal correctors' settings. This routine is faster and more precise than the orbit correction in the real machine. It is worth mentioning that the BPMs are also misaligned by the same amount as the quadrupole they are bound to.

2. Dispersion correction:
   The adjustment of the dispersion level in the FFS, is vital for chromaticity correction.

In the horizontal plane, has to match the design profile. In the vertical plane has to be zero in the whole FFS. Horizontal dispersion is corrected by scanning the strength of QF1X and QF6X quadrupoles. Vertical dispersion is corrected by means of the Σ-knob - strength variations of the skew quadrupoles QS1X and QS2X in the same direction.

3. Adjustment of the beam waist:
   The strengths of the FD quadrupoles QF1FF and QD0FF are scanned to minimize the beam size. For this, the Wire Scanner is utilized.

4. Sextupoles switched on:
   We switch the sextupoles on and we align them. In the simulations, we evaluate the real beam orbit at the sextupole locations and we align them with respect to it, also taking into account the Beam Based Alignement (BBA) precision.

5. Beam size tuning with linear and nonlinear tuning knobs:
   Finally, we scan the tuning knobs to find the smallest beam size. There are linear knobs named: A_y, E_y, and $Coup_2$ to correct the longitudinal shift of the vertical waist, vertical dispersion, and $\langle y^*, x'^* \rangle$ coupling at the IP, respectively. We also use a so-called difference or knob, which tackles $\langle x, y \rangle$ coupling, and the strengths of QS1X and QS2X are changed equally in different directions. There are also nonlinear knobs aimed to correct the residual 2^{nd} order aberrations Y_{24}, Y_{46}, Y_{22}, Y_{26}, Y_{44}, Y_{66}. The summary of all the knobs used in the beam tuning is given in Tab. 3.3. Each knob is scanned in the range [-2.0, +2.0], and the optimum is found within this range. Depending on the vertical beam size, we use either the Wire scanner and fit σ_y^{*2} with a parabola, or the IPBSM, where we fit the modulation with a Gaussian. A detailed overview of IPBSM is given in Sec. 3.1. Since the IPBSM has several working modes, we change the mode depending on the beam size to be measured, see Tab. 3.7.

   The beam size tuning with the tuning knobs is a very time-consuming part of the ATF2 ultra-low β_y^* operation. We estimate that one knob scan takes approximately 30 minutes in experimental real time and set the total number of iterations to 51. It corresponds to the total 25 hours of the beam size tuning. We define a short knobs sequence that it will be used further:

$$\begin{cases} \text{Lin. knobs} & \equiv A_y \rightarrow E_y \rightarrow Coup_2 \\ K_N \text{ knobs} & \equiv Y_{24} \rightarrow Y_{46} \\ K_S \text{ knobs} & \equiv Y_{22} \rightarrow Y_{26} \rightarrow Y_{44} \rightarrow Y_{66} \end{cases} \tag{3.33}$$

   The sequence of the knobs used in the simulations is:

$$3 \times \text{Lin.} \rightarrow 2 \times \{2 \times \text{Lin.} \rightarrow K_N \rightarrow 2 \times \text{Lin.} \rightarrow K_S \rightarrow \text{Lin.}\} \tag{3.34}$$

Enough statistics is acquired by running the tuning simulations on 100 machines with different static errors. Besides, for comparison reasons, we perform the tuning simulations

Table 3.7: Different regimes used to evaluate the vertical beam size at the IP.

	Wire Scanner	IPBSM 6.4°	IPBSM 30°	IPBSM 174°
σ_y^* range [nm]	> 1600	[1600, 360]	[360, 100]	[100, 25]
σ_y^* error [nm]	800	100	20	8

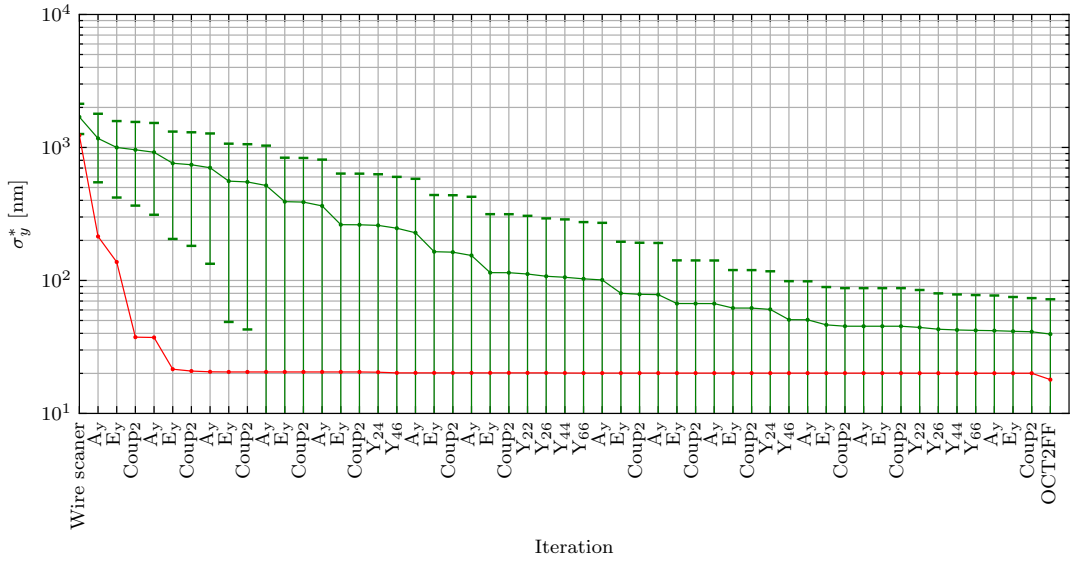

Figure 3.11: Evolution of the vertical beam size throughout the tuning process in the simulations for the ultra-low $25\beta_y^* \times 0.25\beta_x^*$ optics. The green points correspond to the average beam size with a standard error. The red points correspond to the machine with the smallest beam size.

using the tuning knobs constructed for the nominal $\beta_x^* \times 1\beta_y^*$ optics [86]. We will refer to these knobs in the following as "Nominal knobs". In Fig. 3.11 the tuning results for the ultra-low $25\beta_x^* \times 0.25\beta_y^*$ with the new "ultra-low" tuning knobs are shown. The average vertical beam size achieved at the end of the tuning process is 39.5 nm with a rms value of 51 nm. In this case, the final average is skewed by the several machines that have a large final beam size. These machines are stuck at a large beam size. The possible explanation is that in these particular simulations, we have a strict definition of the range of the knobs iterations, as consequence even several knob iterations are not enough to fully cancel this particular aberration. Also, we do not use the optimal sequence of the tuning knobs. The evaluation of the probability to reach a specific beam size and the comparison with the tuning results for the "Nominal" knobs, is shown in Fig. 3.12. In both cases, the median value is approximately 26 nm. But, an improvement appears for the beam sizes larger than 70 nm. The tuning with the "ultra-low" knobs is more resistant to being stuck at large (> 100 nm) beam size. The percentage of the machines that did not reach 100 nm when tuned with the "ultra-low" knobs is 4 %, compared to 12 %, when "nominal" knobs are used. The average vertical beam size reduction for each knob iteration is shown in

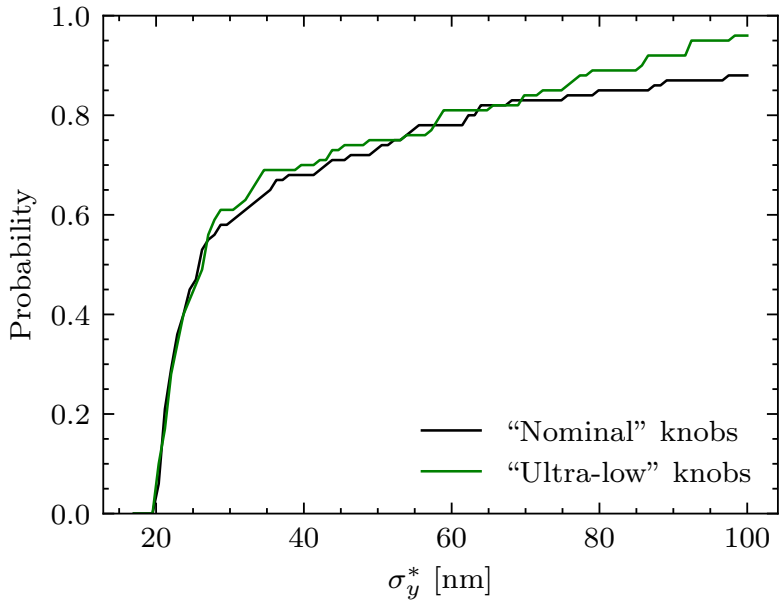

Figure 3.12: Distribution of vertical beam size at the virtual IP at the end of the beam tuning process with "ultra-low" and "nominal" sets of knobs.

Fig. 3.13. We could conclude from these simulations that the linear knobs are the most important for the beam size reduction. Also, Y_{46} has the most significant impact among the nonlinear knobs, and it evaluates to be approximately 15 nm. The reduction from the rest of the nonlinear knobs is less than 10 nm. This reduction might not be visible at the IPBSM due to the presence of dynamic measurement errors.

When we consider the measurement errors of the IPBSM, see Tab. 3.7, the tuning is more challenging compared to the case when only static errors are taken. The median value, in this case, is 33.8 nm, although only 72 % of the machines reached the beam size below 100 nm. To reduce the impact of the dynamic errors, we evaluate the beam size several times for each knob value, using the procedure described before.

3.3.1 Tuning simulations including the octupoles

After the beam size is tuned with the tuning knobs, we could scan the strengths of the two octupoles present in the beamline: OCT1FF and OCT2FF. In the simulations, we adjust their transverse position with respect to the actual orbit evaluated at their positions. At this point, we apply the same BBA error as to the sextupoles. Then, their strength is scanned to minimize σ_y^*. The tuning results are shown in Fig. 3.15. One can see that the octupoles' impact is visible when the beam is tuned at least to 30 nm. In this case, the octupoles reduce the beam size by approximately 2.5 nm. The distribution of the required strengths of the octupoles are shown in Fig. 3.16.

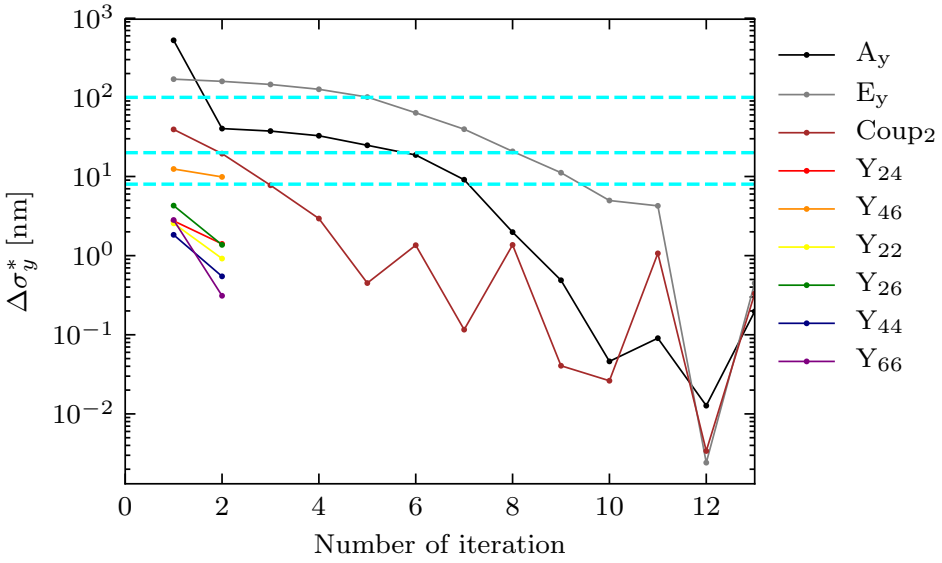

Figure 3.13: Average vertical beam size reduction for each knob iteration. In cyan are shown the IPBSM measurement errors for the three work regimes: 6.4° (100 nm), 30° (20 nm), and 174° (8 nm) modes.

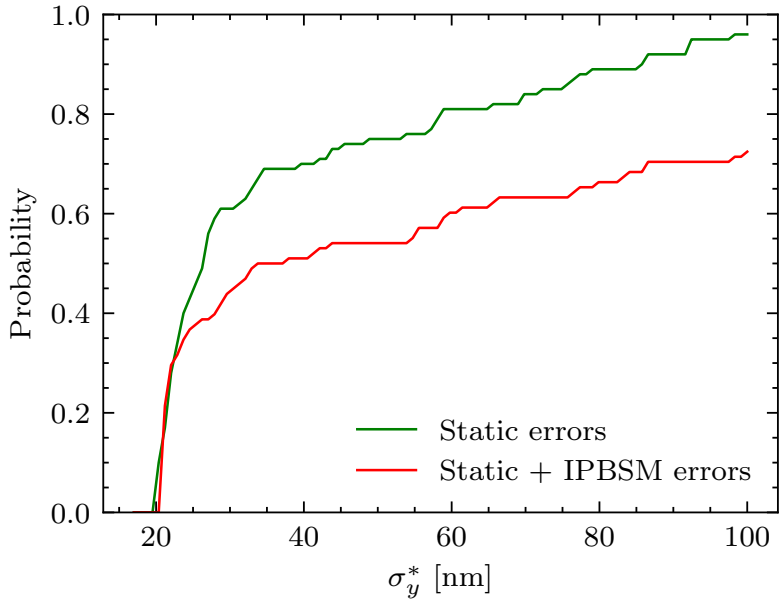

Figure 3.14: Distribution of the vertical beam at the virtual IP at the end of the beam tuning for the cases when only static errors and when static and IPBSM measurement errors are considered. In the simulations the "Ultra-low" knobs are used.

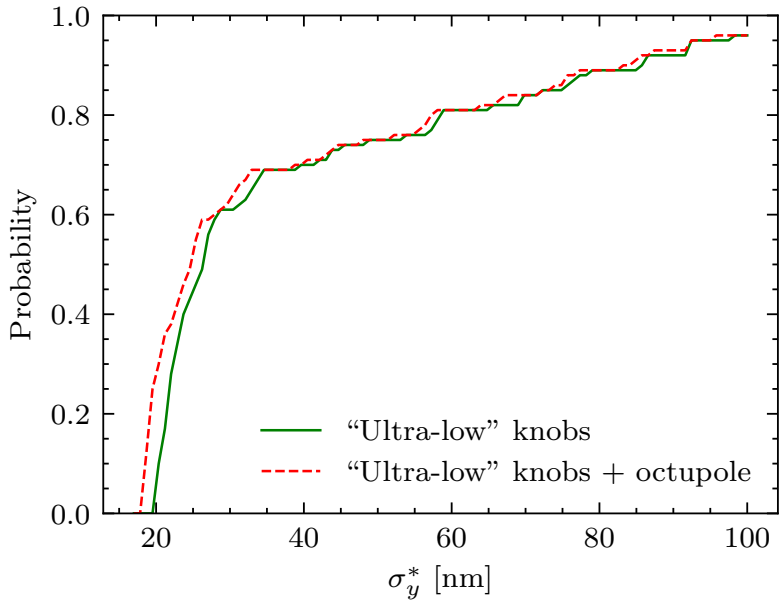

Figure 3.15: Distribution of the vertical beam size at the virtual IP before and after tuning with the octupoles.

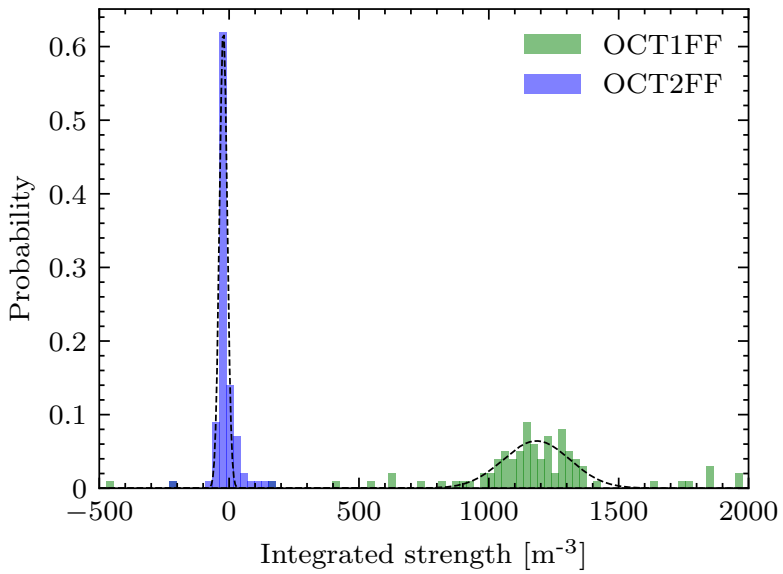

Figure 3.16: Distribution of the optimal octupoles' strength evaluated with tuning simulations.

3.4 Octupole alignment

In order to mitigate the feed down magnetic fields that impact the beam size at the virtual IP is necessary to perform the octupoles alignment. The key parameters of the octupoles are given in Tab. 3.8 and their locations are indicated in Fig. 3.2. When an octupole

Table 3.8: Main parameters of the octupoles.

	OCT1FF	OCT2FF
Max. integr. gradient [T/m^2]	7663	390
Max. integr. strength [m^{-3}]	730	90
Max. current [A]	50	50
Magnetic length [mm]	300	300

is displaced transversely from the beam orbit, it generates sextupolar, quadrupolar and dipolar magnetic fields. For a thin octupole, misaligned by Δx and Δy in the horizontal and vertical planes respectively, the particle's kick in the vertical plane is given by:

$$\Delta y' = \overbrace{\frac{k_{3,L}}{6}(3yx^2 - y^3)}^{\text{Normal Octupole}} - \overbrace{\frac{k_{3,L}\Delta y}{2}(y^2 - x^2)}^{\text{Normal sextupole}} + \overbrace{k_{3,L}\Delta x x y}^{\text{Skew sextupole}} - \overbrace{\frac{k_{3,L}(\Delta y^2 - \Delta x^2)}{2} y}^{\text{Normal quadrupole}} + \overbrace{k_{3,L}\Delta x \Delta y x}^{\text{Skew quadrupole}} + \overbrace{\frac{k_{3,L}}{6}(3\Delta y \Delta x^2 - \Delta y^3)}^{\text{Dipole}} , \tag{3.35}$$

and in the horizontal plane is given by:

$$\Delta x' = \overbrace{\frac{k_{3,L}}{6}(3xy^2 - x^3)}^{\text{Normal Octupole}} - \overbrace{\frac{k_{3,L}\Delta x}{2}(x^2 - y^2)}^{\text{Normal sextupole}} + \overbrace{k_{3,L}\Delta y x y}^{\text{Skew sextupole}} - \overbrace{\frac{k_{3,L}(\Delta x^2 - \Delta y^2)}{2} x}^{\text{Normal quadrupole}} + \overbrace{k_{3,L}\Delta y \Delta x y}^{\text{Skew quadrupole}} + \overbrace{\frac{k_{3,L}}{6}(3\Delta x \Delta y^2 - \Delta x^3)}^{\text{Dipole}} . \tag{3.36}$$

where $k_{3,L}$ is the integrated strength of the octupole. In the traditional BBA, the magnet is aligned by measuring the beam orbit change at the downstream BPMs. In this case, the orbit deviation is based on the dipolar component of the misaligned magnet, and it is given by:

$$\begin{cases} \Delta x = \widetilde{R}_{12}\frac{k_{3,L}}{6}(3\Delta x \Delta y^2 - \Delta x^3) \\ \Delta y = \widetilde{R}_{34}\frac{k_{3,L}}{6}(3\Delta y \Delta x^2 - \Delta y^3) \end{cases} , \tag{3.37}$$

where $\widetilde{R}$ is the transfer matrix between the octupole and the corresponding BPM. The first BBA study was performed on OCT1FF in 2017 using the beam position data from the IPBPMs [20]. At that time, the stronger magnet was located at OCT1FF location. The alignment of the weaker octupole OCT2FF was problematic since the sensitivity of the beamline BPMs was not enough to perform the BBA. After the octupoles were swapped, a new alignment strategy need to be developed for the stronger octupole, which now is located at OCT2FF position. Since the orbit deviation depends on horizontal and vertical shifts simultaneously, we consider two scenarios. In the first scenario, we scan the horizontal location of the magnet and measure the horizontal orbit. Consequently, the horizontal orbit change is cubic on the horizontal offset, see Eq. (3.37). In the second scenario, we scan the horizontal location but we measure the vertical orbit at the BPM. Therefore, the vertical orbit dependence is quadratic, but to measure it, we need to have a constant offset in the vertical plane: $\Delta y \neq 0$. The same considerations are also valid for the vertical alignment of the octupole. We simulate both scenarios and we observe the orbit change on the most sensitive BPMs: MQF5BFF, MQD4BFF, MQF3FF, MQD2BFF, and MQD2AFF. To simulate the alignment, we set the octupole to the maximum current (50 A) and the offset in the range of [-1 mm, 1 mm] in both planes and we perform the orbit scans on an error-free lattice.

In Fig. 3.17 the expected orbit changes evaluated in the first scenario are shown. We see that the orbit change is maximized when we offset the octupole in the opposite plane to the one we perform the alignment. In particular, when the vertical offset is set to 1 mm, the horizontal orbit change at MQF3FF BPM varies in the range approximately $\pm$ 1.4 μm for the octupole offset $\pm$ 1 mm in the horizontal plane. Similarly, the vertical orbit change at MQD4BFF is in the range $\pm$ 1.3 μm for the vertical offsets $\pm$ 1 mm, when the horizontal offset is set to 1 mm. In Fig. 3.18 the orbit scans for the second scenario are shown. For the vertical alignment of OCT2FF, the orbit at MQF3FF changes in the range from -1.4 μm to 0.7 μm. For the horizontal alignment, the orbit change at MQD4BFF varies in the range -1.3 μm to 0.6 μm. Based on these scans, we could conclude that the optimal strategy for octupole alignment in the two planes is to use the horizontal orbit change at MQF3FF. But a good resolution of the orbit measurement at MQF3FF is needed. Figure 3.19 shows the simulation of the octupole alignment when the resolution considered is 1 μm. Based on [85] the resolution of MQF3FF is slightly larger than 1 μm. Also, considering the presence of the orbit jitter, such BBA might be difficult to perform.

3.4.1 Octupole alignment using the waist shift at the virtual IP

In this section we explore a new technique for octupole alignment, which is based on the measurement of the waist shift at the IP. A misaligned octupole generates a normal quadrupole kick via feed-down, see Eqs. (3.35) and (3.36), which propagates to the virtual IP and causes a longitudinal shift of the beam waist that is given by [88]:

$$\Delta s_{x,y} \approx \pm \Delta k \beta_{x,y} \beta^*_{x,y} \cos 2\Delta\mu_{x,y}, \tag{3.38}$$

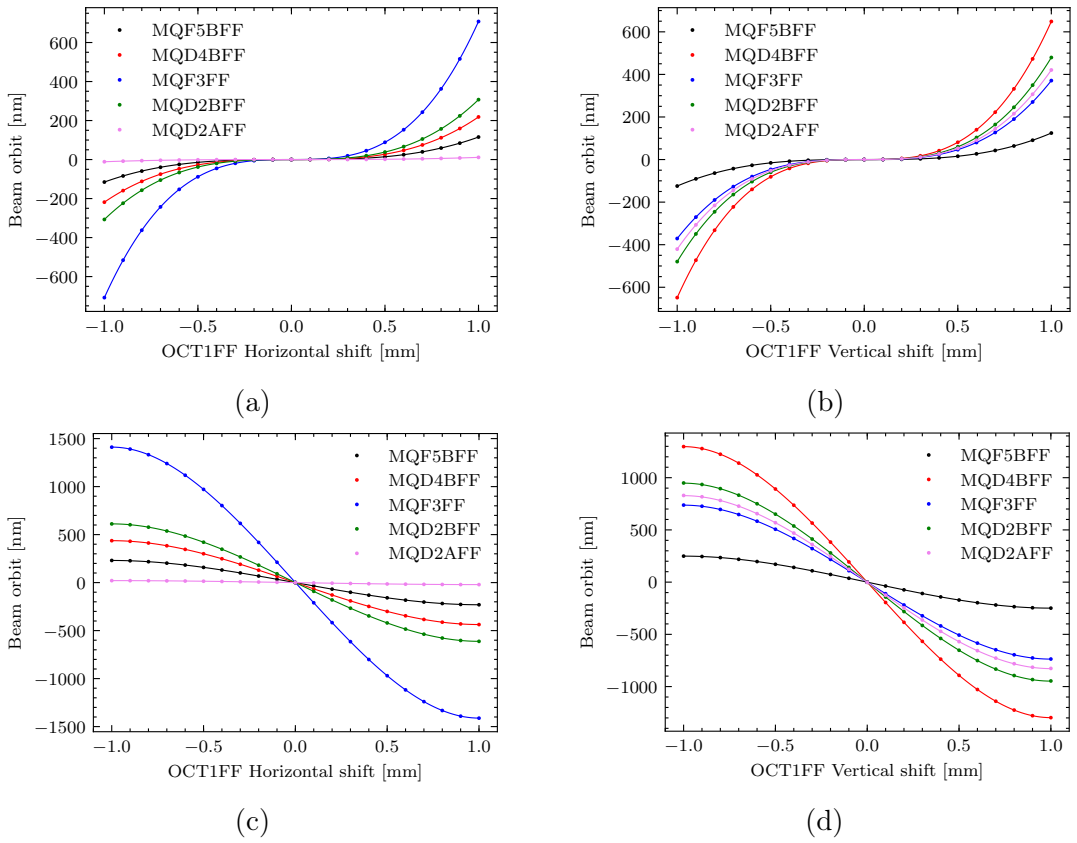

Figure 3.17: (a): Horizontal orbit change at BPMs, for different horizontal offsets of OCT1FF, the vertical offset of OCT1FF is set to $\Delta y = 0$;
(b): Vertical orbit change at BPMs, for different vertical offsets of OCT1FF, the horizontal offset of OCT1FF is set to $\Delta x = 0$.
(c): Horizontal orbit change at BPMs, for different horizontal offsets of OCT1FF, the vertical offset of OCT1FF is set to $\Delta y = 1$ mm;
(d): Vertical orbit change at BPMs, for different vertical offsets of OCT1FF, the horizontal offset of OCT1FF is set to $\Delta x = 1$ mm.

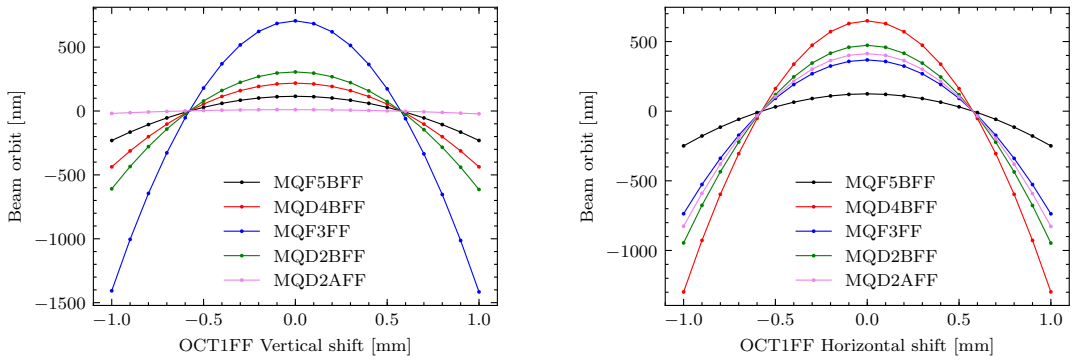

(a) (b)

Figure 3.18: (a): Horizontal orbit change at BPMs, for different vertical offsets of OCT1FF, the horizontal offset of OCT1FF is set $\Delta x = 1$ mm;
(b): Vertical orbit change at BPMs, for different horizontal offsets of OCT1FF, the vertical offset of OCT1FF is set $\Delta y = 1$ mm.

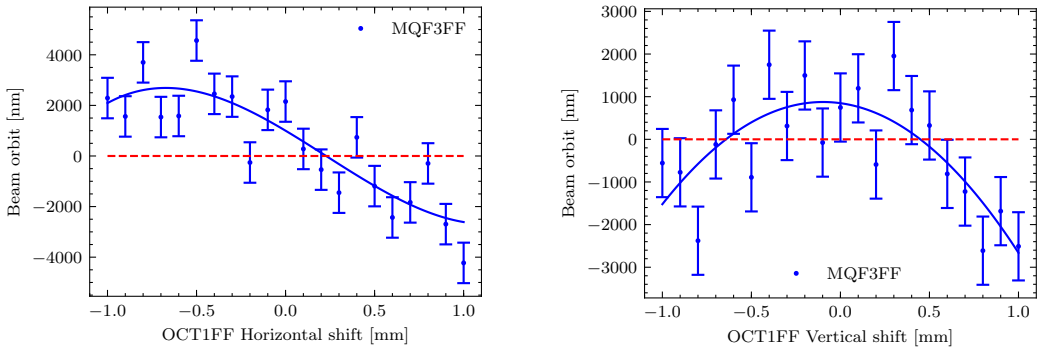

(a) (b)

Figure 3.19: OCT1FF alignment in the horizontal (a) and vertical (b) planes using the horizontal orbit change at MQF3FF BPM fitted based on Eq. (3.37).

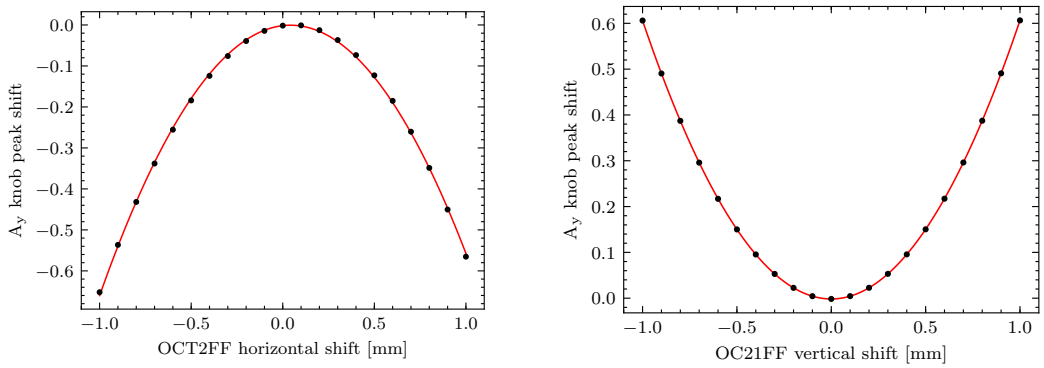

(a) (b)

Figure 3.20: Simulation of the OCT2FF alignment in the horizontal (a) and vertical (b) planes using the waist shift at the virtual IP. The "Ultra-low" knob A_y is used in the scan.

where $\beta_{x,y}$ is the beta-function at the octupole location, $\Delta\mu_{x,y}$ is the phase advance between the octupole and the virtual IP, and $\Delta k = \frac{k_{3L}(\Delta x^2 - \Delta y^2)}{2}$ is the associated quadrupole kick. The shift of the vertical beam waist is quadratic on the octupole offsets as follows:

$$\Delta s_y \propto (\Delta y^2 - \Delta x^2). \tag{3.39}$$

We can measure Δs_y with the IPBSM. Normally, during the beam size tuning, we scan the waist shift knob A_y and check the beam size or the modulation we measure with the IPBSM. The smallest beam size or largest modulation corresponds to the condition when the waist shift is corrected. In this case, the waist shift change is proportional to the amplitude of the A_y knob. So, when we tune the beam, such as the initial waist shift is negligible, and switch on the octupole after, we will observe a waist shift when we perform the A_y knob scan. So we set the octupole at 50 A and we evaluate the maximum modulation with A_y knob scans for each offset Δx and Δy and then we fit it with a parabola. The center of the parabola corresponds to the magnetic center of the octupole. Figure 3.20 shows the scans performed on an error-free lattice. In these scans, we did not include the measurement errors of the IPBSM, and the knobs scans have been performed in the 174° mode of the IPBSM. It is worth noticing that the absolute value of the modulation will change throughout the scan, but it is not critical for the alignment as long as it is reasonable for the fit. When we include the IPBSM measurement errors, they will impact the efficiency of the alignment, especially if we consider a realistic machine. Figure 3.21 shows the octupole alignment in 30° and 174° modes of the IPBSM. Before performing the octupole alignment, the vertical beam size was tuned to approximately 100 nm in 30° mode and to approximately 30 nm in 174° mode. Previously, we have performed all the octupole alignment scans using the "ultra-low" knobs. The results using the "nominal" knobs are shown in Fig. 3.22.

Besides, we need to keep in mind the amount of time required to perform such an

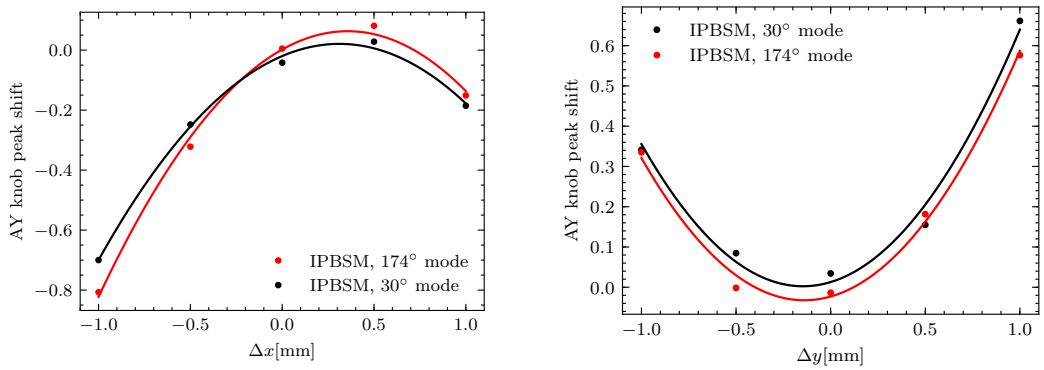

(a) (b)

Figure 3.21: Simulation of the OCT2FF alignment in the horizontal (a) and vertical (b) planes using the waist shift at the virtual IP, including the static and IPBSM measurement errors. The "ultra-low" knob A_y is used in the scan.

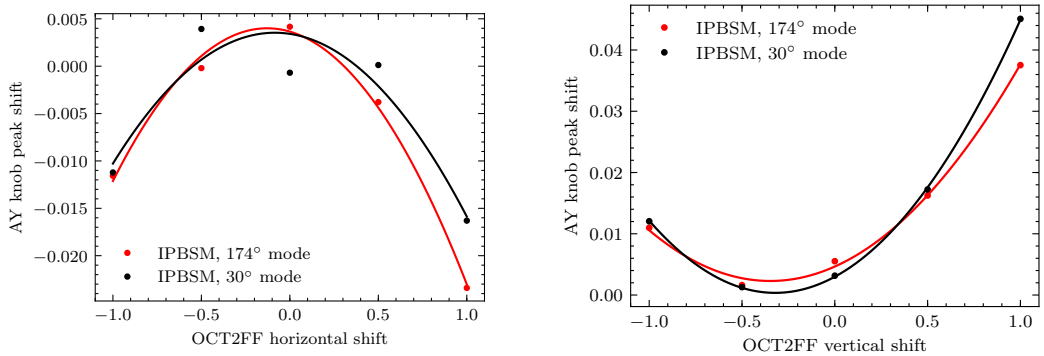

(a) (b)

Figure 3.22: Simulation of the OCT2FF alignment in the horizontal (a) and vertical (b) planes using the waist shift at the virtual IP, including the static and IPBSM measurement errors. The "Nominal" knob A_y is used in the scan.

alignment. Since one knob scan takes approximately 30 minutes, and we require at least 5 points to estimate the magnetic center, the minimum amount needed to perform the octupole alignment is 5 hours. Another aspect is that it could be difficult to perform this with the nominal optics. Table 3.9 shows the vertical beam size at the virtual IP for several configurations of OCT2FF. One can see that in the case of the nominal optics, the octupole increases the beam size greatly when moved in the vertical direction. This means that even in the case of a well-tuned beam, the modulation in 174° mode may vanish when we switch on OCT2FF. One can solve it by either performing the scan in 30° mode or by using the octupole at lower currents, but in this case, the sensitivity of the waist shift will reduce.

		$25\beta_x^* \times 0.25\beta_y^*$	$10\beta_x^* \times 1.0\beta_y^*$
	$(\Delta x, \Delta y)$ [mm]	σ_y^* [nm]	
OCT2FF off	-	35.7	37.3
	(0, 0)	26.6	68.7
	(1, 0)	79.9	95.1
OCT2FF on	(-1, 0)	90.5	85.6
	(0, 1)	67.3	333.6
	(0, -1)	66.3	334.7

Table 3.9: Vertical beam size at the virtual IP evaluated for ultra-low and nominal optics for several octupole offsets.

3.5 Experimental beam size tuning of the ultra-low $25\beta_x^* \times 0.25\beta_y^*$ optics at ATF2

In this section, we present the results of the dedicated ultra-low β_y^* tuning campaigns carried in June 2019, December 2019, and March 2020.

3.5.1 June 2019

The ultra-low β_y^* optics applied in June 2019 is similar to $25\beta_x^* \times 0.25\beta_y^*$ optics used in March 2019 [89] tuning operation. The detailed view of the activities during the tuning week is shown in Tab. 3.10. After the DR tuning, the vertical emittance was evaluated $\epsilon_y \approx 12$ pm for the intensity of 1.5×10^9 particles per bunch. Further, we reduced the dispersion in the Multi-OTR region and we performed the emittance measurements. Although we scanned the skew quadrupoles QK2X, QK4X, the vertical emittance measured with the Multi-OTR remained almost two times larger than the emittance in the DR, $\epsilon_y = 22.3 \pm 0.5$ pm. In the further optics matching, we relied on the measurements in the DR due to the a possible emittance overestimation by the Multi-OTR. Typically, when correcting the orbit, we aim to minimize the BPMs readings to be less than 300 μm with respect to the target orbit.

We kept the same reference orbit that was used in the beam tuning with the nominal optics the week before. We also kept the same sextupole BBA settings. After the beam orbit adjustment, we corrected the horizontal and vertical dispersion with QF1X-QF6X and QS1X-QS2X quadrupole pairs, respectively. To measure the beta-function at the IP, we perform strengths scans of QF1FF and QD0FF. Based on that data, we perform the optics matching.

Table 3.10: Summary table of June 2019 ultra-low β_y^* tuning campaign, indicating each allocated shift. The highest modulation, and consequently smallest vertical beam size achieved in the corresponding shift are also indicated.

Date	Shift	Activity	Comments	Measurements			
				β_x^* [mm]	β_y^* [μm]	M	σ_y^* [nm]
Mon 17.06	Day	Startup and DR tuning	-	-	-	-	-
	Swing	Measurements and tuning of vertical emittance with Multi-OTR; dispersion correction	-	-	-	-	-
Tue 18.06	Owl	Optics matching; evaluation of $\beta_{x,y}^*$; linear knobs tuning with Carbon Wire	Problem with SF1 mover	91.9	28.6	-	∼1500
	Day	IPBSM setup and switch to 6.4° mode; linear knobs tuning	-	-	-	0.58	787
	Swing	Beam tuning with linear knobs in 6.4° and 30° modes; attempt to switch to 174° mode	Switch to 174° mode not successful	-	-	0.57	150
Wed 19.06	Owl	Beam tuning with linear and nonlinear knobs in 30° mode	-	-	-	0.70	107
	Day	IPBSM was switched to 174° mode; beam tuning with linear and nonlinear knobs	-	-	-	0.35	61
	Swing	Beam tuning in 174° mode; scans of the QK2X, and QK3X; consecutive modulation evaluations	-	-	-	0.50	50
Thu 20.06	Owl	Beam tuning in 174° mode; switch to 30° mode to verify modulation	At the start of shift modulation sudden dropped to 0.2 in 174° mode	-	-	0.2	76
	Day	Intensity dependence measurements at 30° mode	-	-	-	0.61	137
	Swing	Beam tuning in 30° mode; switch and beam tuning in 174° mode; intensity dependence scan in 174° mode	Position readout error of the normal sextupoles encountered	-	-	0.4	57
Fri 17.06	Owl	Beam tuning in 174° mode		-	-	0.37	60
	Day	Beam tuning in 174° mode; attempt align octupoles; energy bandwidth scans at 30° mode	-	-	-	0.37	60

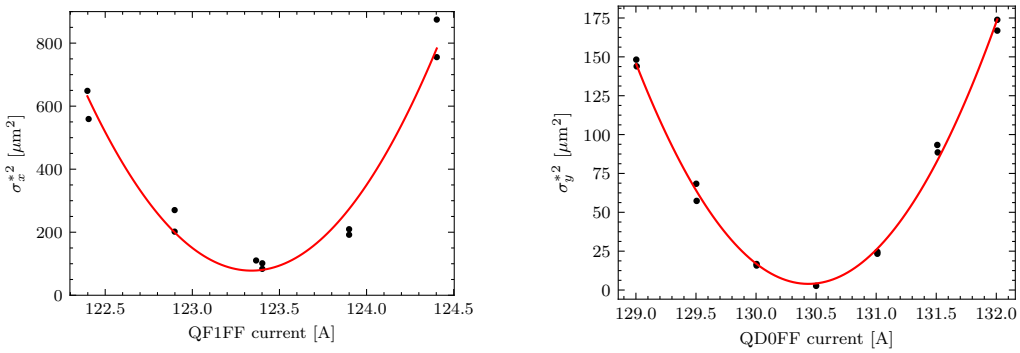

(a) (b)

Figure 3.23: QF1FF (a) and QD0FF (b) waist scans performed during the tuning campaign in June 2019.

Before the matching, we had $\beta_x^* \approx 125$ μm and $\beta_y^* \approx 34.7$ μm, and after the matching we got $\beta_x^* \approx 93$ μm and $\beta_y^* \approx 28.6$ μm. In the calculations we assume, the vertical emittance to be $\epsilon_y \approx 12$ pm. In Fig. 3.23, there are shown the strength scans performed after the optics re-matching. After the fine adjustment of the IPBSM laser, we proceeded to the beam tuning with the tuning knobs. The modulation was easily found in 6.4° mode, and after several iterations of the linear knobs, we proceeded to the beam tuning in 30° mode. The full progress of the beam size throughout the tuning is shown in Fig. 3.24. By using the linear knobs and nonlinear knobs Y_{24} and Y_{46} the modulation was increased to M = 0.65 in 30° mode, and we successfully switched to 174° mode of the IPBSM. After the numerous iterations of the tuning knobs, the vertical beam size was stabilized at the level of approximately 60 nm, with a minimum of 50.1 ± 0.6 nm, see Fig. 3.26. The distribution of the beam size can be justified by the IPBSM measurement error of 8 nm in 174° mode and by the dynamic effects in the beamline. To reduce the impact of the IPBSM precision in the beam tuning, the modulation is measured twice for each knob value. The fringe scan evaluated for the smallest beam size is shown in Fig. 3.25. The discrepancies between the measured and design beam size concerning June 2019 tuning operations are discussed in [33].

At the end of the beam tuning, we tried to investigate the impact of the octupoles on the vertical beam size. In the simulations, it allows canceling the 3$^{\text{rd}}$ order chromatic aberrations. Unfortunately, we were not able to perform the OCT1FF alignment with IPBPMs, so we performed a similar study as in [20]. We evaluated the change of the modulation as the function of the horizontal offset, see Fig. 3.27. Moreover, we did not manage to evaluate the similar dependence for the set of the vertical offsets due to the OCT1FF overheating interlock. We also scanned the dependence of the modulation on the current in OCT1FF, see Fig. 3.28. We observe a significant modulation reduction for

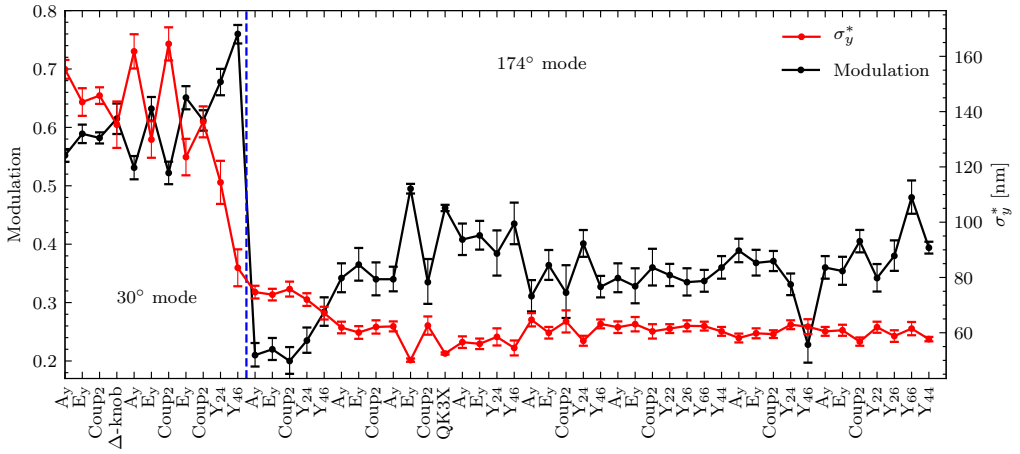

Figure 3.24: Vertical beam size at the virtual IP and IPBSM's modulation depth during the beam tuning with tuning knobs, performed in June 2019 tuning campaign.

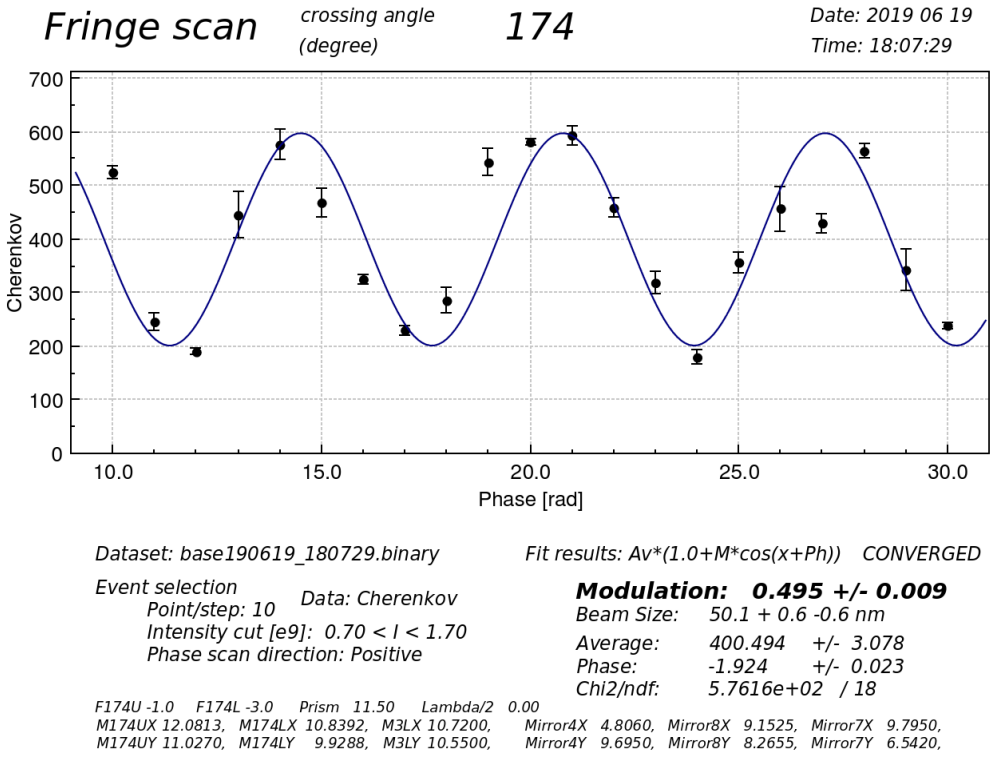

Figure 3.25: Vertical beam size at the virtual IP measured with the Shintake Monitor in 174° in June 2019 ultra-low β_y^* tuning operation.

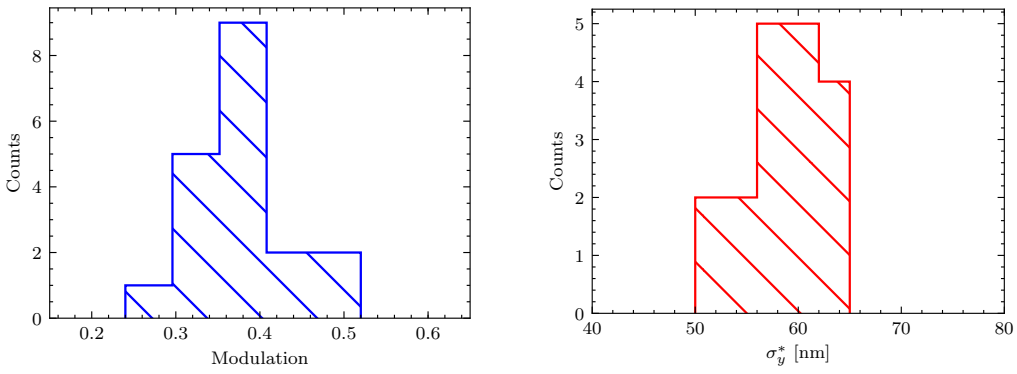

(a) (b)

Figure 3.26: Distribution of 20 consecutive measurements with the IPBSM performed in 174° mode during June 2019 tuning operation.

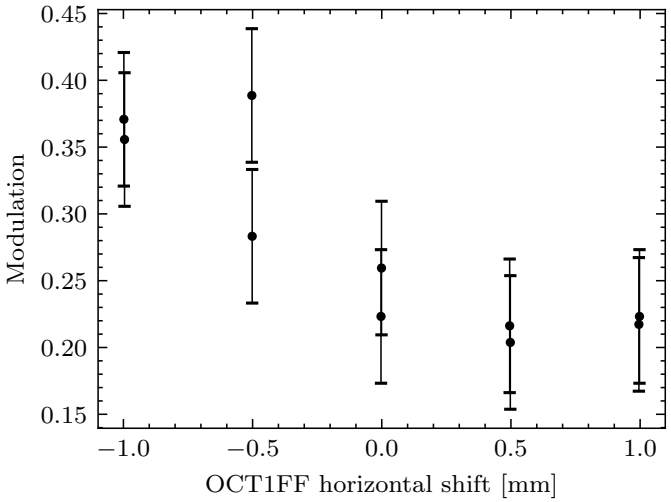

Figure 3.27: Vertical beam size at the virtual IP as the function of the horizontal of OCT1FF performed at 174° mode in June 2019. For the scan OCT1FF was set to the maximum current (50 A).

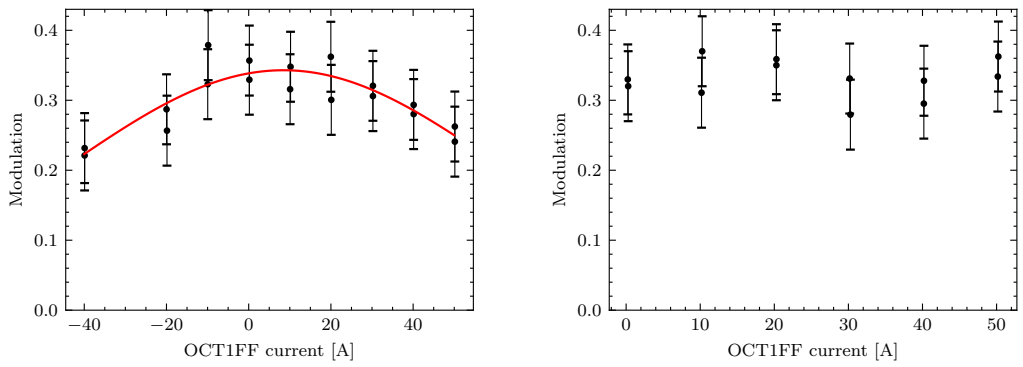

(a) (b)

Figure 3.28: Dependence of the modulation at the IPBSM in 174° mode on the OCT1FF current for original location (a) and when OCT1FF is misaligned by 1 mm in the horizontal plane (b).

the original OCT1FF location. After, we also performed the strength scan, with OCT1FF misaligned by $\Delta x = 1$ mm. In the latter the modulation is somewhat stable in the range of M $\approx$ 0.3 - 0.4. This could indicate that the magnetic center of the octupole is close to the beam orbit. In this case, the beam size reduction might not be visible. As evaluated in the beam tuning simulations in Sec. 3.3, the impact of the octupoles for $25\beta_x^* \times 0.25\beta_y^*$ starts to be visible when the IP vertical beam size is tuned at least to 30 nm. Also, the overall beam size reduction of 2.5 nm might be problematic, considering the dynamic errors and IPBSM measurement errors. But this study is important for the future implementation of $\beta_x^* \times 0.25\beta_y^*$ optics. The difficulties associated with the alignment of the octupoles encountered here led us to explore the alternative alignment techniques discussed in Sec. 3.4.

3.5.2 December 2019

After the startup, the beam tuning in the DR was performed. Vertical emittance was evaluated $\epsilon_y = 14.5$ pm. Similarly, to June 2019 operation, the optics used was $25\beta_x^* \times 0.25\beta_y^*$. The full list of the shifts is given in Tab. 3.11. After the orbit adjustment and dispersion matching with $\sum$-knob and QF1X and QF6X, we proceeded to the vertical beam size measurements at the virtual IP. The reference orbit utilized was the one from the beam tuning of the Nominal optics. Based on the, we also keep the similar BBA alignment setup of the normal sextupoles.

Table 3.11: Summary table of December 2019 Ultra-low β_y^* tuning campaign, indicating each allocated shift. The highest mudulation, and consequently smallest vertical beam size achieved in the corresponding shift are indicated.

Date	Shift	Activity	Comments	Measurements

				β_x^* [mm]	β_y^* [μm]	M	σ_y^* [nm]
Mon 09.12	Day	Startup	-	-	-	-	-
	Swing	DR tuning; orbit correction in the extraction line	QM14 reading jumps	-	-	-	-
Tue 10.12	Owl	Bunch length dependence study	-	-	-	-	-
	Day	Orbit and dispersion corrections; optics matching		70	19	-	-
	Swing	Optics matching	-	117	27	-	-
Wed 11.12	Owl	Beam tuning with linear knobs with Carbon Wire; IPBSM setup; beam tuning in 6.4° mode; beam tuning in 30° mode	Horizontal orbit and dispersion drifts encountered	-	-	0.31	234
	Day	Beam tuning in 30° mode; dispersion and orbit corrections	Modulation in 30° mode was not stable	-	-	0.49	175
	Swing	Beam tuning in 30° mode; dispersion and orbit corrections	Fast orbit drifts encountered in the FFS	-	-	0.61	138
Thu 12.12	Owl	Beam tuning in 30° mode; attempt to switch to 174° mode	Switch to 174° mode was not successful	-	-	0.6	140
	Day	Dispersion correction; Beam tuning in 30° mode	Orbit feedback routine was modified to fix fast orbit drifts	-	-	0.72	99
	Swing	Beam tuning in 30° mode; attempts to switch to 174° mode		-	-	0.4	57
Fri 13.12	Owl	Beam tuning in 174° mode		-	-	0.37	60
	Day	Octupole alignment in 30° mode	-	-	-	-	-

With the wire scanner, the optics was matched to the target values, see the final waist scans of QF1FF and QD0FF in Fig. 3.29. Evaluated beta-functions are the following $\beta_x^* = 117$ mm and $\beta_y^* = 28$ μm, assuming the vertical emittance is $\epsilon_y = 14.5$ pm. The sextupoles were switched on and after several iterations of the linear knobs in 6.4° mode of the IPBSM, we switched to 30° mode, see Fig. 3.31 for the full beam tuning results. After several iterations of the linear and nonlinear tuning knobs, we increased the modulation to the level M $\geq$ 0.55, but it was not stable and could change in the wide region. In December 2019, tuning operations, we observed fast orbit drifts, with the period at the level of several minutes, see Fig. 3.30. It led to a sudden orbit change in the region where sextupoles are located, and the slow orbit feedback that utilizes ZV1FBFF could not correct such drifts. It had a direct impact on the beam size measured with the IPBSM due to the sextupoles being located in the region of the maximum of the orbit drift. Figure 3.32 shows the modulation depth and vertical beam size for 25 consecutive measurements with the IPBSM in 30° mode. The measured beam size, in this case, varies from 165 nm to 300 nm. It contrasts with the results obtained in June 2019 tuning campaign, where the

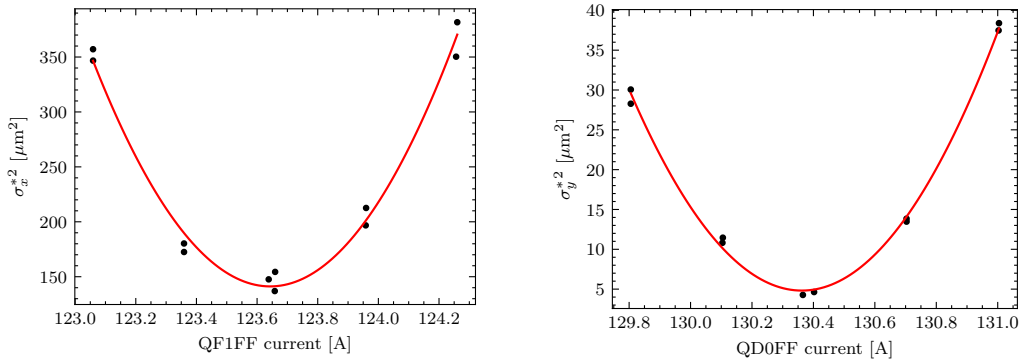

(a) (b)

Figure 3.29: QF1FF (a) and QD0FF (b) waist scans performed at the end of the optics matching during the tuning campaign in December 2019.

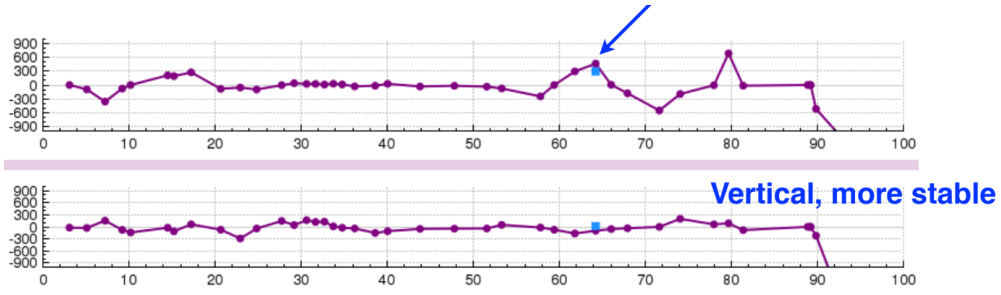

Figure 3.30: Fast horizontal orbit drifts measured during December 2019 tuning operation.

vertical beam size remained between 50 and 65 nm in 174° mode. In the following case, such a distribution cannot be described solely with the IPBSM measurement error, which is around 20 nm in 30° mode. Consequently, it was not possible to perform beam tuning in 174° mode. However, we managed to perform several measurements with modulation of M $\approx$ 0.3, which corresponds to the beam size of approximately 66 nm, see Fig. 3.33.

In December 2019 operations, we made the first attempt to perform the Octupole alignment, based on the waist shift, introduced in Sec. 3.4. Before starting the alignment procedure, the modulation was M $\approx$ 0.6 in 30° mode of IPBSM. We switched on OCT2FF and set it to the maximum current (50 A). After, we misalign OCT2FF in the horizontal plane in the range $\pm$ 1 mm with the step of 0.33 mm. For each offset, we perform A_y knob scan and evaluate the location of the peak, see Fig. 3.34. After, a similar procedure was performed in the vertical plane. Then, we apply the parabolic fit and evaluate the magnetic center of OCT2FF, see Fig. 3.35. It evaluated as $\Delta x = -161 \pm 57$ μm and $\Delta y = 128 \pm 108$ μm. The result is similar to what is predicted in the simulations, see Fig. 3.22.

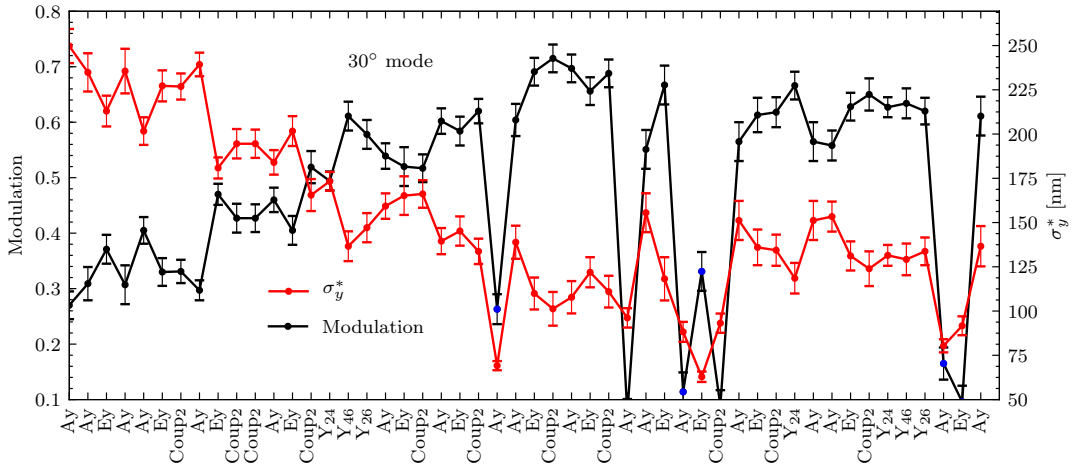

Figure 3.31: Vertical beam size at the Virtual IP and IPBSM's modulation depth progress during the beam size tuning performed in December 2019 tuning campaign. Blue points correspond to the measurements performed in 174° mode of IPBSM.

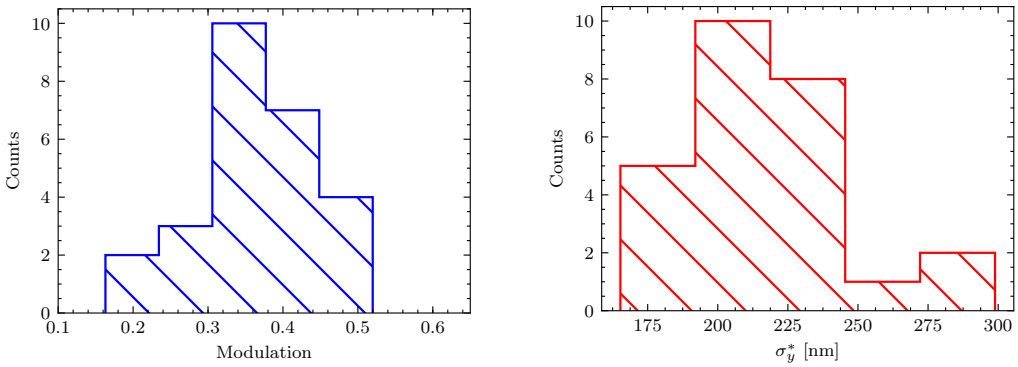

(a) (b)

Figure 3.32: Distribution of 25 consecutive measurements of the vertical beam size with the IPBSM performed in 30° mode during December 2019 tuning operation.

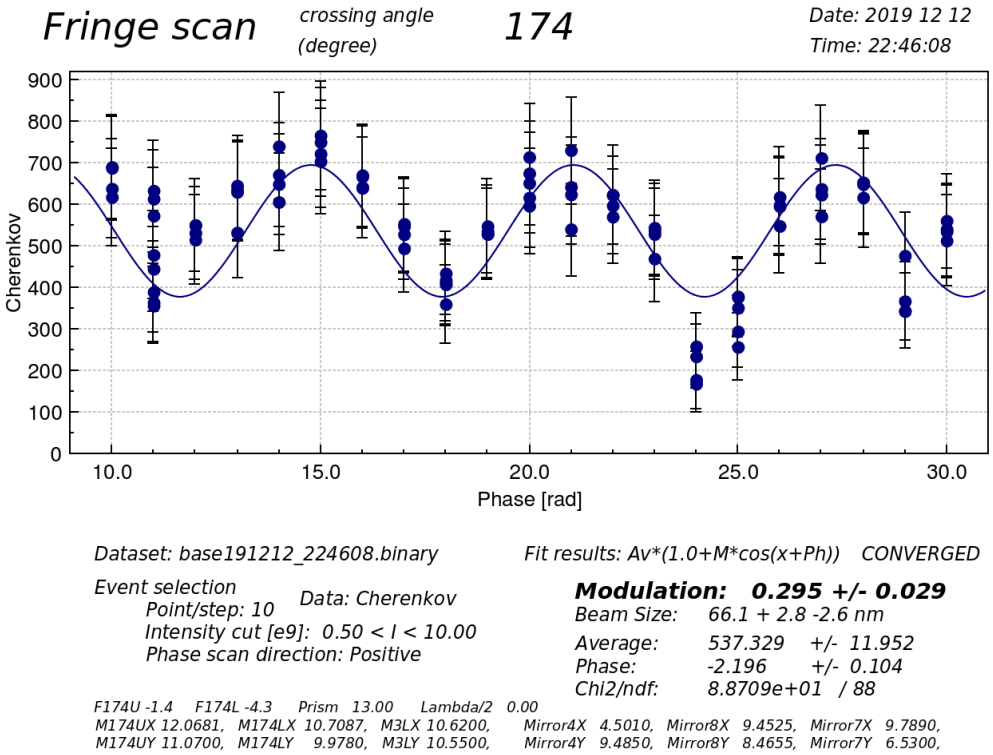

Figure 3.33: Vertical beam size at the Virtual IP measured with Shintake Monitor performed in 174° mode in December 2019 Ultra-low β_y^* tuning operation.

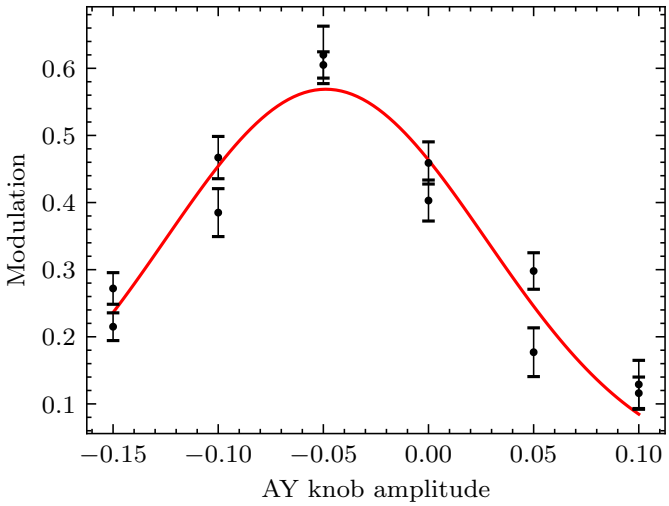

Figure 3.34: A_y knob scan performed with IPBSM at 30° mode when OCT2FF is misaligned by 1 mm in the vertical plane, performed in December 2019 operation. The A_y knob value that maximizes the modulation is estimated to -0.05.

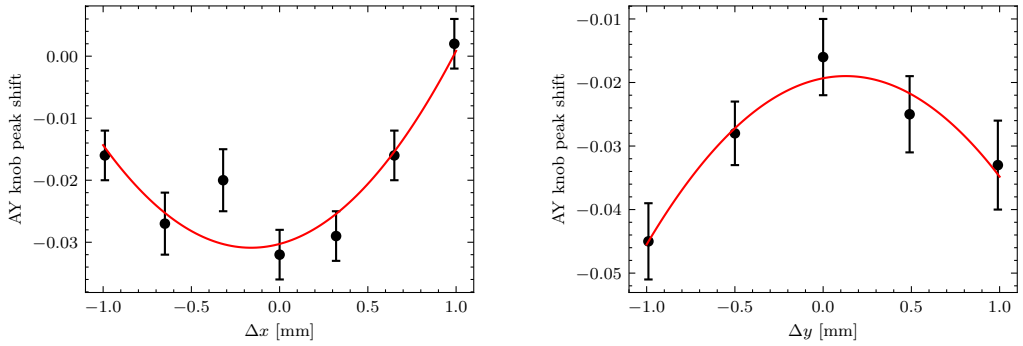

(a) (b)

Figure 3.35: Waist shift measurements at the Virtual IP for horizontal (a) and vertical (b) displacements of OCT2FF performed in December 2019 tuning operation.

3.5.3 March 2020

Similarly, to the previous ultra-low β_y^* operations, the optics $25\beta_x^* \times 0.25\beta_y^*$ was applied. After the initial beam tuning in the DR, the vertical beam emittance measured was approximately 13 pm. After orbit correction and adjusting the dispersion in the Multi-OTR region, ϵ_y measured by the Multi-OTR was 16.76 ± 2.83 pm. Further, we corrected the dispersion in the whole FFS and performed the optics matching by utilizing the matching quadrupoles. The orbit drift encountered in December 2019 tuning operation was partially suppressed by increasing the response frequency of the slow orbit correction with ZX2X and ZV1FBFF. The measured β_x^* and β_y^* are obtained by performing the QF1FF and QD0FF strength scans. Fig. 3.36 shown such scans, performed at the end of the optics matching. The horizontal beta-function was evaluated as $\beta_x^* \approx 97$ mm, and the vertical divergence was $\epsilon_y/\beta_y^* \approx (5.28 \pm 0.06) \times 10^{-7}$. Based on the vertical emittance data from the Multi-OTR, the vertical beta-functions is $\beta_y^* \approx (31.7 \pm 5)\mu$m. Further, normal sextupoles were switched on and the BBA was performed. After, we proceeded to the vertical beam size tuning with the tuning knobs. In March 2020 operation, we used the new tuning knobs, constructed for ultra-low β_y^* optics, described in Sec. 3.2. In Figs. 3.37 and 3.38 are shown the scans of the linear (A_y, E_y, $Coup_2$) and nonlinear (Y_{24}, Y_{46}, Y_{22}, Y_{26}, Y_{44}, Y_{66}) knobs performed during the beam size tuning.

Table 3.12: Summary table of March 2020 Ultra-low β_y^* tuning campaign, indicating each allocated shift. The highest modulation, and consequently smallest vertical beam size achieved in the corresponding shift are also indicated.

Date	Shift	Activity	Comments	Measurements			
				β_x^* [mm]	β_y^* [μm]	M	σ_y^* [nm]
Mon 02.03	Day	Startup; ATF2 orbit feedback study	-	-	-	-	-
	Swing	DR tuning	-	-	-	-	-

Tue 03.03	Owl	Vertical emittance measurement with Multi-OTR; orbit and dispersion correction; optics matching		97	32	-	-
	Day	Sextupoles BBA	-	-	-	-	-
	Swing	Beam size tuning with linear knobs using Wire scanner; attempt to switch to 6.4° mode	No clear modulation in 6.4° mode was found	108	27	-	∼800
Wed 04.03	Owl	Beam tuning in 6.4° mode; beam tuning in 30° mode	Cavity BPM reading was not stable due to the timing jumps; IPBSM interface crushed around 10 times during the shift	-	-	0.49	175
	Day	Beam tuning in 30° mode; attempt to switch to 174° mode	No clear modulation in 174° mode was found	-	-	0.54	160
	Swing	Dispersion correction; beam tuning in 30° mode	Once, high modulation (∼ 0.79) in 30° mode was obtained, but soon after it was lost	-	-	0.54	160
Thu 05.03	Owl	Beam tuning in 30° mode; beam size consecutive measurements; Attempt to measure beam size in 174° mode	Modulation in 174° mode was not stable	-	-	0.19	77
	Day	Beam tuning in 30° mode; Attempt to switch to 174° mode	No clear modulation in 174° mode was found	-	-	0.53	161
	Swing	Beam tuning in 30° mode; attempts to switch to 174° mode	Modulation in 174° mode was not stable	-	-	0.21	75
Fri 06.03	Owl	Octupole alignment studies with IPBSM at 30° mode	-	-	-	0.6	140
	Day	Octupole alignment studies with IPBSM at 30° mode; energy bandiwdth studies	-	-	-	0.58	146

The evolution of the vertical beam size throughout the machine tuning is shown in Fig. 3.40. Large modulation (M $>$ 0.6) was quickly found in 6.4° mode of the IPBSM, and after 6 iterations of the linear knobs, we switched to 30° mode. After several iterations of the linear knobs, modulation was stabilized at the level M $\geq$ 0.5. We performed four attempts to measure the modulation in 174° mode, but they were not successful. Although we managed to measure the small modulation at the level M $\approx$ 0.19 (see Fig. 3.39), but it was not stable enough to perform knobs tuning. The fringe scan of the largest modulation M = 0.65, measured in 30° mode is shown in Fig. 3.41. It corresponds to the vertical beam size of approximately 125 nm. In this operation, we also tested the new octupole alignment

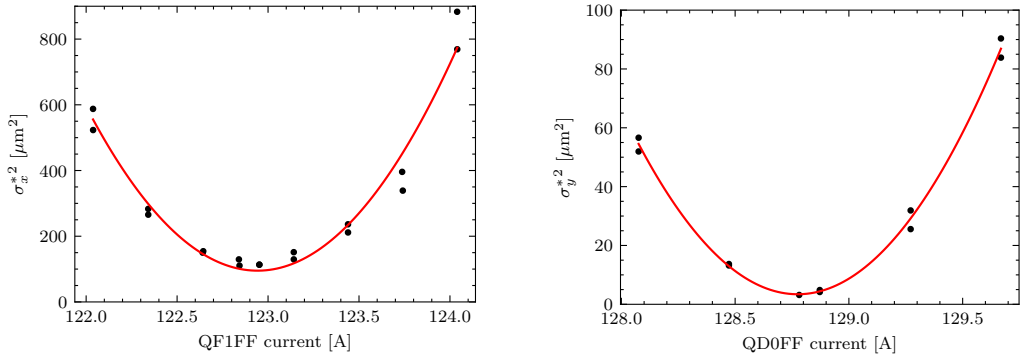

(a) (b)

Figure 3.36: QF1FF (a) and QD0FF (b) waist scans performed during the tuning campaign in March 2020.

technique based on the waist shifts. Before performing the alignment, the modulation was stable at the level M $\approx$ 0.5 in 30° mode. The magnetic center was found at $\Delta x = 87 \pm 135$ μm and $\Delta y = 78 \pm 49$ μm.

3.6 Discussion on the measurements

Three ultra-low β_y^* tuning campaigns are reported in this thesis: the June 2019, the December 2019, and the March 2020. The minimum beam size obtained in these operations combined with the earlier tuning campaigns is shown in Fig. 3.43, including the tuning campaigns carried out in the dedicated ultra-low β_y^* tuning weeks. We could conclude from these results, that June 2019 operation was the most successful among them, with a vertical beam size tuned to approximately 50 nm. Except for the February 2018 tuning run, when the beam tuning was not finished due to the lack of time, the rest tuning campaigns mainly suffered from unstable modulation conditions in the 174° mode of the IPBSM, either no evidence of modulation or not stable enough to perform the tuning knob scans. But for all of them, modulation of at least 0.6 in 30° mode was reached.

Although the small beam size of 50 nm was reached in June 2019, this value is significantly larger than the design beam size of 20 nm or the simulated beam size of: 26 nm (with only static errors) or 34 nm (with static errors and IPBSM measurement error). The discrepancy, as discussed in [33], could be due to: magnets multipolar errors, wakefields, beam jitter, and IPBSM diagnostics errors. Besides, various technical limitation were encountered during the beam tuning that limited the use of the 174° mode of the IPBSM, as the orbit feedback and the BPM readout system. Fast orbit drifts were clearly observed during December 2019 tuning operation. The slow orbit feedback system, to flatten the beam orbit at BPMs, was not effective with the fast orbit drifts. This also led to fluctuation of the modulation measured with the IPBSM. Further, the timing jumps in the C-BPMs readout system make the orbit data in some of the C-BPM to be untrustworthy.

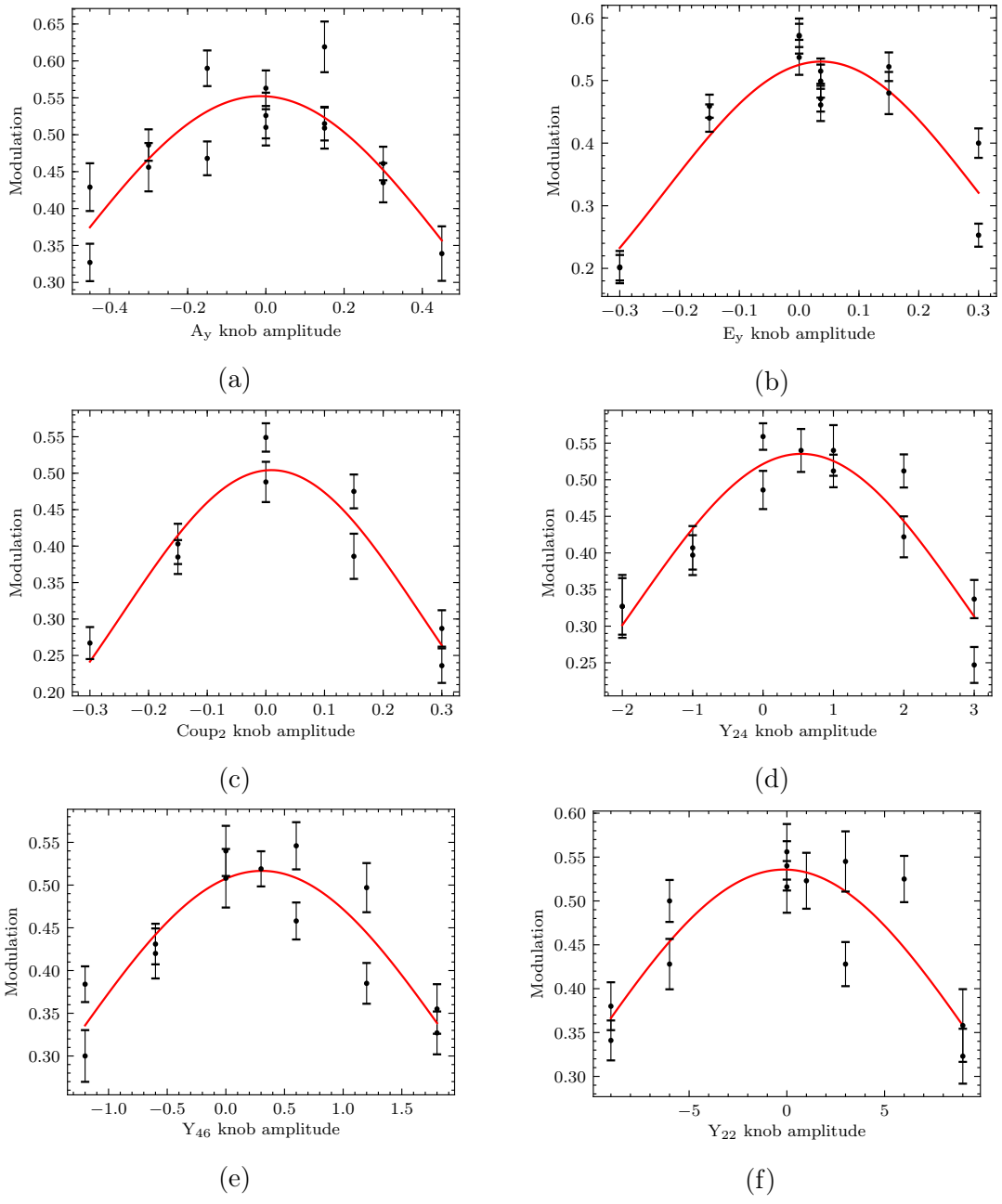

Figure 3.37: "Ultra-low" knobs scans performed in 30° mode of the IPBSM during the tuning campaign in March 2020.

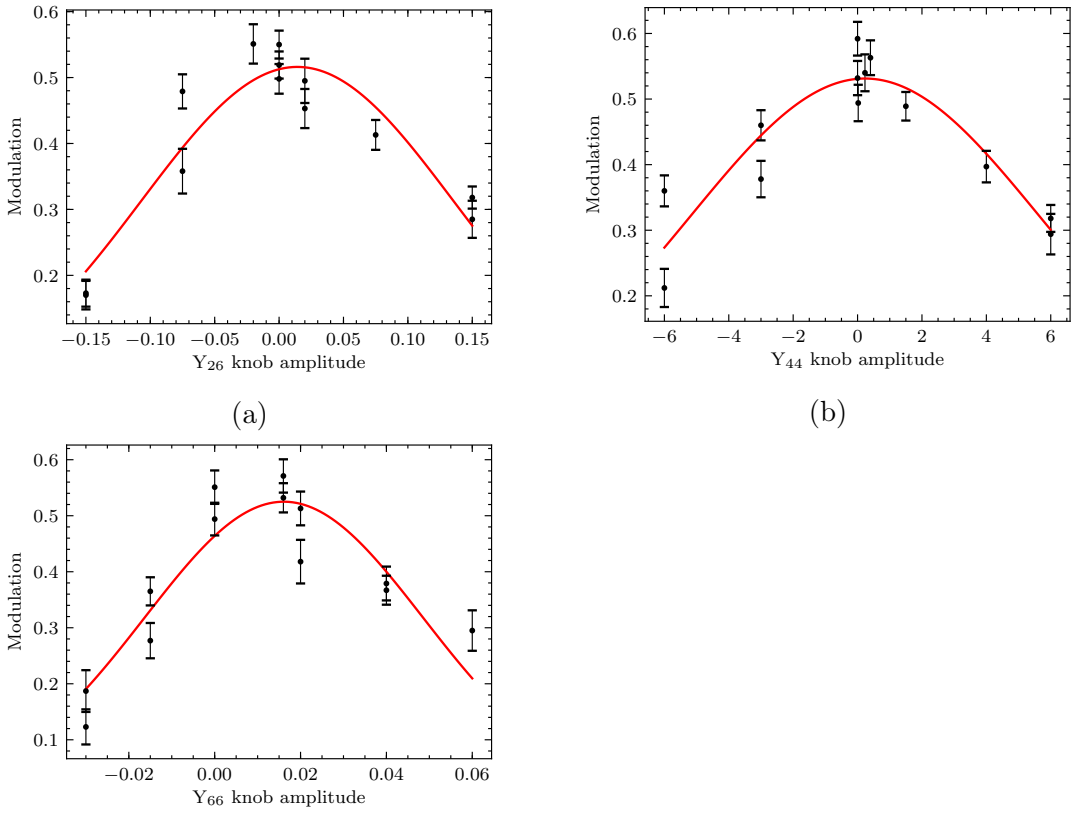

Figure 3.38: "Ultra-low" knobs scans performed in 30° mode of IPBSM during the tuning campaign in March 2020.

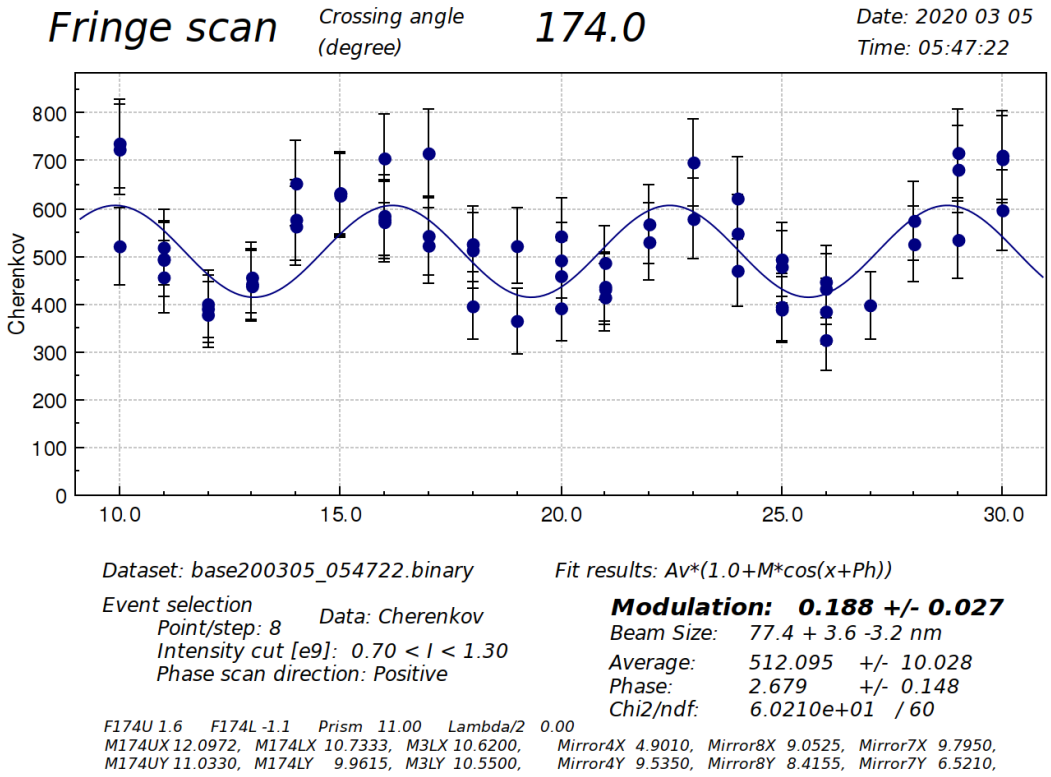

Figure 3.39: Vertical beam size at the virtual IP measured with Shintake monitor in 174° mode during March 2020 Ultra-low β_y^* tuning operation.

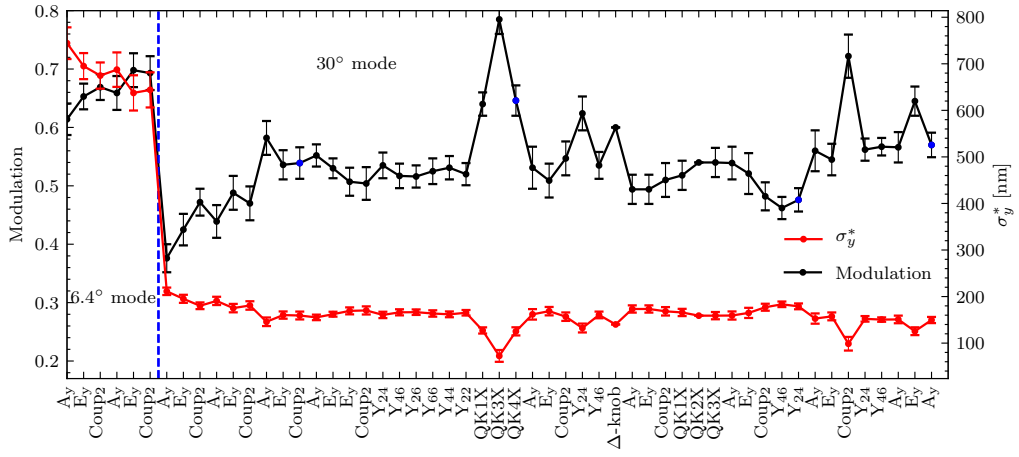

Figure 3.40: Vertical beam size at the Virtual IP and IPBSM's modulation depth during the beam size tuning performed in March 2020 tuning campaign. Blue points indicate the tuning knob scans after which the attempts to switch to 174° mode of IPBSM were performed.

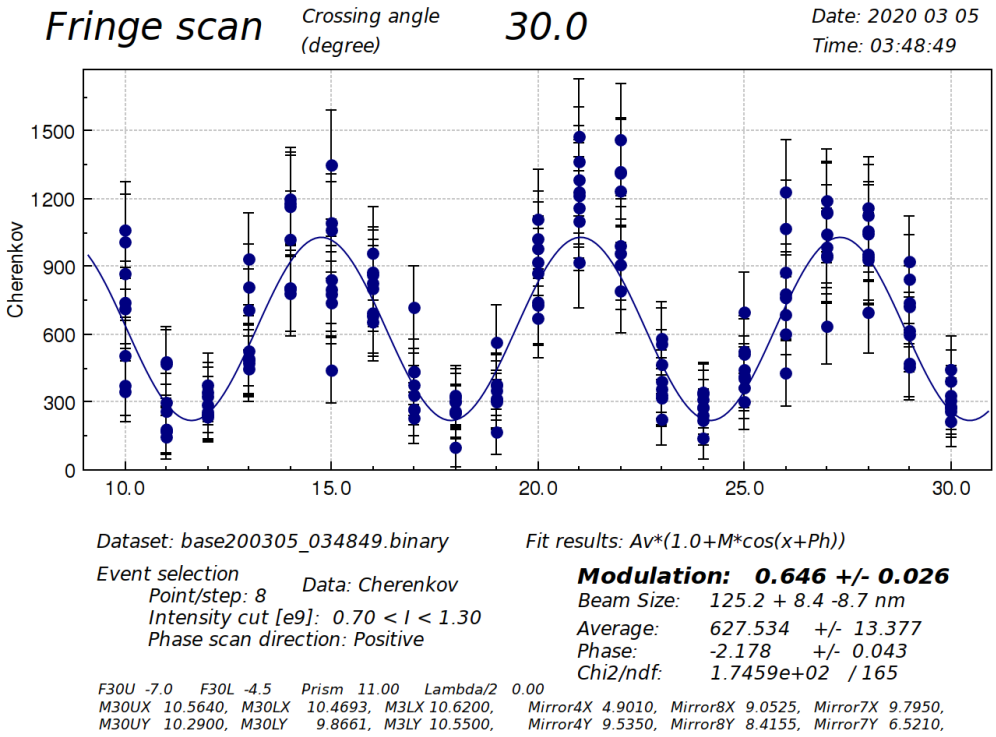

Figure 3.41: Vertical beam size at the Virtual IP measured with Shintake Monitor in 30° mode in March 2020 Ultra-low β_y^* tuning operation.

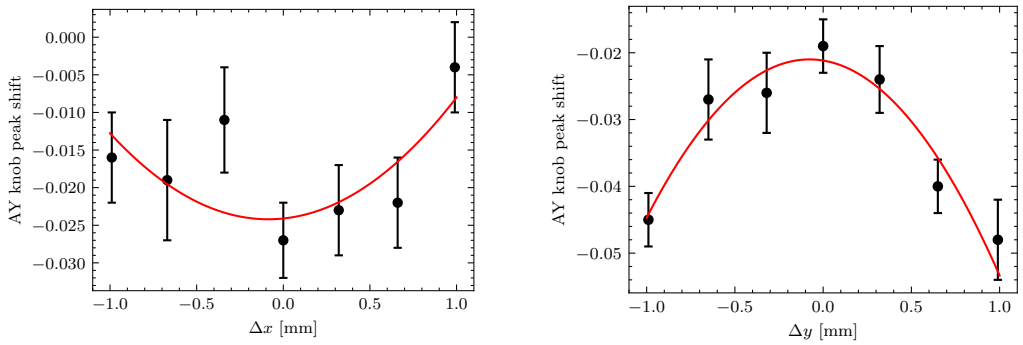

(a) (b)

Figure 3.42: Waist shift measurements at the Virtual IP for horizontal (a) and vertical (b) displacements of OCT2FF performed in March 2020 tuning operation.

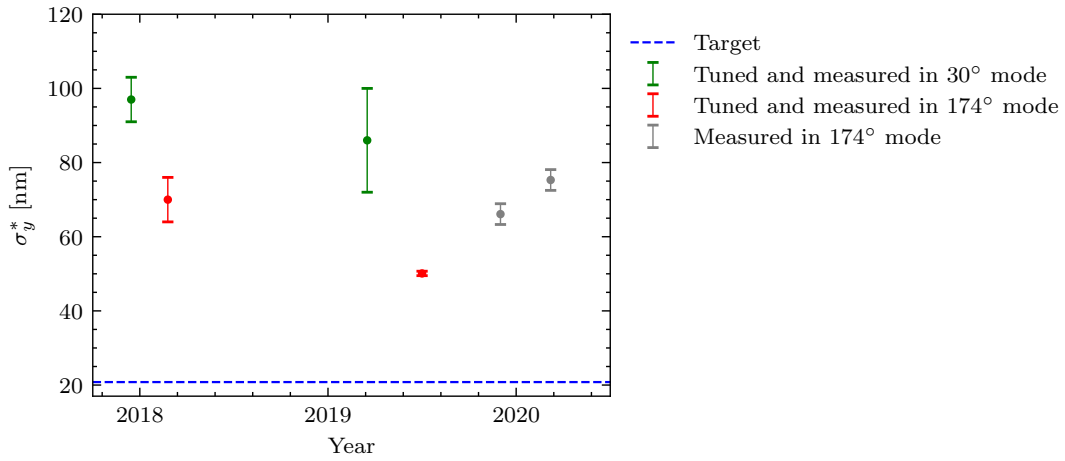

Figure 3.43: Minimum vertical beam size at the Virtual IP achieved in the tuning of ultra-low $25\beta_x^* \times 0.25\beta_y^*$ optics from December 2017 to March 2020. Green points correspond to the measurements performed in 30° mode of IPBSM. Red points correspond to the measurements in 174° mode with stable modulation (the beam tuning was also performed in 174° mode). Grey points correspond to the measurements in 174° mode but without stable modulation (the beam tuning in 174° mode was not performed). The blue dashed line corresponds to the design beam size. In all cases, the beam size was measured for a bunch charge of about $1{\times}10^9$.

In March 2020, we used the new set of the tuning knobs, specially constructed for $25\beta_x^* \times 0.25\beta_y^*$ optics. These new tuning knobs proved to be more robust for the beam tuning in 6.4° and 30° modes and look promising for the beam tuning in 174° mode. The octupole alignment using the new waist shift method was performed twice in December 2019 and March 2020 operations. The magnetic center locations of OCT1FF evaluated in these operations are consistent. To explore the octupoles' potential, a stable performance of 174° mode of IPBSM is needed.

In the next future, addressing the beam orbit stability issue in the FFS and the improvement of the IPBSM performance are the key points required for the a future successful realization of the ultra-low β_y^* optics at ATF2.

Chapter 4

Conclusions

This PhD work has two main objectives. The first one is to understand the optimization process of the FFS in LCs analytically and numerically by simulations. A procedure has been developed and applied to CLIC, but could be used for ILC as well. The second objective is the experimental implementation of these ideas in ATF2 tunability studies.

More in detail, a new optics design of the FFS with Short FD and with a novel dispersion profile for the first energy stage of CLIC at 380 GeV has been designed. The FD in the CLIC FFS at 380 GeV was made two times shorter in the new design. In this case, the impact of the FD chromaticity and the beta-function in the FFS due to the reduction of vertical beta-function from 100 μm to 70 μm was reduced. The FFS optics was fully reoptimized to provide the designed luminosity. Additional changes in the FFS layout were required to preserve the local chromaticity correction scheme. The luminosities achieved for this design are $\mathcal{L}_{total} = 1.66\times10^{34}\text{cm}^{-2}\text{s}^{-1}$ and $\mathcal{L}_{peak} = 0.96\times10^{34}\text{cm}^{-2}\text{s}^{-1}$. Due to the reduced β_y, the 3^{rd} order chromatic aberrations are not significant, and octupoles are no longer needed. Also, the energy bandwidth is 30% larger with respect to the current design. Besides, an alternative optics with short FD and new dispersion in the FFS has been designed. The new design was obtained by inverting the strength of the QD6B quadrupole. To optimize the FFS, additional layout adjustments were performed, such as a SD5 location scan. To deal with the 4^{th} order chromatic aberrations, 2 decapoles were introduced in the lattice. The scan of the disperion level in the FFS, showed that relaxing the dispersion by 12.5% the luminosities coul be increased to the final values of $\mathcal{L}_{total} = 1.74\times10^{34}\text{cm}^{-2}\text{s}^{-1}$ and $\mathcal{L}_{peak} = 1.01\times10^{34}\text{cm}^{-2}\text{s}^{-1}$. The luminosity performance of this FFS design is at least 5% better compared to the other options. But, the drawback of such an optics is the narrower energy bandwidth. Beam tracking simulations with the new FFS designs show that both optics are compatible with the current collimation depth in the BDS.

To support experimentally the tunability of a CLIC-like FFS with similar chromaticity an ultra-low β_y^* optics has been implemented in ATF2.To reduce the impact of the multipole errors, an optics $25\beta_x\times0.25\beta_y$ has been used in the simulations and during the beam tuning experiments at ATF2. With the aim to optimize the existing tuning routine, a new set of tuning knobs has been constructed. The tuning simulations were performed, assuming

realistic beamline errors and tuning time. Compared to the nominal, the new knobs have a similar median beam size at the end of the tuning of around 26 nm, but the percentage of the machines with the large beam size ($>$ 100 nm) is smaller when tuned with the new knobs: 4 % against 12 %.

Furthermore in 2019, the octupoles were swapped to be more consistent with the design model, where OCT2FF is the strongest in the pair. Two strategies for the OCT2FF alignment routine have been considered: a traditional BBA and a novel technique based on the waist shift at the IP. Simulations have shown that the BBA is difficult to perform due to poor BPM resolution and orbit jitter. The novel technique relies on the waist shift, which misaligned octupole creates at the virtual IP through the feed-down to quadrupole field. In this case, the waist shift is quadratic on the octupole offset and is measured with the A_y ATF2 knob scan. The alignment of the weaker octupole, as concluded in [20] is not possible. Simulations show that such an alignment can be performed both in 30° and 174° modes of the IPBSM. Also, the beam size reduction of the octupoles for $25\beta_x^* \times 0.25\beta_y^*$ optics was evaluated to be 2.5 nm. But, in order to measure that, the beam size has to be tuned down to at least 30 nm.

Three dedicated ultra-low β_y^* optics tuning campaigns have been realized during the PhD in June 2019, December 2019, and March 2020. In June 2019, the beam size was reduced down to 51±6 nm and was stabilized at the level of 60 nm for a long period of time. Unfortunately, 174° mode of the IPBSM was not reached in December 2019 and March 2020, so in both operations, the beam was tuned in 30° mode with the modulation in both cases $M \approx 0.6$. Also, in these tuning sessions, OCT2FF alignment using the waist shift was performed and magnetic center was evaluated to be $(87 \pm 135,\ 78 \pm 49)$ μm in December 2019 and $(-161 \pm 57,\ 128 \pm 108)$ μm in March 2020. In December 2019, machine performance was spoiled by the presence of the fast orbit drifts that could not be compensated with the orbit feedback. The first test of the new tuning knobs was carried out in December 2019, and the whole March 2020 tuning session was done with ultra-low knobs.

To conclude, we can say the results obtained in this thesis contribute to a better understanding of optimizing the complex beamlines, such as the FFS of the linear collider. A contribution made in this thesis has an important role in the successful realization of the Ultra-low β^* optics at ATF2 and reaching the ultimate goal of 20 nm beam size.

List of Figures

List of Tables

Bibliography

[1] M. L. Perl. *The Discovery of The Tau Lepton*, pages 277–302. Springer US, Boston, MA, 1996. Available: https://doi.org/10.1007/978-1-4613-1147-8_15. (Cited on page 1.)

[2] L. Di Lella and C. Rubbia. The Discovery of the W and Z Particles. *Adv. Ser. Dir. High Energy Phys.*, 23:137–163, 2015. Available: https://doi.org/10.1142/9789814644150_0006. (Cited on page 1.)

[3] F. Abe et al. Observation of Top Quark Production in $\overline{p}p$ Collisions with the Collider Detector at Fermilab. *Phys. Rev. Lett.*, 74:2626–2631, Apr. 1995. Available: https://link.aps.org/doi/10.1103/PhysRevLett.74.2626. (Cited on page 1.)

[4] CMS collaboration. Observation of a new boson at a mass of 125 GeV with the CMS experiment at the LHC. *Physics Letters B*, 716(1):30–61, 2012. Available: https://doi.org/10.1016/j.physletb.2012.08.021. (Cited on page 1.)

[5] ATLAS collaboration. Observation of a new particle in the search for the Standard Model Higgs boson with the ATLAS detector at the LHC. *Physics Letters B*, 716(1):1–29, 2012. Available: https://doi.org/10.1016/j.physletb.2012.08.020. (Cited on page 1.)

[6] I. Zurbano Fernandez et al. High-Luminosity Large Hadron Collider (HL-LHC): Technical design report. 10/2020, 12 2020. Available: https://doi.org/10.23731/CYRM-2020-0010. (Cited on page 1.)

[7] European Strategy Group. 2020 Update of the European Strategy for Particle Physics. Technical report, Geneva, 2020. Available: https://doi.org/10.17181/ESU202. (Cited on page 1.)

[8] M. Benedikt, A. Blondel, O. Brunner, M. Capeans Garrido, F. Cerutti, J. Gutleber, P. Janot, et al. FCC-ee: The Lepton Collider: Future Circular Collider Conceptual Design Report Volume 2. Future Circular Collider. Technical report, CERN, Geneva, Dec. 2018. Available: https://doi.org/10.1140/epjst/e2019-900045-4. (Cited on page 2.)

[9] CEPC Study Group. CEPC Conceptual Design Report: Volume 1 - Accelerator. Sep. 2018. Available: https://doi.org/10.48550/arXiv.1809.00285. (Cited on page 2.)

[10] M. Benedikt, M. Capeans Garrido, F. Cerutti, B. Goddard, J. Gutleber, J. M. Jimenez, M. Mangano, et al. FCC-hh: The Hadron Collider: Future Circular Collider Conceptual Design Report Volume 3. Future Circular Collider. Technical report, CERN, Geneva, Dec. 2018. Available: https://doi.org/10.1140/epjst/e2019-900087-0. (Cited on page 2.)

[11] M. Aicheler, P. Burrows, M. Draper, T. Garvey, P. Lebrun, K. Peach, N. Phinney, et al. *A Multi-TeV Linear Collider Based on CLIC Technology: CLIC Conceptual Design Report*. CERN Yellow Reports: Monographs. CERN, Geneva, 2012. Available: https://doi.org/10.5170/CERN-2012-007. (Cited on pages 2, 4, 5, 6, 8, and 10.)

[12] C. Adolphsen et al. The International Linear Collider Technical Design Report. Technical report, Geneva, Jun. 2013. Available: https://cds.cern.ch/record/1601969. (Cited on pages 2, 6, 7, and 67.)

[13] R. K. Ellis et al. Physics Briefing Book: Input for the European Strategy for Particle Physics Update 2020. Oct. 2019. Available: https://doi.org/10.48550/arXiv.1910.11775. (Cited on page 3.)

[14] O. Napoly. Beam Delivery System and Beam-Beam Effects. Beijing, China, 2009. Available: https://agenda.linearcollider.org/event/3475/contributions/13202/attachments/10496/17376/BeamDelivery_part1.pdf. (Cited on page 3.)

[15] M. Aicheler, P.N. Burrows, N. Catalan Lasheras, R. Corsini, M. Draper, J. Osborne, D. Schulte, S. Stapnes, and M.J. Stuart. *The Compact Linear Collider (CLIC) – Project Implementation Plan*. CERN Yellow Reports: Monographs. CERN, Mar. 2019. Available: https://doi.org/10.23731/CYRM-2018-004. (Cited on pages 5, 9, 10, and 37.)

[16] P. Raimondi and A. Seryi. Novel final focus design for future linear colliders. *Phys. Rev. Lett.*, 86:3779–3782, Apr. 2001. Available: https://link.aps.org/doi/10.1103/PhysRevLett.86.3779. (Cited on pages 7, 8, 24, and 26.)

[17] W. Singer, A. Brinkmann, R. Brinkmann, J. Iversen, A. Matheisen, W.-D. Moeller, A. Navitski, et al. Production of superconducting 1.3 GHz cavities for the European X-ray Free Electron Laser. *Phys. Rev. Accel. Beams*, 19:092001, Sep. 2016. Available: https://link.aps.org/doi/10.1103/PhysRevAccelBeams.19.092001. (Cited on page 7.)

[18] R. Tomás. Overview of the compact linear collider. *Phys. Rev. ST Accel. Beams*, 13:014801, 2010. Available: https://link.aps.org/doi/10.1103/PhysRevSTAB.13.014801. (Cited on page 8.)

[19] M. J. Boland et al. *Updated baseline for a staged Compact Linear Collider*. CERN, Geneva, Aug. 2016. Available: https://doi.org/10.5170/CERN-2016-004. (Cited on page 8.)

[20] F. Plassard. *Optics optimization of longer L* Beam Delivery System designs for CLIC and tuning of the ATF2 final focus system at ultra-low β^* using octupoles*. PhD thesis, Université Paris-Saclay, Oct. 2018. Available: https://cds.cern.ch/record/2646086. (Cited on pages 8, 26, 29, 37, 68, 69, 92, 99, and 116.)

[21] A. Winter. Physics Potential of CLIC Operation at 380 GeV. pages 189–192. 5, May 2017. Available: https://cds.cern.ch/record/2263676. (Cited on page 8.)

[22] N. Alipour Tehrani, J. Blaising, B. Cure, D. Dannheim, F. Duarte Ramos, et al. CLICdet: The post-CDR CLIC detector model. Technical report, CERN, Mar. 2017. Available: https://cds.cern.ch/record/2254048. (Cited on pages 10 and 61.)

[23] F. Plassard, A. Latina, E. Marin, R. Tomás, and P. Bambade. Quadrupole-free detector optics design for the compact linear collider final focus system at 3 tev. *Phys. Rev. Accel. Beams*, 21:011002, Jan. 2018. Available: https://link.aps.org/doi/10.1103/PhysRevAccelBeams.21.011002. (Cited on page 10.)

[24] CERN. Accelerator Overview. Available: https://clic.cern/accelerator-overview. (Cited on page 11.)

[25] G. Geschonke and A. Ghigo. CTF3 Design Report. Technical report, CERN, Geneva, May 2002. Available: https://cds.cern.ch/record/559331. (Cited on page 10.)

[26] R. Corsini. Experimental Verification of the CLIC Two-beam Scheme, Status and Outlook. In *Proc. IPAC'12*, pages 1101–1103, New Orleans, LA, USA, May 2012. JACoW Publishing, Geneva, Switzerland. Available: https://jacow.org/IPAC2012/papers/TUOBC01.pdf. (Cited on page 12.)

[27] Y. Honda et al. Achievement of Ultralow Emittance Beam in the Accelerator Test Facility Damping Ring. *Phys. Rev. Lett.*, 92:054802, Feb. 2004. Available: https://link.aps.org/doi/10.1103/PhysRevLett.92.054802. (Cited on page 12.)

[28] A. Aryshev, P. Bambade, D. R. Bett, L. Brunetti, P. N. Burrows, V. Cilento, A. Faus-Golfe, et al. ATF report 2020. Technical report, CERN, Geneva, Oct. 2020. Available: https://cds.cern.ch/record/2742899. (Cited on page 13.)

[29] B.I. Grishanov et al. ATF2 Proposal: v. 2. Technical report, CERN, Geneva, Jan. 2006. Available: https://cds.cern.ch/record/926364. (Cited on page 12.)

[30] T. Okugi. Achievement of Small Beam Size at ATF2 Beamline. In *28th International Linear Accelerator Conference*, pages 27–31, 2017. Available: https://doi.org/10.18429/JACoW-LINAC2016-MO3A02. (Cited on page 13.)

[31] ATF2 Technical Review, ILC-GDE. https://agenda.linearcollider.org/event/5973/, Apr. 2013. (Cited on page 13.)

[32] P. Korysko, P. N. Burrows, A. Latina, and A. Faus-Golfe. Wakefield effects and mitigation techniques for nanobeam production at the KEK Accelerator Test Facility 2. *Phys. Rev. Accel. Beams*, 23:121004, Dec. 2020. Available: https://link.aps.org/doi/10.1103/PhysRevAccelBeams.23.121004. (Cited on page 13.)

[33] R. Yang, A. Pastushenko, A. Aryshev, M. Bergamaschi, V. Cilento, A. Faus-Golfe, M. Fukuda, et al. Tuning the ultralow β^* optics at the KEK Accelerator Test Facility 2. *Phys. Rev. Accel. Beams*, 23:071003, Jul. 2020. Available: https://link.aps.org/doi/10.1103/PhysRevAccelBeams.23.071003. (Cited on pages 14, 67, 68, 72, 77, 99, and 109.)

[34] Rogelio Tomás et al. ATF2 Ultra-Low IP Betas Proposal. In *Particle Accelerator Conference (PAC 09)*, page WE6PFP024, 2010. Available: https://accelconf.web.cern.ch/pac2009/papers/we6pfp024.pdf. (Cited on pages 13 and 67.)

[35] M. Patecki et al. Towards Ultra-Low β^* in ATF2. In *Proc. 6th International Particle Accelerator Conference (IPAC'15), Richmond, VA, USA, May 3-8, 2015*, number 6 in International Particle Accelerator Conference, pages 38–41, Geneva, Switzerland, Jun. 2015. JACoW. Available: https://doi.org/10.18429/JACoW-IPAC2015-MOBC1. (Cited on pages 13, 67, and 77.)

[36] M. Patecki, D. Bett, E. Marin, F. Plassard, R. Tomás, K. Kubo, S. Kuroda, et al. Probing half β_y^* optics in the Accelerator Test Facility 2. *Phys. Rev. Accel. Beams*, 19:101001, Oct. 2016. Available: https://link.aps.org/doi/10.1103/PhysRevAccelBeams.19.101001. (Cited on page 13.)

[37] A. Wu Chao, K. H. Mess, M. Tigner, and F. Zimmermann. *Handbook of Accelerator Physics and Engineering*. World Scientific, 2nd edition, 2013. (Cited on pages 15, 19, 26, 28, and 29.)

[38] Helmut Wiedemann. *Particle accelerator physics*. Springer, Berlin, 3rd edition, 2007. (Cited on pages 15 and 26.)

[39] CERN. *CAS - CERN Accelerator School : 5th General Accelerator Physics Course: Jyväskylä, Finland 7 - 18 Sep 1992.*, Geneva, 1994. CERN. Available: https://cds.cern.ch/record/235242. (Cited on page 15.)

[40] S. Y. Lee. *Accelerator physics; 3rd ed.* World Scientific, Singapore, 2012. (Cited on page 15.)

[41] D. A. Edwards and M. J. Syphers. *An Introduction to the Physics of High-Energy Accelerators*. Wiley Series in Beam Physics and Accelerator Technology. Wiley, New York, 1992. (Cited on pages 15 and 16.)

[42] A. Wolski. Maxwell's Equations for Magnets. In *CERN Accelerator School: Course on Magnets*, pages 1–38, 3 2011. Available: https://doi.org/10.48550/arXiv.1103.0713. (Cited on page 15.)

[43] Madx - methodical accelerator design. Available: http://madx.web.cern.ch/madx/. (Cited on pages 16 and 44.)

[44] K. L. Brown. A first- and second-order matrix theory for the design of beam transport systems and charged particle spectrometers. Jan. 1971. Available: https://doi.org/10.2172/4742148. (Cited on pages 18, 20, 23, and 51.)

[45] R. Tomás. Nonlinear optimization of beam lines. *Phys. Rev. ST Accel. Beams*, 9:081001, Aug. 2006. Available: https://link.aps.org/doi/10.1103/PhysRevSTAB.9.081001. (Cited on pages 18 and 45.)

[46] R. Tomás. MAPCLASS: a code to optimize high order aberrations. Technical report, CERN, Jan. 2007. Available: https://cds.cern.ch/record/944769. (Cited on pages 19 and 85.)

[47] D. Martinez, A. Rosam, R. Tomás, and R. De Maria. MAPCLASS2: a code to aid the optimisation of lattice design. Nov. 2012. Available: https://cds.cern.ch/record/1491228. (Cited on page 19.)

[48] D. A. Popescu. Parallel Computing Methods For Particle Accelerator Design. Master's thesis, École polytechnique fédérale de Lausanne, Jul. 2013. Available: https://cds.cern.ch/record/1598904. (Cited on page 19.)

[49] F. Schmidt, E. Forest, and E. McIntosh. Introduction to the polymorphic tracking code: Fibre bundles, polymorphic Taylor types and "Exact tracking". Technical report, CERN, Geneva, Jul. 2002. Available: https://cds.cern.ch/record/573082. (Cited on pages 19 and 45.)

[50] E. Marin Lacoma. *Design and higher order optimisation of Final Focus Systems for Linear Colliders*. PhD thesis, Universitat Politècnica de Catalunya, Institut de Tecniques energetiques, Nov. 2012. Available: https://cds.cern.ch/record/1504285. (Cited on page 21.)

[51] K. L. Brown. Basic optics of the SLC final focus system. In *Workshop on the Physics of Linear Colliders*, Dec. 1988. Available: https://inspirehep.net/files/d60589c30dad183990bf5326fb21dacf. (Cited on page 24.)

[52] K. Oide. Final focus system with odd dispersion scheme. *Int. J. Mod. Phys. Proc. Suppl.*, 2, Suppl. 2B:861–863, 1993. Available: https://inspirehep.net/literature/336299. (Cited on page 24.)

[53] R. W. Assmann, F. Becker, R. Bossart, H. Braun, H. Burkhardt, G. Carron, W. Coosemans, et al. *A 3 TeV e^+e^- Linear Collider Based on CLIC Technology*. CERN Yellow Reports: Monographs. CERN, Geneva, 2000. Available: http://cds.cern.ch/record/461450. (Cited on page 25.)

[54] H. Garcia, A. Latina, and R. Tomas. Traditional Final Focus System for CLIC. In *Proc. IPAC'12*, pages 1858–1860, New Orleans, LA, USA, May 2012. JACoW Publishing, Geneva, Switzerland. Available: https://jacow.org/IPAC2012/papers/TUPPR022.pdf. (Cited on page 26.)

[55] K. Oide. Synchrotron-Radiation Limit on the Focusing of Electron Beams. *Phys. Rev. Lett.*, 61:1713–1715, Oct. 1988. Available: https://link.aps.org/doi/10.1103/PhysRevLett.61.1713. (Cited on page 26.)

[56] O.R. Blanco, R. Tomás, and P. Bambade. 2D-Oide effect. Sep. 2015. Available: https://cds.cern.ch/record/2053941. (Cited on page 27.)

[57] W. Herr and B. Muratori. Concept of luminosity. 2006. Available: https://cds.cern.ch/record/941318. (Cited on pages 27 and 37.)

[58] A. Pastushenko. Beam optics calculations for CLIC. Master's thesis, Université Paris-Saclay, Aug. 2018. Available: https://cds.cern.ch/record/2643797. (Cited on pages 29 and 37.)

[59] A.C. Dexter, G. Burt, P.K. Ambattu, V. Dolgashev, and R. Jones. Clic crab cavity design optimisation for maximum luminosity. *Nuclear Instruments and Methods in Physics Research Section A: Accelerators, Spectrometers, Detectors and Associated Equipment*, 657(1):45–51, 2011. Available: https://www.sciencedirect.com/science/article/pii/S0168900211010229. (Cited on page 30.)

[60] P. Chen and K. Yokoya. Disruption effects from the interaction of round e^+ e^- beams. *Phys. Rev. D*, 38:987–1000, Aug. 1988. Available: https://link.aps.org/doi/10.1103/PhysRevD.38.987. (Cited on page 30.)

[61] D. Schulte. Beam-Beam Effects in Linear Colliders. *ICFA Beam Dyn. Newslett.*, 69:237–245, 2016. Available: https://cds.cern.ch/record/2264414. (Cited on page 30.)

[62] P. Chen. Disruption effects from the collision of quasi-flat beams. In *Proceedings of International Conference on Particle Accelerators*, pages 617–619 vol.1, 1993. Available: https://inspirehep.net/literature/357044. (Cited on page 30.)

[63] R. P. Walker. Synchrotron radiation. 1994. Available: https://cds.cern.ch/record/398429. (Cited on page 31.)

[64] D. R. Bett, P. N. Burrows, C. Perry, R. Ramjiawan, N. Terunuma, K. Kubo, and T. Okugi. A sub-micron resolution, bunch-by-bunch beam trajectory feedback system and its application to reducing wakefield effects in single-pass beamlines. *Journal of Instrumentation*, 16(01):P01005–P01005, Jan. 2021. Available: http://dx.doi.org/10.1088/1748-0221/16/01/P01005. (Cited on page 35.)

[65] J. Tanabe. *Iron Dominated Electromagnets: Design, Fabrication, Assembly and Measurements*. SLAC, Stanford, CA, 2005. Available: https://cds.cern.ch/record/913759. (Cited on page 38.)

[66] M. Modena. CLIC project R&D studies: the magnet system for the 3 TeV. Technical report, CERN, Geneva, Mar. 2017. Available: https://cds.cern.ch/record/2267370. (Cited on page 40.)

[67] PLACET (Program for Linear Accelerator Correction and Efficiency Tests). https://clicsw.web.cern.ch/clicsw/. (Cited on page 47.)

[68] D. Schulte. PLACET: A Program to Simulate Drive Beams. In *Proc. EPAC'00*, Vienna, Austria, Jun. 2000. JACoW Publishing, Geneva, Switzerland. Available: https://jacow.org/e00/papers/TUP7B05.pdf. (Cited on page 47.)

[69] D. Schulte. Beam-Beam Simulations with GUINEA-PIG. Technical report, CERN, Mar. 1999. Available: https://cds.cern.ch/record/382453. (Cited on page 47.)

[70] D. Schulte. *Study of Electromagnetic and Hadronic Background in the Interaction Region of the TESLA Collider*. PhD thesis, Universität Hamburg, 1997. Available: https://cds.cern.ch/record/331845. (Cited on page 47.)

[71] T. O. Raubenheimer. NLC ZDR: Zero Order Design Report for the NEXT Linear Collider (Volume 1). Technical report, Jun. 2018. Available: https://www.osti.gov/biblio/257432. (Cited on page 58.)

[72] J. Resta-Lopez, D. Angal-Kalinin, B. Dalena, J. L. Fernandez-Hernando, F. Jackson, D. Schulte, A. Seryi, and R. Tomás. Status report of the baseline collimation system of CLIC. Part I. Status report of the baseline collimation system of the compact linear collider. Technical report, CERN, Apr. 2011. Available: https://cds.cern.ch/record/1344627. (Cited on page 61.)

[73] J. Resta-Lopez, D. Angal-Kalinin, B. Dalena, J. L. Fernandez-Hernando, F. Jackson, D. Schulte, A. Seryi, and R. Tomás. Status report of the baseline collimation system of CLIC. Part II. Status report of the baseline collimation system of the compact linear collider. Technical report, CERN, Apr. 2011. Available: https://cds.cern.ch/record/1344632. (Cited on page 61.)

[74] D. Arominski, A. Latina, and D. Schulte. Resistive Wall Effects in the CLIC Beam Delivery System. In *Proc. IPAC'19*, pages 258–261, Melbourne, Australia, May 2019. JACoW Publishing, Geneva, Switzerland. Available: https://accelconf.web.cern.ch/ipac2019/doi/JACoW-IPAC2019-MOPGW071. (Cited on page 61.)

[75] E. Marin, R. Tomás, P. Bambade, K. Kubo, T. Okugi, T. Tauchi, N. Terunuma, et al. Design and high order optimization of the Accelerator Test Facility lattices. *Phys. Rev. ST Accel. Beams*, 17:021002, Feb. 2014. Available: https://link.aps.org/doi/10.1103/PhysRevSTAB.17.021002. (Cited on page 68.)

[76] M. Patecki and R. Tomás. Effects of quadrupole fringe fields in final focus systems for linear colliders. *Phys. Rev. ST Accel. Beams*, 17:101002, Oct. 2014. Available: https://link.aps.org/doi/10.1103/PhysRevSTAB.17.101002. (Cited on page 68.)

[77] E. Marin, M. Modena, T. Tauchi, N. Terunuma, R. Tomas, and G. R. White. Specifications of the octupole magnets required for the ATF2 Ultra-low β^* lattice. May 2014. Available: https://www.osti.gov/biblio/1132851. (Cited on page 68.)

[78] J. Yan, Y. Yamaguchi, Y. Kamiya, S. Komamiya, M. Oroku, T. Okugi, N. Terunuma, et al. Measurement of nanometer electron beam sizes with laser interference using Shintake Monitor. *Nuclear Instruments and Methods in Physics Research Section A: Accelerators, Spectrometers, Detectors and Associated Equipment*, 740:131–137, 2014. Proceedings of the first European Advanced Accelerator Concepts Workshop 2013. Available: https://doi.org/10.1016/j.nima.2013.11.041. (Cited on pages 69 and 71.)

[79] T. Suehara, M. Oroku, T. Yamanaka, H. Yoda, T. Nakamura, Y. Kamiya, Y. Honda, et al. A nanometer beam size monitor for ATF2. *Nuclear Instruments and Methods in Physics Research Section A: Accelerators, Spectrometers, Detectors and Associated Equipment*, 616(1):1–8, 2010. Available: https://doi.org/10.1016/j.nima.2010.02.065. (Cited on page 69.)

[80] T. Shintake, H. Hayano, A. Hayakawa, Y. Ozaki, M. Ohashi, K. Yasuda, D. Walz, et al. Design of laser Compton spot size monitor. *Int. J. Mod. Phys. Proc. Suppl.*, 1, Suppl. 2A:215–218, Jul. 1993. Available: https://inspirehep.net/literature/340628. (Cited on page 69.)

[81] T. Shintake. Proposal of a nanometer beam size monitor for e^+e^- linear colliders. *Nuclear Instruments and Methods in Physics Research Section A: Accelerators, Spectrometers, Detectors and Associated Equipment*, 311(3):453–464, 1992. Available: https://doi.org/10.1016/0168-9002(92)90641-G. (Cited on page 69.)

[82] J. Yan, M. Oroku, Y. Yamaguchi, T. Yamanaka, Y. Kamiya, T. Suehara, S. Komamiya, et al. Shintake Monitor Nanometer Beam Size Measurement and Beam Tuning. *Phys. Procedia*, 37:1989–1996, Dec. 2012. Available: https://doi.org/10.1016/j.phpro.2012.02.522. (Cited on page 72.)

[83] S. Bai, A. Aryshev, P. Bambade, D. Mc Cormick, B. Bolzon, J. Gao, T. Tauchi, and F. Zhou. First beam waist measurements in the final focus beam line at the KEK Accelerator Test Facility. *Phys. Rev. ST Accel. Beams*, 13:092804, Sep. 2010. Available: https://link.aps.org/doi/10.1103/PhysRevSTAB.13.092804. (Cited on page 72.)

[84] A. Faus-Golfe, J. Alabau Gonzalvo, C. Blanch Gutierrez, D. McCormick, J. Cruz, M. Woodley, and G. White. Multi-OTR System for ATF2. *Physics Procedia*, 37:2072–2079, 2012. Proceedings of the 2nd International Conference on Technology and Instrumentation in Particle Physics (TIPP 2011). Available: https:

//www.sciencedirect.com/science/article/pii/S1875389212019219. (Cited on page 75.)

[85] Y. I. Kim et al. Cavity beam position monitor system for the Accelerator Test Facility 2. *Phys. Rev. ST Accel. Beams*, 15:042801, Apr. 2012. Available: https://link.aps.org/doi/10.1103/PhysRevSTAB.15.042801. (Cited on pages 75 and 92.)

[86] T. Okugi, S. Araki, P. Bambade, K. Kubo, S. Kurado, M. Masuzawa, E. Marin, et al. Linear and second order optics corrections for the KEK Accelerator Test Facility final focus beam line. *Phys. Rev. ST Accel. Beams*, 17:023501, Feb. 2014. Available: https://link.aps.org/doi/10.1103/PhysRevSTAB.17.023501. (Cited on pages 77, 80, and 87.)

[87] A. Pastushenko. Knobs construction and tuning routines for the ATF2 in Python with the interface to MAD-X and PTC. Available: http://github.com/drozzoff/ATF2_tuning. (Cited on pages 81 and 85.)

[88] Y. Nosochkov, P. Raimondi, T. O. Raubenheimer, Andrei Seryi, and M. Woodley. Tuning knobs for the NLC final focus. In *8th European Particle Accelerator Conference (EPAC 2002)*, pages 476–478, Jun. 2002. Available: https://doi.org/10.48550/arXiv.physics/0206068. (Cited on page 92.)

[89] V. Cilento, A. Pastushenko, R. Yang, R. Tomás Garcia, A. Faus-Golfe, N. Terunuma, T. Okugi, and K. Kubo. ATF2 Ultra-low beta study report for March 2019 run. Jan. 2020. Available: https://cds.cern.ch/record/2706505. (Cited on page 97.)